Nonlinear tidal resonance

Academisch Proefschrift

ter verkrijging van de graad van doctor
aan de Universiteit van Amsterdam
op gezag van de Rector Magnificus
prof. mr. P.F. van der Heijden
ten overstaan van een door het college
voor promoties ingestelde commissie,
in het openbaar te verdedigen
in de Aula der Universiteit
op donderdag 27 oktober 2005, te 14:00 uur
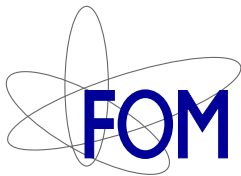
door

Guido Matthias Terra

geboren te Amersfoort

Promotiecommissie

Promotor: Prof. dr. A. Doelman
Copromotor: Dr. L.R.M. Maas

Overige leden: Prof. dr. J.T.F. Zimmerman
                 Prof. dr. H.E. de Swart
                 Prof. dr. J.G. Verwer
                 Prof. dr. T.H. Koornwinder

Faculteit der Natuurwetenschappen, Wiskunde en Informatica

Contents

Chapter 1

Introduction

Tides play an important role in the lives of many coastal communities. Due to resonance huge tidal ranges occur in particular bays whose natural (eigen-)period of oscillation is close to the tidal period. A well-known example is the Bay of Fundy where the highest tides in the world occur with tidal ranges up to 16 m at the end of the basin. But also in other places like the Dutch coast moderate tides still range 2–3 m. These ranges are larger than the *equilibrium tide*, which would occur if the Earth were completely covered by water in instantaneous balance with the forcing by the moon (54 cm) and the sun (26 cm). The change in water depth can have important consequences for docking ships and for navigation. Moreover tidal changes in the water level are accompanied by (strong) tidal currents, that do not only transport water, but also sediment (causing the morphology of the basin to change), nutrients and pollution (with important ecological consequences). An important property of tides is that they are highly predictable and tide tables are routinely prepared for years in advance and are consulted on a daily basis by mariners all around the world. According to Cartwright (1999), therefore the theory of tides is fully developed and finished by now. Although this may be true for the linear theory, describing many important characteristics of the (regular) tidal motion, some questions regarding the nonlinear dynamics of tides can still be raised. In fact, theoretical studies suggest "sudden"

(a) Docked at high tide   (b) Docked at low tide

Figure 1.1: Tanker at its berth in the Bay of Fundy

changes may occur in the resonance characteristics (amplification and phase lag) of coastal basins co-oscillating with the tide in an adjacent sea/ocean (Miles, 1981; Maas, 1997, and chapter 5 in this thesis). Moreover, under certain conditions those changes in tidal amplitude can be mathematically proven to occur in a chaotic way, such that tidal amplitudes and phases would become unpredictable (Maas & Doelman, 2002; Doelman *et al.*, 2002). And indeed, spurious reports on the locally occurring irregular nature of tides are quite old (Honda *et al.*, 1908) and more recently attempts have been made to reveal the chaotic nature of tides by Vittori (1992) and Frison *et al.* (1999).

The focus of this PhD thesis is on nonlinear effects on the resonance characteristics of co-oscillating tidal basins. In section 1.1.1 this introductory chapter begins with an overview of the generation of tides by the gravitational interaction of the Earth with the moon and the sun and of the response of the Earth's oceans to be described as one global resonator. Next two tide prediction techniques, which are based on linear principles, are considered in sections 1.1.2 and 1.1.3. The concept of co-oscillation, which is responsible for the tide in most coastal basins, is discussed in section 1.2. In particular, section 1.2.4 deals with radiation damping, the feedback from the co-oscillating basin on its forcing tide in the adjacent sea. Because this generally diminishes the amplitude of the tide at sea it effectively has a damping effect on the co-oscillating tide. Finally, three sources of nonlinearity are considered in section 1.3: quadratic friction, advective accelerations and water-level feedback on mass fluxes. Three aspects of nonlinear effects are distinguished: distortion of the *tidal curve* (mean tidal signal during the tidal period), changes to the *response curve* (amplification and phase lag between tidal response and forcing) and *modulation* of tidal amplitudes (slow changes of tidal phase and amplitude over time). The effects of quadratic friction are discussed separately in section 1.3.1. Advection and continuity effects distorting the tidal wave are treated in section 1.3.2. Their influence on response curves and modulation of tidal amplitudes is discussed in section 1.3.3. Obviously, section 1.3 does not treat nonlinear dynamics comprehensively. Finally, section 1.4 gives an overview of the respective chapters of this thesis that touch those topics in nonlinear tidal resonance.

1.1   The global tide

The apparent relation between the tide and the moon is so obvious that it was noted already early in history (from 300–400 BC, see Cartwright, 1999, page 6). Explanations of the phenomenon ranged from expansion due to lunar heating to dragging behind the moon through the moon's influence on atmospheric winds or aetheric "vortices". It was Newton (1687) who first put forward the modern view on the generation of tides, being caused by the spatial imbalance between the gravitational attraction of celestial bodies (most notably the sun and the moon) and the centrifugal acceleration by the rotation around their common centre of gravity.

1.1.1   The equilibrium tide

Figure 1.2 shows the tidal forces exerted on the Earth by a celestial body. At the centre of the Earth, the gravitational attraction towards the body balances the centrifugal acceleration due to the rotation around their common centre of gravity. The rotational
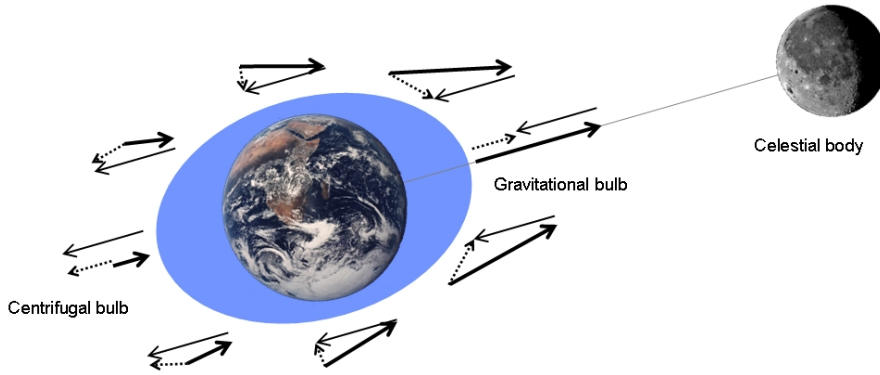
Figure 1.2: Sketch of tidal forcing (scales are exaggerated). Bold vectors represent the gravitational attraction by the celestial body like the moon. It differs in direction and magnitude over the globe. Slender vectors represent the centrifugal acceleration due to the revolution of the Earth around the common centre of gravity. It is the same over the entire globe. The resultant force drives the tide (dotted vectors), which would be as indicated if the Earth were entirely covered by water, responding to the tidal forces instantaneously. Due to the rotation of the Earth two high tides per day pass a specific point on the Earth, one higher than the other because of the declination of the celestial body.

motion being the same for the entire Earth, the centrifugal acceleration does not change over the Earth's surface. The gravitational attraction however, is stronger at the zenith point, near the celestial body, than at the nadir point, away from it. Therefore, net tidal forces occur. The vertical component of those tidal forces is small compared to gravity at the Earth's surface, hence is usually neglected and the equilibrium tide ζ_{eq} is introduced to describe the horizontal components such that the gradient $g\nabla\zeta_{eq}$ equals the horizontal tidal accelerations. In fact, this is the tide that would occur if the Earth were completely covered by water and neither friction nor the inertia of the water masses would play a role. Of course, there happen to be continents dividing the Earth's water masses in separate oceans. Moreover, friction cannot be neglected and the ocean's water depth is not deep enough to sustain tidal waves travelling fast enough to have inertia be neglected. Nevertheless, the equilibrium tide is still a useful concept to describe the direct forcing of the tide.

Because of the daily rotation of the Earth around its axis, the tidal forcing travels around the world at the same speed. This implies that high equilibrium tide at the zenith and nadir points passes a fixed location on the Earth's surface twice daily with low tides in between. This is called the *semi-diurnal tide*. However, because of the declination of the celestial body with respect to the equator (i.e. the latitude of the zenith point), the zenith and nadir do not pass at the same distance. Therefore, there is a *daily inequality* between the two high tides. At some locations this difference can be so profound that the *diurnal* component of the tide (the so-called *diurnal species*) of one high and one low tide per day dominates the tidal signal.

Up to this point, the specific celestial body responsible for the tidal signal was not taken into account. The main contributions to tidal forcing are from the sun and the moon. The equilibrium tide of the sun has a semi-diurnal period of 12 hours (the

S_2-tidal constituent) and an amplitude of about 13 cm. Because the moon revolves around the Earth in the same direction as the Earth's rotation, the semi-diurnal period of the lunar tide is about 12 hours and 25 minutes (the M_2-tidal constituent), with an amplitude of about 27 cm. Both the sun and the moon contribute to the K_1-tidal constituent at the period of one sidereal day, 23 hours and 56 minutes, one of the main diurnal components. Despite its mass, the tide produced by the sun is less than that by the moon, because it is much farther away from the Earth. Hence the M_2-tide is the dominant tidal constituent in most locations, but it is modulated by the S_2-tide; at new and full moon the sun and the moon cooperate to create a stronger (spring) tidal signal, whereas at half-moon the two counteract producing weaker (neap) tides.

However, spring and neap tides do not usually coincide with these lunar phases exactly. This is due to the retarding effects of inertia, friction and the barriers formed by land masses. The oceans and all adjacent seas should be considered as one large oscillator with many degrees of freedom, which responds to the forcing represented by the equilibrium tide. The direct tidal forcing on small closed basins is unable to produce large tidal amplitudes. Only the oceans themselves are large enough to show some resonance and seriously respond to the tidal forcing. From the oceans the tidal signal propagates to adjacent coastal seas through co-oscillation. A tidal signal that exists at the open boundaries of a coastal sea can be amplified due to resonance if the basin's natural modes of oscillation coincide with the frequency components of the tidal signal. Because it takes time for the tidal wave to travel from the ocean into the coastal seas, the *age of the tide*, i.e. the time-lag between lunar phase and subsequent spring/neap tide, increases when progressing into complex tidal systems. In the North Sea for example, the tidal wave comes in from the north, between Scotland and Greenland, propagates along the East Coast of the United Kingdom and gets reflected back to the north from the English Channel, producing a resonating standing wave pattern of about 7 quarters of a wavelength (figure 1.6(d)). The change of tidal phase along the East Coast has nothing to do with the equilibrium tide, which has almost the same phase over the entire basin. Actually the "age of the tide" can even be negative in some locations (Garrett & Munk, 1971), illustrating the fact that the entire world of connected water basins should be considered as one *global resonator*. Even the concept of the tide being generated in the oceans to be subsequently spread out into connected seas appears to be an incomplete description of the problem.

1.1.2   Harmonic analysis

When considering the observed time series of tidal water-level elevations, its spectrum is typically similar to the one shown in figure 1.3(a). It consists of a continuum part which tends to decrease for increasing frequency and a number of conspicuous discrete peaks. Most (if not all) of these peaks can be related to certain periods in the expansion of the forcing equilibrium tide. We already mentioned the M_2- and S_2-constituents and the influence of the declination leading to both diurnal (e.g. K_1) and monthly/yearly constituents. Other important modulations (hence additional constituents) arise due to the fact that the orbit of the moon is an ellipse instead of a circle and the precession of the moon's orbit due to gravitational perturbations by the sun. The tidal forces exerted by the moon are larger when it is closest to the Earth (at *perigee*) and smaller when it is farthest from the Earth (at *apogee*), which causes the M_2-tide to modulate on a monthly time scale, or equivalently the introduction of an
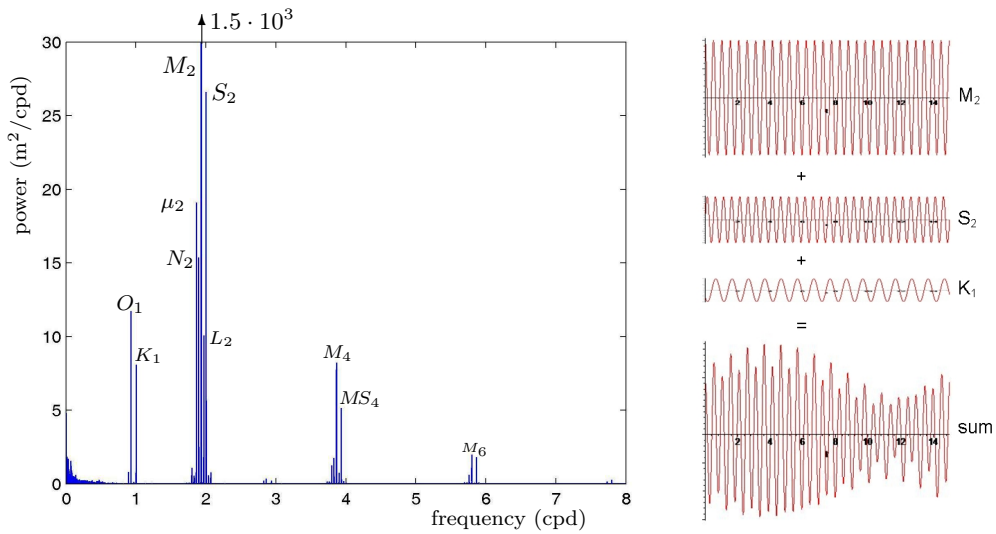
(a) Fourier spectrum of tidal water-level elevations at Harlingen, the Netherlands. Frequency on horizontal axis is in cycles per day. A number of important constituents have been identified by their Darwin symbol.

(b) Harmonic decomposition of a tidal signal in two semidiurnal constituents (M_2 and S_2) and one diurnal (K_1).

Figure 1.3: 1.3(a): Tidal power spectrum for Harlingen, in the Dutch Wadden Sea, calculated from ten-minutes data downloaded from www.waterbase.nl, which provides public access to the measurements by the Dutch National Institute for Coastal and Marine Management (RIKZ), shows the peaked structure of the tidal spectrum. 1.3(b): an illustration of the harmonic decomposition in the important components M_2, S_2 and K_1 in order to illustrate the influence of the two beating semidiurnal frequencies leading to the spring-neap tidal cycle and one diurnal frequency causing a daily inequality between successive high or low tides.

additional tidal constituent one cycle per month apart from M_2. As a consequence, so-called *perigean spring tides* are exceptionally large when constructive interference of the solar and lunar forcing coincides with lunar perigee, followed by significantly smaller *apogean spring tides* half a month later. Other periods of interest are the regression of the lunar perigee in 8.85 years and the precession of the lunar orbit, changing its angle with the equator and the season in which perigean spring tides occur, with a period of 18.61 years (Munk & Cartwright, 1966).

The continuum part of the spectrum is related to nonstationary (i.e. aperiodic) motion. It is often attributed to disturbances of meteorological nature. Apart from a smooth decay for increasing frequencies, the continuum spectrum shows cusp-like peaks around the strong spectral lines (Munk & Cartwright, 1966, p. 534), which may be related to nonstationary modulations of the principal tidal constituents. They are to be distinguished from the periodic modulations of astronomical origin, because the latter produce distinct (discrete) side-peaks. Nonlinear processes that may be responsible will be discussed in section 1.3.3.

It was sir William Thomson (Lord Kelvin) who first capitalized on the peaked structure of the tidal spectrum by expanding time series of tidal water-level elevations into a sum of harmonic functions at a number of distinct tidal frequencies. By

analysing the tidal record at one spot, the so-called *harmonic constants* for that par-
ticular location can be obtained, i.e. the amplitudes and phases of the sinusoids at
the tidal frequencies that are taken into account. This is similar to a Fourier series
expansion except that, instead of using a regular grid of frequencies without consid-
ering the tidal origin of the time series, the frequencies of the sinusoids are chosen
according to the ones occurring in the forcing equilibrium tide. In such manner, the
harmonic constants for many locations have been determined. Having determined the
harmonic constants, one can use the harmonic sum for tide prediction. An illustra-
tion of the decomposition in the three usually most important constituents is given
in figure 1.3(b). The two semi-diurnal constituents M_2 and S_2 interfere, yielding
the spring-neap tidal cycle. The diurnal K_1-constituent causes the daily inequality
between consecutive high and low waters.

Harmonic analysis is still the most widely used method for constructing tide tables.
However, in order to accurately capture all processes in the tidal signal, the required
number of tidal constituents can become quite large, especially in complex coastal
areas where not only constituents directly forced by the equilibrium tide, but also
compound frequencies arising from nonlinear interactions (see also section 1.3.2 and
references therein) need to be included. Moreover, the harmonic constants appear
not to be constant on a longer timescale (Doodson, 1924; Gutiérrez *et al.*, 1981).
Partly, this is explained by the restriction of the expansion to the most important
constituents. Changes due to the nodal cycle (the precession of the moon's orbit in
18.6 years) could be incorporated by including the consequent side-peaks, one cycle
every 18.6 years apart from the principal constituents in the spectrum, but would
imply a very large number of constituents. By not including them, the harmonic
constants for the constituents that are taken into account vary from year to year.
These changes are quite predictable and usually accounted for by using so-called
"nodal factors" to correct the harmonic constants. However, Doodson (1924) reports
that not all changes of the harmonic constants can be explained in this way. Moreover,
the continuum part of the tidal spectrum cannot be captured by the harmonic analysis
at all and is often considered as residual noise.

1.1.3   Response method

Another way to tackle the problem of tide prediction was introduced by Munk &
Cartwright (1966). They criticized harmonic analysis for using astronomical (Kepler-
Newtonian) tidal theory only for determining the frequencies at which tidal energy
is expected. Harmonic constants are determined solely from observed tidal records;
the theoretical information about the amplitude of the different tidal components in
the equilibrium tide is not used at all. This not only weakens the description from a
physical point of view, but also means that potentially useful information is dismissed
while the determination of harmonic constants is contaminated by measurement noise.
Munk & Cartwright (1966) proposed to write the tide prediction directly in terms of
the equilibrium tide (expanded in spherical harmonics) with time lags and weighing
factors:

$$\zeta(t) = \text{Re}\left[\sum_j \int_0^\infty \bar{c}_j(t-\tau)\, w_j(\tau)\, \mathrm{d}\tau\right], \qquad (1.1)$$

in which $\bar{c}_j(t)$ is an input function calculated from the global equilibrium tide at time t
(e.g. the coefficient of the expansion of the equilibrium tide in spherical harmonics)
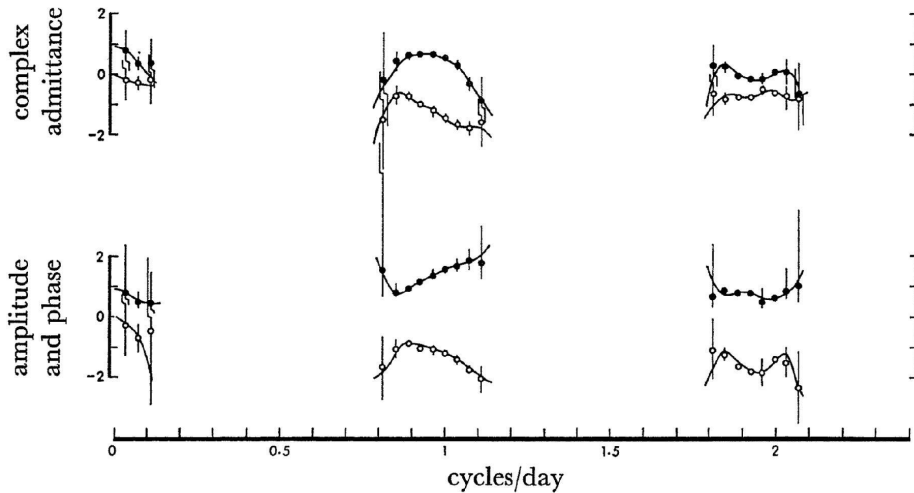
Figure 1.4: Admittances derived by Munk & Cartwright (1966) for Honolulu: by comparing the observed tidal signal at Honolulu with the corresponding components in the equilibrium tide, the complex amplification factor between the response at Honolulu and the astronomical forcing can be obtained as a function of frequency. It can be visualized either by the real and imaginary part or by the modulus and argument, the latter representing the amplification factor and phase lag at the respective frequency. This figure is a reproduction of Figure 1 (lower two panels) from their paper.

and $w_j(\tau)$ is a weighing function describing the tidal response at the particular location to unit tidal forcing, to be found empirically. The Fourier transform of the weights $w_j(\tau)$ corresponds with the admittance of the tidal resonator as a function of frequency, i.e. the amplification factor and phase difference between the observed tide and the equilibrium tide at the respective frequency. By discretising and truncating the integral (1.1) to a discrete and finite set of time lags τ_s, Munk & Cartwright (1966) effectively imposed a "credo of smoothness", limiting the resolution of possible variability in the admittance as a function of frequency. This "credo of smoothness" is equivalent to stating that there are no sharp resonance peaks in the response of the global tidal resonator. In fact, their results for Honolulu show no indications of abrupt changes in the admittance, see figure 1.4. This implies that subsidiary constituents experience essentially the same admittance as nearby principal constituents. Consequently, nodal modulations can be easily incorporated into the theory by modulating the input functions, whereas the number of independent harmonic constants to be determined from the observations becomes very large using harmonic analysis. However, the improvement in predictive accuracy is limited, so the response method has never been commonly used, except for research purposes.

Like harmonic analysis, the response method is basically a linear method in the sense that it describes the response of the global tidal resonator to tidal forcing at specific frequencies by oscillating at the same frequencies. Harmonic analysis can be adapted to accommodate weak nonlinear perturbations by introducing nonlinearly

generated compound constituents. Likewise, the response method can be extended by
adding bilinear input functions $\bar{c}_j(t-\tau)\cdot\bar{c}'_j(t-\tau')$ to the formalism (1.1). Simon (1991)
basically applied this nonlinear extension of the response method when developing the
species concordance method for the prediction of the tide in complex estuaries along
the French coast. He first reduced the tidal signal into "reduced vectors", which are
the complex amplitudes of the species of the tide (the diurnal, semidiurnal, terdiurnal,
etc. component of the tide). Then the response method was applied to predict the
reduced vectors at a certain location, using as input functions the reduced vector in
some nearby reference port for which the tide (hence the reduced vectors) can be
easily predicted by linear methods. By including products of reduced vectors as input
vectors, the nonlinear distortion of the tide (see also section 1.3.2) progressing into the
tidal basin is accounted for. But using either harmonic analysis, the response method
or the species concordance method, the response remains limited to a discrete set of
frequencies, unable to explain the continuum part of the spectrum associated with
nonstationary modulations of response amplitudes.

1.1.4   Classification of the tide

Figure 1.5 shows the actual distribution of the amplitudes of the diurnal K_1-constituent
and the semi-diurnal M_2-constituent. White lines are the *cotidal lines* connecting lo-
cations where high tide occurs simultaneously. The tidal amplitudes are represented
by colour contours. The equilibrium tide discussed in section 1.1.1 is deformed by the
presence of the continents. In the structure of the tide within e.g. the Atlantic Ocean,
one can recognize the normal mode of that basin, with the largest tidal amplitudes
occurring at the coastal boundaries (see also section 1.2 on resonance, section 1.2.1
in particular, and Platzman, 1991). By comparing figure 1.5(a) and 1.5(b) the *type*
of the tide can be inferred: where the M_2-tide is dominant and K_1 is hardly present,
the tide is mainly semi-diurnal with two high and two low tides occurring each day. If
the M_2-tide is weak, whereas the K_1-constituent is important, a diurnal tide with one
period each day is found. Mixed tides occur if both the diurnal and the semi-diurnal
species are significant. In a pre-dominantly semi-diurnal mixed tide, high and low tide
occur twice a day one being much higher/lower than the other (the *daily inequality*).
A pre-dominantly diurnal mixed tide is characterized by a one-day period at spring
tides, but when the diurnal amplitude is small at neap tides, the semi-diurnal signal
with two high tides and two low tides each day becomes more important.

Around the world, large semi-diurnal tides are more common than large diurnal
tides. The diurnal tide is important along the Antarctic, in Southeast Asia and the
Sea of Okhotsk (between Kamchatka and the Russian mainland) and in the Caribbean
Sea/Gulf of Mexico, where the semi-diurnal tide is particularly weak. Moreover, due
to local resonance conditions, which depend on the frequency of the tidal constituents,
the character of the tide can even be different in adjacent reaches of a single bay
(Burling *et al.*, 2002). Extremely large tides are of interest not only as an impressive
natural phenomenon but also because of the possibility to harvest the tidal energy as a
sustainable source of electricity. The feasibility of constructing power plants for com-
mercial exploitation has been studied for a number of locations where large tides
are found (see `http://www.worldenergy.org/wec-geis/publications/reports/`
`ser/tide/tide.asp`). Using the locations that have been identified as potential spots
for tidal power plants as a guideline, an overview of the world's largest tides will be
given in the remainder of this section.
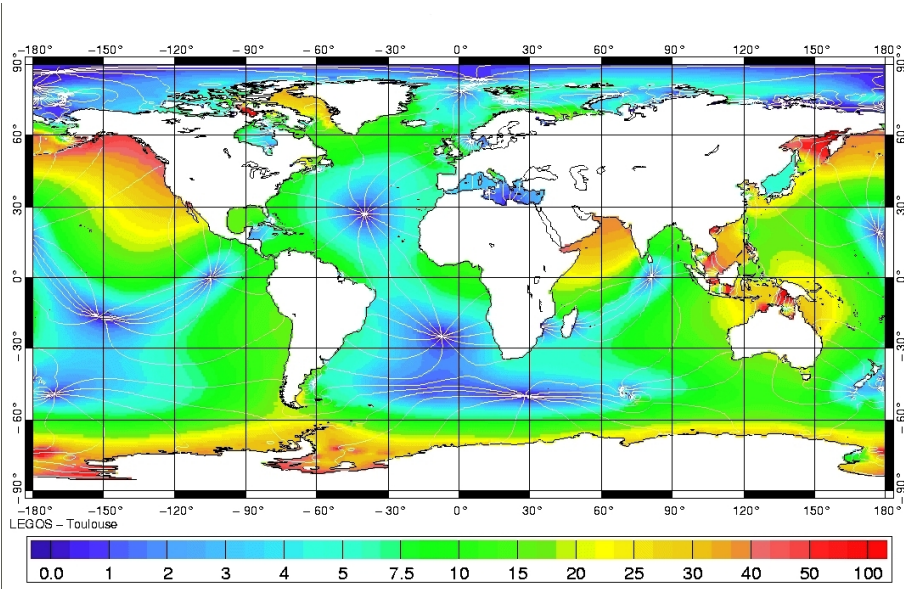
(a) Global distribution of K_1-amplitude (cm) and K_1-cotidal lines
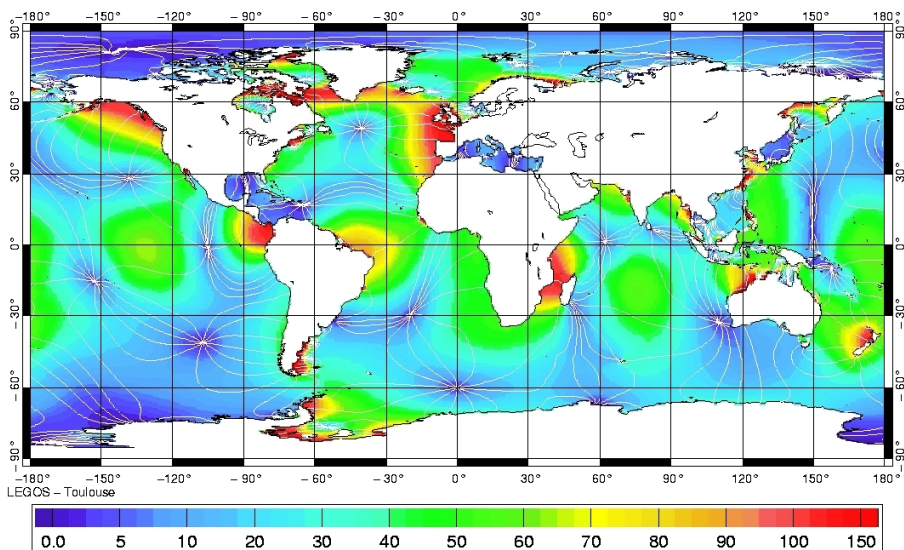
(b) Global distribution of M_2-amplitude (cm) and M_2-cotidal lines

Figure 1.5: Distribution of the diurnal K_1-constituent and the semi-diurnal M_2-constituent. Colours denote amplitude in cm, white cotidal lines connect locations at which high tide occurs simultaneously. A diurnal tide is found at locations where K_1 dominates, a semi-diurnal tide if M_2 is much larger. Mixed tides occur when both are significant. These figures were obtained combining a finite element model with observations from satellite altimetry and in situ measurements by Lefèvre *et al.* (2002), and have been downloaded from http://www.jason.oceanobs.com/html/applications/marees/200010_uk.html.

In the 1960's, a barrage was built across the Rance tidal estuary in Brittany, France, which houses 24 two-way turbines with a total capacity of 240 MW, to generate electricity from the flood and ebb-tidal currents. With 13 m tidal range, this location has one of the world's largest tides. The Bay of Fundy is another likely candidate with the world's largest tides up to 16 m tidal range and the geography of the upper part, the Minas basin, that could be closed relatively easily, but Canada has chosen to focus on the development of conventional hydropower plants. In the northwestern region of Australia, large tides of about 7 metres tidal range occur as well. A two-basin tidal power plant was considered here, one basin filled at high tide, one emptied at low tide, with a channel driving conventional one-way turbines in between. With this scheme, around-the-clock power could be generated as needed circumventing the inherent variability of tidal power, but it has not been implemented at this large scale yet. A number of small scale tidal power plants were built along the southeast coast of China, from 1958 onwards; in the East China Sea large semi-diurnal tides occur, in the South China Sea, large diurnal tides are present. The majority of these early tidal power plants have now been decommissioned, for a variety of reasons. In the Northeast of the Russian federation (Sea of Okhotsk), large diurnal and semi-diurnal tides occur. Design studies for tidal plants in this area have been conducted since the 1930's. Apart from a (successful) pilot plant near Murmansk at the White Sea in northwest Russia, the plans have not progressed beyond the design phase. Other locations with large tides that have been considered as potential spots for tidal power plants are in Mexico (Gulf of California), Chile, Argentina (Patagonian Coast), Korea (East China Sea) and India (both in the northeast and northwest corners of the country. Note that, although the use of tidal energy reduces carbon-dioxide emissions, the local environmental effects on the habitats of fish, birds and other animals can be damaging. The reduction of tidal flow reduces flushing of the basin and a loss in water quality, species that depend on intertidal flats may lose their feeding grounds and fish may be blocked from upstream waters by the barrage, amongst other things.

1.2   Local resonance

Tides in coastal basins are often much larger than the equilibrium tide mentioned in section 1.1.1. Depending on the shape and dimensions of the basin, the tide can be amplified. This is not primarily caused by cumulation of the tidal wave into shallowing and narrowing waters, but mainly by resonance of the tidal frequencies with the natural frequencies of the basin's free oscillations. The eigen-oscillations of the basin are determined by its dimensions. The response characteristics may be as diverse as the number of different coastal basins on the Earth. The potential success of the response method lies in the fact that the *quality* or *Q-factor*, defined as resonance frequency divided by peak width[1] measuring the sharpness of the resonance peak, of the global tidal resonator is low, so the response characteristics do not change much with frequency. For highly resonant coastal basins, such as the famous Bay of Fundy with tidal amplitudes up to 8 m, the response characteristics may be more sharply peaked around the eigenfrequencies of the basin. In this section two types of coastal resonance are discussed: *quarter wavelength resonance* in narrow rectangular basins such as the Bay of Fundy and *Helmholtz resonance* in almost enclosed basins such as

---

[1]This is one of several definitions that can be found in the literature. For a harmonic oscillator with linear friction those different definitions are equivalent.

many basins in the Dutch Wadden Sea, behind inlet between barrier islands. Next, section 1.2.3 briefly introduces secondary undulations at periods of several minutes accompanying the primary tidal signal. Finally, the connection between the tides in coastal basins with the global tidal resonator is discussed in section 1.2.4 which deals with the boundary condition at the open boundary between the co-oscillating basin and the adjacent sea.
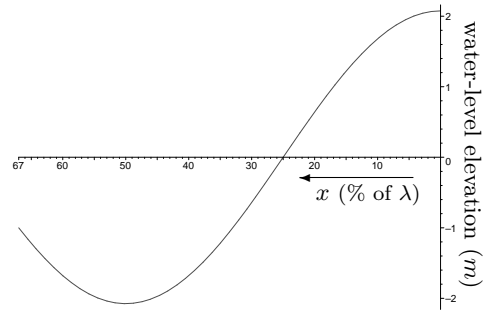
1.2.1   Quarter-wavelength resonance

Consider a rectangular basin of width B, length L and depth H, which co-oscillates with the tide of period T (usually about either 12 or 24 hours) in an adjacent sea or ocean, as shown in figure 1.6(a). The tidal wavelength $\lambda = \sqrt{gH}T$ is usually much larger than the water depth H ($\lambda \approx 450$ km for $H = 10$ m and $T \approx 12$ hours). In that case, the basin can be treated as shallow. Furthermore, if the basin is sufficiently narrow and the tidal amplitude is small compared to the water depth, the water motion is essentially one-dimensional directed along the longitudinal axis of the basin. Under those conditions the linear shallow water equations reduce to a simple wave equation. The tide in such a basin will be a standing wave illustrated in figure 1.6(b), where $L = 0.67\lambda$. Because of the linearity of this model, the vertical axis can be scaled with the exterior tide at the open boundary, which is chosen to be 1 m for the purpose of illustration. During each tidal period the water level oscillates back and forth between this curve and its antipode. The tide is amplified within the basin up to a factor of 2 on the crests, whereas the water level does not change at all at the knots, although the corresponding tidal currents are maximal at those locations. Resonance occurs if the length of the basin is an odd number of times a quarter of a wavelength, hence the name *quarter-wavelength resonance*. Without dissipation of energy, the amplification would become infinite in this case. Radiation damping would cause the tidal amplitude to become zero at the open boundary, such that the knot of the standing wave would be exactly at the entrance of the basin and a finite response is possible despite infinite amplification, see also section 1.2.4. Dissipation of energy is possible due to bottom friction which attenuates the tide decreasing the amplification factor and introducing additional phase lag.

The rotation of the Earth becomes important if the width B is not much smaller than the Rossby radius of deformation $\sqrt{gH}/f$, in which the Coriolis parameter $f = 2\Omega \sin(\theta)$ is the local vertical component of the rotation vector of the Earth, with $\Omega = 7.3 \cdot 10^{-5}$ rad s^{-1} the angular velocity of the Earth around its axis and θ the latitude. In that case, the Coriolis force causes currents to deflect to the right (on the northern hemisphere) and a travelling tidal wave to be stronger at the coast on the right side relative to the direction of propagation. Because the standing wave pattern described above is composed of an incoming and reflected travelling wave, its structure changes. The incoming wave is dominant at the right hand side of the basin (seen from the sea) and the reflected wave is dominant at the other side. The two have equal amplitude at the central axis of the basin only, so the knots from figure 1.6(b) which would be lines of zero amplitude in the two-dimensional setting, collapse into single *amphidromic points* at the central axis. Due to the Coriolis force the tidal wave rotates around these amphidromic points in a counterclockwise fashion. A clear example of such an amphidromic system can be found in the Adriatic sea, for which the tidal amplitudes and phases are shown in figure 1.6(c). Another example is offered by the North Sea. Even though the North Sea is certainly not rectangular nor
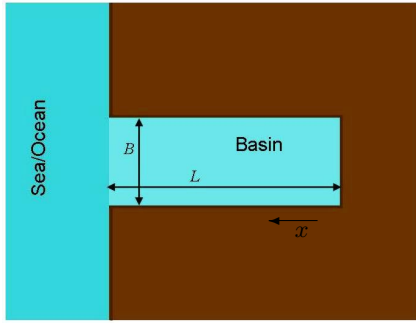
(a) Quarter-wavelength resonator: top view

(b) Snapshot of spatial structure of the tide
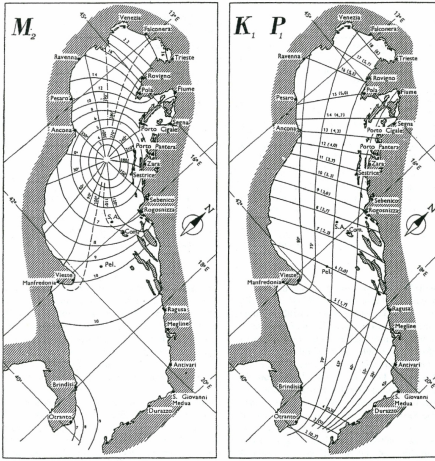
(c) Tidal maps of the Adriatic Sea, iso-range and co-tidal lines for the semidiurnal (M_2) and diurnal (K_1) components respectively
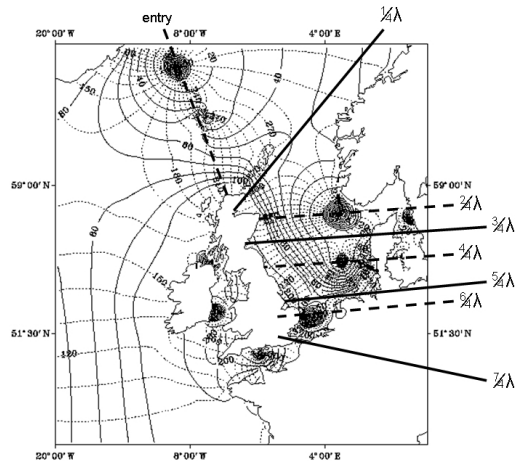
(d) The North Sea interpreted as a $\frac{7}{4}\lambda$-resonator

Figure 1.6: Quarter-wavelength resonators: a rectangular basin of depth H, length L and width B. The tide in such a basin is a standing wave, illustrated for length $L = 0.67\lambda$ in 1.6(b). It shows a snapshot of the tide's spatial structure at low tide at the entrance (high tide at the end of the basin). The water level oscillates up and down between plus and minus this value during one tidal period. Two geophysical examples that can be considered as quarter-wavelength resonators are shown in 1.6(c) and 1.6(d). In the Adriatic Sea the wavelength of the diurnal tide is longer than four times the basin length and behaves as a quarter-wavelength mode with hardly any cross-sectional differences. The semidiurnal tide has a shorter period and wavelength, so an amphidromic point with the tidal wave rotating around it is found. The tide in the North Sea is clearly affected by the Earth's rotation as well. 1.6(c) is reproduced from Cushman-Roisin & Naimie (2002), the results being obtained from coastal observations by Polli (1960). 1.6(d) has been downloaded from www.met.ed.ac.uk/ganes/finalr/report7.

of constant depth, the structure of amphidromic systems can clearly be identified in figure 1.6(d). As such, it makes sense to try to interpret the North Sea as a quarter-wavelength resonator as well. The solid and dashed lines drawn in figure 1.6(d) denote the approximate positions of the crests and knots, according to which it contains seven quarters of a wavelength, explaining the large tides in the English Channel and the German Bight.

1.2.2   Helmholtz resonance

For the eigenfrequencies of quarter-wavelength resonators to be comparable to the tidal frequencies, the length of the basin must be quite large ($\gtrsim$ 100 km). In smaller basins the eigenfrequencies are much higher, such that the slow tidal oscillations are not amplified. However, in a particular class of basins, which are connected with the exterior sea or ocean through a narrow inlet only (see figure 1.7), the lowest eigenmode can be particularly slow. The wavelength of this *Helmholtz* or *pumping mode* is much larger than the dimensions of the basin. Hence the spatial structure of the mode is characterized by a uniform tide within the basin, with all dynamics taking place along the channel between the basin and the exterior sea. The oscillator is forced by the water-level (hence pressure) difference between the sea and the basin. Its inertia is caused by the water mass flowing through the channel. The flux through the channel causes the water level in the basin to rise (or fall) constituting the restoring force sustaining the oscillator.

Because the water level within the basin can be captured by a single value, a relatively simple model can be used to describe the Helmholtz mode. The continuity equation (1.2b) covers mass conservation; the flux of water flowing into the basin accounts for the water-level rise within the basin. The momentum equation (1.2a) is Newton's law equating the acceleration of fluid particles in the channel to the pressure gradient due to water-level differences, counteracted by friction. The corresponding equations are

$$\frac{\mathrm{d}u}{\mathrm{d}t} = \frac{g}{L}\,(\zeta_e - \zeta) - \tau_f, \qquad (1.2a)$$

$$A\,\frac{\mathrm{d}\zeta}{\mathrm{d}t} = O\,u, \qquad (1.2b)$$

in which u is the velocity of the current into the basin, ζ and ζ_e are the water-level elevation within the basin and at sea, respectively, and τ_f is the contribution of friction (see section 3.2 for more details). The basin parameters of interest are the length and cross-sectional area of the channel, L and O respectively, and the area of the basin A. Combining the two equations, one finds the Helmholtz frequency $\omega_0{}^2 = \frac{gO}{AL}$, which is typically much lower than the higher (sloshing) modes for which the water level is not uniform within the basin.

1.2.3   Secondary undulations

The configuration of a narrow channel connecting an almost enclosed basin to the exterior sea or ocean, is common to many (man-made) harbours as well. However, their dimensions are usually much smaller than the geophysical examples mentioned in the previous section. As mentioned before, this increases the basin's eigenfrequencies.

(a) Helmholtz resonator: top view

(b) Snapshot of Helmholtz mode at high tide

(c) Interpretation of the Dutch Wadden Sea as a number of separate Helmholtz resonators
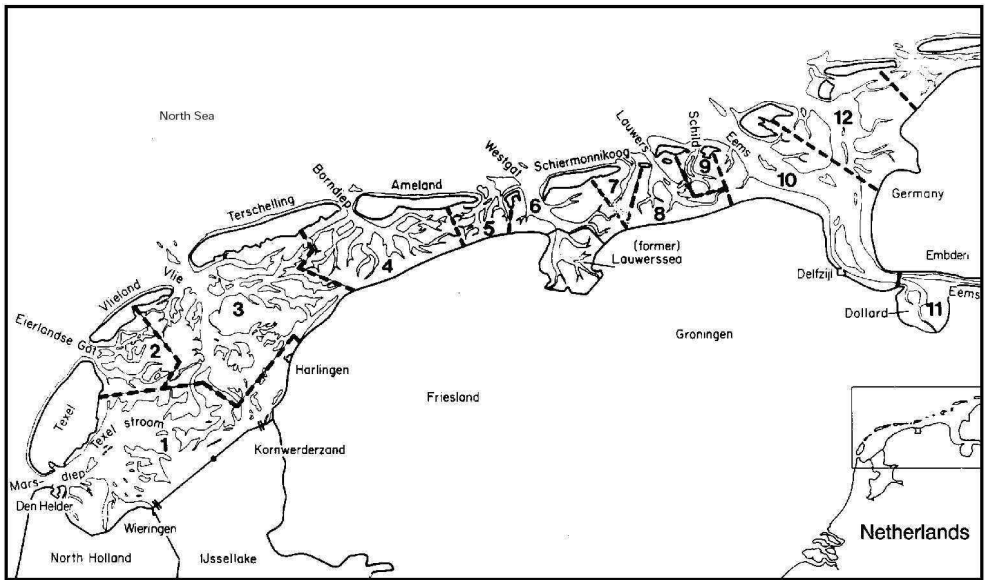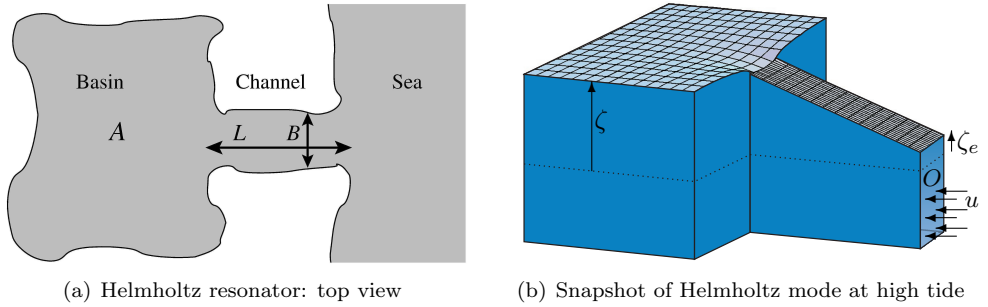
Figure 1.7: Helmholtz resonators: an almost-enclosed basin of area A, connected to the exterior sea by a narrow inlet of length L and cross-section $O = BH$, where B is its width and H the depth. The lowest eigenfrequency corresponds with the Helmholtz mode with almost uniform water level within the basin, as illustrated in 1.7(b). Water level elevations within the basin (ζ) and at sea (ζ_e) are measured relative to the water level in rest. Examples can be found in the Dutch Wadden Sea, where the basins behind the backbarrier islands can be considered as a number of Helmholtz resonators separated by their watersheds (Maas, 1997).

Consequently, *harbour oscillations* with periods of several minutes to hours occur in many harbours, where they may pose a threat to ships docked at the quay to be (un)loaded. Explanations for the origin of these oscillations are diverse: atmospheric pressure perturbations (Hibiya & Kajiura, 1982), internal wave activity (Giese & Chapman, 1990), seismic activity (tsunamis), current shear (Fabrikant, 1995) or non-linear setup/setdown by wave groups (Bowers, 1977; De Girolamo, 1996). In the presence of tides, the oscillations on this timescale are often called *secondary undulations* accompanying the primary tidal signal, which has a larger amplitude over a longer timescale. However, observations of the corresponding currents show that the secondary currents can be of the same order of magnitude as those corresponding to the primary tidal signal (Golmen *et al.*, 1994). Based on observations of water-level elevations in over 50 bays adjacent to Japan, Honda *et al.* (1908) and Nakano (1932) speculate on some nonlinear coupling of the secondary undulations to the tide (Honda *et al.*, 1908; Nakano, 1932), because their persistence seems to indicate an ever-present source.

The emphasis in this thesis is mainly on tides, both in its use of terminology and focus on forcing at a discrete set of frequencies. However, many of the results are equally applicable to the *infragravity waves* (Okihiro & Guza, 1995), with much smaller periods of a few minutes to hours, that are discussed in this subsection. Historically, secondary undulations have been studied less extensively, because they are less important for water-level elevations. Therefore, unexpected observational results are more likely when focusing on secondary undulations than when considering tidal records that have been studied much better already.

1.2.4 Radiation damping

In principle the entire Earth should be considered as one global tidal resonator. When trying to focus on one particular coastal basin, care has to be taken with respect to the open boundary with the adjacent ocean/sea that connects it to the rest of the world's water masses. Tidal motion in such a single basin is partly due to direct astronomical forcing through the equilibrium tide and partly due to co-oscillation with the tide that propagates into the basin from adjacent oceans/seas. The contribution of direct (local) tidal forcing is usually negligible compared to the co-oscillating tide. Garrett (1975) decomposed the tidal water-level elevation ζ_b in a basin and ζ_e in the exterior sea into three terms, $\zeta_b = \zeta_b^{(1)} + \zeta_{bb}^{(2)} + \zeta_{be}^{(2)}$ and $\zeta_e = \zeta_e^{(1)} + \zeta_{ee}^{(2)} + \zeta_{eb}^{(2)}$, see figure 1.8. Following his notation, $\zeta_b^{(1)}$ is the tide in the basin generated by the local tidal forces within the basin if the boundary between the basin and the exterior sea were closed. $\zeta_{bb}^{(2)}$ denotes the correction to the locally generated tide because of the open boundary, whereas $\zeta_{be}^{(2)}$ is the co-oscillating tide within the basin generated by the tidal forces outside of it. Similarly $\zeta_e^{(1)}$ denotes the tide at the exterior sea if the basin were closed, $\zeta_{ee}^{(2)}$ is the scattered wave due to the interaction of $\zeta_e^{(1)}$ with the basin, and the radiated wave $\zeta_{eb}^{(2)}$ contains part of the energy that was locally forced by the equilibrium tide within the basin. This is an improvement on the decomposition by Defant (1961).The latter defined the local tide $\zeta_b^{(loc)}$ to be the tide in the presence of local tidal forces and $\zeta_b^{(loc)} = 0$ at the open boundary. The co-oscillating tide $\zeta_b^{(co)}$ was defined as the tide neglecting local tidal forces and $\zeta_b^{(co)} = \zeta_e$ to be the observed tide at the open boundary. Although this decomposition is possible from a

(a) Local astronomical forcing within the basin   (b) Forcing from the exterior sea
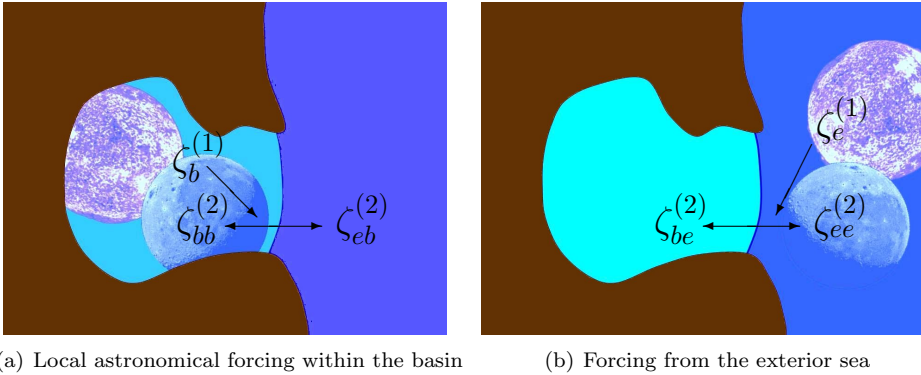
Figure 1.8: Garrett's (1975) decomposition of the tide in a co-oscillating tidal basin. (a) shows the situation if the astronomical forcing were confined within the basin. It forces $\zeta_b^{(1)}$ if the boundary with the exterior sea were closed. The interaction through the boundary causes some energy to radiate outwards as $\zeta_{eb}^{(2)}$ and a correction $\zeta_{bb}^{(2)}$ to the tide within the basin. These contributions are usually negligible compared to the contributions depicted in (b), which would occur if the astronomical forcing were confined to the exterior. In that case $\zeta_b^{(1)}$ were forced in the exterior sea if the basin were closed and the interaction through the open boundary causes the co-oscillating tide $\zeta_{be}^{(2)}$ and the scattered wave $\zeta_{ee}^{(2)}$.

mathematical point of view, it means that if the tidal forces were confined to the basin, the resulting tide ($\zeta_b^{(1)} + \zeta_{bb}^{(2)}$ in Garrett's (1975) notation) would still be interpreted as partly co-oscillating, because it is non-zero at the open boundary.

  Neglecting the locally generated tide in Garrett's (1975) decomposition, in order to focus on the co-oscillation problem, leads to $\zeta_b = \zeta_{be}^{(2)}$ in the basin and $\zeta_e = \zeta_e^{(1)} + \zeta_{ee}^{(2)}$ at the exterior sea. The externally generated tide at sea $\zeta_e^{(1)}$, if the basin were closed, does not depend on the response in the basin, so when investigating the basin's response characteristics (amplification factor and phase lag of the tide in the basin with respect to the tide at the exterior sea) as a function of basin geometry such as depth, width and length scales, $\zeta_e^{(1)}$ will remain constant. Hence, it makes sense to prescribe $\zeta_e^{(1)}$ when developing a model for the co-oscillating tide. The boundary conditions between the basin and the exterior sea then require a match of both $\zeta_b = \zeta_e$ and the flux through the open boundary. This differs from directly prescribing the water level ζ_b at the open boundary, which would be the relevant boundary condition from Defant's (1961) definition, because of the unknown contribution to ζ_e by the scattered wave $\zeta_{ee}^{(2)}$. The open connection between the basin and the exterior sea leads to the scattered wave $\zeta_{ee}^{(2)}$ back into the sea and changes the actual water-level elevations at the boundary. This has a damping effect on ζ_e, hence on the tidal oscillations in the basin, so-called *radiation damping*. The actual boundary condition is the requirement that $\zeta_{ee}^{(2)}$ radiates outwards into the open sea, with no energy flux coming into the system from infinity.

  From a mathematical point of view there is no difference prescribing the actual tide $\zeta_e = \zeta_e^{(1)} + \zeta_{ee}^{(2)}$ at the boundary or the independent part $\zeta_e^{(1)}$ only, but under

changing conditions one should consider consequential changes in actual tidal ampli-
tudes at the boundary as well: when considering the influence of engineering projects
in a tidal basin, Garrett's (1975) method is preferred. In such cases it makes sense to
have $\zeta_e^{(1)}$ remain the same. However, when considering the response of one specific
basin to exterior forcing at different frequencies, the choice between prescribing either
the actual tide ζ_e or the hypothetical tide with a closed basin is somewhat arbitrary.
Actually, when comparing theoretical results with observations, one can only measure
the amplification and phase difference with respect with the actually observed tide ζ_e
at the mouth of the basin. Moreover, the scattered wave $\zeta_{ee}^{(2)}$ depends on the exterior
sea, so in Garrett's (1975) approach one needs to specify the adjacent sea to which
the basin is connected. A common choice is to describe "the rest of the world" as a
half plane extending to infinity with constant depth. This may not be appropriate
either. Therefore, the use of Defant's (1961) approach, prescribing the actual tide ζ_e
at the open boundary, is more convenient when focusing on the changes to the tidal
signal within arbitrary coastal basins.

In the context of the Helmholtz resonator, radiation damping leads to some coun-
terintuitive results. Upon closing the basin by narrowing the entrance channel, one
would expect the basin to become better shielded from the water-level oscillations
at sea, so the amplification factor between basin and sea would decrease. However,
the maximum and mean square response appear to increase, due to the fact that the
radiation of energy is less through a constricted entrance. This is called the *har-
bour paradox*. It is resolved by including the effect of *head loss* (pressure drop) due
to flow separation at the inlet (Hayashi *et al.*, 1966; Terrett *et al.*, 1968; Ito, 1970;
Mei *et al.*, 1974). Using hydraulic theory they show that the head loss term depends
quadratically on the fluid velocity, which increases upon narrowing the entrance width.
Therefore shielding works indeed and the amplification factor decreases.

Finally, note that the reasoning behind the decomposition of both Defant (1961)
and Garrett (1975) is linear, in the sense that they rely on the fact that a linear
combination of two solutions is again a solution. If nonlinear effects are to be taken
into account, the problem of properly prescribing the open boundary conditions be-
comes much more intricate and beyond the scope of this thesis. We choose to simply
prescribe the actual tide ζ_e and neglect local forcing by the exterior tide.

1.3   Nonlinear dynamics

Up to this point linear theoretical concepts have been discussed. Linear theory is well
understood and does in general provide a good description and prediction of the tide
(see e.g. chapter 2). There are however a number of nonlinear processes that play
a role in tidal motion, especially in coastal areas, where the relatively small depth
of the water enhances their significance. Basically, three nonlinear processes can be
identified, quadratic friction/dissipation, advective accelerations and the feedback of
water-level changes on mass flux. Bottom friction is commonly parameterized by the
quadratic Chezy law (e.g. Prandle, 1991). Sometimes a linear friction law is used,
for simplicity or by using Lorentz's linearization procedure (see section 1.3.1 and
references therein). Moreover, the dissipation of energy by turbulent eddies and head
loss (a pressure drop) due to flow separation at sharp edges, can best be described by
the same quadratic dependence on current velocities (Mei *et al.*, 1974). The effects of

this nonlinearity are discussed in more detail in section 1.3.1 and chapter 3. *Advective accelerations*, accelerations of fluid particles due to their movement into areas with different velocities, also lead to a nonlinear term in the hydrodynamic equations as the product of the fluid velocity and the velocity gradient. Finally, the mass flux through a given vertical cross-section of the basin, is the product of the fluid velocity and water depth. If one takes into account only the reference water depth for the fluid in rest, this leads to a linear term depending on the velocity only. This is sufficient if tidal water-level changes are small compared to total water depth. Taking into account the change in total water depth due to water-level changes leads to a nonlinear term as well. Because this term occurs in the continuity equation describing conservation of water mass, it is also referred to as the nonlinear *continuity* effect.

For the purpose of this thesis, the results of the nonlinear processes can be classified in three aspects:

1. Distortion of the tidal curve,

2. Changes of the response curve,

3. Modulation of tidal oscillations.

The *tidal curve* at a particular location is the average graph of water-level elevation (or current) as a function of time within each tidal period. In a simple linear world with monochromatic forcing this would be a sinusoidal signal. Nonlinear effects lead to overtides at exact multiples of the principal tidal frequency, changing the average shape of the tidal curve into e.g. a seesaw or block-wave and introducing tidal asymmetry with (most commonly) shorter flood period, longer ebb period and consequently stronger flood than ebb currents (section 1.3.2). The change of the *response curve*, the amplification and phase lag between the co-oscillating tide in the basin and the forcing tide in the exterior sea, can have a larger overall impact. Friction tends to both damp the peak amplification factor and smooth out the resonance peak increasing the width of the corresponding frequency band. The quality or Q-factor of the resonator is often used to describe the sharpness of the resonance peak, see the beginning section 1.2. The quadratic friction law causes the influence of friction to increase with increasing amplitude, hence the resonator's quality to go down. The nonlinear effects of advection and continuity may also lead to quite dramatic changes of the response curve, introducing the possibility of multiple equilibria, if multiple response regimes are possible under the same exterior conditions. The nonlinear interaction between different tidal components may even lead to *modulations* of the amplitudes and phases (the harmonic "constants") of the tidal oscillations. Those modulations may occur in a regular predictable way, but could also evolve in a chaotic manner, for instance between the different states in the case of multiple equilibria (section 1.3.3). This puts forward the question of long-term predictability of the tidal signal. Some recent studies on this subject will be discussed in section 1.3.4.

1.3.1   The quadratic friction law

Chezy's law represents bottom friction by $c_D |u|u$, where c_D is the drag coefficient and u the velocity of the fluid (Prandle, 1991). The dissipation of energy due to vortices separating from the flow out of a narrow constriction such as a tidal inlet can also by described by $f |u|u$ (Hayashi *et al.*, 1966; Terrett *et al.*, 1968; Mei *et al.*, 1974;

Maas, 1997), in which f is an empirical constant depending on the geometry of the constriction (see Ito, 1970, and chapter 3). Because of the absolute value occurring in the quadratic friction law, its impact is different from ordinary quadratic interactions. In fact, it has the character of a cubic interaction: developing the quadratic friction term in a complete expansion of harmonic components, one can show that it leads to odd overtides (Dronkers, 1962, 1964; Le Provost, 1973; Kabbaj & Le Provost, 1980), distorting the response signal into a seesaw wave, with corresponding block wave currents. It does not lead to *tidal asymmetry*, different behaviour of the flood and ebb phase of the tidal motion, because odd overtides change sign when shifted over half a tidal period in synchrony with the principal component.

The nonlinear friction term poses a problem for analytically solving the equations of tidal motion, which was first addressed by the Dutch physicist H.A. Lorentz (1922, 1926). At the beginning of the previous century, he had already ended his career when he was asked to supervise the senate committee investigating the effect of closing the Zuiderzee by a long dyke. This tidal inlet system covering the centre of the Netherlands was characterized by a dissipating tidal wave propagating into the basin. In order to predict the new tidal motion on the seaward side of the proposed dyke, he had to properly account for the nonlinear nature of friction and devised an ingenious method to resolve this problem. Lorentz's linearization method amounts to replacing the quadratic bottom friction term by a linear one in which the friction coefficient is chosen such that the average dissipation of energy per tidal cycle is the same irrespective of the (linear or quadratic) friction law that is used (Lorentz, 1922, 1926). Consequently, the friction coefficient depends on the amplitude of the solution. Iteratively improving the solution and the friction coefficient, he found that the amplitude of the tide in the Wadden Sea would increase significantly upon closure of the Zuiderzee. His calculations were found to be in good correspondence with the observed tide after closure in 1932, although he did not live to see this (Thijsse, 1972). Lorentz's linearization method has become widely accepted for its ability to provide accurate prediction of the observed tide incorporating the quadratic friction law; Mei (1989) mentions it under the commonly used name "equivalent linearization". Alternative perturbative approaches lead to equivalent results up to first order. Zimmerman (1982, 1992) interprets Lorentz's linearization as a renormalization procedure and the first term in the expansion of the quadratic friction term in higher harmonics by Dronkers (1962, 1964), Le Provost (1973) and Kabbaj & Le Provost (1980) is readily seen to correspond with it as well.

Despite or perhaps because of its common use and validation in theoretical and observational studies, a literature search for laboratory experiments validating Lorentz's linearization method leads to virtually no results. The structure of the linear eigenmodes in circular (McNown, 1952) and rectangular (Apté & Marcou, 1954) laboratory models have been studied. Linear response curves have been shown for almost enclosed circular basins and a half open channel (Lee, 1971), for a more complex model of Long Beach Harbour (Lee, 1971; Lee & Raichlen, 1971) and for harbours with multiple connected basins (Lee & Raichlen, 1972), but all of these without considering the influence of the tidal amplitude, i.e. of nonlinearity. Lepelletier & Raichlen (1987) performed laboratory experiments focussed on the nonlinear distortion of the tidal curve. Horikawa & Nishimura (1970) studied the effect of breakwaters reducing the entrance width of a basin. Although they do present response curves for different incident wave amplitude, they rate the higher amplitude results as "inaccurate owing to the deformation of waves". Bowers (1977) and De Girolamo (1996) consider

the generation of harbour oscillations due to the nonlinear setup/setdown by wave groups. Their preparatory measurements show the dependence of the response curve on tidal amplitude but they do not compare the apparent increase of the frictional importance with a theoretical model either. Martinez & Naverac (1988) do mention equivalent linearization, but the analysis of their good quality data is based on insufficiently developed theory neglecting inertia. As a consequence, they conclude that the coefficient in the nonlinear friction law would depend on tidal amplitude, which renders predictions on the effect of changing amplitude out of reach. The experiments presented in chapter 3 fill this lack of experimental validation by comparing the response curves of a tidal resonator at different amplitudes with an idealized model using Lorentz's linearization procedure. The decreasing quality of the resonator with increasing amplitude appears to be captured very well by the linear increase of the effective friction coefficient predicted by the theory.

1.3.2 Distortion of the tidal curve

Whereas the expansion of the nonlinear friction term leads to odd overtides, the quadratic interactions caused by advection and continuity terms produce overtides at sums and differences of the principal frequencies, including the even ones (Gallagher & Munk, 1971; Aubrey & Speer, 1985; Le Provost, 1991). Hence additional peaks at exact multiples of the principal frequencies emerge in the tidal spectrum, preserving the periodicity of the tidal motion, but introducing asymmetry between the ebb and flood tidal phase. Parker (1991b) discusses the distortion of the tidal wave due to various nonlinear mechanisms, focusing on the physical processes. Because the mass flux is larger through deeper water and the tidal current adds up to the wave velocity due to nonlinear advective accelerations, the propagation speed of a high tide crest is enhanced and the low tide trough is slowed down. Hence the tidal wave steepens such that the duration of the flood period decreases and that of the ebb period increases. In extremis this can lead to *tidal bores*, when high tide progresses into a tidal basin or river as a steep wall of water.

Because the reduction of the flood period is accompanied by an intensification of the flood currents due to mass conservation, this type of tidal asymmetry is called *flood dominance*. According to Speer *et al.* (1991) *ebb dominance* results from the presence of tidal flats that are flooded and store water at high tide, which is released during the ebb phase (see also Speer & Aubrey, 1985; Friedrichs & Aubrey, 1988). This is different for the Helmholtz mode in almost enclosed basins where the tide is uniform within the basin, in which case tidal flats do lead to a reduction of the low tide period and increasing high tide period but the phase of the overtide is such that the symmetry between the ebb and flood period is conserved. Speer *et al.* (1991) provide a diagram indicating flood or ebb dominance as a function of the two parameters a/h, the ratio of the tidal amplitude over total water depth and V_s/V_c, the ratio between the intertidal storage and volume of channels at mean water level. From a bird's-eye view, increasing V_s/V_c leads to ebb dominance, whereas increasing a/h favours flood dominance. Like Godin (1991b) they relate flood dominance to frictional effects. The latter is able to explain most of the aforementioned effects from bottom friction as well, by taking into account the influence of water depth; in shallow water bottom friction is relatively more important. Therefore a high tide crest is attenuated (both in amplitude and phase retardation) less than a low tide trough.
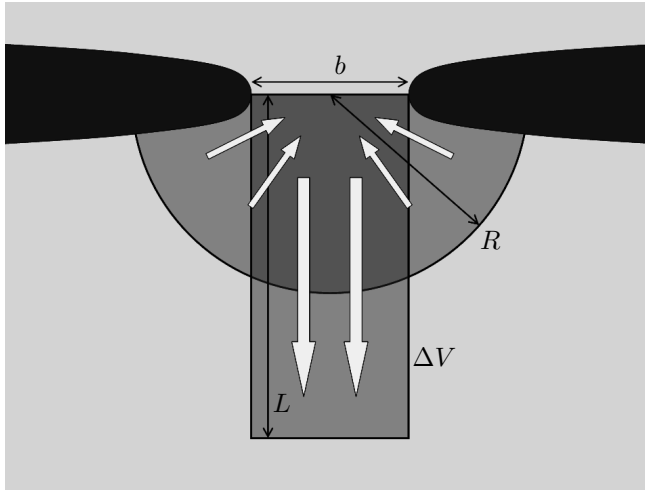
Figure 1.9: Conceptual model for the asymmetry of the flow pattern into and out of the narrow entrance of a basin according to Stommel & Farmer (1952). Due to inertia the outflow is a strong jet of width b and length L, whereas the same amount of water is drawn back radially uniform from a semicircle of radius R, leaving behind the volume ΔV.

The distortion of the tidal curve for the currents is usually even stronger than that of the water-level elevation. The reasons for this are threefold: (a) Because tidal currents through inlets must provide the water flux corresponding with water level changes inside the estuary, it is basically related to the time derivative of water elevation. Hence the relative amplitude of (higher frequency) overtides is enhanced in the currents (see also the Helmholtz model, section 3.5.2). (b) Moreover, an internal tidal asymmetry of the vertical structure of the tidal current between the ebb and flood phase, allows for the currents at specific depth to be different whereas the depth-averaged flux remains the same (Jay, 1991). (c) Finally, currents are more easily affected by local effects near changes in the bathymetry, such as channel bends (Dronkers, 1996), headlands (Geyer & Signell, 1991) and constrictions (Fujiwara *et al.*, 1994). These may cause vortices and residual circulation with a rotational component but zero divergence, hence no influence on water level changes.

The changes to tidal currents have major implications for the transport of water, salt, heat, nutrients and sediment between different parts of the basin and the adjacent sea. For example, the spatial structure of the flow out of and into the narrow entrance of many bays is different during the ebb and flood phase. As the water flows out of the narrow entrance a jet forms due to the advective accelerations causing the water trajectories to remain relatively straight, whereas the water is sucked into the entrance radially according to a potential sink, as indicated in figure 1.9. Based on this simple sketch Stommel & Farmer (1952) came up with the equations describing the exchange between the basin and the adjacent sea, assuming the tidal excursion is much larger than the entrance width:

$$P = bHL = \tfrac{1}{2}\pi R^2 H \approx bHR + \Delta V, \tag{1.3}$$

where P is the *tidal prism* (total volume of water through the inlet during either

the ebb or flood phase), H the (uniform) water depth, b the entrance width, L the length of the jet and R the radius of the semicircle from which water is drawn into the entrance by the potential flow. ΔV is the net volume of water that is exchanged through the inlet during one tidal cycle and equals the tidal prism minus the water in the jet that is drawn back into the inlet after reversal of the flow. By eliminating the radius R one can find ΔV in terms of the tidal prism and inlet dimensions

$$\Delta V = P - b\sqrt{\frac{2PH}{\pi}}. \tag{1.4}$$

Stommel & Farmer (1952) used this simple model for the flow to derive the steady-state salinity within the estuary by adding a constant flux of freshwater to the ebb flow and assuming the water is well-mixed within both the basin and in the sea (see also Fischer *et al.*, 1979, p. 239). Observations performed at the mouth of San Diego Bay confirm this mechanism to be important (Chadwick & Largier, 1999*a*,*b*).

   The flow pattern sketched in figure 1.9 leads to a residual circulation because the mean flow in the jet area is directed away from the inlet and towards it in the withdrawal area outside the jet. This is enhanced by the formation of vortices during the jet-phase due to barotropic shear instability at the edges of the jet. At either side of the jet a vortex forms, constituting a dipole of two counter-rotating vortices. Their interaction causes their inherent movement away from the inlet. Kashiwai (1984) describes three types of life-history for such tidal vortices: (I) the inherent movement of the vortex-pair is large enough to escape from the inlet even when the tidal current reverses, (II) the vortices are drawn back into the inlet after flow-reversal, but return on the same side in the next period of the tide, or (III) the vortices are drawn through the inlet after flow-reversal and remain there indefinitely. With laboratory experiments and a point-vortex model Kashiwai (1984) shows that the two parameters that determine the type of behaviour are the Strouhal number (UT/b, where $UT \sim L$ is the tidal excursion with U the current amplitude and T the tidal period) and the horizontal aspect ratio of inlet length over width. The overall view is that type-I occurs at lower Strouhal numbers, whereas the subsequent distinction between type-II and type-III is based on the length over width ratio with increasing ratio favouring type-II. A similar study was performed by Wells & van Heijst (2003), but they did not distinguish between type-II and type-III behaviour.

   The ebb-flood asymmetry of the tidal currents with strong currents during a short period and weak currents carrying the same amount of water during a longer period does not change the residual circulation, but is very important for transport of sediment in particular. The *bedload* transport of sediment (when the sediment remains on or near the bottom) is usually parameterized by a power law dependence on the current, i.e. strong currents are more effective in transporting sediment than weak currents. Therefore more sediment is moved during the short period of strong currents than during the longer period of weak currents. For *suspended load* transport (when the sediment is brought in suspension and advected with the fluid flow), the turbulent action of the current on the bottom bringing the sediment in suspension introduces a similar nonlinear emphasis on strong currents.

   Because of the importance of the tidal distortion for transport processes, the focus of research on nonlinear effects in tidal dynamics has been on the nonlinear generation of overtides and compound tides (see e.g. the respective chapters in Parker,

1991b, Part 3 in particular). Especially in observational studies, evidence of nonlinear interactions is provided through the occurrence of peaks in the tidal spectrum at frequencies that are not present in the astronomical forcing. As a dynamical system however, this response does not differ much from that of a linear system. The tidal motion described here is still (quasi-)periodic, a sum of a discrete number of harmonic constituents, even though some of them are nonlinearly generated. This aspect of the nonlinear processes is not the primary focus of this thesis.

1.3.3 Modulation of the response

The key topic of this thesis is the overall effect of the nonlinear mechanisms on tidal response such as the amplitude and phase of the primary tidal component. The harmonic constants, the amplitudes and phases of the tidal constituents, found from harmonic analysis of tidal records appear to modulate on several timescales. A number of reasons can be distinguished. First, the linear sum of components at nearby frequencies not taken into account separately by the analysis cause interference. In the species concordance method this is very explicit by restricting to a frequency resolution level up to different (diurnal, semidiurnal, terdiurnal, etc.) species. Hence the spring-neap tidal cycle, which results from the interference between the lunar M_2 and solar S_2 semidiurnal constituents, causes the reduced vectors (complex amplitudes of the tidal species) to modulate on a 14 day period, even though the M_2 and S_2 amplitudes could be considered constant on that timescale. Similarly, yearly tidal analyses modulate on the 18.6 year nodal cycle, due to the the revolution of the lunar node. Assuming that the amplification and phase lag of the response of the tidal resonator to the unresolved nodal components near resolved tidal constituents is the same (cf. the "credo of smoothness" in section 1.1.3), the nodal corrections to the amplitude and phase of the resolved constituents can be predicted theoretically from the expansion of the astronomical forcing, as explained e.g. by Doodson (1924). This leads to "nodal factors" that are commonly applied to correct the amplitudes and phases found from yearly harmonic analyses.

In order to resolve all frequencies up to nodal cycle resolution tidal records of a complete 18.6 year nodal cycle must be analysed[2]. At many locations, the basin itself changes within this timescale. Engineering works may be constructed by man or bathymetric changes of a natural origin may occur. In tidal flat systems like the Wadden Sea for example, the pattern of channels and shoals undergoes significant changes on a yearly basis due to the transport of sediment by tidal currents, wind waves, storm surges or river flux. Because the response of tidal basins depends on their (changing) dimensions, the harmonic constants may consequently vary as well. On a shorter timescale, meteorological forcing causes the water level to differ from harmonic predictions. From a strictly hydrodynamic point of view these modulations are again based simply on modulations of the forcing and are not related to nonlinear hydrodynamics.

Intrinsic nonlinear interactions within tidal basins can be responsible for modulating harmonic constants as well. They lead to additional forcing at sums and

---

[2]As Munk & Cartwright (1966) pointed out, such a lengthy timescale is not necessary in principle under the assumption that one knows exactly what frequencies occur in the tidal spectrum, which is the basis of harmonic analysis. However, such a length is required for the significance of the results to exceed the noise level.

differences of the principal tidal frequencies. Generically, this leads to a slaved response at these frequencies, determined by the amplitude of the nonlinear term and the response characteristics (amplification and phase lag) of the tidal resonator at the respective frequencies. If the nonlinearly generated frequency is close enough to one of the principal frequencies, it cannot be distinguished by the (harmonic) analysis and will show itself as a modulation of that component as well. In fact, Godin & Gutiérrez (1986) show that nodal factors are unable to fully account for the modulation of some of the semidiurnal tidal constituents at St. John, New Brunswick, in the Bay of Fundy. They relate it to the fact that nonlinear friction contributes to spectral peaks exactly at some nodal frequencies. Therefore, the nodal corrections, that are based on the assumption that the response of the basin at the nodal frequencies is proportional to their occurrence in the astronomically forced equilibrium tide, are inappropriate. They suggest to replace the common nodal factors based on the equilibrium tide by a set of "frictional-nodal" corrections, see also Le Provost (1991), section 6 and references therein. Amin (1991) uses the harmonic constants of constituents that can be resolved by the harmonic analysis to derive nonlinear interaction coefficients for both quadratic and cubic interactions in the shallow water equations. By interpolating the coefficients found in this way for compound frequencies that are not resolved, he is able to predict the amplitude and phase of those components as well. This allows him to obtain the nonlinear correction to the nodal factors, i.e. to predict the resulting nonlinear modulation of the harmonic constants, from a relatively short time series.

The studies mentioned in the previous paragraph assume the nonlinear response to be slaved in the sense that the compound components are generated by the principal tidal tide but have no dynamics of their own. However, in the particular case that an eigenmode of the basin is excited by the nonlinear interactions, it may lead to even more interesting behaviour. In chapter 4 of this thesis amplitude evolution equations are derived that govern the evolution of the amplitudes of the tide in such a case. They were derived by performing a weakly nonlinear analysis on the two-dimensional depth-averaged shallow-water equations, assuming small tidal amplitudes compared to the total water depth and *strong resonance*. The nonlinear processes involved are the advective accelerations and nonlinear continuity terms in the shallow water equations. In the present context strong resonance is meant to specify the condition of weak friction and forcing frequency near one of the basin's eigenfrequencies, such that the amplification of the response is huge. The model derived in chapter 4 is a generalization of previous work by Miles (1981) and Maas (1997) that considered the Helmholtz mode in almost enclosed basins. Miles (1981) dealt with the feedback of water-level elevation on the inlet channel cross section: at high tide the flux is increased because the channel cross section through which it flows is larger, at low tide it is reduced. Maas (1997) discussed the influence of non-uniform *hypsometry*, the dependence of the horizontal basin area on water level. In tidal flat systems the basin area at low tide can be much less than at high tide, when the tidal flats are flooded. Hence the change of water level induced by the same flux through the channel is less at high tide, because the water spreads over a larger area in that case. In both cases, the dependence between the current through the channel and the change of the basin's water level, hence the restoring pressure gradient of the tidal resonator, becomes nonlinear, see section 6.3.2 for more details. Basically, both mechanisms deal with the continuity effect as they relate directly to mass conservation.

The shape of the response curve can be changed by these nonlinear effects. In section 1.3.1 the influence of the quadratic friction law on the response curve by de-

creasing the quality of the resonator as a function of forcing amplitude, was discussed. In chapters 4 and 5 it will be shown that advection and continuity can produce a bent resonance curve by creating dependence of the effective eigenfrequency on the amplitude. The bending of the response curve eventually may lead to multiple equilibria: under the same forcing conditions at the exterior sea, different tidal responses are possible inside the basin. Bifurcations can occur upon changing conditions, when the present branch of solutions ceases to exist and the system "suddenly" (on the slow timescale of several periods) has to adjust to a completely different response. The amplitude evolution equations derived in chapter 4, describe the adjustment of the tidal response to changing forcing conditions. The response they describe is the tidal oscillation at the dominant (tidal) forcing frequency, with amplitude and phase evolving on a longer timescale. Modulation of the amplitudes in a periodic or quasi-periodic fashion expresses itself in the tidal spectrum by generating sidepeaks near the principal tidal frequencies, just like the nonlinear interaction in the case of slaved response. However, in chapter 5 it will be shown that the solutions to the amplitude equations can even be chaotic, if the exterior conditions change on the same time scale as that of the adjustment of the amplitudes to the new equilibrium response. In that case the system keeps readjusting to the ever changing steady state. Chaotic modulation of the amplitudes expresses itself by increasing the width of the spectral peaks into a continuum spectrum. Indeed, Munk & Cartwright (1966) describe such a continuum spectrum around the tidal frequencies. It is usually interpreted as the footprint of chaotic dynamics in the meteorological forcing, but the models presented in this thesis suggest that chaotic tidal dynamics may also result from intrinsic nonlinear processes in the hydrodynamics of tidal resonators.

1.3.4   Predictability of the tide

The mathematical theory of chaos deals with systems that are deterministic (i.e. predictable) in principle but whose dynamics are so complex that predictability is limited in practice. The most well-known example of a system that appears to behave chaotically is the weather. It is generally thought to be described by models based on the Navier–Stokes equations, so it would be completely predictable if the initial conditions of each molecule on the Earth were known. However, as Lorenz (1993) illustrated by his famous "butterfly example", small disturbances can have enormous consequences: he remarked that a butterfly flapping its wings in the Brazilian rain forest might cause a tornado in Texas. This does not imply that we should be afraid of butterflies for this reason: its next flap of the wing might again stop the tornado's formation, as could any other perturbation. The point is that small changes in the initial conditions, far below the level of resolution one could ever hope to obtain measurements on, can change the outcome of the behaviour dramatically. Therefore, although the system is deterministic in principle if all knowledge on the initial conditions were available, the validity of predictions is still limited to the timescale on which the chaotic dynamics enables small disturbances to grow to large-scale changes.

In the case of tidal dynamics the conclusion of chapter 5 that chaotic dynamics may play a role in tidal resonance, would be a contradiction in terms. The etymology of the word "tides" stems from the fact that they were always conceived to be periodic and predictable. Still, tides are commonly considered to be predictable for decades in advance by harmonic analysis, as long as no engineering works or natural changes to the basin's bathymetry are involved. Of course, nodal corrections must be applied to

harmonic constants derived from one-year records, in order to account for the nodal changes in the lunar orbit and nonlinearly generated (slaved) compound components have to be dealt with properly, but otherwise deviations would be attributed to external forcing. The results in chapter 5 suggest that the amplitudes and phases (say the harmonic constants) of tidal oscillations in specific tidal basins may evolve in a chaotic way, not because of meteorological forcing or changes in the basin's geometry, but because of intrinsic nonlinear interactions in the hydrodynamics of the tidal resonator. This would make the possibility to predict the tide for decades in advance questionable.

Indeed, recent studies have revealed the footprints of chaotic dynamics within tidal signals. Vittori (1992) investigated the water-level oscillations $\zeta(t)$ in the Lagoon of Venice by techniques that have been developed for the analysis of chaotic time series. A central concept in the process is the reconstruction map that amounts to forming a vector $(\zeta(t), \zeta(t-\Delta t), \zeta(t-2\Delta t), \ldots, \zeta(t-N\Delta t)) \in \mathbb{R}^{N+1}$ of subsequent values of the time series (see Takens, 1981). If N is large enough, the trajectories in the "reconstructed phase space" are topologically equivalent to the attractor of the underlying deterministic (but chaotic) system, if it exists. In that case the dimension of the reconstructed attractor converges to a constant upon increasing the dimension N of the reconstructed phase space. It is a measure for the degrees of freedom in the underlying dynamical system. In the case of stochastic dynamics such a finite number of degrees of freedom is not expected to be found. For the time series of water-level elevations Vittori (1992) found the (fractal) dimension of the attractor to be near 6. She also considered the time series of water-level maxima and found a fractal dimension near 2 in that case, which she explained to be much less (than 6) because a number of degrees of freedom related to the astronomical tide were removed by extracting the envelop of maxima. Next, Lyapunov exponents were calculated that measure the rate of divergence of nearby trajectories, hence (the inverse of) the timescale on which small disturbances grow and beyond which predictions are no longer reliable. Finally, she showed how a prediction method based on the trajectories in reconstructed phase space (Farmer & Sidorowich, 1987), can be used to efficiently predict future water levels from present and past observed values. Its success again confirms the assumption that the oscillations in the Lagoon of Venice arise from a chaotic system characterized by a few degrees of freedom. However, it still remains an observational challenge to determine if the chaos arises within the basin from the nonlinear hydrodynamics or is simply the footprint of chaotic behaviour in the meteorological forcing. A similar study was performed by Frison *et al.* (1999) for a number of locations along the American East Coast. Interestingly, they find that the dimension of the attractor, hence the number of degrees of freedom of the reconstructed dynamics, increases when moving further into complex estuaries. This does suggest that the chaotic dynamics is produced by the co-oscillating response of the basin, although one may also argue that meteorological effects are more pronounced over relatively shallow areas.

Irregularity of secondary tides have been reported by Honda *et al.* (1908), but at that time chaos theory had not been developed yet, so their report can only give qualitative conclusions. They present time series of water-level measurements at over 50 locations along the coast of Japan and conclude that they vary from inconspicuous (at the Pacific coast) to conspicuous (near the Japan Sea) and from regular to irregular. Their persistence suggests an ever-present source, such as due to tidal motion in the adjacent sea. The study of secondary undulations has received less

attention historically, because they are of minor importance for the water level and require a high temporal resolution of measurements. Nowadays automatic tide gauges are available that record water levels at six minutes intervals, which allows secondary undulations of longer period to be studied. Because of the shorter period, the relatively weak signal of the secondary undulations in the water level is boosted when considering the corresponding currents. Measurements by Golmen *et al.* (1994) show that the currents accompanying the secondary undulations can be of the same order of magnitude as the currents related to the principal tide. Perhaps the limited predictability of currents as compared to water level (Godin, 1991*a*) is not only caused by their susceptibility to meteorological influences, but also to nonlinear dynamics of secondary undulations.

The analyses by Vittori (1992) and Frison *et al.* (1999) were performed on the time series of tidal water-level elevations. The theoretical results in chapters 4 and 5 of this thesis describe a mechanism that causes the evolution not of the water level itself but of the amplitudes and phases of water-level oscillations to become chaotic. This suggests to consider the evolution of the harmonic "constants". Using the methods of reduced vectors (Simon, 1991) to obtain the evolution of the complex amplitudes of the tidal species, one could study their evolution on a 14-day timescale to investigate whether or not it is completely determined by the astronomical spring-neap tidal cycle. Doodson (1924) discussed time series of 33 years of harmonic constants derived from yearly tidal records for St. John, New Brunswick (Bay of Fundy). He concluded that only part of the variation he found could be explained from long-term astronomical signals, another part was not accounted for. Gutiérrez *et al.* (1981) used several methods of analysis both on tidal observations at Puntarenas (Pacific coast of Costa Rica) and Trieste (Adriatic Sea) and on a synthetic record to find that the variability of harmonic constants is not caused by nonperfect selectivity of the method applied to obtain them. They do not provide time series of the variation of the harmonic constants however and condense all the information in a single value for their standard deviation. Godin & Gutiérrez (1986) do show time series of the harmonic constants for St. John, New Brunswick in their paper showing the inappropriateness of nodal factors to predict the variation of a number of semidiurnal and diurnal tidal constituents. They are reasonably successful trying to explain this from the (slaved) response due to frictional nonlinear interactions, although their method cannot capture irregular behaviour. For that purpose a combination of the study of time-varying harmonic constants with the approach of Vittori (1992) and Frison *et al.* (1999) could be profitable. Unfortunately, new analyses of tidal observations will not be presented in this thesis.

1.4   In this thesis

The ultimate goal that the work presented in this thesis hopes to get closer to is to answer the question about long-term predictability of the tide, in the absence of basin changes and meteorological influences. The fact that the weather behaves as a chaotic system is widely recognized. Moreover, the morphodynamics of (tidal) basins with erodible bottoms leads to complex fractal patterns of channels and shoals (Cleveringa & Oost, 1999) of which the larger structures evolve on decadal timescales in a highly nonlinear fashion. Tides on the other hand are commonly associated with periodicity and predictability, not with chaos. Still, this thesis discusses a possible connection

between the two. The focus of the thesis will be on the changes due to nonlinear effects on the response curves of co-oscillating tidal resonators.

Chapter 2 is basically an extension of the introduction. It shows an example of the use of a simple linear model for the tide in the Adriatic Sea. In fact, the model can be seen as an application of Prandle (1991, section 3.1), which gives the solutions to the linearized one-dimensional shallow-water equations for basins whose depth and width vary with a power of the longitudinal coordinate. In chapter 2 the bathymetry of the Adriatic Sea is approximated by a number of pieces along which the depth varies linearly and the solutions in the different pieces are matched at the boundaries by continuity of water level and flux. Despite the simplicity of the model, the present distribution of the amplitudes of the K_1 and M_2-tidal constituents along the central axis of the Adriatic Sea are captured quite well. The model is used to comment on the tide in the Adriatic Sea in past ages when the mean sea level was much lower, in order to support a geological study that found distinct sediment layers possibly of tidal origin at specific locations on the bottom of the Adriatic Sea.

When setting out to measure nonlinear bending of the resonance curve in a laboratory experiment, it appeared to be necessary to establish the effect of quadratic friction first. Although Lorentz's (1922) linearization principle to account for the resulting dependence of the resonator's quality on forcing amplitude was developed at the beginning of the previous century already and has been successfully used in many observational studies, its validity had not been tested in the laboratory before. Experimental validation of Lorentz's linearization principle in the context of the Helmholtz mode is shown in chapter 3.

Response curves describe the steady state of amplitude and phase of the tidal response to exterior forcing. In chapter 4 the evolution of the complex amplitude towards this steady state is studied in a weakly nonlinear setting, assuming small tidal amplitudes (compared to total water depth) and strong resonance (i.e. weak friction and forcing near one of the basin's eigenfrequencies, such that amplification of the tidal oscillation is huge), based on the two-dimensional depth-averaged shallow-water equations, that describe the tide in co-oscillating basins. The nonlinear effects of advection and continuity are incorporated in the analysis. The ultimate result is the *Landau equation* (4.30), that describes the weakly nonlinear evolution of the complex amplitudes of the basin's eigenmodes.

In chapter 5 the behaviour of solutions to the Landau equation (4.30) is investigated. It appears that previous results by Maas & Doelman (2002) apply in this more general setting as well: By considering steady states the nonlinear changes to the response curves are identified. It appears that bent resonance occurs because the effective eigenfrequency now depends on amplitude. This may even lead to multiple equilibria: under the same forcing conditions at the exterior sea, different tidal responses are possible inside the basin. This means that one cannot predict the tide within the basin just from knowing the tide in the adjacent sea, because the tide in the basin also depends on the basin's history. Under changing conditions, "sudden" changes may occur during which the amplitude and phase in the basin change over a few tidal periods. If conditions keep changing continuously, for instance due to the spring-neap tidal cycle, those sudden amplitude changes can even occur chaotically. The results in section 5.5 suggest that many different mechanisms may be responsible for this behaviour. In particular, the influence of the Earth's rotation may allow chaotic dynamics to occur even if the forcing is a single sinusoid of constant amplitude.

Finally, laboratory results showing the occurrence of multiple equilibria in a tidal resonator are presented in chapter 6. They were predicted to occur by the weakly nonlinear theory for an almost enclosed basin with sloping sidewalls, but small scale effects proved to render it impossible to have their impact be significant compared to friction. The multiple equilibria were actually found using vertical sidewalls and a curved trumpet-shaped entrance to the basin. The latter appears to be most important. Note that in geophysical reality many tidal basins have funnel-shaped entrances, so the phenomenon might occur in such basins indeed. Multiple equilibria are a prerequisite for the development of chaotic behaviour along the lines of the mechanisms described in chapter 5, so this is a first step towards the investigation of "chaotic tides" in the laboratory. However, more research is needed to draw conclusions on the predictability of the tide, in particular because the range of conditions under which multiple equilibria were found, was very small. Moreover, there still is need for evidence of chaotic dynamics not only in laboratory experiments but also from the field by analysis of geophysical observations.

Chapter 2

Linear model for the tide in the Adriatic Sea

There is hardly any tide in the Mediterranean Sea, because it is too small to resonate with direct astronomical forcing and the narrow passage through the Strait of Gibraltar chokes the co-oscillating tide. Even so the tides in the northern part of the Adriatic Sea are significant. Apparently, the tide from the Mediterranean is amplified when it propagates into the Adriatic Sea. Over the past ages, the mean sea level has been much lower than the present level. Therefore the water depth and also the length of the Adriatic Sea has been different. Geological studies reveal deposits of possibly tidal origin at particular locations along the bottom of the Adriatic Sea. The question arises if these can be explained from the resonance characteristics of the Adriatic Sea that may have been different at past ages when the mean sea level was lower. In this thesis on nonlinear tidal resonance, this problem serves as an example of linear tidal modelling, which appears to capture many facets of the tide already.[1]

2.1   Mathematical model

In this section the one-dimensional depth-averaged linear shallow-water equations are introduced as a mathematical model for co-oscillating tides in geophysical basins. In particular, direct astronomical forcing is not taken into account (see also section 1.2.4). Without narrowing the scope to the Adriatic Sea the general solutions to these equations for a rectangular basin of uniform depth and with a sloping bottom are presented. Actually, they can be considered as a special case of the solutions described by Prandle (1991, section 3.1) for basins whose depth and width vary with some power of the longitudinal distance. The results will be applied to the Adriatic Sea in the next section.

---

[1] The model discussed in this chapter is used for theoretical support of a geological study that is presented in the paper *"Stratigraphic forward modelling of isolated sandbodies in the Holocene transgressive systems tract of the Northern Adriatic shelf, Italy* by Joep E.A. Storms, Gert Jan Weltje, Guido M. Terra and Antonio Cattaneo, in preparation.

2.1.1   One-dimensional linear shallow-water equations

The wavelength of tidal waves are usually much larger than the depth of the water (typically 400 km wavelength in 10 m water depth), justifying the term *long waves*. Under such circumstances, the shallow-water equations can be used. By averaging over the depth of the water a model for the horizontal currents without considering their vertical structure is derived:

$$\frac{\partial \zeta}{\partial t} + \nabla \cdot [D\mathbf{U}] \quad = \quad 0, \tag{2.1a}$$

$$\frac{\partial \mathbf{U}}{\partial t} + [\mathbf{U} \cdot \nabla]\mathbf{U} + f\hat{\mathbf{k}} \times \mathbf{U} \quad = \quad -g\nabla\zeta - \frac{\tau_b}{\rho D}, \tag{2.1b}$$

where ζ is the vertical displacement of the water level, $D = H + \zeta$ is the total water depth, which differs from the water depth in rest H by the tidal water-level elevations, $\mathbf{U} = (u, v)$ is the horizontal current vector and τ_b is the bottom friction stress, to be parameterized. Equation (2.1a) is the continuity equation describing mass conservation (sea surface rises if water flux converges); (2.1b) is the momentum equation which is basically Newton's law relating the acceleration of fluid particles (including the nonlinear advection of momentum and the Coriolis acceleration due to the rotation of the Earth) to the pressure gradient due to the sloping sea surface and friction. The vector $\hat{\mathbf{k}}$ is the vertical unit vector: $\hat{\mathbf{k}} \times \mathbf{U} = (-v, u)$ describing the Coriolis force which deflects moving objects to the right on the northern hemisphere. When the basin is narrow compared to both the tidal wavelength and the Rossby radius of deformation $\sqrt{gH}/f$, which is a length scale related to the Coriolis force, transversal variations can be ignored and the one-dimensional shallow-water equations can be used. Furthermore, if the tidal amplitude is small with respect to the water depth, the nonlinear terms in (2.1) are negligible as well and (2.1) reduce to the one-dimensional depth-averaged linear shallow-water equations

$$\frac{\partial \zeta}{\partial t} + \frac{\partial}{\partial x}[H\,u] \quad = \quad 0, \tag{2.2a}$$

$$\frac{\partial u}{\partial t} \quad = \quad -g\frac{\partial \zeta}{\partial x}, \tag{2.2b}$$

in which we finally neglected frictional effects as well (bottom friction is relatively unimportant at 100 m water depth). Boundary conditions have to be appended to these equations to complete the model. At coastal boundaries one usually prescribes a no-flux condition $D\mathbf{U}\cdot\hat{\mathbf{n}}$ with $\hat{\mathbf{n}}$ the (outward) normal to the coast. If the water depth D tends to zero at the coast, this condition should be interpreted to require $\mathbf{U}$ to remain finite at the boundary. At open boundaries, connecting the model area to adjacent seas, it is less clear what to prescribe. Specifying the observed water-level variations at the boundary should be sufficient to obtain a correct description, but the tide in the adjacent sea may be influenced by changes in the basin (leading to radiation damping). Although a boundary condition taking into account the effect of radiation damping would be more accurate, the simple boundary condition assuming the water-level elevations at the open boundary to be known is used here. It can be convenient to split the model area in different parts and find solutions to (2.1) or (2.2) in each part separately. In that case the respective solutions have to be matched at the boundaries between the parts by requiring both the water-level elevations ζ and the water flux $D\mathbf{U}\cdot\hat{\mathbf{n}}$ through the boundary to be continuous.

2.1.2 Solution for constant depth or straight slope

The linear shallow-water equations can be written completely in terms of a wave equation (with varying coefficients) for the water-level elevation ζ by differentiating the continuity equation (2.2a) with respect to t and substituting u from the momentum equation (2.2b) to obtain

$$\frac{\partial^2 \zeta}{\partial t^2} = \frac{\partial}{\partial x}[g\,H(x)\,\frac{\partial \zeta}{\partial x}]. \qquad (2.3)$$

Prescribing a single sinusoidal forcing at the open boundary $\zeta_e = \alpha_e e^{i\omega t} + c.c.$ the response of the basin will be at the same frequency $\zeta(x,t) = \hat{\zeta}(x)e^{i\omega t} + c.c.$ which is governed by the equation

$$\omega^2 \hat{\zeta} + \frac{\mathrm{d}}{\mathrm{d}x}[g\,H(x)\,\frac{\mathrm{d}\hat{\zeta}}{\mathrm{d}x}] = 0. \qquad (2.4)$$

For basins with constant depth the general solution to this equation is given by

$$\hat{\zeta} = A\cos(\kappa\,(x - x_c)) + B\sin(\kappa\,(x - x_c)), \qquad (2.5)$$

in which one is free to choose the reference point x_c conveniently and the wave number $\kappa = \omega/\sqrt{gH}$ is given in terms of the fixed depth H. For basins with a straight slope from depth H_1 at $x = x_1$ to H_2 at $x = x_2$ with depth profile

$$H(x) = \frac{(x - x_1)H_2 + (x_2 - x)H_1}{x_2 - x_1} = \frac{H_2 - H_1}{x_2 - x_1}\left(x - \frac{x_1 H_2 - x_2 H_1}{H_2 - H_1}\right),$$

the solution can be written in terms of Bessel functions

$$\hat{\zeta} = C\,J_0(2\kappa\sqrt{x - x_0}) + D\,Y_0(2\kappa\sqrt{x - x_0}), \qquad (2.6)$$

where $x_0 = (x_1 H_2 - x_2 H_1)/(H_2 - H_1)$ is the point at which the water depth $H(x)$ is zero and should not lie within the interval between x_1 and x_2. If the depth vanishes at one of the boundary points x_1 or x_2, the integration constant D should be zero for the solution to remain finite.

Note that Prandle (1991) gives the solutions to (2.3) more generally when $H(x) \propto x^n$ for some power n, in terms of Bessel functions of different (fractional) order. In his formula the Bessel function of the second kind does not occur because he chooses the origin of the longitudinal coordinate x at the point where H vanishes.

2.2 Application to the Adriatic Sea

The bathymetry of the Adriatic sea is characterized by a deep (about 1 km) southern part from its mouth at Brindisi connecting it to the Mediterranean Sea to halfway the basin and a shallower (≤ 200 m) shelf in the northern end. This depth profile is sketched in figure 2.1(b), which shows a cross-section through the central axis of the basin along the line indicated in the contour plot in figure 2.1(a). Although the structure of the M_2-tide in the Adriatic Sea is influenced by the rotation of the Earth (note the amphidromic structure in figure 2.2(a)), the simplest approach is to ignore transversal variations and describe the basin as a one-dimensional channel, such that the results in the previous section can be applied. The depth along the central

(a) Contour plot of bathymetry

(b) Longitudinal cross-section
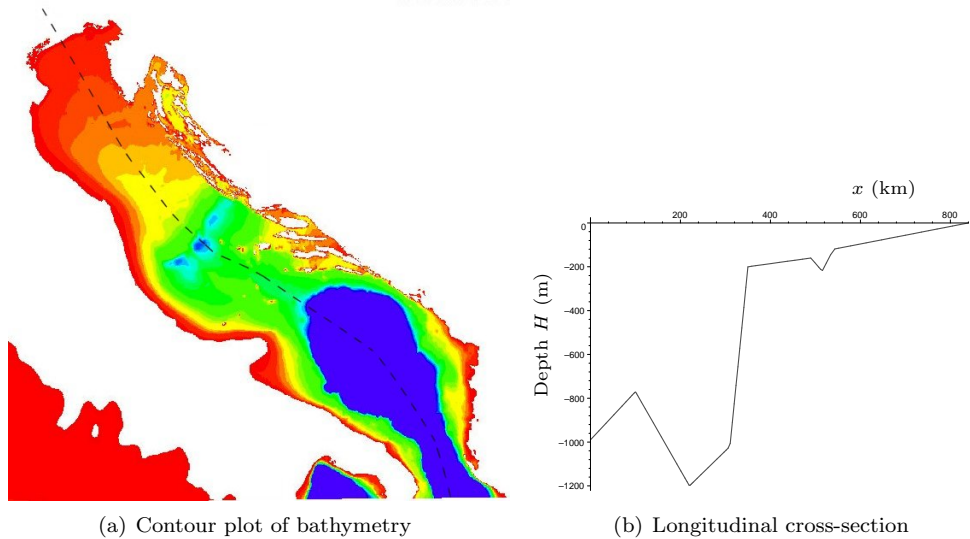
Figure 2.1: Bathymetry of the Adriatic Sea, relatively deep in the southern part and a sloping shelf in the northern part. The data have been provided by Dr. Richard Signell, United States Geological Survey. A longitudinal cross-section along the central axis indicated by the line in the top view is used for the one-dimensional model of the Adriatic Sea neglecting transversal variations.

axis of the basin is not representative for the mean depth along transversal cross-sections. The proper value would be the mean depth, weighted by the magnitude of the tidal currents such that the water flux through transversal cross-sections is properly represented. Because this cannot be evaluated within the context of the one-dimensional model, we simply decrease the depth in figure 2.1(b) by a factor of 75 %.

In order to model the shape of the depth profile, the Adriatic Sea is cut into a number of pieces on which the bottom is described by a straight slope. For the results presented here eight pieces are used, see figure 2.1(b). Within those pieces the solution to the wave equation (2.3) is given by (2.6), or (2.5) if the bottom happens to be flat. The solution in the entire basin is obtained by matching these solutions in the different pieces, determining the respective constants C and D from the fact that water level and water flux should be continuous at the transitions. At the northern end, the water depth tends to zero, so the coefficient D_{end} should be zero there. The matching conditions requiring $\hat{\zeta}$ and $\frac{d\hat{\zeta}}{dx}$ (determining u, hence water flux) to be continuous allow us to express the coefficients C_i and D_i in the other pieces of the basin in terms of the remaining integration constant C_{end} for the end of the basin. In fact, the linearity of the model implies that multiplying the solution by any constant yields a solution again. This final freedom is removed by prescribing the tidal amplitude at the open (southern) end of the basin to equal the observed tide in the Mediterranean Sea. The computer algebra package Maple was used to perform these simple but tedious calculations.

2.2.1   Present situation

In figure 2.2 the solution $\hat{\zeta}(x)$ describing the spatial distribution of tidal amplitude is compared with tidal observations along the central axis of the Adriatic Sea, obtained from figures 2.2(a) and 2.2(b). The amplification of the M_2-tide from 8 cm at the Mediterranean Sea to 22 cm at the northern end of the basin is captured well by the model. In the deep southern part of the basin, the tidal amplitude appears to be fairly constant, both in the model and in observations. The standing wave described by the model has a knot at which there is no vertical tidal motion at all about 625 km from the southern connection with the Mediterranean Sea, which is slightly further inside the shelf than observed. In the realistic two-dimensional setting, it is an amphidromic point on the central axis of the basin around which the tidal wave rotates counterclockwise through the basin. Still, this simple model gives a reasonable approximation of the tide along the central axis. North from the amphidromic point, the amplitudes $\hat{\zeta}$ are indicated to be negative. In view of the formulation $\zeta(x,t) = \hat{\zeta}(x)e^{\mathrm{i}\omega t} + c.c.$ this means that the tides are in the opposite phase from the tide at the Mediterranean mouth of the Adriatic Sea.

For the K_1-tide the period, hence the wavelength, is much larger. As a consequence, the spatial distribution of this component's amplitude is different and there is no amphidromic point for this component of the tide. Near the amphidromic point of the M_2-component, the amplitude of the semidiurnal tide is relatively weak, so the tide in this region is predominantly diurnal, with one high tide and one low tide a day instead of twice a day in regions where the semidiurnal tide prevails. The amplification of the K_1-component is strong, from 2 cm amplitude at the entrance to 18 cm amplitude at the end of the basin, because the length of the basin is close to a quarter of a wavelength, the condition for resonance. Part of the amplification occurs at the mouth which is relatively narrow. This is not captured by the present model because it does not take into account the changes in the width of the basin. From Brindisi, where the tide's amplitude is approximately 4 cm, the width of the Adriatic Sea doesn't change much and the amplification of the K_1-component is also described reasonably well by the one-dimensional model.

2.2.2   Past tides

With the present tide predicted quite well by this simple one-dimensional linear model, one may consider the changes to the tide if the mean sea level were lower, such as it has been in previous ages. Figure 2.3(a) shows the longitudinal depth profile that has been used and the past sea levels for which the consequences for the tide in the Adriatic Sea have been evaluated. Assuming that the bottom profile has not changed much, the reduction in sea level results in lower water depth as well as a reduction of the length of the basin. This may not be good description, especially near the vanishing depth at the northern end of the basin where the action of wind waves and tidal currents may move sediment and change the bathymetry, but the morphodynamics involved is another field of research outside the scope of this thesis. The reduction in water depth causes the tidal wavelength to decrease, but the reduction of the basin length is larger so the relative basin length with respect to the wavelength decreases. The remaining subfigures in Figure 2.3 show the resulting amplitudes of the M_2- and K_1-component of the tide under the assumption that the tide at the Mediterranean entrance remained the same.
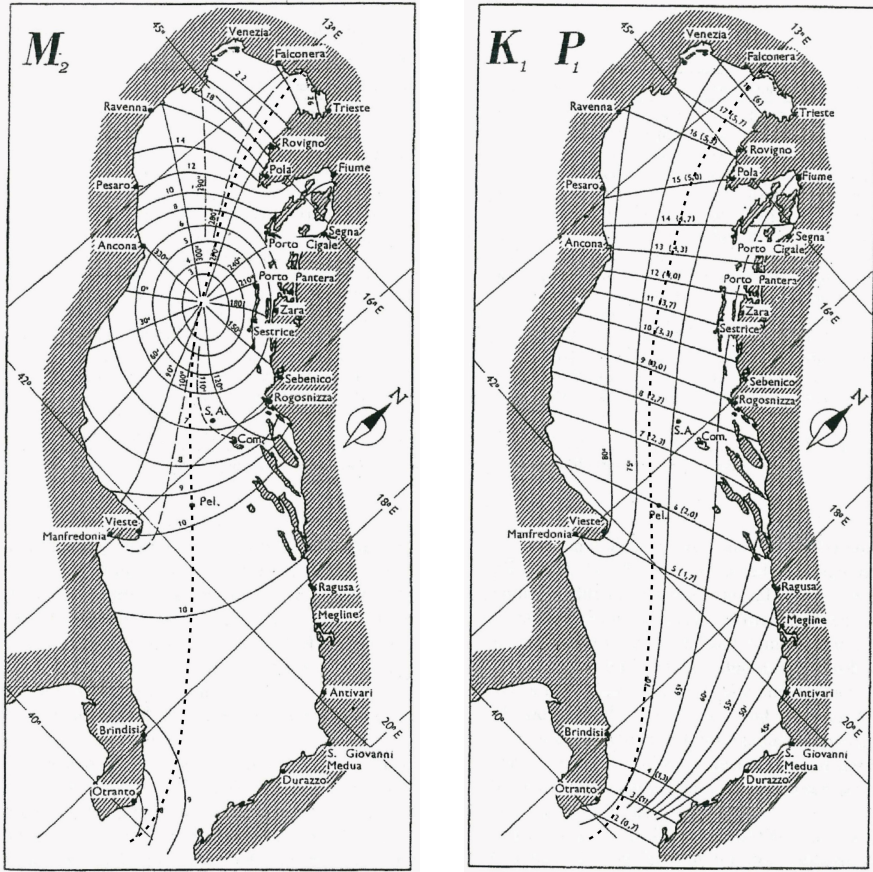
(a) Spatial structure of present M_2-tide

(b) Spatial structure of present K_1-tide
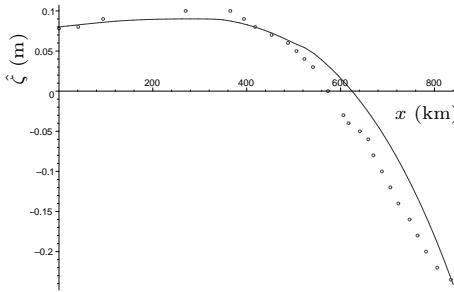
(c) M_2 along central axis
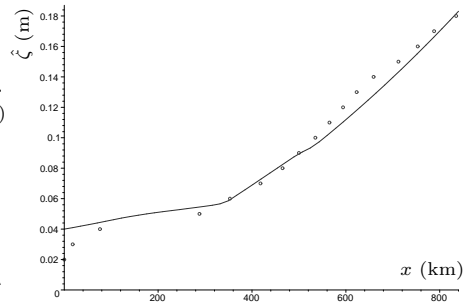
(d) K_1 along central axis

Figure 2.2: (a) and (b) show the structure of the present lunar semidiurnal M_2 (12^h25^m period) and the diurnal K_1-tide (23^h56^m period), after Cushman-Roisin & Naimie (2002, Fig. 2) (originally Polli, 1960). The dashed curve denotes the central axis along which the values have been used for comparison with the model. (c) and (d) compare the tidal elevation amplitude (m) obtained from the one-dimensional linear model (solid line) with those from tidal observations (circles).

(a) Past sea levels and present depth profile

(b) M_2-tides

(c) K_1-tides

(d) M_2-currents

(e) K_1-currents
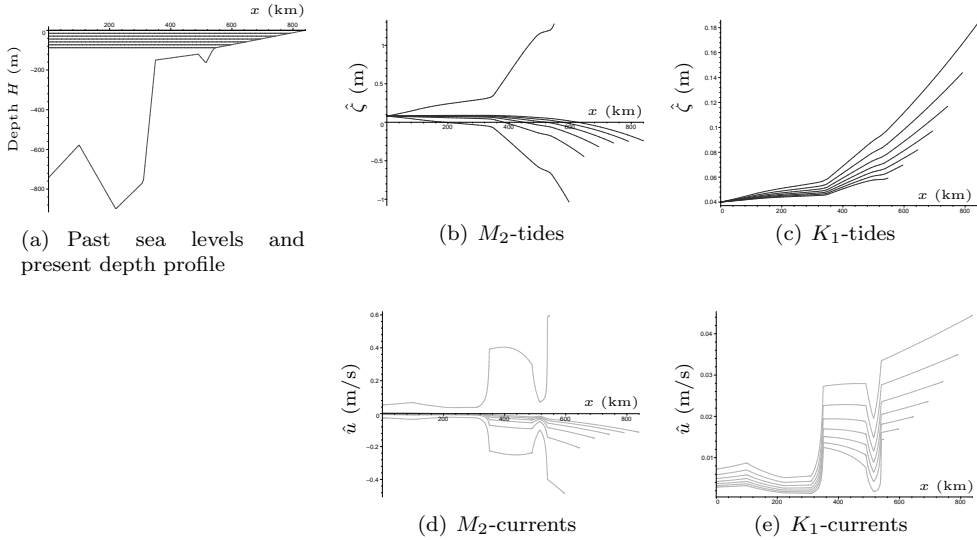
Figure 2.3: The modelled amplitude of the past tide in the Adriatic Sea when the mean sea level was lower, for the lunar semidiurnal M_2-tide and for the diurnal K_1-component. The results are shown for a mean sea level which is $0, 19.5, 39, 58.5, 78, 97.5$ and 117 m less than present, with corresponding reduction in basin length to $840, 791, 743, 694, 645, 596$ and 548 km respectively.

For the M_2-tide we see that, as the basin gets shorter, the amphidromic point shifts towards the basin entrance and the amplitude at the end of the basin increases strongly, because the basin length gets closer to quarter wavelength resonance. In this model, the amplification increases indefinitely when the mean sea level was 109 m below present corresponding with a basin length of 567 km. This singular behaviour is caused by the fact that no damping is taken into account. Radiation of wave energy from the Adriatic Sea back into the Mediterranean Sea would cause the tide at the entrance to vanish exactly at resonance such that the amplitude at the end remains finite, despite the infinite amplification predicted by the inviscid linear model. Dissipation of energy due to bottom friction would also cause the amplitudes to remain bounded as well as introduce phase differences along the basin. However, one still expects increased resonance near the resonant basin length, largest amplification occurring at slightly shorter basin length due to the retarding effect of friction (cf. the discussion on response curves in chapter 3). Note that the estimates for the resonant basin length differ by about 20 km when moderately different depth profiles are used and is typically about 10 km less for the solar semidiurnal S_2-tide whose frequency is slightly above the M_2-frequency.

For the K_1-tide there is no amphidromic point within the Adriatic Sea, corresponding to the fact that the K_1-frequency is below the present eigenfrequency of the Adriatic Sea. Consequently the reduction of the basin length brings the Adriatic Sea farther away from resonance and amplification of the K_1-tide must have been less in past ages at lower mean sea level. This conclusion does not depend critically on the precise depth profile, because it relies solely on the absence of an amphidromic point,

which is derived from present-day tidal observations for the K_1-tide. The amplitudes of tidal currents are shown as well. For K_1 the currents are much less (0.045 m/s maximum) than the M_2-currents (0.113 m/s maximum under present conditions) because its frequency is much lower, so the water motion is spread over a larger period of time. Another conspicuous feature is the fact that the currents are considerably larger over the sill of relatively little depth at the beginning of the shallow shelf where the entire flux water moving towards the shelf is forced through a relatively small cross-section.

2.3   Conclusions

In this chapter linear tidal modelling has been illustrated by considering an inviscid one-dimensional linear shallow-water model for the tide in the Adriatic Sea. The linearity of the model allows us to consider the different tidal frequencies separately and compose the final water-level elevations from the sum of the solutions for the different tidal constituents. In particular, the lunar semidiurnal M_2-tide (12^h25^m period, amplitude ranging from 7 cm at Otranto, the Mediterranean entrance to 26 cm at Trieste, the northern end) and the diurnal K_1-tide (23^h56^m period, amplitude ranging from 2 cm at Otranto to 20 cm at Trieste) have been considered. Another important constituent is the solar semidiurnal S_2-tide (12^h00^m period, amplitude ranging from 4 cm at Otranto to 15 cm at Trieste) but it behaves similar to the M_2-component. Other tidal constituents are small compared to these three. The tide is forced by co-oscillation with the tide in the Mediterranean Sea. Its resonant amplification due to the basin length being close to a quarter wavelength, is described quite well by the linear model. A quarter wavelength of the K_1-component of the tide is larger than the length of the Adriatic Sea. Hence the K_1-tide was not so close to resonance in previous ages when the mean sea level was lower and the basin length smaller. The M_2-tide has an amphidromic point within the Adriatic Sea. In previous ages with lower mean sea level and shorter length of the basin, it must have been closer to the entrance implying that the amplification of the tide must have been larger. The inviscid linear model presented in this chapter fixes the resonant basin length at about 570 km when the mean sea level was 110 m below the present level. Although the conclusion that the M_2 must have been more resonantly amplified than today does not depend much on the particular model, the precise value of the resonance length may differ from this number due to the influence of damping or changes in the depth profile.

Chapter 3

Experimental validation of Lorentz's linearization procedure

Having considered a linear model for the amplification of the co-oscillating tide in a tidal basin at specific forcing frequencies in the previous chapter, this chapter focuses on the response curve (amplification and phase lag of the tide in the basin relative to the tidal signal at sea as a function of forcing frequency) of such a basin. In particular the dependence of the response curve on the tidal amplitude due to the nonlinear influence of dissipation is observed. Although Lorentz's linearization procedure for coping with this nonlinear effect was already developed at the beginning of the previous century, quantitative experimental validation in this context had not yet been provided. In this chapter results from laboratory experiments in a 'tidal tank', demonstrating the resonant response of the so-called Helmholtz mode in an almost enclosed basin, are presented. The experimental results show good agreement with theory. [1]

3.1   Introduction

Tidal motion is a key feature (for navigation, economy, flushing, morphodynamics, ecology, . . .) in many coastal areas, with tidal ranges of 1–3 m (Dutch Wadden Sea) up to 8 m (Bay of Fundy). At those locations, it by far exceeds the *equilibrium tide* which represents direct gravitational forcing (if the Earth were completely covered by water, neglecting inertia) by the moon (54 cm) and the sun (26 cm). The amplification is a result of resonance when the directly driven ocean tide propagates into co-oscillating coastal seas. Linear theory describing this is well established and is reviewed in several publications (Defant, 1961; Raichlen, 1966; LeBlond & Mysak, 1978).

Resonance occurs if the tidal period is close to one of the eigenmodes of the basin, such as the *quarter wavelength* modes in half open channel-like basins, or the

---

[1]This chapter is based on the paper *"Experimental verification of Lorentz' linearization procedure for quadratic friction"* by Guido M. Terra, Willem Jan van de Berg and Leo R.M. Maas, Fluid Dyn. Res. (2005), Vol. 36, pp. 175–188.

Helmholtz or *pumping mode* in almost-enclosed basins. For example, Garrett (1974) shows that the eigenperiod of the Bay of Fundy together with the adjacent Gulf of Maine is 13.3h, in near resonance with the dominant M_2-tide from the Atlantic Ocean. The Bay of Fundy itself, like the Adriatic Sea considered in the previous chapter, can be described as a quarter wavelength resonator in which the tidal amplitude increases into the basin. The Helmholtz mode is a relatively simple mode characterized by uniform water-level elevation within basins that are small compared to the tidal wavelength and co-oscillate with an adjacent sea/ocean through a narrow inlet. The balance between the inertia of the flow through the inlet and the restoring force due to the water-level difference between that at sea and in the basin determines the oscillation (see e.g. Miles, 1974; Carrier *et al.*, 1971*b*; Maas, 1997).

Dissipation of energy in resonant Helmholtz basins, which is the main interest in this chapter, is through radiation damping, bottom friction and *head loss* (pressure drop) due to flow separation. Radiation damping is adequately described linearly (e.g. Miles, 1971; Garrett, 1975; Zimmerman, 1992; LeBlond & Mysak, 1978) but leads to the so-called harbour paradox (Carrier *et al.*, 1971*a*; Miles, 1974): intuitively one would expect suppression of the response to external forcing when decreasing the width of the inlet, due to increased screening. However, the maximum and mean square response appear to increase, because radiation of energy is reduced. By including the effect of *head loss* due to flow separation at the inlet this paradox is resolved (Hayashi *et al.*, 1966; Terrett *et al.*, 1968; Ito, 1970; Mei *et al.*, 1974). Using hydraulic theory they show that the head loss term depends quadratically on the fluid velocity. Actually this has the same form as Chezy's law, commonly used to model bottom friction.

In order to evaluate the influence of the quadratic (bottom) friction term Lorentz (1922, 1926) proposed to replace it by a linear term with the friction coefficient chosen such that the energy dissipation per tidal cycle would be the same as when the nonlinear law were used. Zimmerman (1982) interpreted the method as a renormalization procedure. Mei (1989) mentions Lorentz's linearization method under the name of *equivalent linearization*. Zimmerman (1992) applied the method to the special case of the Helmholtz mode, in which case the results are particularly simple. A more elaborate exploration without assuming the tide to be uniform inside the basin is performed by Ünlüata & Mei (1975) and Gerber (1986), thus including the sloshing modes as well. They conclude that the Helmholtz mode is affected most by the head loss effects. Dronkers (1962, 1964) and Le Provost (1973) give a complete asymptotic expansion of the quadratic friction term, which is used in a perturbation method by Kabbaj & Le Provost (1980). All of these methods are virtually equivalent, at least to first order. Hence the simplest approach of Zimmerman (1992) is followed in this chapter.

The calculations of Lorentz (1926) have been confirmed quite well by field observations in the Dutch Wadden Sea (Thijsse, 1972). Nonlinear aspects express themselves in the generation of higher harmonics distorting the tidal curve to become asymmetric (see section 1.3.2 and references therein).

Besides field observations, laboratory experiments have been performed as well. First, linear theory has been tested: McNown (1952) studied the structure of the eigenmodes in circular basins. Similar experiments have been performed for rectangular basins (Apté & Marcou, 1954; Falconer & Guoping, 1991). Lee (1971) measured

the response curves of almost enclosed circular basins, a half open channel and a more complex model of Long Beach Harbour. Harbours with multiple basins were studied in more detail by Lee & Raichlen (1972). All of them found the linear response curves for these basins without considering the influence of the tidal amplitude, i.e. of nonlinearity.

Lepelletier & Raichlen (1987) investigate the nonlinear distortion of the sinusoidal tidal curve by both laboratory and numerical experiments, but they do not consider the influence of the forcing amplitude on the response curves. Experiments to corroborate Lorentz's linearization theory, by comparing the response curves at different forcing amplitudes, seem to be missing. Although Horikawa & Nishimura (1970) do present results for different amplitudes, they rate them as less accurate owing to the deformation of the waves and do not provide an adequate quantitative comparison with theory. Both Bowers (1977) and De Girolamo (1996) state qualitatively that the head loss effect is found to cause the amplification factor to decrease with increasing amplitude in their preliminary experiments. However, their main focus is on the generation of harbour oscillations due to the nonlinear setup/setdown by wave groups. Although they do mention the quadratic dependence of the energy loss on velocity, no quantitative analysis is given by them either. In particular, no reference to Lorentz's linearization principle is made. Equivalent linearization is mentioned by Martinez & Naverac (1988). They provide good quality experimental data, but their focus is on the effect of changing the entrance width to their basins. Their analysis of the data is based on insufficiently developed theory neglecting inertia. As a consequence the dependence on forcing amplitude is not captured well and they conclude that the coefficient in the nonlinear friction law strongly depends on the forcing amplitude.

In order to fill the lack of experimental validation of Lorentz's linearization principle, we present a quantitative comparison between our measurements and the results of a simple model for the Helmholtz mode with Lorentz's linearized friction, which does predict the dependence of the response curves on the forcing amplitude. After a brief overview of the theory in section 3.2 and a description of the experimental setup in section 3.3, the results are discussed in section 3.4. The chapter is concluded with an estimation of the domain of validity of Lorentz's linearization theory using a renormalization method and numerical integration and a discussion of the relevance in the geophysical context.

3.2   Theory

Consider an almost enclosed basin with horizontal area A connected to the sea by a channel of length L, width B and depth H, as shown in Fig. 3.1, which is forced by a tidal signal at sea with angular frequency ω. Its dimensions are assumed to be much smaller than the tidal wavelength $\lambda = 2\pi\sqrt{gH}/\omega$, such that the tidal wave traverses the basin "instantaneously". Hence the water level in the basin can be described by a single value ζ, the elevation relative to the still water level. Water flows into the basin through the channel with velocity u. All dynamics are concentrated in the channel, where the elevation difference between sea and basin drives the flow, balanced by the inertia of the water in the channel and bottom friction/head loss. Actually, the channel length L in (3.1a) measures the inertia of the system. The (relatively small) contribution of flow outside the channel causes the effective length
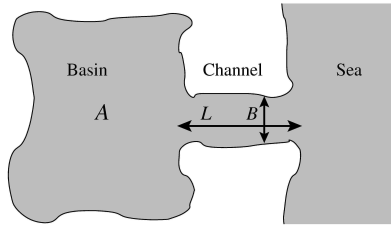
Figure 3.1: Top view sketch of an almost enclosed tidal basin with horizontal area A, co-oscillating with the tide at sea through an inlet channel of width B, length L and depth H.

L_{eff}, which determines the eigenfrequency ω_0 defined below, to be slightly longer than the physical length of the channel, the "added mass effect". From here on each occurrence of L relates to effective length, the notation L_{eff} is used only if confusion with physical length might occur. Bottom friction is commonly described by Chezy's law $(c_D/H)\,|u|u$, with drag coefficient $c_D \approx 0.0025$ determined empirically (Parker, 1991a). The head loss due to flow separation is parameterized by $(f/L)\,|u|u$ and differs only in the formulation of the coefficient; f has to be determined empirically as well. Indeed, based on computer simulations Ito (1970) reports that the harbour paradox is resolved by including this term and the vulnerability of the Port of Ofunato to tsunamis decreased considerably due to the partial closure of the entrance by a breakwater. He found that $f \approx 1.5$ gave the best results when comparing the numerical simulations with observations from tide gauges. The dynamics of the system can be described by the equations for momentum and mass conservation:

$$\frac{\mathrm{d}u}{\mathrm{d}t} = \frac{g}{L}\,(\zeta_e - \zeta) - \frac{\tilde{f}}{L}\,|u|\,u, \tag{3.1a}$$

$$A\,\frac{\mathrm{d}\zeta}{\mathrm{d}t} = O\,u, \tag{3.1b}$$

where $\zeta_e = \alpha_e \cos(\omega t) = \mathrm{Re}\left[\alpha_e\,\mathrm{e}^{\mathrm{i}\omega t}\right]$ is the prescribed elevation at sea and $O = BH$ is the channel cross-section. The head loss coefficient $\tilde{f}/L$ is considered to include bottom friction as well ($\tilde{f}/L = f/L + c_D/H$). Note that radiation damping is not modelled here explicitly but is assumed to be already incorporated in ζ_e, i.e. ζ_e is considered to be the tidal signal at the seaward entrance *with the basin present*. In analysing the experimental results we will also compare the measurements inside the basin with the forcing signal at sea as it is measured simultaneously.

The Lorentz's linearization principle amounts to replacing the nonlinear head loss term $(\tilde{f}/L)\,|u|u$ by ru, with effective linear friction coefficient r to be determined. In that case the system (3.1) is linear and the response will be of the form $\zeta = |\alpha|\cos(\omega t + \varphi) = \mathrm{Re}\left[\alpha\,\mathrm{e}^{\mathrm{i}\omega t}\right]$, where $\alpha = |\alpha|\mathrm{e}^{\mathrm{i}\varphi}$, and consequently $u = -(A/O)\,\omega|\alpha|\sin(\omega t + \varphi)$. Lorentz's energy principle states that the energy dissipation per tidal cycle should be the same for both formulae: $\langle ru^2 \rangle = \langle (\tilde{f}/L)\,|u|u^2 \rangle$, in which $\langle \cdot \rangle$ denotes averaging over a tidal cycle. Evaluation of the corresponding integrals leads to

$$r = \nu_0\,\omega|\alpha|, \quad \text{with } \nu_0 = \tfrac{8}{3\pi}\,\frac{\tilde{f}A}{OL}, \tag{3.2}$$

i.e. effective friction increases linearly with tidal amplitude in the basin. Using the linear expression for friction, (3.1) can be simplified to

$$\frac{d^2\zeta}{dt^2} = \omega_0{}^2 \left(\zeta_e - \zeta \right) - \nu_0\,\omega|\alpha|\,\frac{d\zeta}{dt},$$

in which $\omega_0{}^2 = gO/(AL)$ is the eigenfrequency of the Helmholtz mode. Substituting $\zeta = \mathrm{Re}\left[\alpha\,e^{i\omega t}\right]$ the complex response equation is found:

$$\left(\omega_0{}^2 - \omega^2\right)\alpha + i\,\nu_0\,\omega^2\,|\alpha|\alpha = \omega_0{}^2\,\alpha_e. \tag{3.3}$$

By taking the square modulus of this equation it is possible to solve for $|\alpha|$ and find

$$\frac{|\alpha|}{|\alpha_e|} = \sqrt{\frac{\sqrt{(1-(\frac{\omega}{\omega_0})^2)^4 + 4\nu_0{}^2(\frac{\omega}{\omega_0})^4|\alpha_e|^2} - (1-(\frac{\omega}{\omega_0})^2)^2}{2\nu_0{}^2(\frac{\omega}{\omega_0})^4|\alpha_e|^2}}, \tag{3.4}$$

which can be combined with (3.3) to find the phase lag $\varphi \in (-\pi, 0)$ as well, from $\varphi = \arccos((1-(\frac{\omega}{\omega_0})^2)\frac{|\alpha|}{\alpha_e})$. Differentiating the square modulus of (3.3) with respect to ω, equating the derivative of $|\alpha|$ to zero and using the result to eliminate either ω or α_e, one can maximize (3.4) with respect to ω. As a function of forcing amplitude α_e maximum amplification is given by

$$\frac{|\alpha|_{max}}{\alpha_e} = \sqrt{\frac{1}{2} + \frac{1}{2}\sqrt{1 + \frac{4}{\nu_0{}^2\alpha_e{}^2}}}. \tag{3.5}$$

As a function of ω one has $|\alpha|_{max}/\alpha_e = (1-(\frac{\omega}{\omega_0})^2)^{-1/2}$, which will be indicated by a dotted line in the response diagram (Fig. 3.4(a)).

3.3   Experimental setup

A sketch of the experimental setup is shown in Fig. 3.2. The area of interest is the "basin" of 0.916 m^2. Instead of a channel, a completely submerged pipe is used to connect the basin to the forcing tide at "sea". In this way, the cross-section O does not depend on the water-level elevation ζ, which would otherwise introduce (additional) nonlinear effects (Miles, 1981). The experiments presented in this chapter were performed using a circular pipe with a length of 441 mm and 76.4 mm diameter. Without the "added mass effect" increasing the effective pipe length, the Helmholtz frequency is expected to be $\omega_0 = 0.33$ rad s^{-1} = $53 \cdot 10^{-3}$ Hz (18.8 s period). The water depth at rest was set to be about 15 cm above the bottom of the basin and was checked not to influence the measurements as long as the pipe remains completely submerged. A forcing tank is immersed in the water and is lifted and lowered by a properly counterbalanced servomotor. The control signal can be generated by the computer. In principle the forcing signal may consist of many frequency components, but harmonic forcing only is considered in this chapter. The water expelled by the forcing tank, moves through the conduit underneath the basin area towards the sea. A grating was inserted in order to help the water level at sea to be uniform, but it did not prevent the occurrence of a standing wave: depending on the forcing frequency amplitudes are higher at the far end of the sea. The amplitude of the control

(a) Top view

(b) Side view
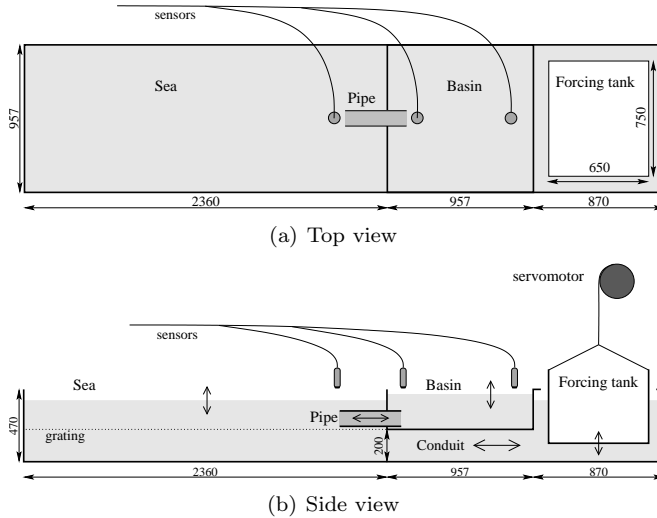
Figure 3.2: Sketch of the experimental setup, dimensions in mm are indicated. The forcing tank is set into motion by a servomotor. The water expelled by the tank moves through the conduit underneath the basin area to the "sea". The tidal signal thus generated at sea, propagates into the basin through a completely submerged pipe. The water-level elevation is measured by acoustic sensors at the indicated positions. Because the tide in the basin is nearly uniform, the measurements for the sensors in the basin are virtually the same.

signal is adjusted to obtain the desired forcing amplitude at the mouth of the basin (cf. the discussion at the end of this section), so this has no influence on the measurements. Acoustic sensors are used for nonintrusive measurements of water-level elevation. They are located above the tank and emit an acoustic signal at 300 kHz down to the water surface and measure the return time of the reflected signal, like an echo sounder. Their resolution is 0.36 mm, the standard deviation of the noise is similar. Significant outliers of some centimetres occur and are dismissed from the analysis.

No dissipators have been installed at the sidewalls of the sea. Raichlen & Ippen (1965) warn that consequent reflections have a dramatic effect on the response curves. They define the amplification factor as the ratio of the tidal response amplitude in the basin over the amplitude at the seaward entrance *if the basin were closed*, i.e. not present. Indeed, radiation damping effects changing the actual tidal forcing signal at the seaward entrance, are quite different in a finite reflective sea than in a semi-infinite reflectionless sea. We however choose to correct the motion of the forcing tank such that the amplitude at the seaward entrance is the same for all frequencies and define the amplification factor as the ratio of the response amplitude in the basin over the amplitude at sea *with the basin connected to it*, as it is measured simultaneously. This effectively boils down to eliminating the effect of radiation damping and circumvents the problems mentioned by Raichlen & Ippen (1965).
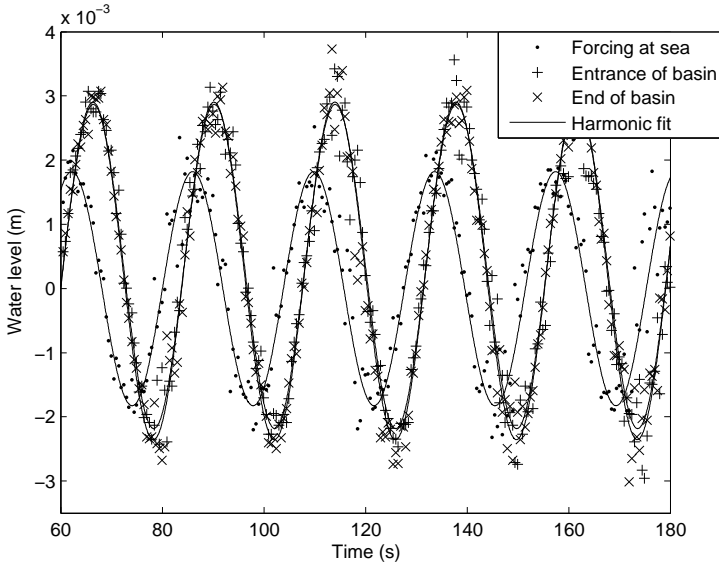
Figure 3.3: Sample time series of measurements at forcing frequency 0.0420 Hz and forcing amplitude approximately 2 mm. Dots indicate measurements from the sensor at sea, pluses and crosses indicate measurements at the entrance and end of the basin respectively. Solid curves show harmonic fits to the respective time series. The two curves inside the basin are nearly indistinguishable, consistent with a Helmholtz mode of uniform basin tide.

3.4   Results

A sample time series from our measurements is shown in Fig. 3.3. This measurement was performed at a forcing frequency $\omega = 0.0420$ Hz $= 0.264$ rad s^{-1} and forcing amplitude α_e approximately 2 mm. Measurements at the seaward pipe entrance are indicated by dots. Pluses and crosses are used for the measurements in the basin. Amplification and phase lag between the tide at sea and in the basin are clearly visible. Note that the signals of both sensors inside the basin are virtually the same, so the assumption of uniform tide within the basin is satisfied indeed. Harmonic analysis has been used to fit the measurements to a sum of sinusoids at the forcing frequency and significant overtides, if any. In most cases, no significant overtides were found. Only for particular frequencies, if one of the overtides was resonant with the eigenfrequency ~ 0.45 Hz of the entire system (sea and forcing tank), secondary oscillations were found at sea. They appeared not to extend into the basin though and there are no indications of their influence on the response curves for the main component. The harmonic fits are shown in Fig. 3.3 as well.

From the amplitudes found this way, the amplification factor and phase lag of the forcing frequency component are calculated. By plotting them as a function of forcing frequency, the response curves are determined, see Fig. 3.4, for three different forcing amplitudes $\alpha_e \approx 1, 2, 5$ mm. The theory according to (3.3) has been fitted to the measurements minimizing the least square error in the complex α/α_e-plane.

(a) Amplification factor   (b) Phase difference
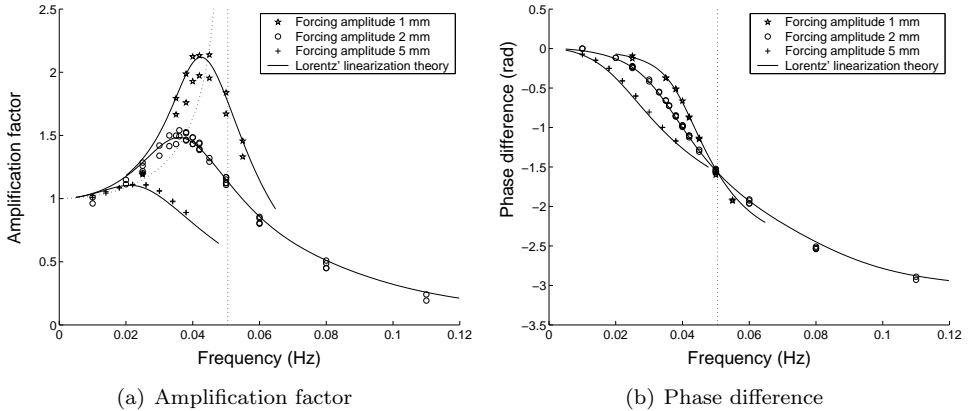
Figure 3.4: Response curves: amplification factor $|\alpha|/\alpha_e$ and phase lag ϕ between the tide at sea and in the basin as a function of forcing frequency $\omega/(2\pi)$. Three series of measurements with forcing amplitudes $\alpha_e \approx 1, 2, 5$ mm are shown, for each of which results for two sensors in the basin have been obtained. Slight amplitude differences between both basin sensors can be noted, in particular at 1 mm forcing amplitude. Solid curves show the fit to the theory (3.4). The Helmholtz frequency $\omega_0 = 0.0505$ Hz is indicated by a dotted vertical line, a dotted curve connects the maxima according to (3.5). Note that one fit is used to describe all three curves. Apparently the decrease of the resonator's quality is adequately described by Lorentz's linearization theory.

Because the effective length differs from the actual pipe length due to the added mass effect it has to be determined empirically. The same holds good for the head loss parameter $\tilde{f}$. Therefore, ω_0 and ν_0 are used as fitting parameters. The curves shown in Fig. 3.4 are for the best fit with $\omega_0 = 50.5 \pm 0.9 \cdot 10^{-3}$ Hz $= 0.317 \pm 0.006$ rad s^{-1}, $\nu_0 = 374 \pm 9$ m^{-1}. So the effective pipe length $L_{\mathrm{eff}} = 48.9 \pm 1.7$ cm is 4.8 cm longer than the actual length of the pipe. Furthermore, $\tilde{f} = 0.97 \pm 0.02$ has the same order of magnitude as Ito (1970) found for motion on real geophysical scale ($f \approx 1.5$). Hence our experiments give validation to his numerical/empirical value.

Although the use of effective instead of physical pipe length amounts to adjusting the theoretical curves to the measurements, note that only one fit is used for all three curves. For a (hypothetical) linear system there would be no dependence of the response curve on the forcing amplitude. Instead the experiments show that the height and sharpness of the resonance peak decrease for increasing amplitudes, due to the fact that effective friction r increases, as was already noted qualitatively by Bowers (1977), De Girolamo (1996) and Martinez & Naverac (1988). This decrease of the resonator's quality (resonance frequency divided by peak width) is captured well by Lorentz's linearization theory. The curves for different forcing amplitude are similar to those for different opening width, in which case the effective friction is increased due to an increase of ν_0 in our terminology (cf. Martinez & Naverac, 1988, Fig. 6). Note that quadratic friction not only causes the response curves to be different for different forcing amplitudes but also changes the shape of the curves, because the effective linear friction coefficient $r \sim \omega\alpha$ is not constant along the individual curves either. Although this effect is hardly visible at first sight it causes the curves to drop off slightly steeper to the right of the peak frequency. A conspicuous feature of the

phase lag curves is the fact that the phase lag is $-\pi/2$ for $\omega = \omega_0$ irrespective of forcing amplitude. It is immediately clear from (3.3) that this is predicted by the theory as well.

3.5   Domain of validity

The correspondence between theory and measurements in figure 3.4 is very good. In the present laboratory setup, conditions for which Lorentz's linearization theory does not perform well have not been found. In order to investigate the domain of validity of Lorentz's linearization theory the model (3.1) has been studied in more detail, both analytically and numerically.

First of all, it is worthwhile to note that the variables in (3.1) can be rescaled to obtain a more simple dimensionless model by scaling

$$\zeta = \tfrac{OL}{A\tilde{f}}\zeta', \qquad \zeta_e = \tfrac{OL}{A\tilde{f}}\zeta'_e, \qquad u = \omega_0 \tfrac{L}{\tilde{f}}u', \qquad t = \tfrac{t'}{\omega_0}, \qquad (3.6)$$

which leads to the dimensionless model

$$\frac{\mathrm{d}u'}{\mathrm{d}t'} = \zeta'_e - \zeta' - |u'|\,u', \qquad (3.7a)$$

$$\frac{\mathrm{d}\zeta'}{\mathrm{d}t'} = u'. \qquad (3.7b)$$

The only parameters that still determine the behaviour of this system are those that determine the forcing water-level elevation ζ'_e at sea, the (dimensionless) forcing frequency $\omega' = \omega/\omega_0$ and amplitude $\alpha'_e = \tfrac{A\tilde{f}}{OL}\alpha_e$. Hence the shape of the response curves is completely determined by the dimensionless parameter α'_e that measures the relative importance of friction.

3.5.1   First-order corrections to Lorentz's linearization theory

Zimmerman (1992) showed that Lorentz's linearization procedure can be considered as a renormalization method. Introducing a formal expansion parameter ε, (3.7a) is replaced by

$$\frac{\mathrm{d}u'}{\mathrm{d}t'} = \zeta'_e - \zeta' - \varepsilon|u'|\,u' - r'u', \qquad (3.8a)$$

which equals (3.7a) for $\varepsilon = 1, r' = 0$. Writing $\zeta' = \bar{\zeta}' + \varepsilon z' + \mathcal{O}(\varepsilon^2), u' = \bar{u}' + \varepsilon v' + \mathcal{O}(\varepsilon^2), r' = \bar{r}' + \varepsilon\rho' + \mathcal{O}(\varepsilon^2)$ and consistently collecting terms of the same order in ε one finds the model with linearized friction to first order. At the next order one has

$$\frac{\mathrm{d}v'}{\mathrm{d}t'} + \bar{r}'\,v' + z' = -|\bar{u}'|\,\bar{u}' - \rho'\bar{u}', \qquad (3.9a)$$

$$\frac{\mathrm{d}z'}{\mathrm{d}t'} = v'. \qquad (3.9b)$$

Truncating at this order, the consistency condition $r' = 0$ for $\varepsilon = 1$ implies that $\rho' = -\bar{r}'$. The renormalization condition, requiring the first order solution $\bar{\zeta}', \bar{u}'$ to correctly capture the behaviour at the forcing frequency ω', consequently leads

to $\bar{r}' = \frac{8}{3\pi}\omega'|\bar{\alpha}'|$, where $\bar{\zeta}' = \mathrm{Re}\left[\bar{\alpha}'\,e^{i\omega't'}\right], \bar{u}' = \mathrm{Re}\left[i\omega'\bar{\alpha}'\,e^{i\omega't'}\right]$ is the Lorentz's linearized solution (to be found from (3.4) with $\nu_0 = \frac{8}{3\pi}$). This is consistent with Lorentz's energy principle. For the correction z' on the Lorentz's linearized results we thus have (writing $\bar{\alpha}' = |\bar{\alpha}'|\,e^{i\bar{\varphi}'}$)

$$\frac{\mathrm{d}^2z'}{\mathrm{d}t'^2} + \bar{r}'\frac{\mathrm{d}z'}{\mathrm{d}t'} + z' = \bar{r}'\,\bar{u}' - |\bar{u}'|\,\bar{u}'$$
$$= -\frac{8}{3\pi}\omega'^2|\bar{\alpha}'|^2\,\sin(\omega't' + \bar{\varphi}') \pm \omega'^2|\bar{\alpha}'|^2\,\sin^2(\omega't' + \bar{\varphi}'), \tag{3.10}$$

with the plus-sign if $\sin(\omega't' + \bar{\varphi}')$ is positive and the minus-sign if it is negative, hence on the intervals, indexed by integer k, $[k\frac{2\pi}{\omega'} - \frac{\bar{\varphi}'}{\omega'}, (k+\frac{1}{2})\frac{2\pi}{\omega'} - \frac{\bar{\varphi}'}{\omega'}]$ or $[(k+\frac{1}{2})\frac{2\pi}{\omega'} - \frac{\bar{\varphi}'}{\omega'}, (k+1)\frac{2\pi}{\omega'} - \frac{\bar{\varphi}'}{\omega'}]$. Up to this point the procedure from Zimmerman (1992) was followed, but he solved (3.10) using a truncated Fourier sum whereas matching exact solutions on the latter intervals is performed here. The solution on the respective intervals is given by

$$
\begin{aligned}
z'^{(k)}_{\pm} = {} & \frac{|\bar{\alpha}'|}{1+\delta_1{}^2}\left(\cos(\omega't' + \bar{\varphi}') - \delta_1\sin(\omega't' + \bar{\varphi}')\right) \\
& \pm \frac{1}{2}\omega'^2|\bar{\alpha}'|^2 \mp \frac{3\pi}{32}\frac{|\bar{\alpha}'|}{1+\delta_2{}^2}\left(\delta_2\cos(2\omega't' + 2\bar{\varphi}') + \sin(2\omega't' + 2\bar{\varphi}')\right) \\
& + B^{(k)}_{\pm}e^{-\frac{\bar{r}'}{2}(t'-t^{(k)}_{\pm})}\cos(\sqrt{1-(\frac{\bar{r}'}{2})^2}\,(t' - t^{(k)}_{\pm})) \\
& + D^{(k)}_{\pm}e^{-\frac{\bar{r}'}{2}(t'-t^{(k)}_{\pm})}\sin(\sqrt{1-(\frac{\bar{r}'}{2})^2}\,(t' - t^{(k)}_{\pm})),
\end{aligned}
\tag{3.11}
$$

where we abbreviate $\delta_1 = \frac{3\pi}{8}(1 - \omega'^2)/(\omega'^2|\bar{\alpha}'|)$, $\delta_2 = \frac{3\pi}{16}(1 - 4\omega'^2)/(\omega'^2|\bar{\alpha}'|)$, $\bar{r}' = \frac{8}{3\pi}\omega'|\bar{\alpha}'|$ and $t^{(k)}_{+} = k\frac{2\pi}{\omega'} - \frac{\bar{\varphi}'}{\omega'}, t^{(k)}_{-} = (k+\frac{1}{2})\frac{2\pi}{\omega'} - \frac{\bar{\varphi}'}{\omega'}$ are the points at which $\sin(\omega't' + \bar{\varphi}')$ changes sign. By matching z' and $\frac{\mathrm{d}z'}{\mathrm{d}t'}$ at $t^{(k)}_{\pm}$, we can relate the integration constants $B^{(k)}_{\pm}, D^{(k)}_{\pm}$ in subsequent intervals:

$$\mathbf{F}X^{(k)}_{-} = e^{-\frac{4}{3}|\bar{\alpha}'|}\,\mathbf{F}\,\mathbf{R}X^{(k)}_{+} + d, \text{ and} \tag{3.12a}$$
$$\mathbf{F}X^{(k+1)}_{+} = e^{-\frac{4}{3}|\bar{\alpha}'|}\,\mathbf{F}\,\mathbf{R}X^{(k)}_{-} - d, \text{ hence} \tag{3.12b}$$
$$X^{(k+1)}_{+} = \delta^2\,\mathbf{R}^2 X^{(k)}_{+} + \delta\,\mathbf{R}\,\mathbf{F}^{-1}d - \mathbf{F}^{-1}d, \tag{3.12c}$$

in which $X^{(k)}_{\pm} = \begin{pmatrix} B^{(k)}_{\pm} \\ D^{(k)}_{\pm} \end{pmatrix}$ is the vector containing the integration constants,

$$\mathbf{F} = \begin{pmatrix} 1 & 0 \\ -\frac{\bar{r}'}{2} & \sqrt{1-(\frac{\bar{r}'}{2})^2} \end{pmatrix}$$

is a skew matrix incorporating phase differences between currents and water level due to friction,

$$\mathbf{R} = \begin{pmatrix} \cos(\frac{\pi}{\omega'}\sqrt{1-(\frac{\bar{r}'}{2})^2}) & \sin(\frac{\pi}{\omega'}\sqrt{1-(\frac{\bar{r}'}{2})^2}) \\ -\sin(\frac{\pi}{\omega'}\sqrt{1-(\frac{\bar{r}'}{2})^2}) & \cos(\frac{\pi}{\omega'}\sqrt{1-(\frac{\bar{r}'}{2})^2}) \end{pmatrix}$$

is the rotation matrix over angle $\frac{\pi}{\omega'}\sqrt{1-(\frac{\bar{r}'}{2})^2}$ related to the eigenoscillation, the

(a) Amplification factor

(b) Phase difference
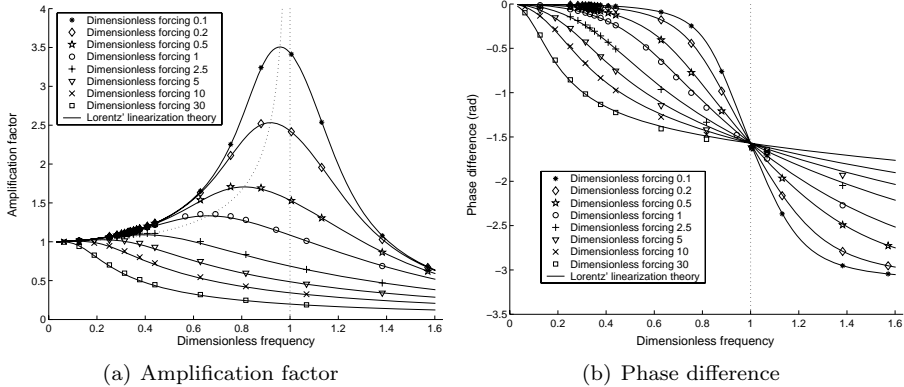
Figure 3.5: Response curves: amplification factor and phase lag between the tide at sea and in the basin as a function of forcing frequency. Numerical results (symbols) for the dimensionless system (3.7) are shown. The dimensionless Helmholtz frequency $\omega_0' = 1$ is indicated by a dotted vertical line, a dotted curve connects the maxima according to (3.5). The theoretical (solid) curves are calculated from (3.4),(3.5), with $\omega_0 = 1, \nu_0 = \frac{8}{3\pi}$.

factor $\delta = \mathrm{e}^{-\frac{4}{3}|\bar{\alpha}'|}$ accounts for frictional damping of the oscillation and

$$
d = \begin{pmatrix} \frac{9\pi^2}{64(1+\delta_2{}^2)}(4\omega'^2 + \bar{r}'^2 - 1) \\ \frac{-3\pi\omega'|\bar{\alpha}'|}{8(1+\delta_2{}^2)} \end{pmatrix}
$$

is the vector representing the forcing at this order. The stationary solution (independent of k) to these equations is found by solving $[\mathbf{I} - \delta^2\mathbf{R}^2]X_+ = -[\mathbf{I} - \delta\mathbf{R}]\,\mathbf{F}^{-1}d$, hence $X_+ = -[\mathbf{I} + \delta\mathbf{R}]^{-1}\,\mathbf{F}^{-1}d$. The complete expression for the water level and current oscillation up to this order is obtained by adding $\zeta_\pm' = \bar{\zeta}' + \varepsilon z_\pm', u_\pm' = \bar{u}' + \varepsilon v_\pm'$, setting $\varepsilon = 1$.

Performing an harmonic analysis, fitting a sum of sinusoids with frequencies $n\omega'$, with $n = 0, 1, 2, \ldots$ to ζ', the correction has no influence on the harmonic fit at the forcing frequency, due to the renormalization condition. So the response curves found using Lorentz's linearization procedure need not be changed to this order of approximation. Still, one can use the results from this section to estimate the changes in the tidal curve due to the nonlinear friction term, see figure 3.6.

3.5.2   Numerical results

The dimensionless model (3.7) has been integrated using the numerical dynamical systems package DsTool (Guckenheimer *et al.*, 1992) for several values of α_e' between 0.1 and 30. They were subsequently processed in the same manner as the experimental results. In line with the observation at the end of the previous section the response curves are not noticeably different from the prediction by Lorentz's linearization theory over this entire range, see figure 3.5. Deviations from Lorentz's linearization theory appear when considering the tidal curves. Figure 3.6(a) shows the tidal curve for one of the numerical runs for which the correspondence between the numerical integration of (3.7) and the theoretical calculations using (3.11) is the worst, with

$\alpha'_e = 2.5, \omega' = 0.377$. One can see that the deviations from a single sinusoid are still predicted quite well by the asymptotic correction (3.11). Note that the current (which has not been measured during the laboratory experiments) is influenced more strongly by the quadratic nature of friction than the water level itself. Subtracting the single sinusoid at the forcing frequency one is left with the deviation from Lorentz's theory in figure 3.6(b), in which it is more clear that the correction (3.11) overestimates the amplitude of the tertiary overtide. This can be seen as well in figure 3.6(c), which shows the maximum deviation relative to the amplitude of Lorentz's sinusoidal response as a function of the forcing frequency for $\alpha'_e = 0.1, 1$ and 30 (asterisks, pluses and crosses). Moreover, it shows the relative change of the high water level (open circles, squares and diamonds), which is less than the maximum deviation because the latter need not be synchronized with high tide. The maximum deviation and the deviation of the maxima according to the asymptotic correction (3.11) is plotted as well, by dashed and dotted curves respectively. Actually, we find peaks of resonant behaviour at forcing frequencies $\omega' = 1/n$, with n odd, $n = 3$ in particular. The amplitude of the peak is overestimated however, because up to this order of approximation the effective friction coefficient $\bar{r}' = \frac{8}{3\pi}\omega'|\bar{\alpha}'|$ is normalized for the dominant (forcing) frequency only. The resonant motion at the eigenfrequency is damped more strongly because its frequency is three times the forcing frequency in this case. The main conclusion to be drawn from this figure though, is the fact that Lorentz's theory is correct within 7% even for $\alpha'_e = 30$, for which the response curve figure 3.5 shows damping for almost all frequencies.

3.5.3   Geophysical context

When extending the model result (3.4) from the laboratory setting to the geophysical context, the main lack of knowledge is in the relative strength of friction. In the laboratory setting, the dominant dissipative effect is the head loss due to the constriction. This clearly depends on the shape of the entrance. Although the quadratic dependence of friction on the velocity should still be valid, the appropriate value of the coefficient $\tilde{f}$ is somewhat uncertain. However, because the value $\tilde{f} = 0.97$ found by our laboratory experiments compares well with Ito's (1970) numerical value $f = 1.5$, one is inclined to use this value in the geophysical context as well. For example, the Amelander Inlet in the Dutch Wadden Sea can be considered to be a Helmholtz basin with the following (approximative) characteristics:

$$A = 2.5{\cdot}10^8 \text{ m}^2, \qquad B = 3{\cdot}10^3 \text{ m}, \qquad H = 10 \text{ m}, \qquad L_{\text{eff}} = 5{\cdot}10^3 \text{ m}, \qquad \alpha_e = 1 \text{ m},$$

which leads to

$$\omega_0 = 4.9 \cdot 10^{-4} \text{ rad s}^{-1}, \qquad \omega'_{M_2} = 0.29, \qquad \alpha'_e = 1.62, \qquad \text{hence} \quad \frac{|\alpha|}{\alpha_e} = 1.082.$$

This compares reasonably well with the observed tide with range 1.4–2.5 m at sea and 1.7–2.8 m on the mainland at neap and spring tide respectively. Abusively extending the results for a Helmholtz basin to a quarter wavelength resonator, the famous Bay of Fundy leads to surprisingly comparable results as well. Considering only the Bay of Fundy by itself, it has a total length of $270 \cdot 10^3$ m and an average width of about $50 \cdot 10^3$ m leading to $A = 1.35 \cdot 10^{10}$ m^2. The entrance, $80 \cdot 10^3$ m wide, on average 50 m deep, is estimated with cross-section $O = 4 \cdot 10^6$ m^2. For the effective length of

(a) Tidal curve

(b) Deviation from single sinusoidal

(c) Maximum deviation and deviation of maxima of water-level response in basin
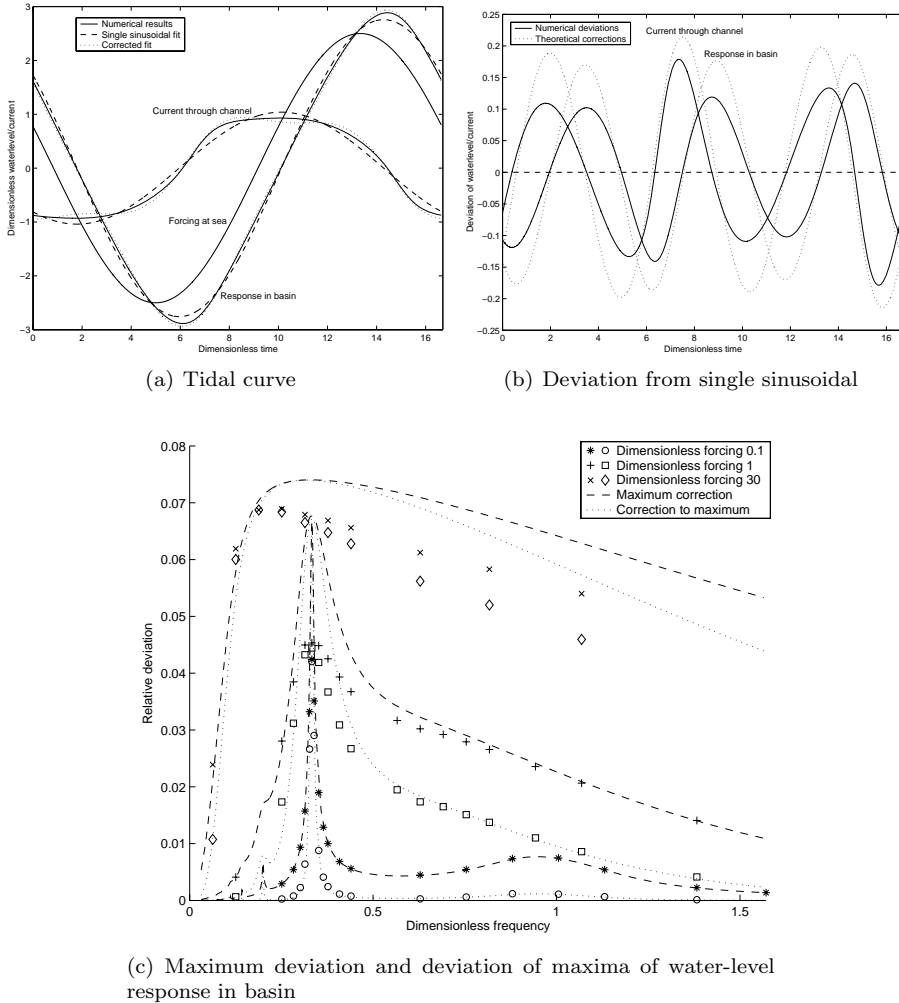
Figure 3.6: Numerical results integrating (3.7) versus theoretical corrections using (3.11): (a) shows a sample tidal curve for $\alpha'_e = 2.5, \omega' = 0.377$. In (b) the dominant signal at the forcing frequency is subtracted. The maximum deviation from this signal (the maximum of the basin's water-level response in (b), asterisks, pluses and crosses) is plotted as a function of forcing frequency ω' in figure (c), as well as the deviation of the maxima (high tide in (a), circles, squares and diamonds) from the single sinusoid's amplitude predicted by Lorentz's linearization theory, both relative to the amplitude of the single sinusoid. Results are obtained by numerical integration using DsTool for $\alpha'_e = 0.1, 1$ and 30. The dashed lines approximate the maximum deviation, the dotted ones the deviation of the maxima, according to (3.11). The peak at $\omega' = \frac{1}{3}$ is predicted well, although the amplitude is overestimated.

the entrance we take $L_{\text{eff}} = 100 \cdot 10^3$ m. Actually, the effective "channel" length for which the Helmholtz frequency corresponds with the first quarter wavelength mode, is found by dividing the total basin length by $\pi^2/4$. The tidal amplitude at the mouth of the Bay of Fundy is 3 m, hence we find, $\omega_0 = 1.7 \cdot 10^{-4}$ rad s^{-1}, $\omega'_{M_2} = 0.82$, $\alpha'_e = 0.098$ and $\frac{|\alpha|}{\alpha_e} = 2.8$, which compares well with the amplification up to 8 m amplitude within the Bay of Fundy.

3.6   Conclusion

Although the theoretical foundations of Lorentz's linearization method were already put forward in Lorentz (1922, 1926), no quantitative high-accuracy experimental validation is found in literature yet. The theory has been developed further (Mei, 1989; Kabbaj & Le Provost, 1980; Zimmerman, 1992), comparison with observations have been made (Ito, 1970; Thijsse, 1972), but studies using laboratory experiments have been restricted to validating linear theory mainly (McNown, 1952; Raichlen & Ippen, 1965; Lee, 1971). Experimental papers in which the effect of nonlinear friction on the response curves has been measured, did not provide an explicit quantitative comparison with theory, mainly because the focus was on another topic (Horikawa & Nishimura, 1970; Bowers, 1977; De Girolamo, 1996; Martinez & Naverac, 1988). The experiments discussed in this chapter give a clear validation of Lorentz's linearization principle to describe the influence of quadratic friction on the response curves for the Helmholtz mode in an almost enclosed basin. A good fit between theory and experiment was found. In particular the observed decrease of the resonator's quality with increasing amplitude corresponds perfectly with the theoretical increase of the effective friction coefficient.

Further research has been focused on improving the quality of the resonator and measuring nonlinear effects from non-uniform hypsometry (Maas, 1997) or continuity/advection (Miles, 1981). The first goal may be achieved by smoothing the pipe ends in order to reduce flow separation or decreasing the basin area, hence the tidal prism. For the second goal, artificial topography can be introduced into the basin mimicking intertidal flats causing the basin area to depend on the water level. According to the theory this may lead to bending of the response curve, multiple equilibria and chaotic behaviour of tidal amplitudes, possibly explaining observational reports of drifting harmonic "constants" (Doodson, 1924; Gutiérrez et al., 1981) and chaotic tidal records (Vittori, 1992; Frison et al., 1999). These topics are investigated theoretically in the forthcoming chapters 4 and 5. Experimental results are presented in chapter 6.

Acknowledgments

Chapter 4

Derivation of the amplitude evolution equations

In this and the next chapter the qualitative nonlinear influence of advection and continuity on the resonance characteristics of co-oscillating coastal basins is investigated. For this purpose a weakly nonlinear analysis is carried out on the shallow-water equations describing a coastal basin resonating with exterior water-level oscillations. It extends previous work (Maas, 1997; Maas & Doelman, 2002; Doelman *et al.*, 2002) on an almost-enclosed basin with one single (Helmholtz) mode to arbitrarily shaped 'shallow' basins with an infinite number of modes. In line with that work, it is necessary to assume friction to be sufficiently weak such that it is in balance with the nonlinear effects, instead of occurring in the linearized equations. The main result of this chapter is the system of Landau equations describing the slow evolution of the amplitudes of the oscillatory eigenmodes of the basin, disregarding a zero-frequency eigenmode, should it exist. The dynamics of the zero-frequency mode neglecting oscillatory eigenmodes have been discussed by others, but a consistently balanced model for small amplitudes incorporating both the zero-frequency and oscillatory modes is not yet available. The behaviour of this system, describing the dynamics of the oscillatory eigenmodes only, is analysed in chapter 5. On the longer time scale, it gives rise to a 'bent resonance curve', multiple equilibria (several tidal regimes under the same tidal forcing), sudden regime changes and even chaotic dynamics (when these regime changes occur in an irregular way).[1]

4.1   Introduction

Tides are generated by the gravitational forces exerted by astronomical objects, mainly the sun and the moon. The direct gravitational forcing accounts for a global tidal amplitude of merely 0.27 m for the lunar and 0.13 m for the solar component (LeBlond & Mysak, 1978, p. 517). In order to explain the strong tidal signal of several metres in many coastal areas, amplification due to resonance is required. A tidal basin connected to a neighbouring ocean or sea can co-oscillate with the tide at sea with increased amplitude if the basin's geometry is such that the period of one

---

[1]This chapter is based on (the first half of) the paper *"Weakly nonlinear cubic interactions in coastal resonance"* by Guido M. Terra, Arjen Doelman and Leo R.M. Maas, J. Fluid Mech. (2004), vol. 520, pp. 93–134.

of its eigenmodes corresponds to that of the tidal motion. The amplification by itself has been described quite well with linear theory (Defant, 1961; LeBlond & Mysak, 1978; Mei, 1989). In this thesis nonlinear corrections to this linear picture are investigated. The nonlinear effects addressed now are due to advective accelerations and to feedback on the water depth. Besides modifying the shape of the tidal curve by generating higher harmonics, they can change the response curve (amplification as a function of forcing frequency) of the basin, which may have dramatic qualitative effects. In this chapter weakly nonlinear evolution equations for the tidal response amplitudes are derived, the steady states of which constitute the response curves.

Traditionally the term *coastal resonance* is used to describe the response of certain large-scale bays to forcing at one of the tidal frequencies. This response is typically classified by the nature of the response, ranging from microtidal (when the coastal tide is choked, i.e. has an amplitude less than that of the tide at open sea), via meso- to macrotidal (coastal tide moderately amplified). Yet, in its strictest sense the term is reserved to designate a so-called megatidal response, the severe amplification such as encountered e.g. in the famous Bay of Fundy (amplitudes ranging up to 8 m), Sea of Okhotsk, or near the coast of Normandy (amplitudes over 6 m). The nonlinear model for coastal resonance which we will present, is, by the approach it takes, particularly of relevance to the latter, megatidal case. It predicts that in certain circumstances the tidal response might be irregular on the longer (e.g. fortnightly) time scale.

Resonance in smaller-scale coastal basins is called *harbour resonance.* These infragravity waves (Okihiro & Guza, 1995) are pronounced oscillations in near-shore sea areas and harbours with periods of a few minutes to hours, which are longer than those associated with surface wind waves, but of shorter duration than a typical tidal period. It can be considered as a special kind of coastal resonance. It is related again to an eigenmode, typical of the particular geomorphology of the area under consideration, resonating due to some forcing mechanism. In this case, the corresponding eigenfrequencies are much higher than the tidal frequencies. Although the terminology in this thesis is adapted to the tidal case, the analysis goes through for the infragravity regime as well. If the infragravity waves are the dominant oscillation in the basin, one only needs to change the time scale from the tidal period to the period of the harbour oscillations.

A model aimed at describing nonlinear tidal resonance has been developed previously by assuming the spatial structure of the response in the bay to be as simple as possible (namely spatially uniform), see Miles (1981), Green (1992) and Maas (1997). Such a uniform spatial structure is a property of the so-called *Helmholtz* (or *pumping*, or *breathing*) mode, and requires a specific geographic setting: an almost-enclosed, relatively deep and small basin, such that the length of the basin is much shorter than the tidal wavelength. Although this allows the nonlinear temporal response to be understood (Maas & Doelman, 2002; Doelman *et al.*, 2002), the stringent requirements on the shape of the resonator render it less applicable to describe the response of a large number of (half open) bays. The derivation in the present chapter forms a direct generalization of Maas (1997), Maas & Doelman (2002) and Doelman *et al.* (2002) for the Helmholtz mode in almost-enclosed basins to the case of eigenoscillations in half-open, quarter-wavelength basins. Note that the term *quarter-wavelength* is used here to describe modes in a two-dimensional basin with non-uniform depth as well, i.e. to denote modes with spatial structure, in contrast to the Helmholtz mode.

In line with the observations, we will assume the resonating oscillation to be nearly absent outside the bay. As will be shown here, one can derive amplitude equations that govern the evolution of the quarter-wavelength-type eigenmodes, the simplest of which is identical to the equation governing the Helmholtz mode in the more specific setting of an almost-enclosed basin.

The analysis of the nonlinear quarter-wavelength resonances, starts from the shallow-water equations (section 4.2). Assuming small amplitudes of the oscillations a perturbation analysis similar to the one employed by Pratt & Llewellyn Smith (1997), is carried out in section 4.3. Starting from the basic state at rest, the first-order equations are linear and yield the quarter-wavelength modes of a half-open basin. Realness of eigenvalues and orthogonality of these first-order eigenmodes can be established, but the amplitude of the resonating mode is still undetermined at this level of description. The linear modes interact at the next (second) order, non-resonantly in our case, leading amongst others to the generation of a zero-frequency component. The eigenmodes are assumed to be forced (and damped) and interact *resonantly*[2] only at the next order. It is thus at third order that closed-form equations governing the slow evolution of the amplitudes of the quarter-wavelength modes are finally obtained, in the form of Landau equations. This is in contrast with the analysis in Pratt & Llewellyn Smith (1997). Whereas the focus of this thesis is on the oscillatory modes, their paper deals primarily with the zero-frequency (in rotating systems: geostrophic) mode. Hence their basic first-order modes are the eigenmodes of an entirely closed basin. Moreover, the presence of the zero-frequency eigenmode causes resonant interactions to occur at second order. In the half-open oscillatory case, one is forced to continue up to higher order to find the amplitude equations and assume friction to be still weaker. On the other hand, by the choice of focusing on the oscillatory modes only, we were able to evaluate the qualitative form of the amplitude equation more explicitly.[3] However, although circumstances can be indicated for which there is no zero-frequency eigenmode, it is likely to exist in many basins. A proper description would combine the approach of Pratt & Llewellyn Smith (1997) for the zero-frequency mode and the one presented here for oscillatory modes. At present, the mathematical problems involved with it remain a challenge to be solved. In this thesis, the zero-frequency eigenmode is simply ignored in order to focus on the interaction between the oscillatory eigenmodes.

The depth-averaged two-dimensional shallow-water equations for a co-oscillating tidal basin are formulated in section 4.2. The derivation of the amplitude evolution equations takes place in three steps. The first-order equations lead to a linear eigenvalue problem whose properties are discussed in section 4.3.1. The next section deals with the generation of compound components by the quadratic interaction between eigenmodes due to advection and continuity. In section 4.3.3 the application of a solvability condition leads to the goal of this chapter, the Landau equation (4.29) or the reduced version (4.30). In order to provide order of magnitudes for the coefficients in the Landau equation, three examples for one-dimensional basins are discussed in section 4.4. The concluding section 4.5 includes a discussion of the relevance of the results to natural basins, and points out a few deficiencies in the theory.

---

[2]Note that resonance is used in its mathematical meaning here: exact correspondence of forcing frequency and eigenfrequency in the frictionless limit, hence giving rise to infinite amplification, i.e. the necessity to remove secular terms.

[3]Compare the final equation (4.30) in this chapter with the amplitude equation (3.5) in Pratt & Llewellyn Smith (1997). In fact, the latter is the second-order equivalent of (4.23) in this work.

(a) Top view   (b) Side view
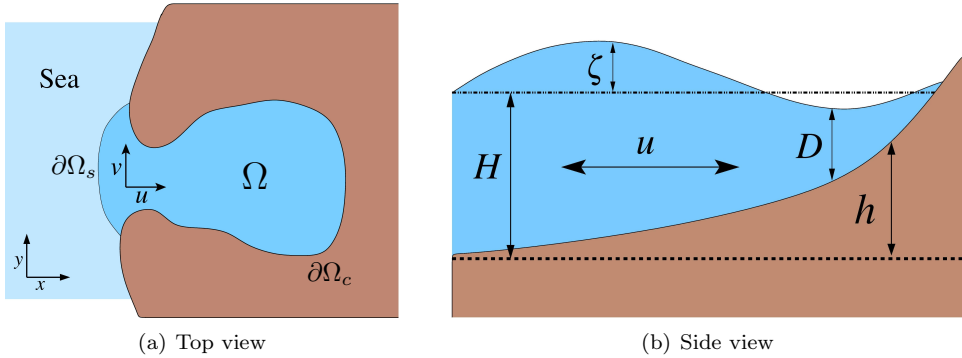
Figure 4.1: Sketch of the tidal basin.

4.2   Formulation of the model

A tidal basin as shown in figure 4.1 is considered in this chapter. The top view, figure 4.1(a), shows Ω, the area of interest. It is connected to the sea. The seaward boundary of the area Ω is denoted by $\partial\Omega_s$, the coastal boundary by $\partial\Omega_c$. The choice of the precise location of the seaward boundary $\partial\Omega_s$ is somewhat arbitrary and is fixed in time. In the side view, figure 4.1(b), a reference depth H is introduced, chosen to be the undisturbed water depth at sea. The bathymetry is measured relative to this depth level by $h(\mathbf{x})$, where $\mathbf{x} = (x, y)$ is the horizontal position. The free-surface elevation from the undisturbed water level is denoted by $\zeta(\mathbf{x}, t)$. The total instantaneous water depth is thus given by $D(\mathbf{x}, t) = H - h(\mathbf{x}) + \zeta(\mathbf{x}, t)$. In fact, the area Ω depends on time. When the water level rises, part of the coast is flooded, increasing the area Ω. The coastal boundary $\partial\Omega_c$ is defined by the condition that the total water depth D is zero, hence is moving in time.[4]

The water motions are described by the depth-averaged two-dimensional shallow-water equations. They describe the depth-averaged flow of water when the horizontal scales of the motion are much larger than the vertical scale (depth) of the water. Depth-averaged velocities are denoted by $\mathbf{U} = (u, v)$. In vectorial form the equations are

$$\frac{\partial \zeta}{\partial t} + \nabla\cdot[D\mathbf{U}] \quad = \quad 0, \tag{4.1a}$$

$$\frac{\partial \mathbf{U}}{\partial t} + [\mathbf{U}\cdot\nabla]\mathbf{U} + f\hat{\mathbf{k}} \times \mathbf{U} \quad = \quad -g\nabla\zeta - \frac{\tau_b}{\rho D}, \tag{4.1b}$$

where τ_b is the bottom friction stress, to be parameterized. Equation (4.1a) is the continuity equation, (4.1b) is the momentum equation. The vector $\hat{\mathbf{k}}$ is the vertical unit vector: $\hat{\mathbf{k}} \times \mathbf{U} = (-v, u)$. These equations are completed with the boundary conditions

---

[4]In principle this gives rise to a slight mismatch between the fixed boundary $\partial\Omega_s$ and the moving boundary $\partial\Omega_c$, so $\partial\Omega_s$ should be lengthened and shortened respectively to keep the connection with $\partial\Omega_c$. These notational futilities do not play a role in this derivation however, because the location of $\partial\Omega_c$ is fixed as well to first order of approximation.

$$\frac{\partial D}{\partial t} + [\mathbf{U}{\cdot}\nabla]D = 0, \qquad \text{at } \partial\Omega_c. \tag{4.2a}$$

$$\zeta = \zeta_e(\mathbf{x}, t), \qquad\qquad \text{at } \partial\Omega_s. \tag{4.2b}$$

At the seaward boundary the free-surface elevation is prescribed to follow the exterior tide $\zeta_e(\mathbf{x}, t)$, i.e. radiation damping is not taken into account explicitly. If one intends to properly incorporate this effect, the following considerations could be helpful: (a) Including radiation damping effectively boils down to correcting the exterior tide $\zeta_e(\mathbf{x}, t)$ for the waves leaving the basin. Although this correction is important when trying to model the response of a particular basin to a certain exterior forcing, our model still describes the processes in the basin subject to the (possibly corrected) exterior tide $\zeta_e(\mathbf{x}, t)$ accurately. In other words, ζ_e describes the water level at sea when the basin is present (i.e. after correcting for radiation damping, although it is not done in this thesis), not the tide that would be present if the basin were not there at all. (b) Radiation damping usually leads to linear damping terms in the seaward boundary condition see e.g. Miles (1971), Garrett (1975), LeBlond & Mysak (1978), Zimmerman (1992) and Nycander & Döös (2001). Because the focus of this work is on nonlinear dynamics, a detailed investigation of radiation damping is beyond the scope of this project. In the present weakly nonlinear context, it would simply lead to an additional contribution to the linear friction term in the Landau equations.

The condition at the coastal boundary states that $\partial\Omega_c$ is a material boundary, i.e. $\partial\Omega_c$ is a moving boundary whose location varies due to the motion of the fluid. The condition is that particles forming the boundary, which is defined by the condition $D = 0$, remain at the boundary. For vertical sidewalls, the local gradient of the depth profile D is infinite. In that case, the appropriate condition is to require the normal component of the velocity to vanish. In the presented derivation condition (4.2a) is used. The alterations for vertical sidewalls are straightforward and do not influence the nature of the results.

A common parametrization for the bottom friction is the quadratic Chezy law $\tau_b = \rho c_D |\mathbf{U}|\mathbf{U}$, in which $c_D \sim 0.0025$ is a dimensionless drag coefficient (Parker, 1991a, p. 247). This parametrization could be used here as well. However, in order to simplify the calculations a linear parametrization $\tau_b = \rho r_* \mathbf{U}$ will be used. In this so-called Lorentz-linearization the friction parameter r_* should be chosen such that the tidally averaged dissipation of energy is the same for both parameterizations, see Lorentz (1922) and Zimmerman (1992). Note that the results of this chapter would be the same if the Chezy law were used. In that case the Taylor series expansion for $|\mathbf{U}|\mathbf{U}$ must be used, in which the even powers are absent (Dronkers, 1962, 1964; Le Provost, 1973; Kabbaj & Le Provost, 1980). The first term in this expansion corresponds to the linear friction law used for the derivation in this chapter, whereas the cubic term enters the calculation only at higher order.

4.3   Formal asymptotic expansion of the solution

A weakly nonlinear analysis is carried out, so the amplitude of the motion is assumed to be small. This is incorporated in the equations by scaling the hydrodynamic variables with a small parameter. It is convenient to bring (4.1) and (4.2) into non-

dimensional form first. The scalings that are used read

$$\zeta = Z\zeta', \quad D = HD', \quad h = Hh',$$
$$x = Lx', \quad y = Ly', \qquad t = \frac{T}{2\pi}t', \quad \mathbf{U} = \frac{2\pi L}{T}\frac{Z}{H}\mathbf{U}'. \tag{4.3}$$

In these expressions, Z is a measure of the amplitude of the free-surface elevation, $\alpha = Z/H$, the non-dimensional amplitude, is assumed to be small. The non-dimensional depth is $D' = 1 - h' + \alpha\zeta'$. L and T are the length and time scale of the motion. A sensible choice for L would be the length of the basin and for T the period of the main component of the exterior tide, in the tidal case. In the case of secondary undulations, the eigenperiod of the basin would be a more appropriate time scale.

Apart from assuming small amplitude $\alpha \ll 1$, some additional assumptions are necessary in order to obtain a tractable, consistently balanced model. The parameter α will be used as a scaling parameter to reflect these assumptions. For mathematical convenience a single small parameter is used without implying a physical relationship with basin amplitude Z. The scaling assumptions are equivalent to the ones used in Maas & Doelman (2002) and Doelman *et al.* (2002) for Helmholtz basins and correspond to significant degeneration: under these conditions all processes enter the equation at the same order of approximation. First, the system is assumed to be in resonance. Hence the exterior tide will be amplified in the interior. The exterior tide is scaled by α^3, assuming an amplification factor of α^{-2}. This assumption implies that non-resonant components will not play a role at first order. Secondly, the friction parameter $r_* = \alpha^2 \sigma H\, r$ is assumed to be $\mathcal{O}(\alpha^2)$, i.e. very small as well. Note that, in view of Lorentz's linearization principle, r_* is expected to depend linearly on the velocity amplitude. The scaling with α^2 instead of α is obtained when assuming the drag coefficient c_D to be $\mathcal{O}(\alpha)$. The main motivation is mathematical though: this choice leads to the significant degeneration in which friction enters the equation to balance the nonlinear terms.

After removing the primes, the scaling (4.3) leads to

$$\frac{\partial\zeta}{\partial t} + \nabla\!\cdot\![D\mathbf{U}] \;=\; 0, \tag{4.4a}$$

$$\frac{\partial\mathbf{U}}{\partial t} + \alpha[\mathbf{U}\!\cdot\!\nabla]\mathbf{U} + F\hat{\mathbf{k}}\times\mathbf{U} \;=\; -\gamma\nabla\zeta - \alpha^2 r\frac{\mathbf{U}}{D}, \tag{4.4b}$$

where $F = f/\sigma$ is the scaled Coriolis parameter and $\gamma = gH/(\sigma^2 L^2)$, acting as the non-dimensional gravitational acceleration, is (the square of) the ratio between the free tidal wavelength and the length scale of the basin. The scaled version of the boundary conditions is

$$\frac{\partial\zeta}{\partial t} + \alpha[\mathbf{U}\!\cdot\!\nabla]\zeta = [\mathbf{U}\!\cdot\!\nabla]h, \qquad \text{at } \partial\Omega_c, \tag{4.5a}$$

$$\zeta = \alpha^2\zeta_e(\mathbf{x},t), \qquad\qquad \text{at } \partial\Omega_s. \tag{4.5b}$$

The equations (4.4), with (4.5), will be solved by an asymptotic multiple-time-scale expansion in terms of the small amplitude $\alpha \ll 1$: substitute

$$\begin{cases} \zeta(\mathbf{x},t) &=\; \zeta^{(1)}(\mathbf{x},t,\tau) + \alpha\zeta^{(2)}(\mathbf{x},t,\tau) + \alpha^2\zeta^{(3)}(\mathbf{x},t,\tau) + \dots, \\ \mathbf{U}(\mathbf{x},t) &=\; \mathbf{U}^{(1)}(\mathbf{x},t,\tau) + \alpha\mathbf{U}^{(2)}(\mathbf{x},t,\tau) + \alpha^2\mathbf{U}^{(3)}(\mathbf{x},t,\tau) + \dots, \end{cases} \tag{4.6}$$

in (4.4). The functions $\zeta^{(n)}$ and $\mathbf{U}^{(n)}$ depend on the spatial variable $\mathbf{x}$, time t and a slow time scale $\tau = \alpha^2 t$. The equations for the evolution of those functions will

be derived in the subsequent sections by collecting terms of equal order in α in (4.4) and (4.5). It will be found in section 4.3.2 that the derivatives are zero on the time scale αt, so the time scale τ is the first slow time scale on which evolution is possible, due to the (scaling) assumptions in this section.

4.3.1   First-order solutions

The first-order equations are

$$\frac{\partial \zeta^{(1)}}{\partial t} + \nabla\cdot[D^{(0)}\mathbf{U}^{(1)}] \;=\; 0, \tag{4.7a}$$

$$\frac{\partial \mathbf{U}^{(1)}}{\partial t} + F\hat{\mathbf{k}} \times \mathbf{U}^{(1)} \;=\; -\gamma\nabla\zeta^{(1)}, \tag{4.7b}$$

where the notation $D^{(0)}(\mathbf{x}) = 1 - h(\mathbf{x})$ has been introduced. The corresponding boundary conditions are

$$\frac{\partial \zeta^{(1)}}{\partial t} = [\mathbf{U}^{(1)}\cdot\nabla]h, \qquad \text{at } \partial\Omega_c^{(0)}, \tag{4.8a}$$

$$\zeta^{(1)} = 0, \qquad\qquad \text{at } \partial\Omega_s^{(0)}. \tag{4.8b}$$

The boundary $\partial\Omega_c^{(0)}$ is the fixed boundary at which the still water depth $D^{(0)}$ vanishes, $\partial\Omega_s^{(0)}$ is the fixed seaward boundary. Note that $\partial\Omega_s^{(0)}$ could be replaced by $\partial\Omega_s$ since the location of this part of the boundary is fixed anyway.

The linear equations (4.7) and (4.8) allow separation of the temporal and spatial behaviour of the solutions. Thus, we write

$$\begin{cases} \zeta^{(1)}(\mathbf{x},t,\tau) &=& \sum_j A_j(\tau)\zeta_j(\mathbf{x})\mathrm{e}^{\mathrm{i}\omega_j t}, \\ \mathbf{U}^{(1)}(\mathbf{x},t,\tau) &=& \sum_j A_j(\tau)\mathbf{U}_j(\mathbf{x})\mathrm{e}^{\mathrm{i}\omega_j t}, \end{cases} \tag{4.9}$$

in which summation is over all eigenmodes of the system (4.10) below. The functions $\zeta_j, \mathbf{U}_j$ are the eigenfunctions corresponding to the eigenvalues ω_j. The eigenvalues ω_j will be shown to be real-valued, hence correspond to the angular frequency of the jth eigenmode. The amplitudes A_j are constant to first order; the temporal behaviour of (4.9) on the fast time scale t is determined by the eigenfrequencies ω_j. On the slow time scale $\tau = \alpha^2 t$ however, the amplitudes A_j are still allowed to vary. Their evolution depends on higher-order nonlinear interactions between the eigenmodes. In section 4.3.3 the evolution equations (4.30), which form the central goal of this chapter, for the amplitudes A_j on the slow time scale τ are derived.

The eigenmodes $\zeta_j, \mathbf{U}_j, \omega_j$ should satisfy

$$\mathrm{i}\omega_j\zeta_j + \nabla\cdot[D^{(0)}\mathbf{U}_j] \;=\; 0, \tag{4.10a}$$

$$\mathrm{i}\omega_j\mathbf{U}_j + F\hat{\mathbf{k}} \times \mathbf{U}_j \;=\; -\gamma\nabla\zeta_j, \tag{4.10b}$$

together with the boundary conditions

$$\mathrm{i}\omega_j\zeta_j = [\mathbf{U}_j\cdot\nabla]h, \qquad \text{at } \partial\Omega_c^{(0)}, \tag{4.11a}$$

$$\zeta_j = 0, \qquad\qquad \text{at } \partial\Omega_s^{(0)}. \tag{4.11b}$$

Instead of trying to solve these equations for explicit examples of tidal basins (shape Ω and depth profile $D^{(0)}$, see section 4.4 however), more general results will be derived here, based on the assumption that we have solved (4.10), (4.11). Moreover, a few generic assumptions (4.14) on the set of eigenmodes and eigenvalues are made. Because it is easier to formulate those assumptions having gathered some basic information about the solutions of the eigenvalue problem (4.10), (4.11), their formulation is postponed till the end of this section.

Let $\zeta_j, \mathbf{U}_j$ be eigenfunctions of (4.10) with eigenvalue ω_j, and $\zeta_k, \mathbf{U}_k$ be eigenfunctions with eigenvalue ω_k. Following Pratt & Llewellyn Smith (1997), consider the following 'generalized inner product'[5] with the equations

$$\gamma \zeta_k^* \, \mathrm{cont}_j^{(1)} + \gamma \zeta_j \, \mathrm{cont}_k^{(1)*} + D^{(0)} \mathbf{U}_k^* \cdot \mathrm{mom}_j^{(1)} + D^{(0)} \mathbf{U}_j \cdot \mathrm{mom}_k^{(1)*},$$

where $\mathrm{cont}_j^{(1)}$ denotes the continuity equation (4.10a) for the jth eigenmode, $\mathrm{cont}_k^{(1)*}$ is its complex conjugate for the kth eigenmode. Analogously, $\mathrm{mom}_j^{(1)}$ and $\mathrm{mom}_k^{(1)*}$ denote the (complex conjugate) momentum equation (4.10b), for eigenmodes j and k respectively. This leads to

$$\mathrm{i}(\omega_j - \omega_k^*)\left(\gamma \zeta_k^* \zeta_j + D^{(0)} \mathbf{U}_k^* \cdot \mathbf{U}_j\right) + \nabla \cdot \left[\gamma D^{(0)}(\zeta_k^* \mathbf{U}_j + \zeta_j \mathbf{U}_k^*)\right] = 0.$$

Integrating this over the still water area $\Omega^{(0)}$ of the basin, yields the interesting 'inner product equation'

$$(\omega_j - \omega_k^*) \iint_{\Omega^{(0)}} \left(\gamma \, \zeta_k^* \zeta_j + D^{(0)} \, \mathbf{U}_k^* \cdot \mathbf{U}_j\right) \mathrm{d}x\mathrm{d}y = 0. \qquad (4.12)$$

The divergence term results in an integral over the boundary $\partial\Omega^{(0)}$ of $\gamma D^{(0)}(\zeta_k^* \mathbf{U}_j + \zeta_j \mathbf{U}_k^*) \cdot \hat{\mathbf{n}}$, with $\hat{\mathbf{n}}$ the outward normal along $\partial\Omega^{(0)}$. Using the boundary condition (4.11) for ζ_j and its complex conjugate for ζ_k^* we see that this integral vanishes. Note that $D^{(0)} = 0$ on $\partial\Omega_c^{(0)}$.

In analogy with the arguments in Pratt & Llewellyn Smith (1997), some important conclusions can be drawn from (4.12). First, choosing $k = j$ implies that $\omega_j = \omega_j^*$, hence the eigenfrequencies ω_j are real. Because the temporal behaviour of the eigenmodes is $\mathrm{e}^{\mathrm{i}\omega_j t}$, it is purely periodic without decay. Note that the eigenfunctions cannot be chosen to be real-valued, i.e. there will be phase differences within the basin. This is a consequence of the Coriolis acceleration. Moreover, comparing (4.10), (4.11) with their complex conjugate counterparts, it can be concluded that if $\zeta_j, \mathbf{U}_j$ are eigenfunctions corresponding to eigenvalue ω_j, then $\zeta_j^*, \mathbf{U}_j^*$ are eigenfunctions corresponding to eigenvalue $-\omega_j$. Therefore, it is possible to distinguish the eigenfrequencies $\omega_j \geq 0$ and consider the negative ones as complex conjugates of the positive eigenvalues. If the positive eigenvalues are indexed by positive j, it is convenient to let $\omega_{-j} = -\omega_j$ denote the conjugate eigenvalue. Moreover, they can be numbered in increasing order, $\omega_k \geq \omega_j$ if $k \geq j$.

The second conclusion to be drawn from (4.12) is that the eigenfunctions corresponding to different eigenvalues are orthogonal with respect to the following inner product:

$$\left\langle \begin{pmatrix} \zeta_k \\ \mathbf{U}_k \end{pmatrix}; \begin{pmatrix} \zeta_j \\ \mathbf{U}_j \end{pmatrix} \right\rangle = \iint_{\Omega^{(0)}} \left(\gamma \, \zeta_k^* \zeta_j + D^{(0)} \, \mathbf{U}_k^* \cdot \mathbf{U}_j\right) \mathrm{d}x\mathrm{d}y. \qquad (4.13)$$

---

[5]This becomes an inner product only after integrating the integrand over $\Omega^{(0)}$.

Hence, the set of eigenfunctions can be chosen orthonormal. Physically this inner product is just the dimensionless measure of the energy related to the respective eigenmode; the eigenfunctions are normalized with respect to their energetic content. We assume that they form a complete set. This implies that the expansion (4.9) is indeed the general form in which all solutions $\zeta^{(1)}, \mathbf{U}^{(1)}$ to (4.7), (4.8) can be written. Note that, although (4.10), (4.11) is not a classical Sturm–Liouville problem because of the boundary conditions, the conclusions drawn in the preceding paragraph are the same.

The analysis in this chapter is carried out for the generic situation. In order to exclude some degenerate cases the following assumptions on the set of eigenmodes and eigenfrequencies are made:

- the eigenfunctions $(\zeta_j(x), \mathbf{U}_j(x))$ form a complete set;   (4.14a)
- there are no degenerate eigenvalues: $\omega_k \neq \omega_l$;   (4.14b)
- there are no second-order resonances: $\omega_k - \omega_l - \omega_m \neq 0$;   (4.14c)
- there are no non-trivial third-order resonances: $\omega_k - \omega_l - \omega_m \pm \omega_n \neq 0$; (4.14d)

where the eigenfrequencies ω_j should be ordered as described before and $k > l \geq m \geq n \geq 1$. Note that (4.14b) is implied by (4.14d) through considering it for m equal to n. Trivial third-order resonances exist for $k = l$ (contrasting with $k > l$ in the assumption) and $m = n$. Generically the conditions (4.14) are met: situations in which second or third-order resonances are present are exceptional in the sense that slight changes of the basin, hence the eigenfrequencies, would cause the resonances to disappear. In particular cases for which the assumptions are not satisfied, the forthcoming analysis should be carried out more carefully. In section 4.4 three examples are given for which the assumptions are checked.

Remark (zero-frequency mode): The eigenvalue problem (4.10), (4.11) may have a continuum of solutions for $\omega_0 = 0$. For $F \neq 0$ the momentum equation shows that $\gamma\zeta_0/F$ serves as a streamfunction. From the continuity equation it subsequently follows that ζ_0 should be constant along depth contours. Because of the boundary condition at $\partial\Omega_s^{(0)}$, $\zeta_0 = 0$ along depth contours that intersect $\partial\Omega_s^{(0)}$, whereas the boundary condition at $\partial\Omega_c^{(0)}$ implies that $\mathbf{U}_0 = 0$ (whence $\nabla\zeta_0 = 0$) along those intersecting $\partial\Omega_c^{(0)}$. So $\omega_j = 0$ is not an eigenvalue unless there are closed depth contours (in the case of a separate crest or trough) in the interior Ω of the basin. On the other hand, if the Coriolis acceleration is negligible, i.e. if $F = 0$ at this order, then $\zeta_0 \equiv 0$ everywhere, whereas $\mathbf{U}_0$ is completely free as long as $D^{(0)}\mathbf{U}_0$ has zero divergence.

The calculations are much more elaborate if this zero-frequency mode consisting of a continuum of solutions is present. A method to analyse the evolution of this mode by considering circulation integrals is developed by Pratt & Llewellyn Smith (1997) and Pratt (1997). In their work the geostrophic mode (with $\omega_0 = 0$, for $F \neq 0$) is considered, whereas the oscillatory modes play a minor role. The evolution equations, with quadratic nonlinearities, essentially amount to quasi-geostrophic theory for the zero-mode.

Because the focus is on the oscillatory modes and the interactions between them, the zero-mode is omitted in this work without further justification. Combining the zero-mode and oscillatory modes in a single theory leads to a fundamentally different regime, beyond the scope of this thesis. For the terms to balance at the right order, one can argue that the zero-mode should appear only at $\mathcal{O}(\alpha^2)$, resonantly forced by

quadratic self-interaction of oscillatory modes (note that non-resonant forcing at zero frequency is taken into account in section 4.3.2). Moreover it could potentially cause much richer (chaotic) behaviour because it interacts quadratically with the oscillatory modes, effectively introducing parametric forcing terms in the Landau equation (4.30) for those modes; this is similar to the effect of the Earth's rotation (see section 5.5.2) in that it invalidates the arguments in section 5.2.

Remark (vertical sidewalls): The only change for the case of vertical sidewalls is the boundary condition at $\partial\Omega_c$. Instead of (4.5a), (4.8a) and (4.11a) one has $\mathbf{U}\cdot\hat{\mathbf{n}} = 0$, $\mathbf{U}^{(1)}\cdot\hat{\mathbf{n}} = 0$ and $\mathbf{U}_j\cdot\hat{\mathbf{n}} = 0$ respectively. Apart from modifying the eigenvalue problem to be solved, this has no influence on the analysis leading to the Landau equations (4.30). The boundary condition at $\partial\Omega_c{}^{(0)}$ was used in the argument following (4.12) showing the integral of $\gamma D^{(0)}(\zeta_k^*\mathbf{U}_j + \zeta_j\mathbf{U}_k^*)\cdot\hat{\mathbf{n}}$ over the boundary $\partial\Omega_c{}^{(0)}$ to be zero because $D^{(0)} = 0$. For vertical sidewalls, $D^{(0)} \neq 0$ at $\partial\Omega_c{}^{(0)}$, but $\mathbf{U}_j\cdot\hat{\mathbf{n}}$ and its complex conjugate are zero, which leads to the same conclusion.

The boundary $\partial\Omega_c$ is not moving, but fixed at vertical sidewalls. The moving boundary causes additional terms in the boundary conditions at higher order. They do not play a role however in the analysis in the remainder of this chapter either. At higher order integrals over $\partial\Omega^{(0)}$, similar to the one found in this section, appear. The integrals over $\partial\Omega_c{}^{(0)}$ are zero because $D^{(0)} = 0$. For vertical sidewalls, when this is not the case, the boundary condition $\mathbf{U}\cdot\hat{\mathbf{n}} = 0$ implies that the integrals are zero in that case as well.

4.3.2   Second-order corrections

Having solved the first-order equations (4.7), (4.8) by specifying the general solution (4.9), the next step towards the evolution equation for the amplitudes $A_j(\tau)$ is to find the second-order corrections to this approximation. The second-order equations are

$$\frac{\partial\zeta^{(2)}}{\partial t} + \nabla\cdot[D^{(0)}\mathbf{U}^{(2)}] \;\; = \;\; -\nabla\cdot[\zeta^{(1)}\mathbf{U}^{(1)}], \tag{4.15a}$$

$$\frac{\partial\mathbf{U}^{(2)}}{\partial t} + F\hat{\mathbf{k}}\times\mathbf{U}^{(2)} + \gamma\nabla\zeta^{(2)} \;\; = \;\; -[\mathbf{U}^{(1)}\cdot\nabla]\mathbf{U}^{(1)}. \tag{4.15b}$$

Boundary conditions should be added to these equations. They are different from (4.8) because of the nonlinear terms and due to correction terms for the moving boundary. Because we will expand $\zeta^{(2)}, \mathbf{U}^{(2)}$ in terms of the first-order eigenmodes and take the inner-product (4.13), it appears that the second-order boundary conditions are not needed. Hence they are omitted. Again it makes sense to take the 'inner product'[6] with the equations in the form

$$\gamma\zeta_k^*\,\mathrm{cont}^{(2)} + \gamma\zeta^{(2)}\,\mathrm{cont}_k^{(1)*} + D^{(0)}\mathbf{U}_k^*\cdot\,\mathrm{mom}^{(2)} + D^{(0)}\mathbf{U}^{(2)}\cdot\,\mathrm{mom}_k^{(1)*},$$

where $\mathrm{cont}^{(2)}$ and $\mathrm{mom}^{(2)}$ stand for the continuity and momentum equation (4.15a,b); $\mathrm{cont}_k^{(1)*}$ and $\mathrm{mom}_k^{(1)*}$ refer to the complex conjugate of (4.10a,b) as before. This leads

---

[6]Again this becomes an inner product only after integrating over $\Omega^{(0)}$.

to the equation

$$
\left[\frac{\partial}{\partial t} - \mathrm{i}\,\omega_k\right] (\gamma \zeta_k^* \zeta^{(2)} + D^{(0)} \mathbf{U}_k^* \cdot \mathbf{U}^{(2)}) + \nabla \cdot \left[\gamma D^{(0)} (\zeta_k^* \mathbf{U}^{(2)} + \zeta^{(2)} \mathbf{U}_k^*)\right]
$$
$$
= -\gamma \zeta_k^* \nabla \cdot [\zeta^{(1)} \mathbf{U}^{(1)}] - D^{(0)} \mathbf{U}_k^* \cdot [\mathbf{U}^{(1)} \cdot \nabla] \mathbf{U}^{(1)}.
\tag{4.16}
$$

Because the eigenfunctions of (4.10) were assumed to form a complete set, the second-order corrections $\zeta^{(2)}, \mathbf{U}^{(2)}$ can be expanded in terms of those eigenfunctions, i.e.

$$
\begin{cases}
\zeta^{(2)}(\mathbf{x}, t, \tau) &=& \sum_j \tilde{B}_j(t, \tau) \zeta_j(\mathbf{x}), \\
\mathbf{U}^{(2)}(\mathbf{x}, t, \tau) &=& \sum_j \tilde{B}_j(t, \tau) \mathbf{U}_j(\mathbf{x}).
\end{cases}
\tag{4.17}
$$

The dependence of the amplitudes $\tilde{B}_j$ on the fast time scale t can be found by integrating (4.16) over the still water basin area $\Omega^{(0)}$ to obtain the ordinary differential equation

$$
\left[\frac{\partial}{\partial t} - \mathrm{i}\,\omega_k\right] \tilde{B}_k = -\iint_{\Omega^{(0)}} \left(\gamma \zeta_k^* \nabla \cdot [\zeta^{(1)} \mathbf{U}^{(1)}] + D^{(0)} \mathbf{U}_k^* \cdot [\mathbf{U}^{(1)} \cdot \nabla] \mathbf{U}^{(1)}\right) \mathrm{d}x \mathrm{d}y
$$
$$
= -\sum_{l,m} ({}_k\mathcal{C}_{l,m} + {}_k\mathcal{A}_{l,m}) A_l A_m \mathrm{e}^{\mathrm{i}(\omega_l + \omega_m)t},
\tag{4.18}
$$

where

$$
{}_k\mathcal{C}_{l,m} = \iint_{\Omega^{(0)}} \gamma \zeta_k^* \nabla \cdot [\zeta_l \mathbf{U}_m] \, \mathrm{d}x \mathrm{d}y,
\tag{4.19a}
$$

$$
{}_k\mathcal{A}_{l,m} = \iint_{\Omega^{(0)}} D^{(0)} \mathbf{U}_k^* \cdot [\mathbf{U}_l \cdot \nabla] \mathbf{U}_m \mathrm{d}x \mathrm{d}y,
\tag{4.19b}
$$

are coefficients which can be regarded as inner products of the (normalized) kth eigenvector with the nonlinear terms. Note that the divergence term on the left-hand side of (4.16) integrates to zero again by the same reasoning (following equation (4.12)) as before because $\zeta^{(2)} = 0$ on $\partial \Omega_s^{(0)}$ as well and $D^{(0)} = 0$ on $\partial \Omega_c^{(0)}$. This equation can be solved assuming the non-resonance condition (4.14c): $\omega_k \neq \omega_l + \omega_m, \forall k, l, m$. Under this assumption the solution of (4.18) is given by

$$
\tilde{B}_k(t, \tau) = B_k(\tau) \mathrm{e}^{\mathrm{i}\omega_k t} - \mathrm{i} \sum_{l,m} \frac{{}_k\mathcal{C}_{l,m} + {}_k\mathcal{A}_{l,m}}{\omega_k - \omega_l - \omega_m} A_l(\tau) A_m(\tau) \mathrm{e}^{\mathrm{i}(\omega_l + \omega_m)t},
\tag{4.20}
$$

with $B_k(\tau)$ some unknown second-order amplitudes. This expression should be substituted into (4.17) to find the second-order corrections. The non-resonance condition implies that the second-order corrections remain slaved and second order and do not lead to secularities. If the non-resonance condition is not satisfied, then the amplitudes $\tilde{B}_k(t, \tau)$ would increase linearly in time t, violating the regularity of the asymptotic expansion (4.6). In that case a solvability condition should be applied at this order already (as is next done in section 4.3.3) leading to free dynamics of the first-order amplitudes by quadratic interactions (instead of cubic). In general however, the non-resonance condition will be met.

4.3.3   Third-order: evolution

Finally, the equations at third order in α are given by

$$\frac{\partial \zeta^{(1)}}{\partial \tau} + \frac{\partial \zeta^{(3)}}{\partial t} + \nabla\cdot[D^{(0)}\mathbf{U}^{(3)}] = -\nabla\cdot[\zeta^{(1)}\mathbf{U}^{(2)} + \zeta^{(2)}\mathbf{U}^{(1)}], \quad (4.21\text{a})$$

$$\frac{\partial \mathbf{U}^{(1)}}{\partial \tau} + \frac{\partial \mathbf{U}^{(3)}}{\partial t} + F\hat{\mathbf{k}}\times\mathbf{U}^{(3)} + \gamma\nabla\zeta^{(3)} = -[\mathbf{U}^{(1)}\cdot\nabla]\mathbf{U}^{(2)} - [\mathbf{U}^{(2)}\cdot\nabla]\mathbf{U}^{(1)}$$

$$-r\frac{\mathbf{U}^{(1)}}{D^{(0)}}. \qquad (4.21\text{b})$$

As before, boundary conditions should be added, but they are not needed and hence omitted, because we will not actually try to solve for $\zeta^{(3)}, \mathbf{U}^{(3)}$ and merely use (4.21) to derive a solvability condition. In addition to the contributions of the nonlinear terms on the right-hand side of these equations, the slow evolution of the first-order solutions appears. In order to find bounded solutions for $\zeta^{(3)}, \mathbf{U}^{(3)}$, a solvability condition must be satisfied. This condition yields the slow evolution of the amplitudes $A_k(\tau)$ of the first-order solution, which is determined by friction and the nonlinear interactions. To derive the equation for the slow evolution, consider the 'inner product'

$$\gamma\zeta_k^* \, \text{cont}^{(3)} + \gamma\zeta^{(3)} \, \text{cont}_k^{(1)*} + D^{(0)}\mathbf{U}_k^*\cdot \text{mom}^{(3)} + D^{(0)}\mathbf{U}^{(3)}\cdot \text{mom}_k^{(1)*},$$

which yields

$$\frac{\partial}{\partial \tau}(\gamma\zeta_k^*\zeta^{(1)} + D^{(0)}\mathbf{U}_k^*\cdot\mathbf{U}^{(1)}) + \left[\frac{\partial}{\partial t} - \mathrm{i}\,\omega_k\right](\gamma\zeta_k^*\zeta^{(3)} + D^{(0)}\mathbf{U}_k^*\cdot\mathbf{U}^{(3)})$$

$$+\nabla\cdot\left[\gamma D^{(0)}(\zeta_k^*\mathbf{U}^{(3)} + \zeta^{(3)}\mathbf{U}_k^*)\right] \qquad (4.22)$$

$$= -\gamma\zeta_k^*\nabla\cdot[\zeta^{(1)}\mathbf{U}^{(2)} + \zeta^{(2)}\mathbf{U}^{(1)}] - D^{(0)}\mathbf{U}_k^*\cdot\left([\mathbf{U}^{(1)}\cdot\nabla]\mathbf{U}^{(2)} + [\mathbf{U}^{(2)}\cdot\nabla]\mathbf{U}^{(1)}\right)$$

$$-r\mathbf{U}_k^*\cdot\mathbf{U}^{(1)}.$$

When integrating this expression over the still water basin area $\Omega^{(0)}$ to obtain the global energy balance the divergence term on the left-hand side requires special attention: it integrates to

$$\oint_{\partial\Omega^{(0)}} \gamma D^{(0)}(\zeta_k^*\mathbf{U}^{(3)} + \zeta^{(3)}\mathbf{U}_k^*)\cdot\hat{\mathbf{n}}\,\mathrm{d}s,$$

which can be divided into an integral over $\partial\Omega_c^{(0)}$ and an integral over $\partial\Omega_s^{(0)}$. The integrand is zero on $\partial\Omega_c^{(0)}$ as before, see the discussion following (4.12), but along $\partial\Omega_s^{(0)}$ more care has to be taken. In fact, the boundary condition (4.5b) leads to $\zeta^{(3)} = \zeta_e$ at $\partial\Omega_s^{(0)}$ at third order. Using the fact that $\zeta_k^* = 0$ at $\partial\Omega_s^{(0)}$, we see that the first part of the integrand still vanishes on $\partial\Omega_s^{(0)}$. Therefore, integration of (4.22) over $\Omega^{(0)}$ leads to

$$\left[\frac{\partial}{\partial t} - \mathrm{i}\,\omega_k\right]\left\langle\begin{pmatrix}\zeta_k \\ \mathbf{U}_k\end{pmatrix}; \begin{pmatrix}\zeta^{(3)} \\ \mathbf{U}^{(3)}\end{pmatrix}\right\rangle + \frac{\partial}{\partial \tau}\left\langle\begin{pmatrix}\zeta_k \\ \mathbf{U}_k\end{pmatrix}; \begin{pmatrix}\zeta^{(1)} \\ \mathbf{U}^{(1)}\end{pmatrix}\right\rangle + \int_{\partial\Omega_s^{(0)}} \gamma D^{(0)}\zeta_e\mathbf{U}_k^*\cdot\hat{\mathbf{n}}\,\mathrm{d}s$$

$$= -\iint_{\Omega^{(0)}} \gamma\zeta_k^*\nabla\cdot[\zeta^{(1)}\mathbf{U}^{(2)} + \zeta^{(2)}\mathbf{U}^{(1)}]\,\mathrm{d}x\mathrm{d}y$$

$$-\iint_{\Omega^{(0)}} D^{(0)}\mathbf{U}_k^*\cdot\left([\mathbf{U}^{(1)}\cdot\nabla]\mathbf{U}^{(2)} + [\mathbf{U}^{(2)}\cdot\nabla]\mathbf{U}^{(1)}\right)\,\mathrm{d}x\mathrm{d}y - \iint_{\Omega^{(0)}} r\mathbf{U}_k^*\cdot\mathbf{U}^{(1)}\,\mathrm{d}x\mathrm{d}y.$$

A solvability condition must be satisfied in order for this equation to yield bounded third-order corrections: all terms for which the temporal behaviour on the fast time scale t is given by $e^{i\omega_k t}$ must cancel, otherwise $\left\langle \begin{pmatrix} \zeta_k \\ \mathbf{U}_k \end{pmatrix}; \begin{pmatrix} \zeta^{(3)} \\ \mathbf{U}^{(3)} \end{pmatrix} \right\rangle$ will grow due to resonance. For an efficient evaluation of this condition, the expansions (4.9), (4.17) and (4.20) are substituted. Because of the orthonormality of the eigenfunctions the derivative with respect to τ evaluates to $\frac{\mathrm{d}A_k}{\mathrm{d}\tau} e^{i\omega_k t}$, whose t-temporal behaviour is clearly resonant. Consequently, the solvability condition reads

$$
\begin{aligned}
\frac{\mathrm{d}A_k}{\mathrm{d}\tau} &= -\int_{\partial\Omega_s{}^{(0)}} \gamma D^{(0)}\{\zeta_e\}_k \mathbf{U}_k^* \cdot \hat{\mathbf{n}} \; \mathrm{d}s \\
&\quad - \left\{ \iint_{\Omega^{(0)}} \gamma \zeta_k^* \nabla \cdot [\zeta^{(1)}\mathbf{U}^{(2)} + \zeta^{(2)}\mathbf{U}^{(1)}] \; \mathrm{d}x\mathrm{d}y \right\}_k \\
&\quad - \left\{ \iint_{\Omega^{(0)}} D^{(0)}\mathbf{U}_k^* \cdot \left([\mathbf{U}^{(1)} \cdot \nabla]\mathbf{U}^{(2)} + [\mathbf{U}^{(2)} \cdot \nabla]\mathbf{U}^{(1)} \right) \; \mathrm{d}x\mathrm{d}y \right\}_k \\
&\quad - \left\{ \iint_{\Omega^{(0)}} r\mathbf{U}_k^* \cdot \mathbf{U}^{(1)} \; \mathrm{d}x\mathrm{d}y \right\}_k ,
\end{aligned}
\tag{4.23}
$$

where $\{\cdot\}_k$ denotes the operator that selects the Fourier component with frequency ω_k, i.e. $\{e^{i\omega t}\}_k \sim \delta(\omega - \omega_k)$. Next, each term on the right-hand side of (4.23) will be studied.

For the forcing term, we define

$$
F_k(\tau) = -\int_{\partial\Omega_s{}^{(0)}} \gamma D^{(0)}\{\zeta_e(\mathbf{x}, t, \tau)\}_k \mathbf{U}_k^* \cdot \hat{\mathbf{n}} \; \mathrm{d}s.
\tag{4.24}
$$

For single-frequency forcing at one of the resonant frequencies ω_k (i.e. $\zeta_e = \alpha_e \, e^{i\omega_k t}$) $\{\zeta_e\}_k = \alpha_e$ is constant, hence $F_k(\tau) \equiv F_k$ is constant as well. For nearly resonant forcing, $F_k(\tau)$ will be periodic, see section 5.3 for more details.

Defining

$$
\mathcal{R}_{k,j} = \iint_{\Omega^{(0)}} \mathbf{U}_k^* \cdot \mathbf{U}_j \; \mathrm{d}x\mathrm{d}y
\tag{4.25}
$$

the frictional term in (4.23) can be rewritten as

$$
\sum_j r\mathcal{R}_{k,j} A_j \{e^{i\omega_j t}\}_k.
\tag{4.26}
$$

The summation is over all eigenvalues of (4.10) like in the expansion (4.9). Because friction was linearized in this model, this expression is linear in the amplitudes A_j. Note that $\{e^{i\omega_j t}\}_k = \delta_{jk}$, with δ_{jk} the Kronecker delta, because of the assumed non-degeneracy: $\omega_j \neq \omega_k$ if $j \neq k$. This simplification will be used shortly. For a quadratic or cubic friction law, the calculations would be more elaborate, but in principle no more difficult than those for the quadratic nonlinear terms considered in this thesis.

Substituting the expansions (4.9), (4.17) and (4.20) into the nonlinear terms

of (4.23) leads to

$$-\left\{\iint_{\Omega^{(0)}} \gamma\zeta_k^* \nabla\cdot[\zeta^{(1)}\mathbf{U}^{(2)} + \zeta^{(2)}\mathbf{U}^{(1)}] \; \mathrm{d}x\mathrm{d}y\right\}_k$$

$$= \left\{ \mathrm{i}\sum_j \sum_{n,l,m} A_j \mathrm{e}^{\mathrm{i}\omega_j t} \frac{{}_n\mathcal{C}_{l,m} + {}_n\mathcal{A}_{l,m}}{\omega_n - \omega_l - \omega_m} A_l A_m \mathrm{e}^{\mathrm{i}(\omega_l+\omega_m)t} \iint_{\Omega^{(0)}} \gamma\zeta_k^* \nabla\cdot[\zeta_j\mathbf{U}_n + \zeta_n\mathbf{U}_j] \; \mathrm{d}x\mathrm{d}y \right\}_k$$

$$= \mathrm{i}\sum_{j,n,l,m} \frac{{}_n\mathcal{C}_{l,m} + {}_n\mathcal{A}_{l,m}}{\omega_n - \omega_l - \omega_m}({}_k\mathcal{C}_{j,n} + {}_k\mathcal{C}_{n,j})A_j A_l A_m \{\mathrm{e}^{\mathrm{i}(\omega_j+\omega_l+\omega_m)t}\}_k$$

(4.27)

for the continuity term and for the advection

$$-\left\{\iint_{\Omega^{(0)}} D^{(0)}\mathbf{U}_k^* \cdot \left([\mathbf{U}^{(1)}\cdot\nabla]\mathbf{U}^{(2)} + [\mathbf{U}^{(2)}\cdot\nabla]\mathbf{U}^{(1)}\right) \; \mathrm{d}x\mathrm{d}y\right\}_k$$

$$= \mathrm{i}\sum_{j,n,l,m} \frac{{}_n\mathcal{C}_{l,m} + {}_n\mathcal{A}_{l,m}}{\omega_n - \omega_l - \omega_m}({}_k\mathcal{A}_{j,n} + {}_k\mathcal{A}_{n,j})A_j A_l A_m \{\mathrm{e}^{\mathrm{i}(\omega_j+\omega_l+\omega_m)t}\}_k,$$

(4.28)

in which each of the indices j, n, l and m runs over all eigenvalues. Note that the contributions with $B_n(\tau)\mathrm{e}^{\mathrm{i}\omega_n t}$ are omitted because they lead to the selection criterion $\{\mathrm{e}^{\mathrm{i}(\omega_j+\omega_n)t}\}_k$ which is zero due to the assumption (4.14c). Combining (4.24), (4.26), (4.27), (4.28) with (4.23) we find the so-called Landau (or amplitude) equation for the slow evolution of the first-order amplitudes:

$$\frac{\mathrm{d}A_k}{\mathrm{d}\tau} = F_k(\tau) - \sum_j {}_r\mathcal{R}_{k,j}\{\mathrm{e}^{\mathrm{i}\omega_j t}\}_k A_j$$

$$+ \mathrm{i}\sum_{j,n,l,m} \frac{{}_n\mathcal{N}_{l,m}}{\omega_n - \omega_l - \omega_m}({}_k\mathcal{N}_{j,n} + {}_k\mathcal{N}_{n,j})\{\mathrm{e}^{\mathrm{i}(\omega_j+\omega_l+\omega_m)t}\}_k A_j A_l A_m,$$

(4.29)

where the shorthand notation ${}_k\mathcal{N}_{l,m} = {}_k\mathcal{C}_{l,m} + {}_k\mathcal{A}_{l,m}$ was used. Note that the operator $\{\cdot\}_k$ effectively selects the terms in the summation for which $\omega_j = \omega_k$ or $\omega_j + \omega_l + \omega_m = \omega_k$ respectively. Our final step is to evaluate these conditions using the assumptions in (4.14).

First, it has been noted already that the non-degeneracy of the eigenfrequencies implies that $\{\mathrm{e}^{\mathrm{i}\omega_j t}\}_k = \delta_{jk}$, so the friction term reduces to

$$\sum_j {}_r\mathcal{R}_{k,j} A_j \{\mathrm{e}^{\mathrm{i}\omega_j t}\}_k = c_k A_k,$$

defining $c_k = {}_r\mathcal{R}_{k,k}$, which is clearly positive for all k, in view of (4.25).

Secondly, (4.14d) helps evaluate the condition $\omega_j + \omega_l + \omega_m = \omega_k$. There are 'trivial' solutions $\omega_j + \omega_{-j} + \omega_k = \omega_k$ to this condition in view of the chosen order of numbering $\omega_{-j} = -\omega_j$, see the discussion following (4.12). These 'trivial resonances' stem from symmetry in the eigenvalue problem (4.10). The assumption (4.14d) amounts to assuming that these 'trivial resonances' are the only ones, apart from permutations. In fact, by reformulating the condition in terms of positive eigenfrequencies only, and reordering in such a way that $\omega_k \geq \omega_j \geq \omega_l \geq \omega_m$, the condition reads $\omega_k \pm \omega_j \pm \omega_l \pm \omega_m = 0$ without loss of generality. The cases $+++$, $++-$, $+-+$

n	j	l	m	Corresponding term
$+$	$+k$	$+m$	$-m$	$\mathrm{i}\frac{1}{\omega_n}\,_n\mathcal{N}_{m,\bar{m}}\,(_k\mathcal{N}_{k,n}+_k\mathcal{N}_{n,k})\,A_kA_mA_m^*$
$-$	$+k$	$+m$	$-m$	$-\mathrm{i}\frac{1}{\omega_n}\,_{\bar{n}}\mathcal{N}_{m,\bar{m}}\,(_k\mathcal{N}_{k,\bar{n}}+_k\mathcal{N}_{\bar{n},k})\,A_kA_mA_m^*$
$+$	$+k$	$-m$	$+m$	$\mathrm{i}\frac{1}{\omega_n}\,_n\mathcal{N}_{\bar{m},m}\,(_k\mathcal{N}_{k,n}+_k\mathcal{N}_{n,k})\,A_kA_m^*A_m$
$-$	$+k$	$-m$	$+m$	$-\mathrm{i}\frac{1}{\omega_n}\,_{\bar{n}}\mathcal{N}_{\bar{m},m}\,(_k\mathcal{N}_{k,\bar{n}}+_k\mathcal{N}_{\bar{n},k})\,A_kA_m^*A_m$
$+$	$+m$	$+k$	$-m$	$\mathrm{i}\frac{1}{\omega_n+\omega_{\bar{m}}-\omega_k}\,_n\mathcal{N}_{k,\bar{m}}\,(_k\mathcal{N}_{m,n}+_k\mathcal{N}_{n,m})\,A_mA_kA_m^*$
$-$	$+m$	$+k$	$-m$	$-\mathrm{i}\frac{1}{\omega_n-\omega_{\bar{m}}+\omega_k}\,_{\bar{n}}\mathcal{N}_{k,\bar{m}}\,(_k\mathcal{N}_{m,\bar{n}}+_k\mathcal{N}_{\bar{n},m})\,A_mA_kA_m^*$
$+$	$-m$	$+k$	$+m$	$\mathrm{i}\frac{1}{\omega_n-\omega_{\bar{m}}-\omega_k}\,_n\mathcal{N}_{k,m}\,(_k\mathcal{N}_{\bar{m},n}+_k\mathcal{N}_{n,\bar{m}})\,A_m^*A_kA_m$
$-$	$-m$	$+k$	$+m$	$-\mathrm{i}\frac{1}{\omega_n+\omega_{\bar{m}}+\omega_k}\,_{\bar{n}}\mathcal{N}_{k,m}\,(_k\mathcal{N}_{\bar{m},\bar{n}}+_k\mathcal{N}_{\bar{n},\bar{m}})\,A_m^*A_kA_m$
$+$	$+m$	$-m$	$+k$	$\mathrm{i}\frac{1}{\omega_n+\omega_{\bar{m}}-\omega_k}\,_n\mathcal{N}_{\bar{m},k}\,(_k\mathcal{N}_{m,n}+_k\mathcal{N}_{n,m})\,A_mA_m^*A_k$
$-$	$+m$	$-m$	$+k$	$-\mathrm{i}\frac{1}{\omega_n-\omega_{\bar{m}}+\omega_k}\,_{\bar{n}}\mathcal{N}_{\bar{m},k}\,(_k\mathcal{N}_{m,\bar{n}}+_k\mathcal{N}_{\bar{n},m})\,A_mA_m^*A_k$
$+$	$-m$	$+m$	$+k$	$\mathrm{i}\frac{1}{\omega_n-\omega_{\bar{m}}-\omega_k}\,_n\mathcal{N}_{m,k}\,(_k\mathcal{N}_{\bar{m},n}+_k\mathcal{N}_{n,\bar{m}})\,A_m^*A_mA_k$
$-$	$-m$	$+m$	$+k$	$-\mathrm{i}\frac{1}{\omega_n+\omega_m+\omega_k}\,_{\bar{n}}\mathcal{N}_{m,k}\,(_k\mathcal{N}_{\bar{m},\bar{n}}+_k\mathcal{N}_{\bar{n},\bar{m}})\,A_m^*A_mA_k$

Table 4.1: Systematic list of non-zero nonlinear terms assuming 'trivial resonances' only.

and $-++$ are ruled out immediately, because the left-hand side is always strictly positive (note that we ordered them such that ω_k is the largest one and $\omega_0 = 0$ is not considered in this thesis). Similarly, the cases $+--$ and $-+-$ can only satisfy the condition in the trivial cases. In the latter case, for example, note that both $\omega_k - \omega_j \geq 0$ and $\omega_l - \omega_m \geq 0$, with equality only if $k = j$ and $l = m$, i.e. in the trivial cases. This leaves the cases $--+$ and $---$, for which solutions with $k > j$ are ruled out by (4.14d). For $k = j$ it is clear that $\omega_k - \omega_j - \omega_l - \omega_m < 0$ does not constitute a solution either. Hence one is left with the trivial cases $\omega_k - \omega_k - \omega_l + \omega_l = 0$.

In (4.29) all permutations of j, n, l and m occur as well, so twelve situations can be distinguished in which $\{\mathrm{e}^{\mathrm{i}(\omega_j+\omega_l+\omega_m)t}\}_k \neq 0$. The corresponding non-zero terms in the summation over j, n, l and m are shown in table 4.1. In this table, the indices j, n, l and m are positive; $\bar{m}$ is a shorthand notation for $-m$. Note that $\omega_{\bar{n}} = -\omega_n$ and $A_{\bar{n}} = A_n^*$. The latter follows from equating (4.9) with its complex conjugate, using the fact that $\zeta^{(1)}, \mathbf{U}^{(1)}$ are real. Note that all terms are proportional to $|A_m|^2 A_k$.

Summing the terms in table 4.1 finally leads to the following simplified Landau equation:

$$\frac{\mathrm{d}A_k}{\mathrm{d}\tau} = F_k(\tau) - c_k\,A_k + \sum_m \mathrm{i}\,\Gamma_{k,m}\,A_m^*A_mA_k \tag{4.30}$$

with coefficient $\Gamma_{k,m}$ in the nonlinear term given by

$$\Gamma_{k,m} = \sum_{n\geq 1} \begin{array}{l} \frac{1}{\omega_n}(_k\mathcal{N}_{k,n}+_k\mathcal{N}_{n,k})(_n\mathcal{N}_{m,\bar{m}}+_n\mathcal{N}_{\bar{m},m}) \\ -\frac{1}{\omega_n}(_k\mathcal{N}_{k,\bar{n}}+_k\mathcal{N}_{\bar{n},k})(_{\bar{n}}\mathcal{N}_{m,\bar{m}}+_{\bar{n}}\mathcal{N}_{\bar{m},m}) \\ +\frac{1}{\omega_n+\omega_{\bar{m}}-\omega_k}(_k\mathcal{N}_{m,n}+_k\mathcal{N}_{n,m})(_n\mathcal{N}_{k,\bar{m}}+_n\mathcal{N}_{\bar{m},k}) \\ -\frac{1}{\omega_n-\omega_{\bar{m}}+\omega_k}(_k\mathcal{N}_{m,\bar{n}}+_k\mathcal{N}_{\bar{n},m})(_{\bar{n}}\mathcal{N}_{k,\bar{m}}+_{\bar{n}}\mathcal{N}_{\bar{m},k}) \\ +\frac{1}{\omega_n-\omega_{\bar{m}}-\omega_k}(_k\mathcal{N}_{\bar{m},n}+_k\mathcal{N}_{n,\bar{m}})(_n\mathcal{N}_{k,m}+_n\mathcal{N}_{m,k}) \\ -\frac{1}{\omega_n+\omega_m+\omega_k}(_k\mathcal{N}_{\bar{m},\bar{n}}+_k\mathcal{N}_{\bar{n},\bar{m}})(_{\bar{n}}\mathcal{N}_{k,m}+_{\bar{n}}\mathcal{N}_{m,k}). \end{array} \tag{4.31}$$

In (4.30) we have essentially separated the slow evolution of the amplitudes from the dependence of the hydrodynamic system on the geometry of the basin (from its 'fast'

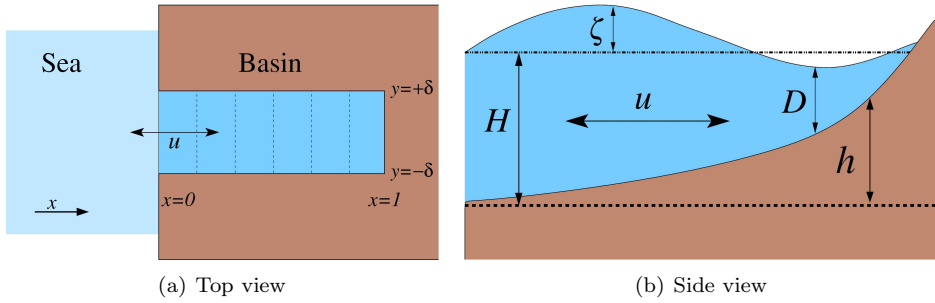(a) Top view   (b) Side view

Figure 4.2: Sketch of the one-dimensional basin. Its width is much smaller than its length, the bottom profile $h(x)$ depends on the longitudinal coordinate only, hence the motion is assumed to be restricted to the longitudinal direction.

oscillatory eigenmodes in particular). All information about the geometry of the basin is contained in the coefficients c_k and $\Gamma_{k,m}$. The geometry of the basin determines the eigenvalues and eigenfunctions, hence the coupling coefficients $\mathcal{R}_{k,j}$, ${}_k\mathcal{C}_{l,m}$, ${}_k\mathcal{A}_{l,m}$ and $\{e^{i(\omega_j+\omega_l+\omega_m)t}\}_k$, which finally give c_k and $\Gamma_{k,m}$. Once these coefficients are fixed, the dynamical system given by (4.30) can be studied. The analysis of this dynamical system is postponed till chapter 5. In order to illustrate the procedure and obtain knowledge about the order of magnitude of the coefficients $\Gamma_{k,m}$, three relatively simple one-dimensional examples will be worked out in the next section. From the definition (4.25) for the coefficient $\mathcal{R}_{k,k}$ it is clear that $c_k > 0$ always. Omitting the Coriolis acceleration ($F = 0$), the coefficients $\Gamma_{k,m}$ can be shown to be real-valued. The reason for this is that the eigenfunctions ζ_j can be chosen real-valued in that case, whereas the corresponding velocities $\mathbf{U}_j$ will be imaginary. Therefore ${}_k\mathcal{N}_{l,m} = {}_k\mathcal{C}_{l,m} + {}_k\mathcal{A}_{l,m}$ is imaginary for all indices k, l, m, in view of the definitions (4.19).

4.4   Some example bedforms

In this section the results of the previous section are illustrated by calculating the coefficients $\Gamma_{k,m}$ for three basins of simple planform. For simplicity, rectangular basins are considered for which the width is much smaller than the length of the basin, see figure 4.2. As a consequence the motion can be assumed to be one-dimensional, uniform in the transverse direction; the transverse velocities are zero. Indeed, rescaling $y \mapsto \delta y, v \mapsto \delta v$ and introducing an asymptotic expansion in terms of the Kelvin number δF, where $\delta \ll 1$ is the width over length aspect ratio, it readily follows that up to first order $v = 0$ and the equations (4.10), (4.11), describing the linear free modes of the system, reduce to (see e.g. Krauss, 1973, pp. 154–155)

$$\gamma \frac{d}{dx}\left[(1 - h(x))\frac{d\zeta_j}{dx}\right] + {\omega_j}^2 \, \zeta_j \;=\; 0, \quad \text{for } x \in [0,1], \tag{4.32a}$$

$$\zeta_j \;=\; 0, \quad \text{at } x = 0, \tag{4.32b}$$

$$\gamma\left(1 - h(x)\right)\frac{d^2\zeta_j}{dx^2} \;=\; 0, \quad \text{at } x = 1, \tag{4.32c}$$

after eliminating the longitudinal velocity component $u_j = i\frac{\gamma}{\omega_j}\frac{d\zeta_j}{dx}$. Note that the coastal boundary condition (4.32c) should be interpreted to require $\frac{d^2\zeta_j}{dx^2}$ to be bounded

for vanishing depth (if $h(1) = 1$). Three examples will be discussed here: a basin with constant depth, $h(x) \equiv 0$; a basin with constant slope, $h(x) = x$; and a basin with a quadratically sloping bottom, $h(x) = x^2$. This results in standard equations whose solutions are given by either

$$\left. \begin{aligned} \zeta_j(x) &= \tfrac{1}{\sqrt{\gamma}} \sin((j + \tfrac{1}{2})\pi x), \\ u_j(x) &= \mathrm{i} \cos((j + \tfrac{1}{2})\pi x), \\ \omega_j &= (j + \tfrac{1}{2})\pi\sqrt{\gamma}, \end{aligned} \right\} \tag{4.33}$$

for constant depth (with boundary condition $\frac{\mathrm{d}\zeta_j}{\mathrm{d}x} = 0$, at $x = 1$, because in this case the wall is vertical),

$$\left. \begin{aligned} \zeta_j(x) &= \frac{J_0(p_j\sqrt{1-x})}{\sqrt{2\gamma}\,J_1(p_j)}, \\ u_j(x) &= \mathrm{i}\frac{J_1(p_j\sqrt{1-x})}{\sqrt{2}\,J_1(p_j)\,\sqrt{1-x}}, \\ \omega_j &= \tfrac{1}{2}\sqrt{\gamma}p_j, \end{aligned} \right\} \tag{4.34}$$

for constant slope, where J_0 and J_1 are Bessel functions of the first kind and p_j the positive roots of J_0, or

$$\left. \begin{aligned} \zeta_j(x) &= \sqrt{\tfrac{4j-1}{2\gamma}}P_{2j-1}(x), \\ u_j(x) &= \mathrm{i}\sqrt{\tfrac{(4j-1)(2j-1)}{4j}}\frac{P_{2j-2}(x) - xP_{2j-1}(x)}{1-x^2}, \\ \omega_j &= \sqrt{\gamma}\sqrt{2j(2j-1)}, \end{aligned} \right\} \tag{4.35}$$

for the quadratically sloping bottom, where P_{2j-1} is the Legendre polynomial of degree $2j - 1$. These eigenfunctions are normalized with respect to the inner product (4.13).

For these examples, the assumptions (4.14) can be checked. The eigenvalues are non-degenerate in all cases. The completeness of the eigenfunctions follows from standard expansion theorems for Fourier series, Bessel functions and Legendre polynomials. The remaining two assumptions need some more attention. For the basin with constant depth we find that $\omega_k - \omega_l - \omega_m = (k - l - m - \tfrac{1}{2})\pi\sqrt{\gamma}$, which clearly is non-zero, because $k - l - m$ is an integer. The final condition however, $0 = \omega_k - \omega_l - \omega_m \pm \omega_n = (k - l - m \pm n - \tfrac{1}{2} \pm \tfrac{1}{2})\pi\sqrt{\gamma}$ is fulfilled whenever $k = l + m - n$ or $k = l + m + n + 1$ respectively; many non-trivial resonances occur for this basin. Apparently the special symmetries of this basin cause the resonance condition to be fulfilled even though they are not generic.

In order to check the non-resonance conditions (4.14c,d) for $\omega_j = \tfrac{1}{2}\sqrt{\gamma}p_j$ and $\omega_j = \sqrt{\gamma}\sqrt{2j(2j-1)}$, for the linear and quadratic bottom respectively, an approximation of the eigenfrequencies is helpful. In fact, the approximations for both cases are very similar:

$$\varpi_j = a(j - \tfrac{1}{4}) - \frac{1}{4j-1} + \frac{\chi_j}{(4j-1)^3} \tag{4.36}$$

where $\varpi_j = -4\pi\omega_j/\sqrt{\gamma}, a = -2\pi^2$ and $0.3089 < \chi_j < 31/(3\pi^2)$, in the case of a linearly sloping bottom, or $\varpi_j = 4\omega_j/\sqrt{\gamma}, a = 8$ and $\tfrac{1}{4} < \chi_j < \tfrac{27}{128}\sqrt{2}$, in the

case of a quadratic bottom. For the linear bottom this approximation is McMahon's
expansion for zeros of Bessel functions (see Gatteschi & Giordano, 2000, (6) or The-
orem 4), for the second case it follows from a Taylor expansion of $\sqrt{2j(2j-1)} = (2j-\frac{1}{2})\sqrt{1-(4j-1)^{-2}}$. The estimate (4.36) is sufficient to prove both non-resonance
conditions (4.14c,d). In fact, one finds $\varpi_k - \varpi_l - \varpi_m = a(k - l - m + \frac{1}{4} + \varepsilon)$ with ε
strictly within the interval $(-\frac{1}{4}, \frac{3}{4})$ and $\varpi_k - \varpi_l - \varpi_m - \varpi_n = a(k-l-m-n+\frac{1}{2}+\varepsilon)$
with ε strictly within $(-\frac{1}{2}, \frac{1}{2})$, by straightforward estimation of the second and third
term in (4.36) using $k \geq 2$ and $l, m, n \geq 1$. Because k, l, m and n are integer, this
implies that neither $\varpi_k - \varpi_l - \varpi_m$ nor $\varpi_k - \varpi_l - \varpi_m - \varpi_n$ can be zero.

Proving $\varpi_k - \varpi_l - \varpi_m + \varpi_n = 0$ only if $k = l$ and $m = n$ is more difficult.
A simple argument based on an estimate as for the other cases cannot be sufficient
because this would rule out the trivial resonances, which we know to exist, as well.
In order to exclude the non-trivial resonances, the fact that $k > l$ must play a role in
the proof. It is given in the Appendix to this chapter.

The friction coefficient c_k in (4.30) is proportional to the empirical value r. The
dependence on the mode number k is determined by the interaction integral $\mathcal{R}_{k,k} = \int_0^1 u_k^* u_k \, dx$. The calculations yield

$$\mathcal{R}_{k,k} = \tfrac{1}{2}, \qquad\qquad \text{for constant depth,} \qquad\qquad (4.37a)$$

$$\mathcal{R}_{k,k} = \frac{1 - J_1{}^2(p_k)}{2J_1{}^2(p_k)}, \quad \text{for constant slope,} \qquad\qquad (4.37b)$$

$$\mathcal{R}_{k,k} = k - \tfrac{1}{4}, \qquad\quad \text{for the quadratically sloping bottom.} \qquad (4.37c)$$

$\mathcal{R}_{k,k}$ is constant for the basin with vertical sidewalls, but increases to infinity for
$k \to \infty$ in the other two cases.

In order to calculate the coefficients $\Gamma_{k,m}$, the interaction integrals

$$_k\mathcal{C}_{l,m} = \int_0^1 \gamma \zeta_k^* \frac{d}{dx}[\zeta_l u_m] \, dx,$$

$$_k\mathcal{A}_{l,m} = \int_0^1 D^{(0)} u_k^* u_l \frac{du_m}{dx} \, dx,$$

the one-dimensional equivalents of (4.19), must be evaluated. For this purpose the
software packages Maple and *Mathematica* were used. In the case of constant water
depth, the integrals can be evaluated analytically. These packages even managed to
obtain an (elaborate) analytical expression for the Landau coefficients $\Gamma_{k,m}$. The
first four values of the coefficients are $\Gamma_{1,1} = -9.57, \Gamma_{1,2} = -12.01$, $\Gamma_{2,1} = -16.79$
and $\Gamma_{2,2} = -16.11$. We have already found that the third-order non-resonance condi-
tion (4.14d) is not fulfilled for this basin. Although this implies that additional terms,
not proportional to $|A_m|^2 A_k$, arise in the amplitude equation (4.30) (cf. (4.29)), these
$\Gamma_{k,m}$ are the proper coefficients in front of the $|A_m|^2 A_k$-term.

In the cases of a linear or quadratic bottom profile, the corresponding integrals
had to be evaluated numerically. Consequently the infinite sum over n in (4.31),
defining $\Gamma_{k,m}$, has to be truncated. The results are shown in figures 4.3(a) and 4.3(c)
as a function of the truncation number N. The convergence is quite slow and seems
to be alternatingly too low and too high. On plotting the variations on a doubly
logarithmic scale they appear to converge at a rate $1/\sqrt{N}$, which might be expected
from the fact that this generally is the rate of convergence in a Galerkin expansion.
The convergence can be improved by taking the average between two subsequent
values. Those averages are shown in figures 4.3(b) and 4.3(d).
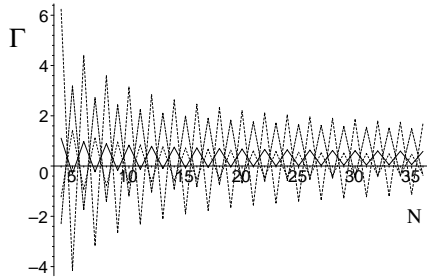
(a) Truncated $\Gamma_{k,m}$ for the linear bottom.
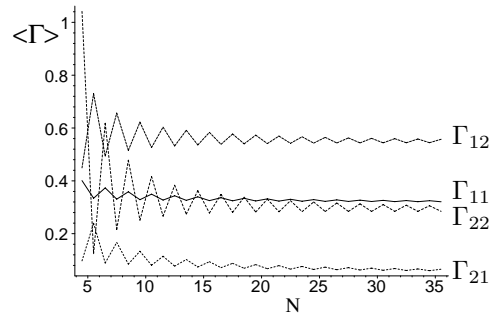
(b) Smoothed $\Gamma_{k,m}$ for the linear bottom.
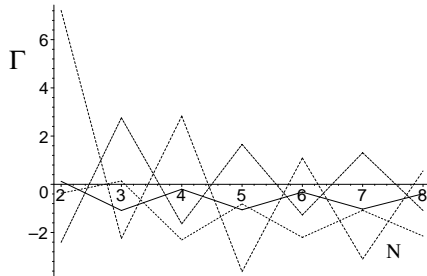
(c) Truncated $\Gamma_{k,m}$ for the quadratic bottom.
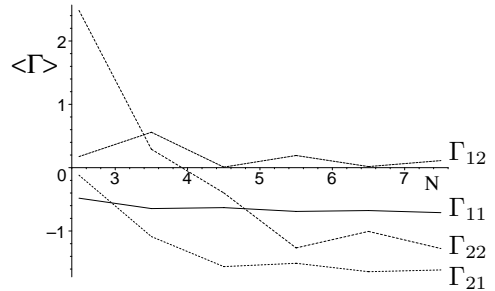
(d) Smoothed $\Gamma_{k,m}$ for the quadratic bottom.

Figure 4.3: Numerical estimation of the interaction coefficients $\Gamma_{k,m}$ for $(k,m) = (1,1), (1,2), (2,1)$ and $(2,2)$. The sum of terms in (4.31) are shown as a function of truncation number N in 4.3(a) for the linear bottom and 4.3(c) for the quadratic bottom. Because of the oscillatory nature of the convergence, subsequent outcomes are averaged in 4.3(b) and 4.3(d).

4.5   Conclusions and discussion

In this chapter a weakly nonlinear analysis was performed on the two-dimensional depth-averaged shallow-water equations (4.1), (4.2) in a basin co-oscillating with an adjacent sea. In that respect the scope is fairly general; except for assuming the aspect ratio (depth over width) to be small enough to ignore vertical differences, no additional assumptions on the shape of the basin are required for using (4.1). This system is investigated in the limit of small amplitudes (compared to the depth of the basin) and strong resonance (amplitude in basin much larger than at sea, i.e. for forcing frequency close to one of the eigenfrequencies and weak friction). In this limit, the behaviour of the system is dominated by its linear eigenmodes to first order. They are found from first-order (linearized) theory, with constant but unknown amplitudes. Nonlinear interactions between eigenmodes occur at higher order, causing the amplitudes of the eigenmodes to vary slowly in time. The ultimate result of the weakly nonlinear analysis is the Landau equation (4.30) describing the (slow) modulation of the amplitudes.

The corresponding tidal motion is an oscillation of the water level at (or near) the eigenfrequency, with spatial structure determined by the eigenmode and modulating amplitude. In practice this would mean that the "harmonic constants" are not constant. Variation of harmonic constants also occurs according to linear theory because of variations of the astronomical forcing which on long timescales that are not included in the harmonic analysis. Because these variations, due to e.g. the precession of the elliptic orbit of the moon, are known one can correct for them using so-called nodal factors. The theory presented here suggests that modulation of the harmonic constants may also originate from intrinsic nonlinear dynamics within the resonating basin, which cannot be accounted for from astronomical forcing.

Because the focus of this work is on the interaction of the oscillatory modes with themselves, the zero-mode has been omitted (see the first remark at the end of section 4.3.1). Technical aspects are more involved for the zero-mode because it cannot be described with a single amplitude. Pratt & Llewellyn Smith (1997) provide a method to deal with the latter aspect, but the incorporation of both the zero- and oscillatory modes into a consistent theory for small amplitudes still forms a mathematical challenge that remains to be solved. However, the effect of the zero-mode on the oscillatory modes is expected to cause some interesting behaviour, because the interaction with the zero-mode may trigger internal excitation of oscillatory modes that are not excited by the tide at sea directly. This may lead to chaotic behaviour similar to the results discussed in chapter 5.

In view of the assumptions in this chapter, one might wonder about the geophysical relevance of the amplitude equation (4.30). The parameter $\alpha = Z/H$ measures the importance of the nonlinear terms in (4.4). Moreover, it has been used as a scaling parameter to reflect the assumptions of strong resonance, so α also appears in the amplification factor, frequency detuning and bottom friction. The slow time scale τ on which the amplitudes evolve is $\mathcal{O}(\alpha^{-2})$, typically some tens of periods (note that time was scaled with the eigenperiod T and a factor of 2π according to (4.3)), i.e. tens of days for tidal systems and one or two days in the case of secondary undulations. The results in this chapter suggest that the dynamics can be chaotic if modulation of the exterior tide occurs at the same time scale, due to e.g. the spring-neap tidal cycle (14 day period) in the tidal case or the basic (semi)diurnal tide in the case of

secondary undulations.

The assumption of strong resonance may seem to be in contradiction with the assumption of small amplitudes. In reality however, tidal motion usually is small compared to the total water depth. Moreover, tides at sea are smaller than those in the basin due to amplification by resonance. The assumptions in this work pertain to this limit of the observations. However, the main reason for the assumption of small detuning and large amplification is to maintain analytical tractability. The nonlinear effects will be equally important as long as the tidal amplitude in the basin remains large enough. Physically the important processes are friction and nonlinearity. The nonlinear effects change the effective eigenfrequency as a function of the tidal amplitude in the basin, i.e. of α, hence bending the resonance curve. Apart from the fact that friction reduces the tidal amplitude, it tends to smooth the response curve and thereby hides the nonlinear effects. Still, if α, hence the nonlinear effects, is less small, friction may not need to be that small either. Although the validity of the results of the weakly nonlinear analysis may be confined to this limit, it is quite possible that the processes described here do play a role beyond the small-amplitude limit. After all, dependence of the effective eigenfrequency on amplitude, multiple equilibria and other nonlinear effects are generally enhanced for increasing amplitude. No analytical methods are available yet to substantiate this however.

In order to quantify the balance between friction and the nonlinear effects, one needs to consider a single equation in which both nonlinear advection and the nonlinear continuity term can be compared with friction. The main effect of the nonlinear terms considered in this chapter is to change the effective eigenfrequency. This introduces phase differences between the tide in the basin and at sea. Consequently it changes the absorption of energy from the exterior tide. In line with the analysis in this chapter the local energy equation can be obtained by forming the 'inner product' $g\zeta$ (4.1a) $+ D\mathbf{U} \cdot$ (4.1b):

$$g\,\zeta\frac{\partial\zeta}{\partial t}+g\,\zeta\,\nabla\cdot(H\mathbf{U})+g\,\zeta\,\nabla\cdot(\zeta\mathbf{U})+D\mathbf{U}\cdot\frac{\partial\mathbf{U}}{\partial t}+D\mathbf{U}\cdot([\mathbf{U}\cdot\nabla]\mathbf{U})+gD\mathbf{U}\cdot\nabla\zeta+D\mathbf{U}\cdot\frac{\tau_b}{\rho D}=0.$$

$$\quad\;\text{A}\qquad\qquad\text{B}\qquad\qquad\;\text{C}\qquad\qquad\text{D}\qquad\qquad\;\;\text{E}\qquad\qquad\;\;\text{F}\qquad\quad\text{G}$$

$$(4.38)$$

The terms in this equation are listed in table 4.2 together with order of magnitude estimates based on the scales introduced in (4.3). By considering the dominant balance in the continuity equation between elevation change (A) and the linear continuity term (B), one obtains the easily interpretable relationship $UHT = 2\pi LZ$, which allows us to write $\alpha = Z/H$ for the ratio between the nonlinear terms (C and E) and the time derivative (A resp. D) in both the continuity and momentum equation. The balance between inertia (D) and the pressure gradient (F) holds if the length scale L is comparable to the wavelength $\lambda = (gH)^{1/2}T$. The balance between friction (G) and advection (E) requires $c_D \sim H/L$. Because resonant basins are considered, the length of the basin L is related to H through the dispersion relation $L = \varepsilon\lambda$, where $\varepsilon = 1/4, 3/4, ...$ for a half-open rectangular channel, cf. (4.33), whereas $\varepsilon \ll 1$ for an almost-enclosed Helmholtz resonator. Consequently the balance $\varepsilon c_D \sim H/\lambda = (H/g)^{1/2}/T$ appears to hold for reasonable depth only in the case of an almost-enclosed basin. However, comparing the nonlinear continuity term (C) with friction (G), one finds analogously $\varepsilon^3 c_D \sim H/\lambda$ according to which the balance does hold for $\varepsilon = 1/4$ and $H \sim 10\text{--}100$ m, so this balance could occur in quarter-wavelength resonators of reasonable depth as well.

	formula	estimate	Bay of Fundy	Gulf of Nicoya	Moldefjord
a. length (km)		L	270	40	10
b. depth (m)		H	70	20	30
c. elevation (m)		Z	6	1	0.1
d. velocity (m s^{-1})		U	1	0.2	0.1
e. time scale (10^3 s)		$\frac{T}{2\pi}$	7.1	7.1	0.46
A. elevation (m^{3}s^{-3})	$g\,\zeta\,\frac{\partial \zeta}{\partial t}$	$2\pi\frac{gZ^2}{T}$	$5.0 \cdot 10^{-2}$	$1.4 \cdot 10^{-3}$	$2.1 \cdot 10^{-4}$
B. lin. cont. (m^{3}s^{-3})	$g\,\zeta\,\nabla\cdot(H\mathbf{U})$	$\frac{gHZU}{L}$	$1.5 \cdot 10^{-2}$	$9.8 \cdot 10^{-4}$	$2.9 \cdot 10^{-4}$
C. nl. cont. (m^{3}s^{-3})	$g\,\zeta\,\nabla\cdot(\zeta\mathbf{U})$	$\frac{gZ^2U}{L}$	$1.3 \cdot 10^{-3}$	$4.9 \cdot 10^{-5}$	$9.8 \cdot 10^{-7}$
D. inertia (m^{3}s^{-3})	$D\mathbf{U}\cdot\frac{\partial \mathbf{U}}{\partial t}$	$2\pi\frac{HU^2}{T}$	$9.8 \cdot 10^{-3}$	$1.1 \cdot 10^{-4}$	$6.5 \cdot 10^{-4}$
E. advection (m^{3}s^{-3})	$D\mathbf{U}\cdot([\mathbf{U}\cdot\nabla]\mathbf{U})$	$\frac{HU^3}{L}$	$2.6 \cdot 10^{-4}$	$4.0 \cdot 10^{-6}$	$3.0 \cdot 10^{-6}$
F. gradient (m^{3}s^{-3})	$gD\mathbf{U}\cdot\nabla\zeta$	$\frac{gHZU}{L}$	$1.5 \cdot 10^{-2}$	$9.8 \cdot 10^{-4}$	$2.9 \cdot 10^{-4}$
G. friction (m^{3}s^{-3})	$D\mathbf{U}\cdot\frac{\tau_b}{\rho D}$	$c_D\,U^3$	$2.5 \cdot 10^{-3}$	$2.0 \cdot 10^{-5}$	$2.5 \cdot 10^{-6}$

Table 4.2: Estimates for the order of magnitudes of the terms in the local energy equation corresponding to (4.1). Summing the terms A–G and integrating over the basin area leads to the global energy. Rough quantitative scaling estimates for a couple of example basins, that were studied by Doodson (1924), Gutiérrez *et al.* (1981) and Golmen *et al.* (1994) respectively. Numbers have been taken from `http://www.town.stgeorge.nb.ca/bay.html`, `http://www.bayoffundy.com/tidetables`, Godin & Gutiérrez (1986) for the Bay of Fundy, `http://data.ecology.su.se/mnode/CentralAmerica/GulfofNicoya/nicoyabud.htm`, `http://ilikai.soest.hawaii.edu/uhslc/htmld/d0396A.html` for the Gulf of Nicoya and Golmen *et al.* (1994) for the Moldefjord.

Quantitative estimates of the respective scales are given in table 4.2 for a couple of example basins to which the presented model might be applicable. In view of the observation that many different processes lead to the same amplitude equations (4.30), its relevance may be broader, with many processes contributing to $\Gamma_{k,m}$. Whenever the effective eigenfrequency depends on the amplitude of the motion, (4.30) describes the first-order evolution of the amplitudes on a longer time scale, possibly leading to chaotic behaviour. Obviously, identifying such qualitative effects of nonlinearity in time series of observed tidal amplitudes would be the best proof of the relevance of (4.30).

In this chapter the Landau equations (4.30) have been derived. The behaviour of solutions to this dynamical system will be analysed in the next chapter. Truncation of the system (4.30) for infinitely many eigenmodes to a finite number of modes appears to be natural. Truncation to one mode leads to the same equations as the ones found by Maas (1997), Maas & Doelman (2002) and Doelman *et al.* (2002) for the Helmholtz mode in an almost-enclosed basin. In the two-mode system the nonlinear interaction between modes comes into play. In both cases multiple steady states can be found: under the same external conditions the tidal response in the basin can be different. Moreover, the evolution of the amplitudes may become chaotic.

Acknowledgments

Appendix. Excluding non-trivial resonances for the examples in section 4.4.

In this appendix it is shown that the estimate (4.36) implies that there are no non-trivial resonances for which $\varpi_k - \varpi_l - \varpi_m + \varpi_n = 0$. First of all, direct application of the estimate leads to

$$
\begin{aligned}
\varpi_k - \varpi_l - \varpi_m + \varpi_n = \quad & a(k - l - m + n) - \frac{1}{4k - 1} + \frac{1}{4l - 1} + \frac{1}{4m - 1} - \frac{1}{4n - 1} \\
& + \frac{\chi_k}{(4k - 1)^3} - \frac{\chi_l}{(4l - 1)^3} - \frac{\chi_m}{(4m - 1)^3} + \frac{\chi_n}{(4n - 1)^3} \\
= \quad & a(k - l - m + n + \varepsilon)
\end{aligned}
$$

with $-1 < \varepsilon < 1$. This does not rule out resonances of this kind, but it does show that one must have $\varepsilon = 0$ and $k + n = l + m$ for these resonances to occur. Because $0 < \chi_j < \bar{\chi}$, with $\bar{\chi} = 31/(3\pi^2)$ for the linear, or $\bar{\chi} = \frac{27}{128}\sqrt{2}$ for the quadratic bottom, we can estimate

$$
\left| \frac{\chi_k}{(4k - 1)^3} - \frac{\chi_l}{(4l - 1)^3} - \frac{\chi_m}{(4m - 1)^3} + \frac{\chi_n}{(4n - 1)^3} \right| < \frac{2\bar{\chi}}{(4n - 1)^3},
$$

for $k > l \geq m \geq n \geq 1$. Next, we introduce

$$
\chi = (4n - 1)^3 \left(\frac{1}{4k - 1} - \frac{1}{4l - 1} - \frac{1}{4m - 1} + \frac{1}{4n - 1} \right). \tag{4.39}
$$

If it can be shown that $\chi > 2\bar{\chi}$ if $k > l \geq m \geq n \geq 1$ and $k + n = l + m$, the possibility that $\varpi_k - \varpi_l - \varpi_m + \varpi_n = 0$ is ruled out. In fact, we will show that $\chi \geq \frac{288}{77}$ and clearly $\frac{288}{77} > 2\bar{\chi}$ both for the linear and for the quadratic bottom.

In order to prove that $\chi \geq \frac{288}{77}$, factor (4.39) into

$$
\chi = 2^5 \frac{(4n - 1)^2 (2s - 1)(lm - kn)}{(4k - 1)(16lm - 4s + 1)}
$$

writing $s = k + n = l + m$. As a function of lm for fixed k, n (and s), this is minimized for minimal lm, hence for $l = k - 1, m = n + 1$ (note that $k > l$ implies $m > n$ because $k + n = l + m$). Therefore

$$
\chi \geq 2^5 \frac{(4n - 1)^2 (2s - 1)}{(4k - 1)} \frac{(k - 1)(n + 1) - kn}{(16(k - 1)(n + 1) - 4s + 1)} = 2^5 \frac{(4n - 1)^2 (s - 2n - 1)(2s - 1)}{(4n + 3)(4k - 1)(4k - 5)},
$$

which is minimal with respect to n, k for $n = 1$, $k = s - 1$, so $\chi \geq 2^5 \frac{9}{7} \frac{(2s - 1)(s - 3)}{(4s - 5)(4s - 9)}$. For $s \geq 4$ (which follows from the fact that $s > k > l \geq m > n \geq 1$) this is minimized at $s = 4$, so finally the estimate $\chi \geq \frac{288}{77}$ is reached.

Chapter 5

Analysis of solutions to the amplitude evolution equations

In the previous chapter the Landau equations (4.30) governing the weakly nonlinear modulation of the amplitudes of co-oscillating tides due to advection and continuity were derived from the shallow-water equations in the limit of small amplitudes and strong resonance. In this chapter, the behaviour of the resulting dynamical system is investigated. The Landau equations (4.30) describe the evolution of the amplitudes for an infinite number of eigenmodes. However, truncation to a finite number of modes appears to be natural. For one mode, the equations reduce to the same equations as the ones found in Maas (1997), Maas & Doelman (2002) and Doelman *et al.* (2002). Hence the results in those papers also apply for the present model. They found a 'bent resonance curve', multiple equilibria (several tidal regimes under the same tidal forcing), sudden regime changes and even chaotic dynamics (when these regime changes occur in an irregular way). On truncating to two modes, interaction between different eigenmodes comes into play. This enables the phenomena mentioned above to occur under different circumstances as well. In section 5.5 a number of mechanisms that may lead to chaos are discussed. In particular, the Coriolis force (due to the Earth's rotation) and non-trivial internal resonances between eigenmodes, may trigger eigenmodes that are not generated by the exterior forcing directly. As a consequence, chaotic dynamics might even occur with harmonic forcing in the present model, in contrast with the conclusions for one (Helmholtz) mode in earlier work.[1]

5.1   Introduction

The response of small-scale coastal basins to direct astronomical forcing by the moon and the sun is weak. Nevertheless strong tidal oscillations occur in many coastal basins around the world because they are forced through co-oscillation with adjacent oceans/seas at one of their natural frequencies. Under such conditions tides can be amplified to huge amplitudes up to 8 m in the Bay of Fundy between Nova Scotia and the American/Canadian mainland. Reviews on the linear theory predicting the

---

[1]This chapter is based on (the second half of) the paper *"Weakly nonlinear cubic interactions in coastal resonance"* by Guido M. Terra, Arjen Doelman and Leo R.M. Maas, J. Fluid Mech. (2004), vol. 520, pp. 93–134.

resonance behaviour can be found in many publications (e.g. Defant, 1961; LeBlond & Mysak, 1978; Mei, 1989). In the previous chapter, a weakly nonlinear analysis led to Landau equations (4.30) describing the modulation of the tidal response amplitudes in such co-oscillating basins. The behaviour of solutions to those equations will be analysed in this chapter.

A number of assumptions have been made in order to derive the Landau equations (4.30) in the previous chapter. First of all, the depth-averaged two-dimensional shallow-water equations (4.1) have been used as the starting point, with the implicit assumption that the horizontal scales of the motion are much larger than the vertical scale (water depth), but small compared to the Earth's radius. Moreover the small parameter α was introduced to implement the additional assumptions of small $\mathcal{O}(\alpha)$ amplitude (of water-level elevation relative to total water depth), weak friction $\mathcal{O}(\alpha^3)$ and strong $\mathcal{O}(\alpha^{-2})$ multiplication, i.e. small forcing amplitude $\mathcal{O}(\alpha^3)$. The latter assumption amounts to assuming near resonance, because non-resonant components of $\mathcal{O}(\alpha^3)$ will not be amplified by a factor of $\mathcal{O}(\alpha^{-2})$ to result in water-level elevations of $\mathcal{O}(\alpha)$ within the basin.

The resonant components can be of several origin. The terminology in the previous chapter 4 has been primarily aimed at the case of coastal resonance in large-scale basins at tidal frequencies. Harbour resonance in smaller-scale coastal basins occurs at higher frequencies. These infragravity waves (Okihiro & Guza, 1995) are pronounced oscillations in near-shore sea areas and harbours with periods of a few minutes to hours, which are longer than those associated with surface wind waves, but of shorter duration than a typical tidal period. The importance of the more pronounced oscillations of this kind can be inferred from the fact that the phenomenon is locally often identified by a certain name: e.g. *Abiki* in Nagasaki Bay (Hibiya & Kajiura, 1982), *Risagga* at Menorca (Gomis *et al.*, 1993) and *Marrobbio* in the Strait of Sicily (Candela *et al.*, 1999). These oscillations, also called *secondary undulations* (small-amplitude, 'high'-frequency undulations accompanying the tidal, 'primary' oscillation), are perhaps less spectacular in overall appearance than megatidal oscillations, but their importance is boosted when one considers the associated currents, of importance for the flushing of the coastal areas. Observations by Golmen *et al.* (1994) show that these 'perturbation' currents may in fact be of similar strength to those associated with the generating, primary tide. Several different forcing mechanisms have been put forward to explain their origin: atmospheric pressure perturbations (Hibiya & Kajiura, 1982), internal wave activity (Giese & Chapman, 1990), seismic activity (tsunamis), or current shear (Fabrikant, 1995).

The derivation in chapter 4, in particular the scaling assumptions following (4.3), primarily applies to the tidal case, but after a few modifications the analysis can be adapted to the case of secondary undulations as well. If the infragravity waves are the dominant oscillation in the basin, one only needs to change the time scale from the tidal period to the period of the harbour oscillations. Usually however, the infragravity waves will be secondary undulations superimposed on the dominant tidal oscillation. This case can be studied along the lines of chapter 4 too. The frequency spectrum of the tide near the bay entrance is then supposed to contain a continuum part (cf. Munk & Cartwright, 1966) besides the peaks at the (low) tidal frequency, including a small-amplitude, but resonating frequency that will be picked out by the bay. Because the tidal oscillation period is much longer than those of the basin's eigenmodes, which determine the time scale of the model (4.4), (4.5), the primary

tidal oscillation amounts to a slow change of the reference water depth $D^{(0)}$. As a consequence the eigenmodes of the basin change on the tidal time scale. If the tidal time scale is of the same order of magnitude as the slow time scale $\tau = \alpha^2 t$, this change must be incorporated in the amplitude equations. Under the same assumptions (4.14) on the eigenmodes as before, this would lead to a parametric forcing term in the Landau equations (4.30). For the simpler case of the Helmholtz mode in an almost-enclosed basin this situation has been explored more explicitly by Maas & Doelman (2002, section 5). Although similar in principle, the technical details become much more involved for the more general approach in the previous and present chapter.

At present we have no knowledge of field observations analysed to corroborate the behaviour described in this chapter. However, most certainly there are indications that the linear picture describing the tide as a sum of harmonic tidal components is incomplete. Doodson (1924) studied the yearly variations of harmonic constants in Bombay and St. John, Bay of Fundy (see also Defant, 1961, p. 309). The variation can be explained partly by long-term astronomical signals, such as the regression of the moon with a period of about 19 years, but another part is not accounted for. A similar study by Gutiérrez *et al.* (1981), investigating year to year variability of the harmonic constants for Trieste, shows that it cannot be attributed to deficiencies of the filtering methods. Although the etymology of the word 'tides' stems from their periodicity, reports of irregular tides have been made throughout time. More recently, Frison *et al.* (1999) argue that, in a number of tidal areas, the astronomical constituents account for only 50–70% of water-level variability. The residual spectral contributions have often been qualified as 'noise', due to meteorological influences, river inflow and tidal interactions. Frison *et al.* (1999) analysed water-level data using new data analysis techniques that have been developed for chaotic systems. They calculate attractor dimensions and Lyapunov exponents for some tidal signals and conclude that they come from a relatively noise-free but chaotic system. Tidal predictions based on harmonic constants, describing the tidal signal as a linear sum of astronomical constituents, do not capture this. The model derived in chapter 4 yields possible chaotic behaviour of the harmonic 'constants'. Hence it differs from the observations by Frison *et al.* (1999) who studied chaotic behaviour in the time series of water-level elevation itself instead of the amplitudes. In that sense it relates to the research of Doodson (1924) and Gutiérrez *et al.* (1981), although they considered the variability of yearly averaged results whereas the changes described here would occur on a smaller time scale.

In the case of harbour resonance, reports on irregular behaviour are more common. Based on the study of surface elevations in over 50 bays adjacent to Japan, Honda *et al.* (1908) speculate that this type of coastal resonance is forced by the tide as well, for which a possible explanation is given by Fabrikant (1995). Regarding the nature of the secondary undulations these authors conclude that they

- vary from inconspicuous (at the Pacific coast) to conspicuous (near the Japan Sea),
- vary from regular to irregular,
- may often change their periods continuously,
- often appear in phase with the tide,
- often have periods reflecting quarter-wavelength resonance,
- often disappear outside the bay,

- have the same period as when excited in response to a storm.

Although this does not rule out the possibility of incidental forcing by strong winds
or intense atmospheric pressure disturbances, the persistence of the secondary undu-
lations suggests an ever-present source, such as due to tidal motion in the adjacent
sea. The observations of the secondary undulations accompanying the tide show that
the response of a local eigenoscillation may differ in character from periodic, tidally
phase-locked, to aperiodic (Nakano, 1932). This indicates some kind of nonlinear
coupling to the tide.

Having found the Landau equations (4.30) describing the (slow) evolution of the
amplitudes of the eigenoscillations of the basin, the behaviour of the corresponding
dynamical system is analysed further in this chapter. The number of modal equations
depends on the number of modes that are excited at this order. Neglecting the
Coriolis force leads to real-valued coefficients $\Gamma_{k,m}$. In that case, the equations have
some symmetry (that disappears again with the introduction of the Earth's rotation).
Therefore, (4.30) will be considered first for real-valued coefficients $\Gamma_{k,m}$. The effects
of the Earth's rotation will be investigated later. For different basins, different values
for the coefficients $\mathcal{R}_{k,k}$ and $\Gamma_{k,m}$ will be found, see section 4.4. Therefore the idea
is not to consider the problem for specific values of the coefficients, but to study it
for arbitrary values in general. In sections 5.3 and 5.4 one- and two-mode systems
are discussed. The one-mode system is interesting because its amplitude equation
is identical to that governing the Helmholtz mode in an almost-enclosed basin, as is
found by Maas (1997), Maas & Doelman (2002) and Doelman *et al.* (2002). As the
temporal behaviour of the forcing can contain multiple (near-resonant) frequencies,
the response of even this single mode can still be quite rich (ranging up to chaotic).
However, a complex response can also be facilitated by the interaction between modes,
as the two-mode system shows. Note that equations similar to (4.30) have been
studied by Nayfeh & Mook (1979), but only up to the point of steady states. Multiple
equilibria are found by them as well, but chaotic dynamics are beyond the scope of
that book. This chapter ends with a discussion of a number of mechanisms that
may lead to chaotic dynamics of tidal amplitudes, before jumping to conclusions in
section 5.6.

5.2   Boundedness and truncation

The forcing terms $F_k(\tau)$ in (4.30) are essentially the amplitudes of the components of
the external tide with frequency near ω_k. They form the (generalized) Fourier com-
ponents of the exterior tidal curve with respect to the eigenfrequencies ω_k. It follows
from Fourier theory that these amplitudes will be bounded. Moreover, they tend to
zero for $\omega_k \to \infty$, and hence for $k \to \infty$.

The Landau equation (4.30) is an equation for the slow evolution of the *complex*
amplitudes A_k. Hence, for each k it amounts to two equations for two unknowns in
real coordinates. In order to state the equations in polar coordinates the modulus
and argument of the amplitudes are introduced: $A_k = R_k \mathrm{e}^{\mathrm{i}\Phi_k}$ and $F_k = Z_k \mathrm{e}^{\mathrm{i}\Psi_k}$. In

these coordinates (4.30) become

$$\frac{\mathrm{d}R_k}{\mathrm{d}\tau} = -c_k\,R_k + Z_k \cos(\Psi_k - \Phi_k), \qquad (5.1a)$$

$$R_k\frac{\mathrm{d}\Phi_k}{\mathrm{d}\tau} = \sum_m \Gamma_{k,m}{R_m}^2 R_k + Z_k \sin(\Psi_k - \Phi_k). \qquad (5.1b)$$

From the radial equation (5.1a) it is clear that the amplitude R_k decreases if $R_k > Z_k/c_k$. We conclude that $|A_k| \le Z_k/c_k$ for $\tau \to \infty$. The estimate $|A_k| \le Z_k/c_k$ ensures that the (absolute) convergence of the response amplitudes A_k follows from the convergence of the forcing amplitudes Z_k. If a certain mode k is not excited by the external tide ($Z_k = 0$) then it is not excited by other modes either. In particular for harmonic forcing, if the exterior tide ζ_e consists of a single tidal constituent, then Z_k is non-zero, hence A_k is as well, for a single component k only. Because the amplitudes Z_k of the tidal harmonics ultimately decrease with increasing frequency, it makes sense to truncate the model and consider (4.30) for a finite number of modes. This will be done in sections 5.3 and 5.4.

Note that the form of (5.1a) depends on the assumption that $\Gamma_{k,m}$ is real, and hence on neglecting the Earth's rotation. For complex-valued $\Gamma_{k,m}$ there is a contribution of the nonlinear terms in the radial equation as well. This invalidates the preceding argument. In combination with the Earth's rotation the nonlinear effects of continuity and advection can cause growth of the solution's amplitudes. For real-valued $\Gamma_{k,m}$ the interaction between modes is not present in the radial equations. The interaction between the modes is entirely through the phases Φ_k.

5.3   Single-mode solution

In this section, the external tide is assumed to be in effective resonance with only one eigenmode of the basin, hence $F_k \ne 0$ for one k only. According to the reasoning in the previous section, the dynamics will be dominated by this single resonant eigenmode k; all other modes will be negligible. The (complex) amplitude A_k of this mode is governed by

$$\frac{\mathrm{d}A_k}{\mathrm{d}\tau} = F_k(\tau) - c_k\,A_k + \mathrm{i}\,\Gamma_{k,k}\,|A_k|^2 A_k,$$

which is just the truncation of (4.30) to a single mode. In this section the connection with previous work by Doelman *et al.* (2002) will be established first. Consequently an overview of the results of their analysis is given: the determination of stationary states, yielding multiple equilibria, mechanisms leading to chaotic dynamics and the construction of a chaotic set for one of those mechanisms are discussed.

If the external tide is in perfect resonance with eigenmode k, i.e. $\zeta_e \sim \mathrm{e}^{\mathrm{i}\omega_k t}$, then $F_k(\tau)$ is a constant, related to the amplitude of the tidal signal. A more natural situation is the case of near resonance, when the temporal behaviour of the external tidal component is $\mathrm{e}^{\mathrm{i}\omega t}$, where the forcing frequency $\omega = \omega_k + \alpha^2\sigma$ deviates slightly ($\mathcal{O}(\alpha^2)$ only for the modulation to be on the same time scale as the evolution due to the nonlinear effects) from the eigenfrequency ω_k. In this case one has $\mathrm{e}^{\mathrm{i}\omega t} = \mathrm{e}^{\mathrm{i}\omega_k t}\mathrm{e}^{\mathrm{i}\sigma\alpha^2 t} = \mathrm{e}^{\mathrm{i}\sigma\tau}\mathrm{e}^{\mathrm{i}\omega_k t}$ from which it follows that $F_k(\tau)$ is proportional to $\mathrm{e}^{\mathrm{i}\sigma\tau}$, say $F_k(\tau) = Z\mathrm{e}^{\mathrm{i}(\sigma\tau+\Psi)}$. It is convenient to write $A_k(\tau) = A(\tau)\mathrm{e}^{\mathrm{i}\sigma\tau}$, which introduces an

additional term $-\mathrm{i}\sigma A$ in the amplitude equation. Suppressing the subscript k, this leads to

$$\frac{\mathrm{d}A}{\mathrm{d}\tau} = -(c + \mathrm{i}\sigma)\, A + \mathrm{i}\,\Gamma\, |A|^2 A + Z\mathrm{e}^{\mathrm{i}\Psi}, \tag{5.2}$$

which in polar coordinates $A = R\mathrm{e}^{\mathrm{i}\Phi}$ becomes

$$\frac{\mathrm{d}R}{\mathrm{d}\tau} = -c\,R + Z\cos(\Psi - \Phi), \tag{5.3a}$$

$$R\frac{\mathrm{d}\Phi}{\mathrm{d}\tau} = -\sigma R + \Gamma\,R^3 + Z\sin(\Psi - \Phi), \tag{5.3b}$$

and in Cartesian coordinates $A = X + \mathrm{i}Y$

$$\frac{\mathrm{d}X}{\mathrm{d}\tau} = (\sigma - \Gamma\,R^2)Y - cX + Z\cos(\Psi), \tag{5.4a}$$

$$\frac{\mathrm{d}Y}{\mathrm{d}\tau} = -(\sigma - \Gamma\,R^2)X - cY + Z\sin(\Psi), \tag{5.4b}$$

with $R^2 = X^2 + Y^2$. In this form the equations are completely equivalent to the ones studied in Maas (1997), Maas & Doelman (2002) and Doelman *et al.* (2002).[2] In those papers, the equations were derived by averaging methods in a zero-dimensional model for so-called Helmholtz oscillators, see section 5.1. Averaging is another way to dissect the slow from the fast behaviour of the model. The results are equivalent: an equation for the slow evolution of the amplitudes of oscillations on the fast time scale. Because equations (5.3) and (5.4) are essentially the same as the ones found in Maas & Doelman (2002) and Doelman *et al.* (2002), their results apply here as well. Those results will only be summarized here, for details refer to the original papers. Note that, although the form of the amplitude equations is essentially the same, the difference between them lies in the fact that the equations were derived for a much larger class of basins in the previous chapter. The restriction to almost-enclosed Helmholtz resonators was lifted in this thesis.

The system exhibits stationary solutions. They correspond to a response of the system at the same frequency as the forcing and with constant amplitude. From (5.2) one can derive the amplitude response equation, describing the response amplitude R as a function of the forcing frequency σ and amplitude Z. However, it is much easier to give the frequency σ in terms of Z and R, which yields

$$\sigma = \Gamma R^2 \pm \frac{Z}{R}\sqrt{1 - (\frac{cR}{Z})^2}, \tag{5.5}$$

The resulting response curve is plotted in figure 5.1, for three values of the forcing amplitude Z. It clearly shows the effect of the nonlinear terms in bending the resonance horn because the effective eigenfrequency now depends on the response amplitude. In linear theory one would find a single response amplitude for each value of the frequency σ. In this case however, it is possible to find multiple stationary solutions. It appears that, if there are three response solutions for given parameters σ and Z, the response with largest and the response with smallest amplitude are stable. The

---

[2]Compare (5.3) and (5.4) with respectively (3.6) and (3.8) in Doelman *et al.* (2002), where $F_{sol} = 0$ at this point.
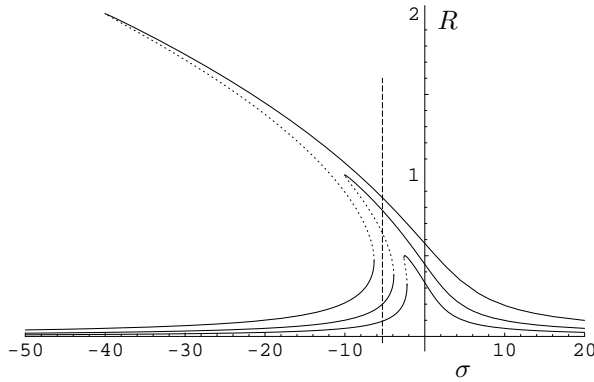
Figure 5.1: Frequency response curves for $\Gamma = -10$, $c = 1$ and several forcing amplitudes, $Z = \frac{1}{2}, 1, 2$. Solid curves denote stable branches, the dotted curves are unstable. A vertical line at $\sigma = -5.3$ indicates that multiple equilibria are found under certain conditions.

'medium amplitude response' is an unstable solution of (5.2), represented in figure 5.1 by a dotted line. This means that under those external conditions, the system can be found in either an amplified or a choked tidal regime, depending on the history of the system.

Under slow changes of external conditions, like mean sea-level rise or changing morphology, the system will follow one of the stable branches. However, if such a branch 'folds', hence ceases to exist, the system will make a sudden transition to the remaining stable branch if the external conditions change further. If the parameters change very slowly, the system will have time to settle down to the new regime. If however the parameters change back and forth before the system has time to reach the corresponding stationary states, the reaction of the system can be chaotic, as will be discussed below. There are two obvious ways in which the forcing parameters σ (frequency) and Z (amplitude) can be changed on the time scale τ of the transient amplitude behaviour in (5.2): either a slow change in water depth or forcing amplitude modulations, the latter due to e.g. the spring-neap tidal cycle. In relatively small basins, a slow change in water depth could be due to large scale tidal motion, with the resonant eigenmode representing secondary undulations on a much smaller time scale. It constitutes a slow change in the basin's characteristics, hence its eigenfrequency. This effectively amounts to changing the forcing frequency σ relative to the eigenfrequency, see Maas & Doelman (2002, section 5). The analysis in chapter 4 does not capture this process accurately, although it is in principle possible to incorporate this effect in the present model as well.

In the case of amplitude modulations a so-called 'horseshoe' has been found as a subsystem of the model under some additional assumptions, thus constituting a proof of the occurrence of chaos in the system (Doelman *et al.*, 2002). This construction will be illustrated here. The external forcing is assumed now to consist of two tidal components, one much smaller in amplitude than the other, and both almost in resonance with the one eigenfrequency ω_k, as is appropriate for many areas where the tidal signal is dominated by the lunar M_2-tidal component, with a small modulation
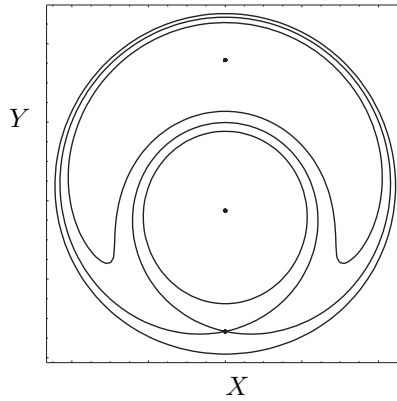
Figure 5.2: Phase portrait of Hamiltonian flow for $Z_1 = \frac{1}{24}\sqrt{3}$. This choice for Z_1 is arbitrary. When $0 < Z_1 < \frac{2}{9}\sqrt{3}$, there are three stationary states and the result is similar.

due to the solar S_2-constituent. As explained for one tidal component at the beginning of this section, this leads to $F_k(\tau) = Z_1 e^{i(\sigma_1 \tau + \Psi_1)} + Z_2 e^{i(\sigma_2 \tau + \Psi_2)}$. The assumption formulated above can be written as $Z_2/Z_1 = \delta$, with $\delta \ll 1$, which leads to

$$
\begin{aligned}
F_k(\tau) &= Z_1 e^{i(\sigma_1 \tau + \Psi_1)} + Z_2 e^{i(\sigma_2 \tau + \Psi_2)} \\
&= Z_1 e^{i(\sigma_1 \tau + \Psi_1)}(1 + \delta e^{i(\Delta \sigma \, \tau + \Delta \Psi)}) \\
&= Z(\tau) e^{i(\sigma \tau + \Psi(\tau))},
\end{aligned}
$$

where $\sigma = \sigma_1$, $\Delta \sigma = \sigma_2 - \sigma_1$, $\Delta \Psi = \Psi_2 - \Psi_1$, $Z(\tau) = Z_1 (1 + \delta \cos(\Delta \sigma \, \tau + \Delta \Psi)) + \mathcal{O}(\delta^2)$, and $\Psi(\tau) = \Psi_1 + \delta \sin(\Delta \sigma \, \tau + \Delta \Psi) + \mathcal{O}(\delta^2)$. The expression for $F_k(\tau)$ is similar to that for a single tidal component. Therefore, (5.2), (5.3) and (5.4) are equally valid, with the only difference that Z and Ψ depend on τ now. Moreover, in conjunction with assuming small modulation, friction is assumed to be additionally small as well, by writing $c = \delta C$. By rescaling, the system is brought into the form

$$
\frac{\mathrm{d}X}{\mathrm{d}\tau} = (1 - R^2)Y + Z_1 + \delta\big[- CX + Z_1 \sin(\Delta \sigma \, \tau)\big], \tag{5.6a}
$$

$$
\frac{\mathrm{d}Y}{\mathrm{d}\tau} = -(1 - R^2)X + \delta\big[- CY - Z_1 \cos(\Delta \sigma \, \tau)\big], \tag{5.6b}
$$

which is the same as (3.16) in Doelman *et al.* (2002) upon interchanging X and Y.

System (5.6) is Hamiltonian for $\delta = 0$; the Hamiltonian is given by

$$
\mathcal{H}(X, Y) = -\tfrac{1}{4}(1 - R^2)^2 + Z_1 Y. \tag{5.7}
$$

The resulting phase portrait is shown in figure 5.2 under conditions for which there are multiple equilibria. One of the critical points is a saddle, the other two are centre points. The saddle corresponds to the unstable stationary solution from figure 5.1. The centres correspond to the stable stationary solutions in figure 5.1. The 'inner'

one is the choked mode with small amplitude, the 'outer' one is the amplified mode with an amplitude which is larger than the amplitude of the saddle. Two homoclinic orbits are connected to the saddle.

For $\delta \neq 0$ the system (5.6) is not autonomous, so the phase portrait in figure 5.2 is not appropriate anymore. For small $\delta \ll 1$ it can be used as a first approximation however. The persistence of the homoclinic orbits can be investigated using the Melnikov method. In fact, the deviation from the unperturbed homoclinic orbit in figure 5.2 is approximated by calculating the approximate change of the Hamiltonian $\mathcal{H}$ due to the $\mathcal{O}(\delta)$ perturbations by friction and modulation. This determines if they are connected still, or if the stable and unstable manifolds of the saddle point — the points that tend to respectively come from it — do not meet and spiral down to the critical points. The analysis by Doelman *et al.* (2002) shows that the stable and unstable manifolds do intersect transversely if friction is not too large (for $C < C_{max}(Z_1, \Delta\sigma)$). Note that transverse intersections between stable and unstable manifolds are possible due to the non-autonomous nature of (5.6). In that case the well-known 'horseshoe' can be constructed (the Smale–Birkhoff theorem), which yields a chaotic set, consisting of chaotic orbits which evolve close to the homoclinic orbits of figure 5.2 again and again in an irregular way. The physical consequence is that harmonic 'constants' cannot be found because they evolve chaotically on longer time scales (cf. Doodson, 1924; Gutiérrez *et al.*, 1981).

A final remark should be made about the value of the parameter δ. It must be small in order for the Melnikov method to be applicable. The parameter α should be even smaller, to maintain the validity of the amplitude equation (5.2). However, though this assumption on δ is needed to construct the horseshoe map by the Melnikov method, the smallness of δ, i.e. of the modulation of the external forcing, is likely not to be required at all. It is to be expected that for larger δ, chaotic motion still occurs. This is motivated for example by the numerical observations in Maas (1997) and Maas & Doelman (2002).

5.4 Two-mode solutions

In order to investigate the influence of one mode on the other, it is natural to consider the model with two modes. Hence, in this section the external forcing is assumed to be in resonance with two eigenmodes of the basin. Without loss of generality we call them mode 1 and mode 2, referring to these modes by means of corresponding indices. The external forcing will give rise to $F_k = Z_k e^{i(\sigma_k \tau + \Psi_k)}$, for $k = 1, 2$. Continuing as in the previous section, we replace $A_k(\tau)$ by $A_k e^{i\sigma_k \tau}$ resulting in the equations

$$\frac{dA_1}{d\tau} = -c_1 A_1 - i\sigma_1 A_1 + i(\Gamma_{1,1} |A_1|^2 + \Gamma_{1,2} |A_2|^2)A_1 + Z_1 e^{i\Psi_1}, \quad (5.8a)$$

$$\frac{dA_2}{d\tau} = -c_2 A_2 - i\sigma_2 A_2 + i(\Gamma_{2,1} |A_1|^2 + \Gamma_{2,2} |A_2|^2)A_2 + Z_2 e^{i\Psi_2}. \quad (5.8b)$$

In polar coordinates $A_k = R_k \mathrm{e}^{\mathrm{i}\Phi_k}$ we have

$$\frac{\mathrm{d}R_1}{\mathrm{d}\tau} = -c_1 R_1 + Z_1 \cos(\Psi_1 - \Phi_1), \tag{5.9a}$$

$$R_1 \frac{\mathrm{d}\Phi_1}{\mathrm{d}\tau} = -(\sigma_1 - \Gamma_{1,1}{R_1}^2 - \Gamma_{1,2}{R_2}^2)R_1 + Z_1 \sin(\Psi_1 - \Phi_1), \tag{5.9b}$$

$$\frac{\mathrm{d}R_2}{\mathrm{d}\tau} = -c_2 R_2 + Z_2 \cos(\Psi_2 - \Phi_2), \tag{5.9c}$$

$$R_2 \frac{\mathrm{d}\Phi_2}{\mathrm{d}\tau} = -(\sigma_2 - \Gamma_{2,1}{R_1}^2 - \Gamma_{2,2}{R_2}^2)R_2 + Z_2 \sin(\Psi_2 - \Phi_2). \tag{5.9d}$$

The next subsection deals with the stationary solutions of these equations which can be studied analytically. Figure 5.3 shows the four-dimensional response graphs of the response amplitudes R_1 and R_2 as a function of the forcing frequencies σ_1 and σ_2 for fixed forcing amplitudes Z_1 and Z_2. In order to clarify this figure, a classification of (σ_1, σ_2) parameter space is given in figure 5.4. The stability of the stationary states is discussed here as well. Moreover, cross-sections of the graphs in figure 5.3 are shown in figure 5.5. Finally, the section ends with numerical investigations of the system, showing periodic orbits, period doublings and chaos.

Note that the behaviour described here is that of the amplitudes themselves. The resulting water-level variations will be oscillations with frequencies ω_1, ω_2 of the respective eigenmodes, but with amplitudes and phases modulating slowly in time, according to the dynamics described here. This behaviour would manifest itself if one performs harmonic analyses on tidal signals over moving windows in time. Instead of being constant over all time frames, the amplitudes and phases found for a tidal component would vary slowly in time. It is this variation of the amplitudes and phases that is studied here.

5.4.1   Analytical results

Stationary solutions to these equations correspond again to the response of the system at the same frequencies as the forcing. They follow by equating the derivatives in (5.9) to zero and eliminating the angle coordinates. This leads to

$$\sigma_1 = \Gamma_{1,1}{R_1}^2 + \Gamma_{1,2}{R_2}^2 \pm \sqrt{\frac{{Z_1}^2}{{R_1}^2} - {c_1}^2}, \tag{5.10a}$$

$$\sigma_2 = \Gamma_{2,1}{R_1}^2 + \Gamma_{2,2}{R_2}^2 \pm \sqrt{\frac{{Z_2}^2}{{R_2}^2} - {c_2}^2}. \tag{5.10b}$$

Compare this with (5.5) for one mode. For each mode, the response curve R_k as a function of σ_k would be just a shifted copy of figure 5.1, if the other mode's amplitude were constant. Obviously R_1 depends on σ_1 but it depends on σ_2 as well through the interaction with R_2. The influence of one mode on the other is to change its effective eigenfrequency. Because the shift depends on the amplitude, the result can nevertheless be quite complicated. As in the case of one mode, it is much harder to find the response amplitudes R_1 and R_2 as a function of the detuning frequencies σ_1, σ_2. However, by plotting the frequencies as a function of the amplitudes, one can still parametrically describe the response-'curves'. Figure 5.3 shows the results.

The plots are made with coefficients $\Gamma_{k,m}$ according to the first two eigenmodes of a rectangular basin with vertical sidewalls, i.e. $\Gamma_{1,1} = -10$, $\Gamma_{1,2} = -12$, $\Gamma_{2,1} = -17$, $\Gamma_{2,2} = -16$ and friction $c_1 = c_2 = \frac{1}{2}$, see section 4.4. Cross-sections, shown in figure 5.5, will be described later.

Because the response amplitudes depend on both frequencies σ_1 and σ_2, the graphs are three-dimensional. In fact, they should be considered together as four-dimensional graphs of (R_1, R_2) as a function of (σ_1, σ_2). For a given pair of frequencies (σ_1, σ_2) a stationary state is characterized by a pair of amplitudes (R_1, R_2). These states constitute the branches in figure 5.3; the graphs are not independent from each other. The number of stationary states at given frequencies can be read off from the colours in figure 5.4. The solid lines in this figure mark the frequency values for which saddle-node bifurcations occur, where two steady states appear or vanish. They are obtained by considering the Jacobian of (5.9):

$$
\begin{pmatrix}
-c_1 & Z_1 \sin(\Psi_1-\Phi_1) & 0 & 0 \\
2\Gamma_{1,1}R_1 - \frac{Z_1 \sin(\Psi_1-\Phi_1)}{R_1{}^2} & -\frac{Z_1 \cos(\Psi_1-\Phi_1)}{R_1} & 2\Gamma_{1,2}R_2 & 0 \\
0 & 0 & -c_2 & Z_2 \sin(\Psi_2-\Phi_2) \\
2\Gamma_{2,1}R_1 & 0 & 2\Gamma_{2,2}R_2 - \frac{Z_2 \sin(\Psi_2-\Phi_2)}{R_2{}^2} & -\frac{Z_2 \cos(\Psi_2-\Phi_2)}{R_2}
\end{pmatrix}
$$

$$(5.11)$$

Using the fact that $Z_k \cos(\Psi_k-\Phi_k) = c_k R_k$, for $k = 1, 2$, in steady states, the Jacobian can be conveniently expressed in terms of the two variables $t_k = \tan(\Psi_k - \Phi_k)$. The characteristic polynomial of (5.11) is

$$p(\lambda) = \lambda^4 + a\lambda^3 + b\lambda^2 + c\lambda + d,$$

where

$$
\begin{aligned}
a &= 2(c_1 + c_2), \\
b &= 4c_1 c_2 + c_1{}^2(1 + t_1{}^2) + 2c_1\Gamma_{1,1}R_1{}^2 t_1 + c_2{}^2(1 + t_2{}^2) + 2c_2\Gamma_{2,2}R_2{}^2 t_2, \\
c &= 2c_2(c_1{}^2(1 + t_1{}^2) + 2c_1\Gamma_{1,1}R_1{}^2 t_1) + 2c_1(c_2{}^2(1 + t_2{}^2) + 2c_2\Gamma_{2,2}R_2{}^2 t_2), \quad (5.12) \\
d &= (c_1{}^2(1 + t_1{}^2) + 2c_1\Gamma_{1,1}R_1{}^2 t_1)(c_2{}^2(1 + t_2{}^2) + 2c_2\Gamma_{2,2}R_2{}^2 t_2) \\
&\quad - 4c_1 c_2\Gamma_{1,2}\Gamma_{2,1}R_1{}^2 t_1 R_2{}^2 t_2,
\end{aligned}
$$

with $R_k = Z_k/(c_k\sqrt{1 + t_k{}^2})$. Saddle-node bifurcations occur when $\lambda = 0$ is a root. Solving $d = 0$ for t_2 hence leads to a parametric description of the solid bifurcation lines in figure 5.4 in terms of t_1.

The stability of the steady states in figure 5.3 can also change due to Hopf bifurcations. These occur if $\lambda = i\omega$, with $\omega \in \mathbb{R}$, is a root of $p(\lambda)$, i.e. $\omega^4 - b\omega^2 + d - ia\omega^3 + ic\omega = 0$. From the imaginary part $c\omega - a\omega^3$ we find that either $\omega = 0$, resulting in the saddle-node bifurcations already considered, or $\omega^2 = c/a$, which subsequently can be substituted in the real part of $p(\lambda)$. Solving the resulting condition $c^2 - abc + a^2 d = 0$ leads to a parametrization of the dashed bifurcation lines that are also shown in figure 5.4. At those values for the frequencies σ_1 and σ_2, one of the branches of steady states undergoes a Hopf bifurcation, generically giving birth to a periodic solution.

Three basic components can be distinguished in figure 5.3. First one has the steady states with R_1 finite and R_2 very small, or with R_1 very small and R_2 finite. In the first case, because R_2 is negligible, the corresponding frequency σ_2 has hardly any influence on these states. This results in a graph parallel to the σ_2-axis, with
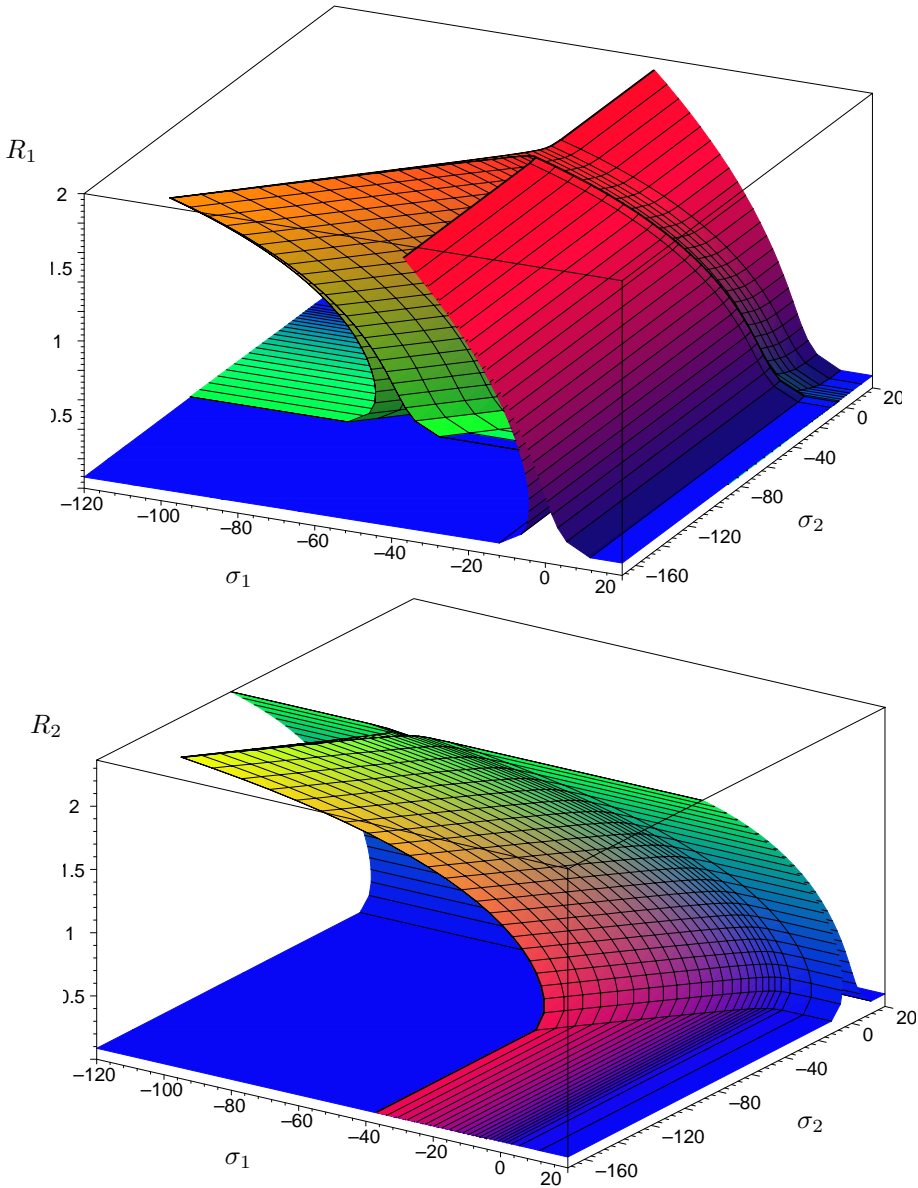
Figure 5.3: The response amplitudes R_1 and R_2 as a function of forcing frequencies. Bay parameters are chosen in accordance with the first two modes of a rectangular basin ($c_1 = c_2 = \frac{1}{2}$, $\Gamma_{1,1} = -10$, $\Gamma_{1,2} = -12$, $\Gamma_{2,1} = -17$, $\Gamma_{2,2} = -16$). The choice $(Z_1, Z_2) = (1, 13/11)$ of forcing amplitudes is arbitrary. Other choices lead to different but similar pictures. The surfaces are parameterized by R_1 and R_2; the black gridlines are for constant R_1 and R_2 respectively. Corresponding branches are in the same colour in both figures: along the blue branches both R_1 and R_2 are small, red is for R_1 finite and small R_2, green denotes small R_1 and finite R_2, orange/yellow branches have both R_1 and R_2 finite.
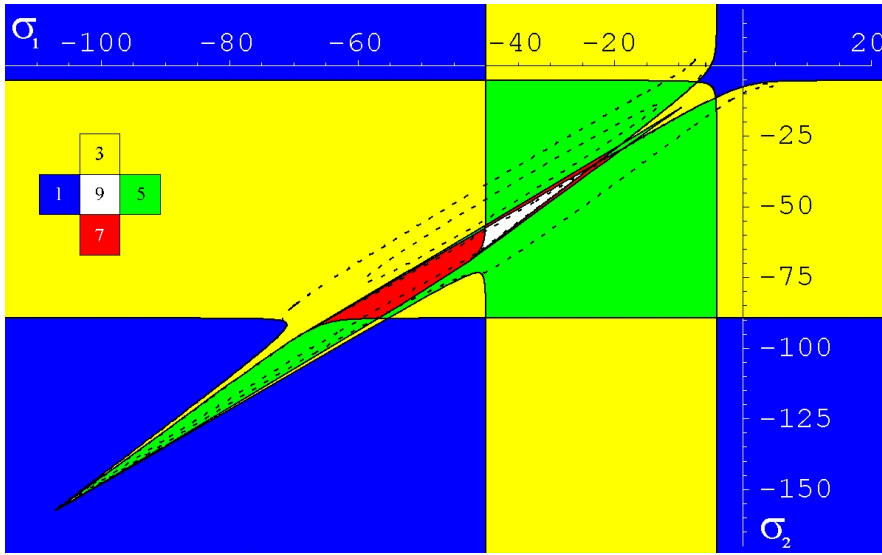
(a)
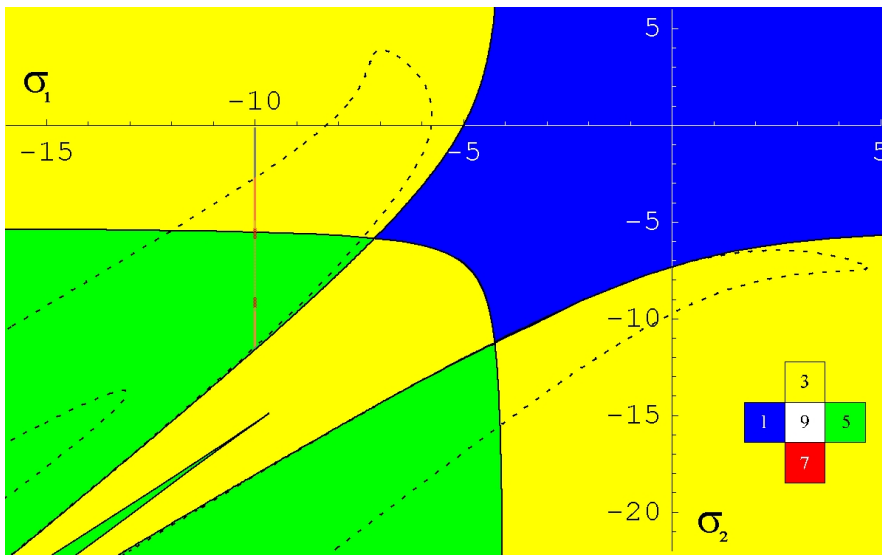
(b)

Figure 5.4: Bifurcation lines in (σ_1, σ_2) parameter space for $Z_1 = 1$, $Z_2 = \frac{13}{11}$, bay parameters as in figure 5.3. Solid lines mark saddle-node bifurcations and divide the space into regions with a different number of steady states (regions are colour-coded). Dashed lines represent Hopf bifurcations. (b) A zoom of the part of parameter space for which numerical experiments were performed, along the indicated line for $\sigma_1 = -10$.

(a) At $\sigma_2 = -1$.

(b) At $\sigma_2 = -1$.

(c) At $\sigma_2 = -18$.

(d) At $\sigma_2 = -18$.

(e) At $\sigma_2 = -80$.

(f) At $\sigma_2 = -80$.
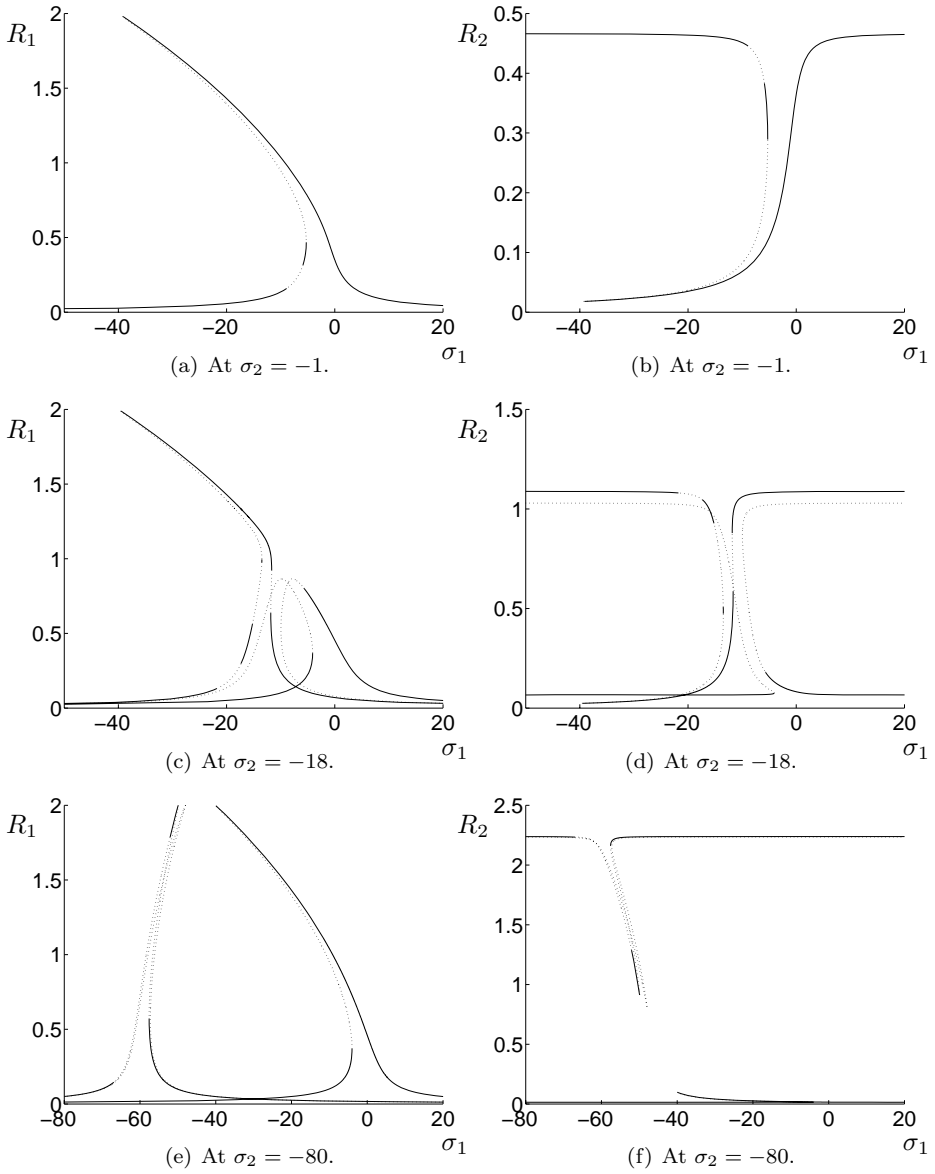
Figure 5.5: (a–f), For caption see facing page.

(g) At $\sigma_1 = -36$.

(h) At $\sigma_1 = -36$.

(i) At $\sigma_1 = -60$.

(j) At $\sigma_1 = -60$.

(k) At $\sigma_1 = -80$.

(l) At $\sigma_1 = -80$.
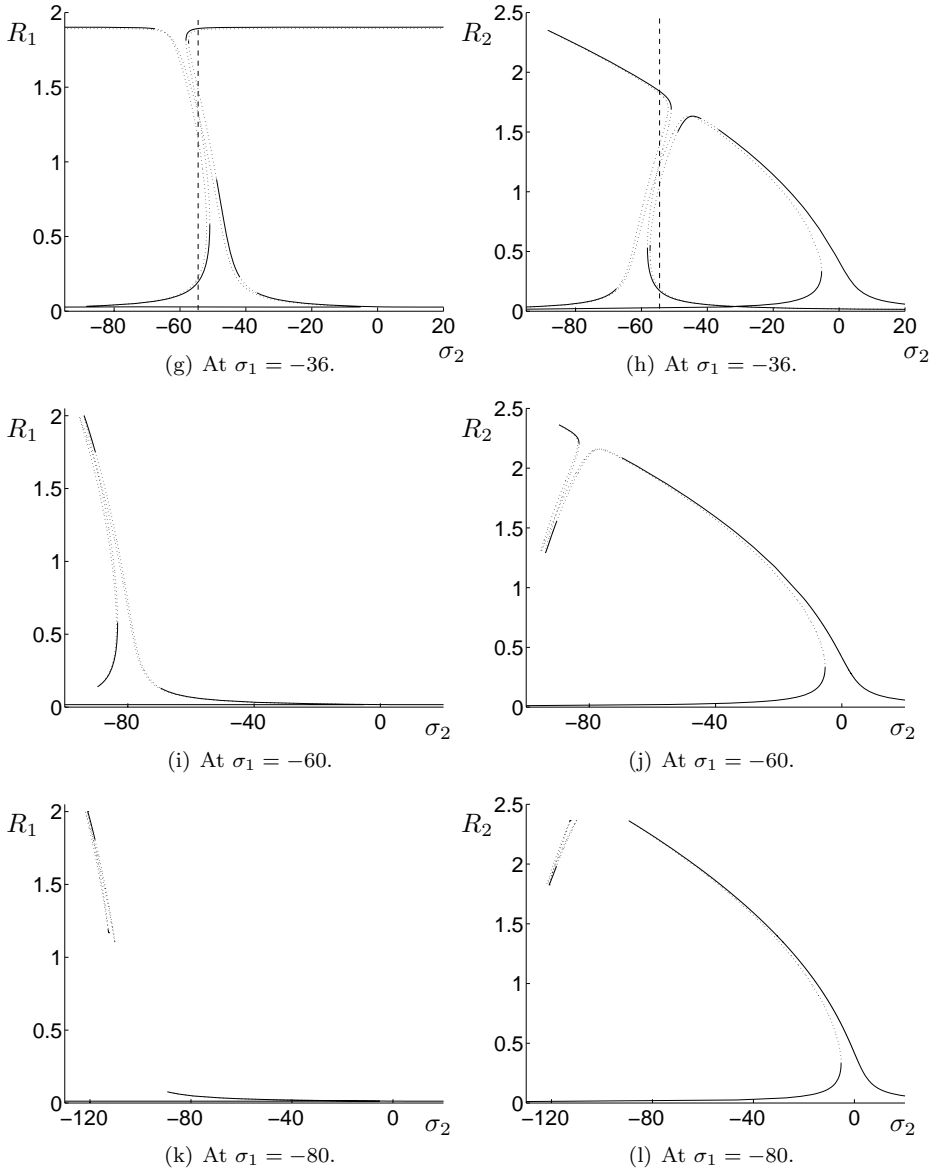
Figure 5.5: Several cross-sections of the response surfaces from figure 5.3, for the same bay parameters and forcing amplitudes as in the previous figures. (a–f) show the response amplitudes R_1 and R_2 as a function of σ_1 for (a,b) $\sigma_2 = -1$, (c,d) $\sigma_2 = -18$, (e,f) $\sigma_2 = -80$; (g–l) show R_1 and R_2 as a function of σ_2 for (g,h) $\sigma_1 = -36$, (i,j) $\sigma_1 = -60$, (k,l) $\sigma_1 = -80$. The dashed line at $\sigma_2 = -54.5$ in (g) and (h) indicates conditions for which nine different equilibria exist.

constant cross-section perpendicular to that axis, following the one-mode response curve for R_1 versus σ_1 (figure 5.1). The same holds, *mutatis mutandis*, for the steady states with R_1 very small. Besides those two branches, there are new equilibria with both R_1 and R_2 finite, to be called *two-mode equilibria*. The backbone of these equilibria is described by $\sigma_1 = \Gamma_{1,1} R_1{}^2 + \Gamma_{1,2} R_2{}^2$ and $\sigma_2 = \Gamma_{2,1} R_1{}^2 + \Gamma_{2,2} R_2{}^2$, for $0 \le R_k \le Z_k/c_k$. Hence this 'backbone' exists in a parallelogram in (σ_1, σ_2) frequency space. The square roots in (5.10) cause the steady states to deviate from it, but the (distorted) parallelogram is still recognizable as such in figure 5.4(a).

Several cross-sections of figure 5.3 are shown in figure 5.5. They are obtained using another parametrization of the response-surfaces. In fact, by solving (5.10a) with respect to R_2, one can obtain (R_2, σ_2) as a function of (R_1, σ_1). Solving (5.10b) for R_1 yields a parametrization of (R_1, σ_1) as a function of (R_2, σ_2). The former can be used to plot intersections for constant σ_1 by choosing a judicious range of values for R_1, the latter for intersections with σ_2 constant. The stability of the respective steady states was determined by calculating the eigenvalues of the Jacobian (5.11). Solid lines indicate stable equilibria, unstable branches are dashed.

The common feature in these cross-sections (for fixed σ_k) is the one-mode response curve when one mode (R_k) is very small. Its stability generally corresponds to that of the one-mode solution, the higher and lower modes being stable and the 'medium amplitude mode' unstable. In figure 5.5(a) (with corresponding figure 5.5(b)) the lower mode is unstable due to a Hopf bifurcation over a small interval of σ_1-values, apparently due to the influence of the second mode. The new two-mode equilibria are separated from the one-mode response curve in figures 5.5(k), 5.5(l) for $\sigma_1 = -80$. In figures 5.5(e), 5.5(f) the two-mode equilibria are disconnected from the one-mode response curve for R_1 as well. The fact that these branches extend to $\sigma_1 \to \pm\infty$ reflects that they are connected with the one-mode solutions for which R_1 is very small. In the other figures the two-mode equilibria and the one-mode response curves are connected. Although they often are unstable, which implies that they would not appear in practice, there are conditions for which the new two-mode equilibria are stable, hence observable in principle. They can occur, even though the one-mode response curve shows low-amplitude solutions at those conditions only. The nonlinear interaction between modes allows the basin to resonate at other frequencies than its linear eigenfrequencies. Multiple equilibria occur in the two-mode system as well (see figure 5.4), with a maximum of nine equilibria under conditions indicated by intersections with the dashed line in figures 5.5(g), 5.5(h).

There is hardly any difference (apart from interchanging R_1 and R_2) between the cross-sections perpendicular to the σ_2-axis and those perpendicular to the σ_1-axis. All figures are shown here for $Z_1 = 1$ and $Z_2 = \frac{13}{11}$. For other choices the differences are similar to those between the cross-sections for constant σ_1 or σ_2. Increasing friction (parameters c_1 and c_2) blurs the picture: the width of the resonance peaks increases, thus obscuring their backbone structure. In particular the bending of the resonance 'curves', hence the multiple equilibria, ultimately disappears.

5.4.2   Numerical integrations

Using the numerical dynamical systems package DsTool (Guckenheimer *et al.*, 1992), the system (5.8) was investigated near one of the Hopf bifurcations. In fact, some experiments were carried out for $\sigma_1 = -10$ and σ_2 ranging between 0 and -11.5,

(a) Time series, $\sigma_2 = -9.416$

(b) Time series, $\sigma_2 = -9.3$

(c) Zoom of time series 5.6(b)

(d) First mode, $\sigma_2 = -9.416$

(e) First mode, $\sigma_2 = -9.3$

(f) Poincaré section, lower left section in (X_2, Y_2)-space

(g) Amplitudes, $\sigma_2 = -9.416$

(h) Amplitudes, $\sigma_2 = -9.3$
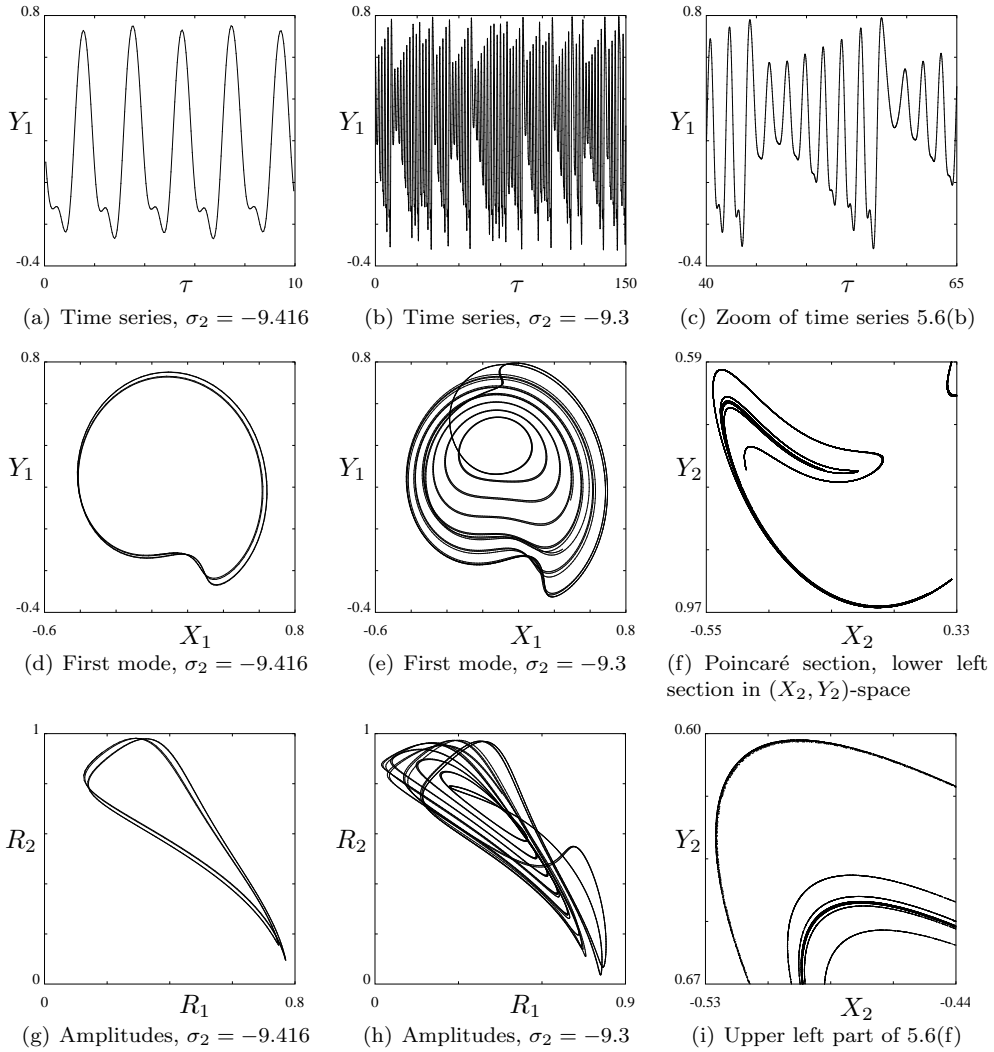
(i) Upper left part of 5.6(f)

Figure 5.6: Time series and projections of the orbit in phase space for the chaotic attractor at $\sigma_1 = -10, \sigma_2 = -9.3$. The Poincaré section for the return map to the plane $R_1 = 0.4$ is shown in 5.6(f) and 5.6(i). For comparison, the periodic attractor at $(\sigma_1, \sigma_2) = (-10, -9.416)$, after two period doublings, is shown as well.

along the line indicated in figure 5.4(b). There are multiple equilibria under these circumstances, but we focused on one particular branch only, with R_1 being lowest and R_2 highest of three at $\sigma_2 = 0$ (this order is not preserved throughout). Therefore some of the bifurcation lines that are crossed in figure 5.4(b) are not relevant because they occur on other branches. On the selected branch a Hopf bifurcation occurs when the dashed line is crossed. The solid line crossed at $\sigma_2 = -11.6$ marks a saddle-node bifurcation, thus ending this branch. The solid line which is crossed at about $\sigma_2 = -5.2$, marks a saddle-node bifurcation that occurs on another branch.

The stationary state is stable for σ_2 just above the saddle-node bifurcation at $\sigma_2 = -11.6$. On increasing σ_2 from there a supercritical Hopf bifurcation occurs: a stable periodic solution to (5.8) appears for σ_2 just above -11.48. This solution undergoes period doubling at $\sigma_2 = -9.44, -9.42, \ldots$. This orbit is shown in the left-hand column of figure 5.6 at $\sigma_2 = -9.416$, after two period doublings. The difference between subsequent oscillations is hardly visible in the time series 5.6(a) for the imaginary part Y_1 of the first mode, although the fourfold symmetry breaking is still reasonably distinct in the phase portraits 5.6(d) and 5.6(g). After a cascade of period doublings a chaotic attractor is found, for which the time series for Y_1 and projections of the orbit in phase space are shown for $\sigma_2 = -9.3$. Regime behaviour, a common feature in chaotic systems, is found: the amplitude of the oscillations collapses suddenly and starts to grow again, until at some moment another collapse occurs. Although the growth process seems to behave regularly, the period between two collapses is irregular. The chaotic nature of the motion is corroborated furthermore by the Poincaré section in figures 5.6(f), 5.6(i), showing the return map to the plane $R_1 = 0.4$. A Hénon-like fractal attractor is found.

At $\sigma_2 = -9.29$ the chaotic attractor becomes unstable: orbits starting close to the chaotic set stay close for some time, but end up at one of the remaining stable fixed points ultimately. It remains unstable till $\sigma_2 = -5.61$, above which a stable chaotic attractor is found again. It originates from a cascade of period doublings at $\sigma_2 = -5.00, -5.38, \ldots$ when decreasing σ_2 below the (supercritical) Hopf bifurcation at $\sigma_2 = -2.72$. For $\sigma_2 > -2.72$ the stationary solutions is stable again: no periodic orbit is found anymore.

5.5   Mechanisms for chaos

Chaotic behaviour is found in system (4.30), both in section 5.3 for one mode, and in section 5.4 for two modes. The mechanism responsible for the chaos is different however. In this section a number of mechanisms that can lead to chaos are discussed. For a system with only one eigenmode, such as an almost-enclosed basin with its corresponding Helmholtz mode (the dynamics of which was discussed by Maas, 1997; Maas & Doelman, 2002; Doelman *et al.*, 2002) no chaotic behaviour was found if the exterior tide ζ_e is harmonic. Quasi-periodic forcing, i.e. multiple tidal constituents in ζ_e, is necessary to obtain complex dynamics. In the present model however, chaotic behaviour is possible for harmonic forcing as well, due to the possible interaction between eigenmodes. Mechanisms of this kind are discussed in a separate section 5.5.2.

5.5.1 Quasi-periodic forcing

If **two components** of the tidal signal ζ_e at sea (for example the M_2- and S_2-components, causing the spring-neap tidal cycle) are nearly in resonance with a **single eigenfrequency** of the basin, this single mode is forced with slowly modulating forcing amplitude (and phase). As discussed in section 5.3, it was shown in Doelman *et al.* (2002) that this leads to chaotic behaviour of the system. The mechanism stems from the fact that the response curve (5.5) changes with changing forcing amplitude Z. The system has to adapt to a new stable equilibrium when it passes the end of a stable branch. However, before the system has settled to the new regime, the forcing amplitude has changed again, causing continuous regime changes in a chaotic manner. In Maas (1997) this was observed first for a model describing an almost-enclosed basin, with only one mode, the Helmholtz or pumping mode. In this thesis it is shown that those conclusions hold for more general basins as well, if one of its eigenmodes is resonantly forced with two components.

Another mechanism, mentioned already by Maas & Doelman (2002), occurs if the external tide ζ_e consists of one component which is very slow compared to the eigenmodes of the basin and one which is nearly resonant with one of the eigenfrequencies. This might happen for relatively small basins, such as fjords or harbours, with large eigenfrequencies (periods of hours or less), the 'slow' component being M_2 and an eigenfrequency being resonant with one of its overtones M_{2n} or with another 'high'-frequency component in (the continuum part of) the water-level spectrum (cf. Munk & Cartwright, 1966). The **slow component** of the external tide amounts to a slow change of the reference water depth in the basin. As a consequence its eigenmodes change. For an almost-enclosed basin, where the relatively simple Helmholtz mode is the only eigenmode of interest, determination of the change in eigenfrequency is quite straightforward. Because the frequency σ in (5.5) is relative to the eigenfrequency, this causes a slow change of σ. Hence a mechanism similar to the previous case occurs. The system will change between regimes while σ moves along the response curve (5.5). Under appropriate conditions the regime changes will occur in a chaotic manner. In principle this mechanism applies for the model derived in the previous chapter as well. A detailed analysis is more complicated however, because it necessitates calculating the change of the eigenmodes due to a slow change in water depth.

In contrast with previous studies, the model derived in chapter 4 deals with more than one eigenmode. This allows the possibility of **two different eigenmodes** being resonantly forced by the external tide ζ_e. This situation is discussed in section 5.4. With a single tidal component forcing each of the two eigenmodes, the forcing amplitudes Z_1 and Z_2 are constant. In the corresponding case for one mode (section 5.3) this leads to multiple equilibria, but no chaos. In the two-mode case however, the behaviour of the system can be richer. Periodic orbits for the response *amplitudes* are found and numerical evidence of chaos has been provided. The interaction between modes is only through the phase equation, where it can be seen as one mode modifying the effective eigenfrequency of the other. In that respect the mechanism is comparable with the previous one, although the time dependence results from an instability in the interaction between the two modes in this case. Although explicit time dependence of the amplitude equations was needed for the one-mode cases, whereas Z_1 and Z_2 may be constant in the two-mode case for chaos to occur, this is not an essential difference either. For all three mechanisms discussed so far, chaos occurs

only if the forcing tide ζ_e at sea comprises at least two components. For the first and third mechanism both need to be in resonance with an eigenmode, either a single one or two different ones. For the second mechanism only one component needs to be resonant; the other component must be slowly evolving on the same time scale at which the system adapts to new equilibria.

The mechanism discussed in the previous paragraph dealt with both amplitudes Z_1 and Z_2 being $\mathcal{O}(1)$ (note that this still amounts to small amplitudes at sea due to the scaling of ζ_e compared to ζ). If one forcing component, say Z_2, were even smaller, then the corresponding response amplitude R_2 would be equally small. This situation gives rise to an approximate mathematical approach. For this we assume $Z_2 = \delta z = \mathcal{O}(\delta)$ with $\delta \ll 1$. Similar to the analysis in Doelman *et al.* (2002) we assume friction to be additionally small, $c_1 = \delta^2 C_1 = \mathcal{O}(\delta^2)$, but $c_2 = \mathcal{O}(1)$ may not be small. This is a realistic scenario if mode 1 is one of the first eigenmodes, whereas mode 2 is, although denoted here by the subscript 2, a fairly high eigenmode, because c_k generally increases with k (see section 4.4). This scaling implies that R_2, the amplitude of the second eigenmode, is $\mathcal{O}(\delta)$. Hence we write $R_2 = \delta r$, $X_2 = \delta x$ and $Y_2 = \delta y$ to obtain the following amplitude equations in Cartesian coordinates (cf. (5.8)):

$$\frac{dX_1}{d\tau} = (\sigma_1 - \Gamma_{1,1}R_1{}^2 - \delta^2\Gamma_{1,2}r^2)Y_1 - \delta^2 C_1 X_1 + Z_1 \cos(\Psi_1), \qquad (5.13a)$$

$$\frac{dY_1}{d\tau} = -(\sigma_1 - \Gamma_{1,1}R_1{}^2 - \delta^2\Gamma_{1,2}r^2)X_1 - \delta^2 C_1 Y_1 + Z_1 \sin(\Psi_1), \quad (5.13b)$$

$$\frac{dx}{d\tau} = (\sigma_2 - \Gamma_{2,1}R_1{}^2 - \delta^2\Gamma_{2,2}r^2)y - c_2 x + z \cos(\Psi_2), \qquad\qquad (5.13c)$$

$$\frac{dy}{d\tau} = -(\sigma_2 - \Gamma_{2,1}R_1{}^2 - \delta^2\Gamma_{2,2}r^2)x - c_2 y + z \sin(\Psi_2), \qquad\qquad (5.13d)$$

where $R_1{}^2 = X_1{}^2 + Y_1{}^2$ and $r^2 = x^2 + y^2$. Up to $\mathcal{O}(\delta^2)$, the first mode is governed by the Hamiltonian flow with Hamiltonian

$$\mathcal{H}(X, Y) = \frac{-1}{4\Gamma_{1,1}}(\sigma_1 - \Gamma_{1,1}R_1{}^2)^2 + Z_1 \cos(\Psi_1)Y_1 - Z_1 \sin(\Psi_1)X_1,$$

which is the unscaled variant of (5.7), whereas the equation for the second mode is linear. Hence the phase portrait of the first-order flow for the first mode is known, see Doelman *et al.* (2002). Evolving along one of those periodic or homoclinic orbits, the first mode drives the second parametrically. The second mode couples back to the first mode at $\mathcal{O}(\delta^2)$, in a similar way as in the second mechanism discussed before, by modulating the effective eigenfrequency. The modulation by R_2 reflects the first-order behaviour of R_1 in this case. This is the setting in which perturbation theory could be applied, using Melnikov functions to estimate the change of the Hamiltonian, due to friction and the interaction with the second mode, while evolving along the first-order orbits of the one-mode system. One may be able to construct (stable) periodic and homoclinic orbits in the full two-mode system in this way and possibly chaos of the Shilnikov-type (Guckenheimer & Holmes, 1983; Wiggins, 1988).

5.5.2 Harmonic forcing

For all mechanisms described in the previous subsection, the external tide needs to be non-harmonic for chaos to occur. A harmonic external tide ζ_e with one tidal constituent can lead to chaos as well if one mode can excite another. This is possible if **Coriolis effects** are taken into account. In the context of the present work, Coriolis forces cause the eigenfunctions of (4.10), (4.11) to be non-real. Physically this means phase differences within the eigenmode over the basin; mathematically it leads to non-real coefficients $\Gamma_{k,m}$. Writing $\Gamma_{k,m} \mapsto \Gamma_{k,m} + \mathrm{i}\Delta_{k,m}$ and $Z_2 = 0$, the equivalent of (5.9) is

$$\frac{\mathrm{d}R_1}{\mathrm{d}\tau} = -(c_1 + \Delta_{1,1}R_1{}^2 + \Delta_{1,2}R_2{}^2)R_1 + Z_1\cos(\Psi_1 - \Phi_1), \quad (5.14a)$$

$$R_1\frac{\mathrm{d}\Phi_1}{\mathrm{d}\tau} = -(\sigma_1 - \Gamma_{1,1}R_1{}^2 - \Gamma_{1,2}R_2{}^2)R_1 + Z_1\sin(\Psi_1 - \Phi_1), \quad (5.14b)$$

$$\frac{\mathrm{d}R_2}{\mathrm{d}\tau} = -(c_2 + \Delta_{2,1}R_1{}^2 + \Delta_{2,2}R_2{}^2)R_2, \quad (5.14c)$$

$$R_2\frac{\mathrm{d}\Phi_2}{\mathrm{d}\tau} = -(\sigma_2 - \Gamma_{2,1}R_1{}^2 - \Gamma_{2,2}R_2{}^2)R_2. \quad (5.14d)$$

The essential difference with the system for real $\Gamma_{k,m}$ is that one mode can now excite others. More specifically, if $\Delta_{2,1} < 0$, the first mode can destabilize the global attractor $R_2 = 0$ to which the second mode would otherwise decay for $Z_2 = 0$. If one of the diagonal elements $\Delta_{k,k}$ is negative, then mode k causes positive feedback to itself and will grow without bound, thus escaping the validity of the present model. In that case higher-order terms should be taken into account. Positive $\Delta_{k,k}$ provide an additional damping mechanism, manifested at high values of R_k. In order to investigate the possible effects of the interaction terms $\Delta_{k,m}$, the model (5.14) was run (in Cartesian coordinates) using DsTool, with parameters as in figure 5.6, except for $Z_2 = 0$, $\Delta_{1,1} = \Delta_{1,2} = \Delta_{2,2} = 0$ and $\Delta_{2,1} = -5$. A periodic orbit, period doublings and chaotic behaviour were found. The mechanism for the chaotic behaviour is similar to the two-mode mechanism in the previous subsection, when two modes are excited externally: both modes influence each others eigenfrequency, hence causing continuous regime changes towards the bent resonance curves. The difference is that the second mode is internally excited by the first one. The external tide ζ_e is a single sinusoid.

The previous paragraph considered the influence of new interaction terms in the amplitude equations due to Coriolis effects. Another possible source of additional terms is if the non-resonance conditions (4.14d) for the derivation of the Landau equation are violated. In fact, the intermediate equation (4.29) shows the nonlinear terms in the amplitude equations without assuming the absence of third-order resonances. Many of those terms also allow for the possibility of one mode exciting (or rather destabilizing) another. Although the non-resonance conditions (4.14d) are fulfilled generically, there may be symmetrical situations causing some **internal resonances** between eigenmodes to occur. For a rectangular basin the eigenfrequencies are $\omega_j = (j + \frac{1}{2})\sqrt{\gamma}\pi$ (section 4.4), whence second-order resonances are clearly absent, but $\omega_k = \omega_l + \omega_m - \omega_n$ holds whenever $k = l + m - n$. The resulting extra terms in the amplitude equations may also lead to complicated behaviour in the presence of only one harmonic component in the external tidal forcing.

Several mechanisms leading to chaotic behaviour in co-oscillating tidal basins have been discussed in this and in the previous subsection. It is not predicted to always occur in all real basins, but would be found under several types of specific conditions on the external forcing and the geometry of the basin. A mathematically rigorous proof of the existence of chaotic dynamics has been elaborated for the first case (two components in near resonance with a single mode) only, although there are clear indications that it occurs in many more situations. We conclude this section with the observation that there are several mechanisms that could in principle lead to chaotic tidal dynamics.

5.6   Conclusions and discussion

In the preceding chapter the depth-averaged two-dimensional shallow-water equations (4.1) were investigated in a small-amplitude, strongly resonant limit to obtain the Landau equations (4.30) that govern the modulation of the amplitudes of the linear eigenmodes of the basin. Truncation of the nonlinear dynamical system (4.30), which describes the behaviour of all amplitudes, to a finite number of modes is natural, see section 5.2. Truncating to a single mode, one finds that the effective eigenfrequency of the eigenmode is changed with increasing amplitude. This causes bending of the response curve, the response amplitude as a function of forcing frequency, leading to multiple equilibria: under the same external conditions the basin can be in either a high- or low-amplitude regime, depending on the history of the sea state within the basin. Sudden regime changes may occur under slight changes of the external conditions. Moreover, if the forcing tide at sea is quasi-periodic, i.e. consisting of multiple constituents such as the lunar M_2 and solar S_2 components, chaotic behaviour of regime changes is possible. Truncating at two modes, interactions between modes come into play. The response is *not* a simple superposition of the results for one mode. Interaction between modes alters the region in parameter space for which resonance occurs; it leads to Hopf bifurcations, periodic orbits and chaos.

Several mechanisms leading to chaos under different circumstances were described in section 5.5. Moreover, many other nonlinear processes lead to the same amplitude equations: the truncation of (4.30) to one mode leads to (5.3) and (5.4), which are the same equations as those found by Maas (1997), Maas & Doelman (2002) and Doelman *et al.* (2002) for the amplitude of the Helmholtz mode in an almost-enclosed basin, where the nonlinearity results from non-uniform hypsometry, i.e. an increase of the wet area with rising tide as is the case for a sloping bottom and tidal flat systems. The nonlinear effect due to the change in cross-sectional area of the inlet channel as a function of the water level, described in Miles (1981), leads to similar results. Actually, a change in cross-sectional area of the inlet channel is equivalent to a hypsometry change. Both cause a nonlinear relationship between the current through the channel and the resulting water-level change in the basin. In summary, advection and continuity (which are the nonlinear processes in the shallow-water equations (4.1)), changing cross-section of the inlet channel (Miles, 1981) and non-uniform hypsometry (Doelman *et al.*, 2002) all lead to similar results. The fact that many nonlinear processes lead to the same description suggests that (4.30) is a universal equation whose coefficients $\Gamma_{k,m}$ are determined by many contributions, possibly including ones that have not yet been identified. Whenever the effective eigenfrequencies of the tidal resonator

depend on the amplitudes, the generic behaviour of the system would be governed by (4.30).

Although the terminology used in this thesis and the scaling assumptions following (4.3) are appropriate for basins with megatides in particular, the analysis performed here may be relevant for secondary undulations as well. In that case the primary tidal oscillation period is much longer than that of the basin's eigenmodes. Because the latter determine the time scale of the model (4.4), (4.5), the tidal oscillation would be incorporated as a slow change of the reference water depth $D^{(0)}$. The calculations become much more involved because one has to include the effect of the tidal change in water depth on the eigenmodes of the basin. In principle the analysis can be performed and is expected to introduce parametric forcing terms just as in Maas & Doelman (2002, section 5) for the simpler Helmholtz case. Chaotic dynamics can be expected under certain conditions for this case as well. Another mechanism that would lead to chaos occurs if a zero-frequency eigenmode is present. Just like the Earth's rotation and non-trivial third-order resonances, it may trigger internal excitation of modes that are not excited by the tide at sea directly. The presence of multiple modes with non-zero amplitude can lead to chaotic behaviour through their interaction described in this chapter, cf. section 5.5 in particular.

Predictions of tides are often based on tidal harmonics, the amplitudes and phases of which are constant in linear theory, describing the tidal signal as a superposition of harmonic components. In many cases this works quite well, but there are clearly deviations. They are usually attributed to meteorological disturbances. The observational challenge is to distinguish between meteorological effects and internally induced deviations (Vittori, 1992). Some first steps using an approach apt for chaotic systems have been made in Frison *et al.* (1999). They state that the tidal signal becomes increasingly irregular when progressing into complicated basins. This is consistent with our findings, attributing chaotic behaviour to nonlinear resonance phenomena. However, note that their work is on the time series of *in situ* water levels themselves, whereas in this work the amplitudes of eigenmodes are considered. More specifically, we suggest to consider the time series describing the evolution of harmonic constants, as was done on a year to year time scale by Doodson (1924). He identified three perturbations on the harmonic constants for St. John, Bay of Fundy and Bombay, two of which he found to be related to astronomical forcing and one of which remained unaccounted for. More recently Gutiérrez *et al.* (1981) studied fluctuations of the harmonic constants for Puntarenas (situated at the Gulf of Nicoya, Pacific coast of Costa Rica) and Trieste (North Adriatic Sea) and found that they do not result from non-perfect selectivity of the analysis. They condensed the variation into a single value for its variance however; we have no knowledge of studies in which time series of harmonic constants have been tested for chaotic dynamics. We hope that our findings may spur further data investigation of this kind, both on tidal records (on a fortnightly time scale) and on secondary undulations (on a daily time scale). Because the latter are relatively unimportant for the water level, they have been investigated less extensively until recently, but their influence on currents can be considerable and irregular behaviour of secondary undulations had already been reported at the beginning of the twentieth century, see Honda *et al.* (1908) and Nakano (1932). Clear evidence of nonlinearity would be the occurrence of sudden regime changes and hysteresis: the response of the basin depending on its history, disturbances having lasting effects after the decay of transient behaviour. Sudden changes of the tidal regime in

the past may be detected from their geological signature (Oost, 1995).

Apart from reinvestigating time series of observed water levels, the nonlinear mechanisms can also be studied by means of laboratory experiments. Elaborating on the work by Maas (1997) on the nonlinear effects due to non-uniform hypsometry in an almost-enclosed basin, a laboratory tank has been created to simulate a Helmholtz resonator. The results in chapter 3 validating Lorentz's linearisation principle for quadratic friction were obtained from preliminary measurements with this tank. The experimental results on the nonlinear effects are discussed in the next chapter of this thesis. Bending of the response curves and multiple equilibria were observed, although other processes than the hypsometry also play an important role in causing this.

Acknowledgments

Chapter 6

Experimental evidence for multiple equilibria

Laboratory experiments have been performed with a laboratory tank to study the Helmholtz response of a semi-enclosed tidal basin co-oscillating with an adjacent sea. As opposed to the well-known effect of distortion of the tidal curve due to the generation of overtides, we focus on nonlinear effects on the response curve: amplification factor and phase difference between basin and sea as a function of forcing frequency and amplitude. Motivated by the results in chapter 5, the aim of this work is to investigate whether for specific parameter settings nonlinear processes result in the possibility of multiple tidal regimes in the basin: different responses in the basin under the same forcing conditions at sea, the actual state of the basin depending on initial conditions c.q. its history. Consequently, sudden regime changes may occur, even in a chaotic fashion according to model studies. A number of different physical mechanisms have been identified to lead to the same generic behaviour, among which non-uniform hypsometry (if the basin area depends on tidal phase), advective accelerations and the feedback of water-level changes on depth-averaged mass flux. The main conclusion of this chapter is that, although non-uniform hypsometry is not significant at the laboratory scale, multiple equilibria do occur with a crucial role played by the shape of the inlet between basin and sea. The precise nature of the physical mechanism responsible for the observed effect is still open to further research and a discussion of possible mechanisms is included.[1]

6.1   Introduction

Although direct tidal forcing by the gravitational forces from the moon and the sun is relatively weak (0.27 m, 0.13 m amplitude respectively), tidal motion up to 8 m (Bay of Fundy) amplitude occurs due to resonance in coastal basins co-oscillating with an adjacent sea. This resonance phenomenon is successfully explained with linear models (reviewed in e.g. Defant, 1961; Raichlen, 1966; LeBlond & Mysak, 1978) which provide us with response curves (amplification of the tide as a function of forcing frequency) of particular tidal basins.

---

[1]This chapter is based on the paper *"Experimental evidence of multiple equilibria in a tidal resonator"* by Guido M. Terra, Willem Jan van de Berg and Leo R.M. Maas, in preparation.

Nonlinear effects arise due to many mechanisms, such as advective acceleration, water-level feedback on mass fluxes, non-uniform hypsometry (dependence of basin area on the water level as in the case of tidal flats) and quadratic friction. In observational studies nonlinear effects manifest themselves in the generation of higher harmonics (Gallagher & Munk, 1971; Parker, 1991b) distorting the tidal curve from purely sinusoidal to an asymmetric curve. However, from a dynamical systems point-of-view nonlinear terms may also cause more complex behaviour. Indeed, there have been reports of drifting harmonic 'constants' (Doodson, 1924; Gutiérrez et al., 1981) and even chaotic tidal behaviour (Vittori, 1992; Frison et al., 1999). In this work the focus is on changes in a basin's response curve.

An almost-enclosed basin, which is connected to an adjacent sea through a narrow inlet only, constitutes a fairly simple example of a tidal resonator. The first eigen-mode of such a basin is almost uniform within the basin since its tidal wavelength is much larger than the dimensions of the basin. As such, this *Helmholtz mode* can be described by an ordinary differential equation for the water level inside the basin. Miles (1981) extended his linear theory for the Helmholtz mode (Miles, 1971) to include the effect of changing channel cross-section with water level. This shortens the high water period and increases the low water period. Moreover, the total period of free oscillations increases with amplitude and the response curve is tilted. As a result *multiple equilibria* are found: for the same tidal signal at sea, different tidal response amplitudes in the basin are possible. Consequently hysteresis may occur under changing exterior conditions. Elaborating upon the work of Green (1992), it was shown that non-uniform hypsometry has a similar but opposite effect on the tidal response: reduction of the low water period and lengthening of the high water period (Maas, 1997). In the limit of small friction and near resonance, he found multiple equilibria as well. Moreover, if the tidal signal at sea is not purely sinusoidal but consists of a couple of nearly resonant components (such as M_2 and S_2, causing the spring-neap tidal cycle) chaotic behaviour of the response amplitude was shown to occur (Maas & Doelman, 2002; Doelman et al., 2002). By performing a similar weakly nonlinear analysis on the depth-averaged shallow water equations, their results can be shown to apply to more general basins as well and not be restricted to Helmholtz basins with non-uniform hypsometry (chapters 4 and 5). In that case the nonlinear effects stem from advective acceleration and water-level feedback on mass fluxes. In fact, many nonlinear mechanisms lead to the same weakly nonlinear results. The occurrence of multiple equilibria is a key ingredient in this route to chaos. This chapter describes experiments that have been performed in order to find multiple equilibria in a real (though on a small experimental scale) tidal resonator of the Helmholtz type.

The experimental setup is described in section 6.2. Although this work was originally motivated by the results on the effect of hypsometry in Helmholtz basins, the weakly nonlinear results appear to be of generic nature applicable to several nonlinear physical mechanisms. Still, the introduction to the theory in section 6.3 is restricted to the relatively simple Helmholtz case in which hypsometry is causing nonlinear effects. Discussion of other physical mechanisms that may lead to the same phenomena is postponed until section 6.5, after having described the experimental results in section 6.4.
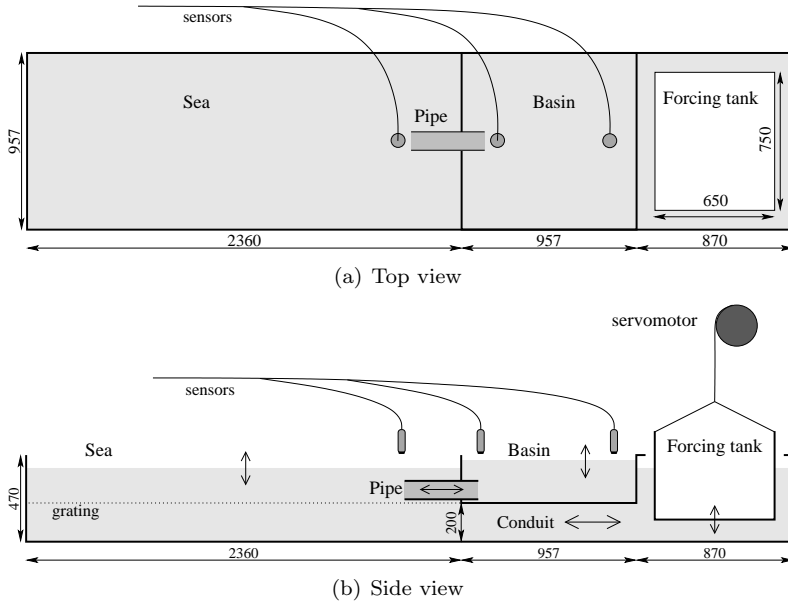
(a) Top view

(b) Side view

Figure 6.1: Sketch of the experimental setup, dimensions in mm are indicated. The forcing tank is set into motion by a servomotor. The water expelled by the tank moves through the conduit underneath the 'basin' area to the 'sea'. The tidal signal thus generated at sea, propagates into the basin through a completely submerged pipe. The water-level elevation is measured by acoustic sensors at different positions. The sensor positions indicated in the figure represent the standard configuration. Because the tide in the basin is nearly uniform, the measurements for the sensors in the basin are virtually the same.

6.2   Experimental setup

A sketch of our experimental setup is shown in Fig. 6.1. The area of interest is the 'basin' with a size of 957×957 mm. A completely submerged pipe is used to connect the basin to the forcing tide at 'sea'. In this way, its cross-section O does not depend on water-level elevation ζ, in contrast to an open channel which would introduce additional nonlinear effects (Miles, 1981). A number of different pipes have been used, with lengths between 300 and 550 mm and diameters of 75–95 mm. The water depth at rest ranged 15–22 cm above the bottom of the basin, making sure that the pipe remained completely submerged, in which case it has no influence the measurements. A forcing tank is immersed in the water and is lifted and lowered by a properly counterbalanced servomotor. The control signal can be generated by the computer. The applied forcing frequencies varied from 0.02 Hz to 0.25 Hz. In principle the forcing signal may consist of many frequency components, but harmonic forcing only is considered in this chapter. The water expelled by the forcing tank, moves through the conduit underneath the basin area towards the sea. A grating was inserted in order to help the water level at sea to be uniform, but it did not prevent the occurrence of a standing wave: depending on the forcing frequency, amplitudes are higher at the far end of the sea. The amplitude of the control signal is adjusted
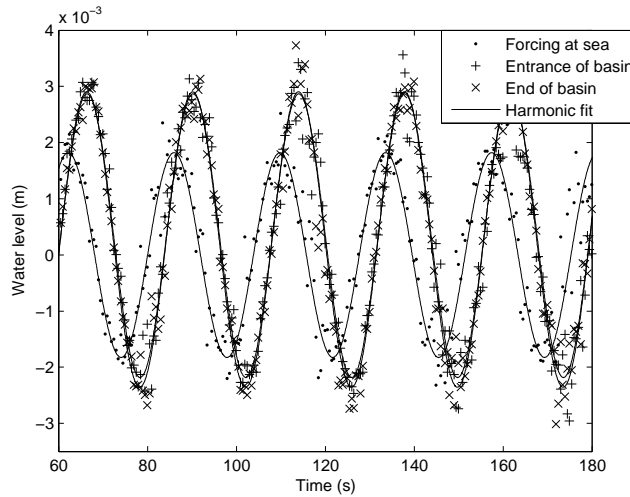
Figure 6.2: Sample time series of measurements at forcing frequency 0.0420 Hz and forcing amplitude approximately 2 mm, for uniform hypsometry with $A_0 = 0.916$ m^2, $L = 441$ mm, $O = 4.6 \cdot 10^{-3}$ m^2. Dots indicate measurements from the sensor at the seaward pipe entrance, pluses and crosses indicate measurements at the entrance and end of the basin, respectively. Solid curves show harmonic fits to the respective time series. The two curves inside the basin are nearly indistinguishable, consistent with a Helmholtz mode of uniform basin tide.

to obtain the desired forcing amplitude at the mouth of the basin (cf. the discussion at the end of this section), so this has no influence on the measurements. Acoustic sensors are used for nonintrusive measurements of water-level elevation. They are located above the tank and emit an acoustic signal at 300 kHz down to the water surface and measure the return time of the reflected signal, like an echo sounder. Their resolution is 0.36 mm, the standard deviation of the noise is similar. Significant outliers occur and were dismissed from the analysis if they differ by more than 3.5 times the standard deviation from a harmonic fit to the time series.

Figure 6.2 shows time series of laboratory experiments using the full basin area ($A_0 = 0.916$ m^2), a straight pipe ($L = 441$ mm long) with circular cross-section ($O = 4.6 \cdot 10^{-3}$ m^2). At least at three locations the water level was measured, above the seaward and basin end of the pipe and at the end of the basin. In correspondence with a Helmholtz mode inside the basin the water level was found to be almost uniform. Although the amplitude is usually somewhat higher at the end of the basin, the phases correspond very well. The time series were analysed by performing a harmonic fit with the dominant frequencies, determined from the Fourier power spectrum. Response curves are determined by comparing the amplitudes and phases of the forcing frequency component both for the sensor at sea and inside the basin.

No dissipators have been installed at the sidewalls of the sea. Raichlen & Ippen (1965) warn that consequent reflections have a dramatic effect on the response curves (amplification factor and phase difference between response in the basin and forcing at sea as a function of forcing frequency). They define the amplification factor as the ratio of the tidal response amplitude in the basin over the amplitude at the seaward

entrance *if the basin were closed*. Indeed, radiation damping effects changing the actual tidal signal at the seaward entrance, are quite different in a finite reflective sea than in a semi-infinite reflectionless sea. We however choose to correct the motion of the forcing tank such that the amplitude at the seaward entrance is the same for all frequencies and define the amplification factor as the ratio of the response amplitude in the basin over the amplitude at sea *with the basin connected to it*. This boils down to eliminating the effect of radiation damping and circumvents the problems mentioned by Raichlen & Ippen (1965).

6.3   Theory

By considering the momentum and mass balance a simple model can be derived describing the Helmholtz mode of a basin, the dimensions of which are assumed to be much smaller than the tidal wavelength $\lambda = 2\pi\sqrt{gH}/\omega$ (where g is the gravitational acceleration, H the water depth at rest and ω the angular forcing frequency). In that case the water level in the basin will rise and fall almost uniformly and can be described by a single parameter ζ, the elevation relative to the still water level. Water flows into the basin through the pipe of length L, cross-section O, into the basin with horizontal area A. In the case of non-uniform hypsometry the basin area $A = A(\zeta)$ depends on the water level: at low tide the wet area is less than at high tide when tidal flats are flooded. All dynamics are concentrated in the connecting pipe, where the elevation difference between sea and basin drives the flow, balanced by the inertia of the water in the channel and dissipation by friction/flow separation. Bottom friction is commonly described by Chezy's law $(c_D/H)\,|u|u$, with drag coefficient $c_D \approx 0.0025$ determined empirically (Parker, 1991a). The head loss due to flow separation is parameterized by $(f/L)\,|u|u$ (Hayashi *et al.*, 1966; Terrett *et al.*, 1968; Mei *et al.*, 1974; Maas, 1997) and differs only in the formulation of the coefficient; f has to be determined empirically as well. For our configuration $f \approx 1$ appears to be a good estimate (cf. section 3.4 or 6.4.1). The equations for the momentum and mass balance are:

$$\frac{\mathrm{d}u}{\mathrm{d}t} \;=\; \frac{g}{L}\,(\zeta_e - \zeta) - \frac{\tilde{f}}{L}\,|u|\,u, \tag{6.1a}$$

$$A(\zeta)\,\frac{\mathrm{d}\zeta}{\mathrm{d}t} \;=\; O\,u, \tag{6.1b}$$

where $\zeta_e = \alpha_e \cos(\omega t) = \mathrm{Re}\left[\alpha_e\,\mathrm{e}^{\mathrm{i}\omega t}\right]$ is the prescribed elevation at sea. The head loss coefficient $\tilde{f}/L$ is considered to include friction with sidewalls as well ($\tilde{f}/L = f/L + c_D/H$, where "$H$" should be related to the radius of the pipe). Head loss due to flow separation seems to be more important here. As in the experiment radiation damping is not modelled here explicitly but is assumed to be already incorporated in ζ_e. In analysing the experimental results we will also compare the measurements inside the basin with the forcing signal at sea as it is measured simultaneously.

   In section 6.3.1 the Helmholtz model (6.1) with uniform hypsometry ($A(\zeta) = A_0$ independent of ζ) when friction is the only nonlinear term will be dealt with by Lorentz's linearization procedure. In section 6.3.2 the strong resonance limit for weak friction and forcing frequency ω close to the eigen- (Helmholtz) frequency $\omega_0 = \sqrt{gO/(A_0L)}$ is investigated for linearized friction. The nonlinear effect of non-uniform

hypsometry is used to illustrate the generic results of the weakly nonlinear analysis (in Doelman *et al.*, 2002, and chapters 4 and 5 in this thesis as well) in a simple way. Finally, the two are combined to obtain a correction to the quasi-linear theory from section 6.3.1 consistent with the strong resonance limit in section 6.3.2.

6.3.1   Quasi-linear (Lorentz's) theory

In order to overcome problems with the nonlinear friction term in (6.1), Lorentz (1922) proposed to replace it by a linear term ru, with effective linear friction coefficient r to be determined. In the case of uniform hypsometry the system (6.1) becomes linear and the response will be of the form $\zeta = |\alpha| \cos(\omega t + \varphi) = \mathrm{Re}\left[\alpha\, e^{i\omega t}\right]$, where $\alpha = |\alpha| e^{i\varphi}$, and consequently $u = -(A_0/O)\,\omega|\alpha|\sin(\omega t + \varphi)$. Lorentz's energy principle states that the energy dissipation per tidal cycle should be the same for both formulae: $\langle ru^2 \rangle = \langle (\tilde{f}/L)\,|u|u^2\rangle$, in which $\langle \cdot \rangle$ denotes averaging over a tidal cycle. Evaluation of the corresponding integrals leads to

$$r = \nu_0\,\omega|\alpha|, \quad \text{with } \nu_0 = \tfrac{8}{3\pi}\frac{\tilde{f}A_0}{OL}, \tag{6.2}$$

i.e. effective friction increases linearly with tidal amplitude in the basin. This leads to the dispersion (frequency response) relation

$$(\omega_0{}^2 - \omega^2)\,\alpha + i\,\nu_0\,\omega^2\,|\alpha|\alpha = \omega_0{}^2\,\alpha_e, \tag{6.3}$$

which can be solved for the amplification factor to find the frequency response function

$$\frac{|\alpha|}{\alpha_e} = \sqrt{\frac{\sqrt{(1 - (\frac{\omega}{\omega_0})^2)^4 + 4\nu_0{}^2(\frac{\omega}{\omega_0})^4\alpha_e{}^2} - (1 - (\frac{\omega}{\omega_0})^2)^2}{2\nu_0{}^2(\frac{\omega}{\omega_0})^4\alpha_e{}^2}}, \tag{6.4}$$

which can be combined with (6.3) to find the phase lag $\varphi \in (-\pi, 0)$ as well, from $\varphi = \arccos((1 - (\frac{\omega}{\omega_0})^2)\frac{|\alpha|}{\alpha_e})$.

6.3.2   Weakly nonlinear theory for strong resonance

Elaborating upon the work of Green (1992), Maas (1997) showed that non-uniform hypsometry $A(\zeta)$ in a Helmholtz basin leads to a reduction of the low tide period and an increase of the high tide period. In order to illustrate the analysis of possible nonlinear effects on the response curves, it will be discussed here as a relatively simple example, although the analysis in chapter 4 shows that it is applicable to more general basins as well. A mathematical investigation of (6.1) with linearized friction and non-uniform hypsometry was carried out in the small-amplitude strongly resonant limit (Maas & Doelman, 2002; Doelman *et al.*, 2002). Introducing the asymptotic parameter $\varepsilon \ll 1$ as a measure for the assumption of small amplitudes $\tilde{\zeta} = \mathcal{O}(\varepsilon)$, weak linear friction $\tilde{r} = \mathcal{O}(\varepsilon^2)$ and nearly resonant $\omega = \omega_0(1+\varepsilon^2\sigma)$ small forcing $\tilde{\zeta}_e = \mathcal{O}(\varepsilon^3)$, where tildes are used to denote rescaled dimensionless variables (for details, see Maas, 1997), a dynamical system was derived by averaging methods describing the (slow) evolution of the response amplitude and phase. In this strongly resonant limit, the resonance peak is high $\mathcal{O}(\varepsilon^{-2})$ and narrow $\mathcal{O}(\varepsilon^2)$. The dispersion relation describing it, after translating their results back to dimensional variables and using the effective friction coefficient r from Lorentz's procedure, is given by

$$(\omega_0 - \omega)\,\alpha + \omega_0\Gamma|\alpha|^2\alpha + i\,\frac{1}{2}\nu_0\,\omega_0\,|\alpha|\alpha = \frac{1}{2}\omega_0\,\alpha_e, \tag{6.5}$$
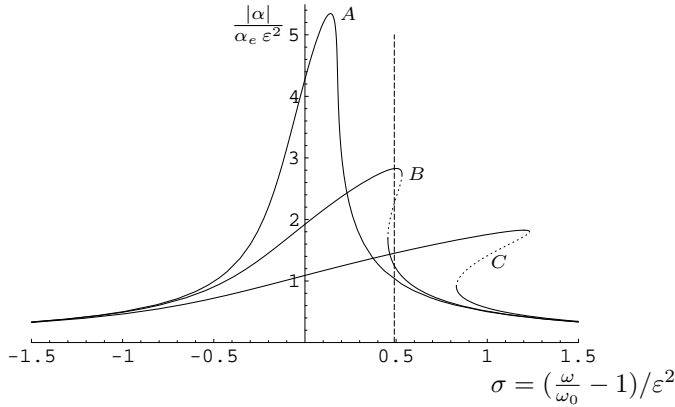
Figure 6.3: Frequency response curves according to (6.5) for fixed friction parameter ν_0 and hypsometry coefficient Γ and increasing forcing amplitudes for curves A, B and C, respectively. Solid curves denote stable branches, the dotted curves are unstable. A dashed vertical line at $\sigma = 0.49$ indicates that multiple equilibria are found under certain conditions.

in which $\Gamma = \frac{1}{16A_0}\frac{\mathrm{d}^2 A}{\mathrm{d}\zeta^2}|_0 - \frac{7}{24A_0{}^2}(\frac{\mathrm{d}A}{\mathrm{d}\zeta}|_0)^2$ is a coefficient resulting from the non-uniform hypsometry term. The subscript $|_0$ expresses that the respective value should be calculated for the situation at rest ($\zeta = 0$). Note that (6.5) is applicable to many more processes, see the discussion in section 6.5.1. The hypsometry term causes the response curve to tilt, see figure 6.3, because the effective eigenfrequency depends on the amplitude in this case, with $\Gamma|\alpha|^2$ being the relative change of the effective eigenfrequency. As indicated in the figure, this can lead to multiple equilibria: different response regimes are possible under the same forcing conditions. At the indicated forcing frequency (dashed line), with medium forcing amplitude (curve B), three steady states are found, one with relatively high amplification and one with less amplification. The middle one is unstable hence will not occur in practice. Consequently sudden regime changes will occur if the forcing conditions change such that the present branch is not a solution anymore. When conditions subsequently return to the original situation, the system will remain in the newly found regime and does not return to the original response (hysteresis). Moreover, Maas & Doelman (2002) and Doelman *et al.* (2002) showed that the regime changes may occur *chaotically* under continuously evolving forcing conditions.

Clearly, there are some major flaws in this picture. For $\omega \downarrow 0$ the amplification factor should tend to 1, because for very slow oscillations the basin and sea simply serve as communicating vessels. However, $\omega = 0$ is not special in (6.5), because of the scaling which is designed to apply near resonance $\omega \simeq \omega_0$. We should consider the limit $\sigma \to -\infty$, in which case the amplification tends to zero, because the weakly nonlinear theory zooms in on an allegedly very high resonance peak $\mathcal{O}(\varepsilon^{-2})$ such that 1 and 0 are indistinguishable in this limit. As a consequence, (6.5) by itself is inadequate to describe the results of the experiments, for which the resonance is not infinitely strong.

6.3.3   Heuristic incorporation of weakly nonlinear limit within quasi-linear theory

In order to obtain a theory with which the laboratory measurements can be compared, the weakly nonlinear results for the strong resonance limit must be incorporated within the quasi-linear theory for finite amplitude from section 6.3.1. The combined theory should satisfy the restriction that it *a)* equals (6.3) in the absence of nonlinearity ($\Gamma = 0$), *b)* reduces to (6.5) for $\omega \to \omega_0$, *c)* implies amplification factor $|\alpha|/\alpha_e \to 1$ for $\omega \downarrow 0$ and $|\alpha|/\alpha_e \to 0$ for $\omega \to \infty$.

Dividing (6.3) by $2\omega_0$ one can see (6.5), with $\Gamma = 0$, emerging from (6.3) by taking the limit $\omega \to \omega_0$ except in the difference term $\omega_0 - \omega$. Reverting the process, multiplying (6.5) by $2\omega_0$ to

$$2\omega_0(\omega_0 - \omega)\,\alpha + 2\omega_0{}^2\Gamma|\alpha|^2\alpha + \mathrm{i}\,\nu_0\,\omega_0{}^2\,|\alpha|\alpha = \omega_0{}^2\,\alpha_e,$$

one regains (6.3) with an additional term $2\omega^2\Gamma|\alpha|^2\alpha$ upon replacing $2\omega_0$, $2\omega_0{}^2\Gamma$ and $\nu_0\omega_0{}^2$ by $\omega_0 + \omega$, $2\omega^2\Gamma$ and $\nu_0\omega^2$ and leaving the right-hand side as it is. Although restriction *a)* confines the finite resonance result for the terms that also occur in (6.3), the additional 'hypsometry' term could be anything with the correct limiting behaviour for $\omega \to \omega_0$. The restriction *c)* requires the 'hypsometry' term to vanish for $\omega \downarrow 0$. In fact, every combination $2\omega^n\omega_0{}^{2-n}\Gamma|\alpha|^2\alpha$ with $n > 0$ would do, but $n = 1, 2$ are the most likely choices in view of the derivation. Because the resulting equation is more easily solved for ω^2 as a function of $|\alpha|$ if we choose $n = 2$, we use

$$(\omega_0{}^2 - \omega^2)\,\alpha + 2\omega^2\Gamma|\alpha|^2\alpha + \mathrm{i}\,\nu_0\,\omega^2\,|\alpha|\alpha = \omega_0{}^2\,\alpha_e \qquad (6.6)$$

as the simplest combined dispersion relation for finite resonance with nonlinearity. The experimental results in section 6.4 will be compared with this equation.

6.4   Results

In this section the response curves for a number of cases with different pipes and basin area are presented. First measurements with full basin area without hypsometry are shown as reference case for which quasi-linear theory (6.3) applies. Next, the influence of non-uniform hypsometry is investigated by introducing artificial 'tidal flats'. Its effect on the response curve appears not to be significant compared to the width of the resonance peak due to friction. Multiple equilibria were found when introducing smooth pipe ends and reducing the basin area in order to reduce the effect of friction and are discussed in section 6.4.3. The smooth shape of the pipe ends appears to be the key difference in section 6.4.4 and the section is concluded showing the dependence on the basin area.

6.4.1   Quasi-linear case: straight pipe entrance

As a reference, measurements were performed with uniform hypsometry, using the full basin area ($A_0 = 0.916$ m^2) with vertical sidewalls and a straight pipe ($L = 441$ mm) with circular cross-section ($O = 4.6 \cdot 10^{-3}$ m^2). The quasi-linear theory according to (6.4) has been fitted to the measurements minimizing the least square error in the complex α/α_e-plane. Because the effective pipe length differs from the actual
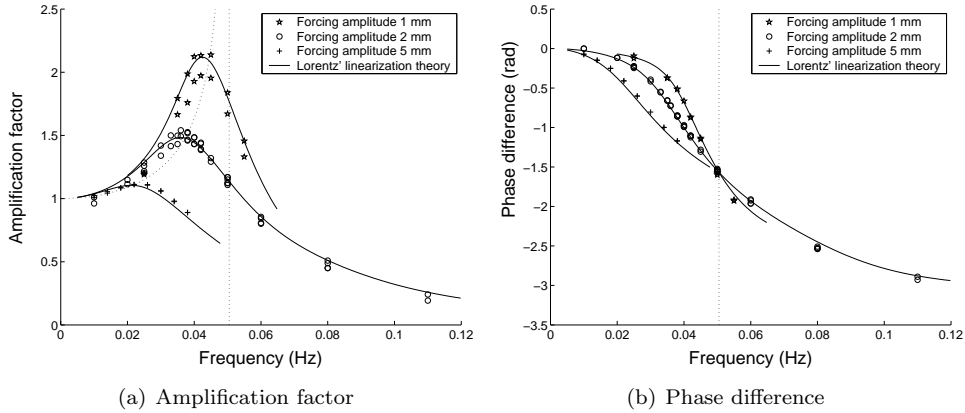
(a) Amplification factor

(b) Phase difference

Figure 6.4: Response curves: amplification factor $\frac{|\alpha|}{\alpha_e}$ and phase lag φ between the tide at sea and in the basin as a function of forcing frequency, for the same configuration as in figure 6.2. Three series of measurements with forcing amplitudes $\alpha_e \approx 1, 2, 5$ mm are shown, for each of which results for two sensors in the basin have been obtained. Slight amplitude differences between both basin sensors can be noted, in particular at 1 mm forcing amplitude. Solid curves show the fit to Lorentz's theory (6.4). The Helmholtz frequency $\omega_0 = 0.0505$ Hz is indicated by a dotted vertical line. Note that one fit is used to describe all three curves. Apparently the decrease of the resonator's quality is adequately described by Lorentz's linearization theory.

pipe length due to the added mass effect it has to be determined empirically from the apparent eigenfrequency of the basin. The same holds good for the head loss parameter $\tilde{f}$. Therefore, ω_0 and ν_0 are used as fitting parameters. The curves shown in Fig. 6.4 are for the best fit with $\omega_0 = 50.5 \pm 0.9 \cdot 10^{-3}$ Hz $= 0.317 \pm 0.006$ rad s^{-1}, $\nu_0 = 374 \pm 9$ m^{-1}. So the effective pipe length $L_{\text{eff}} = 48.9 \pm 1.7$ cm is 4.8 cm longer than the actual length. Furthermore, $\tilde{f} = 0.97 \pm 0.02$ has the same order of magnitude as Ito (1970) found for motion on real geophysical scale ($f \approx 1.5$) by comparing the results of his numerical model with tidal data after the partial closure of the entrance of the Port of Ofunato. Hence our experiments corroborate his numerical/empirical value. So, although fitting is involved to determine the precise value of ω_0 and ν_0, they do not differ much from their rough independent estimate. Moreover, the decrease of the resonator's quality (the height and sharpness of the resonance) due to increased effective friction with increasing tidal amplitude, is explained well by the theory. Note that the phase lag is $-\pi/2$ for $\omega = \omega_0$ irrespective of forcing amplitude. This is in perfect correspondence with quasi-linear theory (6.3), but will be different if additional nonlinear effects become important in equation (6.6). See chapter 3 for a more extensive discussion on the validation of Lorentz's linearization procedure.

6.4.2   Non-uniform hypsometry

In order to measure the nonlinear effect of non-uniform hypsometry, artificial 'tidal flats' were introduced in the basin, see figure 6.5. The mean tidal curve was constructed by wrapping the measurements onto a single period subtracting an integer number of tidal periods (14.3 s in this case) from each time value. Figure 6.6 clearly
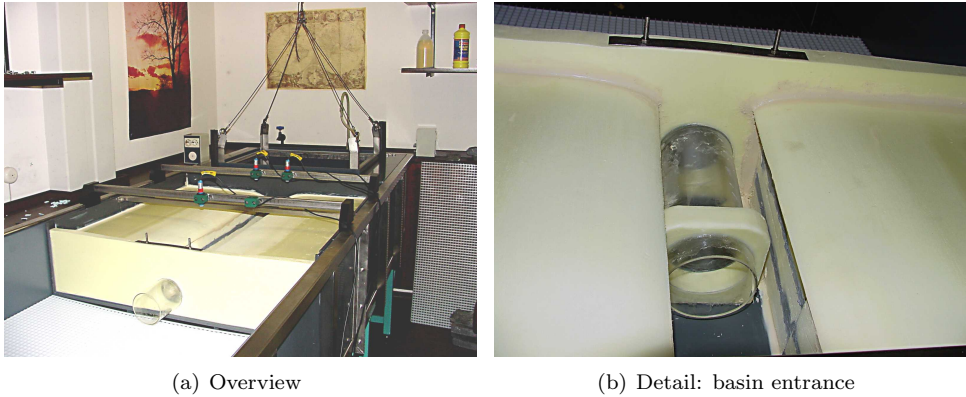
(a) Overview

(b) Detail: basin entrance

Figure 6.5: Pictures of the laboratory basin with 'tidal flats', to the left and right side of the main channel.

shows that the low tide period decreases and the high tide period increases because water spreads over a smaller or larger basin area, respectively. In principle one would expect this to be visible in the response curves as well, which should get tilted because of the dependence of the effective eigenfrequency on the oscillation's amplitude. However, the response curves for this basin with non-uniform hypsometry do not differ significantly from the ones shown in figure 6.4 for the basin with vertical sidewalls. The reason is that friction widens the response curves. Possible tilting of the response curves is invisible relative to the frictional width of the peaks.

The effect of non-uniform hypsometry increases if the difference between the basin area at high and low tide is larger, but the effective friction is smaller when tidal ranges are low (cf. section 6.4.1). Therefore, we tried to maximize the relative effect of hypsometry by decreasing the slope of the 'tidal flat', such that a small change in water level results in a large change in basin area. However, this leads to a number of small scale effects that destroy the uniform nature of the Helmholtz mode: cohesion and adhesion of the water to the slope causes a significant delay when wetting/drying the tidal flat. More importantly, because the water depth is increasingly small over the tidal flat when decreasing its slope, the tidal wave velocity and wavelength decrease. As a consequence there will be a phase lag between the tidal flat and the deeper part of the basin, contradicting the assumption of uniformity of the Helmholtz mode. This invalidates the model (6.1) and effectively leads to additional damping.

The effects of cohesion and adhesion are not likely to be important in large-scale natural basins. The decrease of the tidal wavelength can indeed be observed in natural tidal flats as well, although its effect may be diminished by the fractal nature of the tidal channel system (Cleveringa & Oost, 1999). In fact, this causes the total length of the water line to be much larger than with a straightforward construction as shown in figure 6.5. Consequently, the actual slope and in particular the water depth near the water line need not be that small to achieve large changes in basin area with small changes in water level. From a physical point of view, the gullies transport the water to and from the shoals, hence causing the tide to remain uniform, thus eliminating the damping effect of the phase differences between the water level in channels and above shoals.
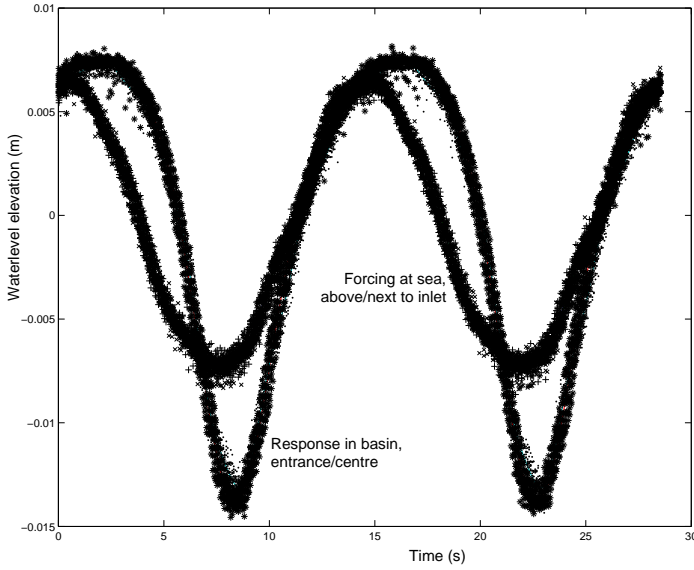
Figure 6.6: Tidal curve of measurements with tidal flats at forcing frequency 0.0700 Hz and forcing amplitude approximately 7 mm. The two curves measured at sea are indistinguishable. The two curves measured at different positions inside the basin are almost the same as well.

6.4.3 Multiple equilibria

In order to reduce the effect of friction, the basin area A_0 was reduced[2] (from 0.916 m^2 to 0.255 m^2) and smooth trumpet-shaped pipe ends (figure 6.9(b)) were introduced. Both pipe ends of increasing diameter are 145 mm long. With a straight part of 30 mm, 92.9 mm interior diameter, in between the total length of the pipe is 320 mm. Indeed the response curves are much higher and sharper in this case. Actually, although no artificial topography had yet been introduced, multiple equilibria were found. Apparently, another nonlinear effect is at play. A number of processes possibly explaining the observed phenomena, will be discussed in section 6.5.

Figure 6.7 shows the response curve found under these conditions at 1 mm forcing amplitude. It is different from figure 6.4 in that this curve tilts to the right. In particular the phase difference deviates from $-\pi/2$ at $\omega = \omega_0$, which is an indication of the influence of nonlinear effects as well. Indeed the response curve according to Lorentz's linearization theory (solid curve) fits less well in this case, whereas the (dashed) curve corresponding with the extended nonlinear theory (6.6) describes the global behaviour of the response curve much better. Multiple equilibria occur in a small but reproducible frequency range only, see figure 6.7(c). Note the gap in this figure in which phase differences between -2.6 and -2.5 do not occur because the corresponding branch of steady solutions is unstable. Although the formula (6.6) does predict multiple equilibria as well for Γ large enough, it apparently does not describe the system well enough to predict the correct parameter range, as it does not predict multiple equilibrium for the value of Γ that best fits the data. This may be caused

---

[2]This reduces the amplitude of currents through the pipe. Hence, due to the quadratic dependence of friction on the current, the effective friction decreases.

(a) Amplification factor

(b) Phase difference

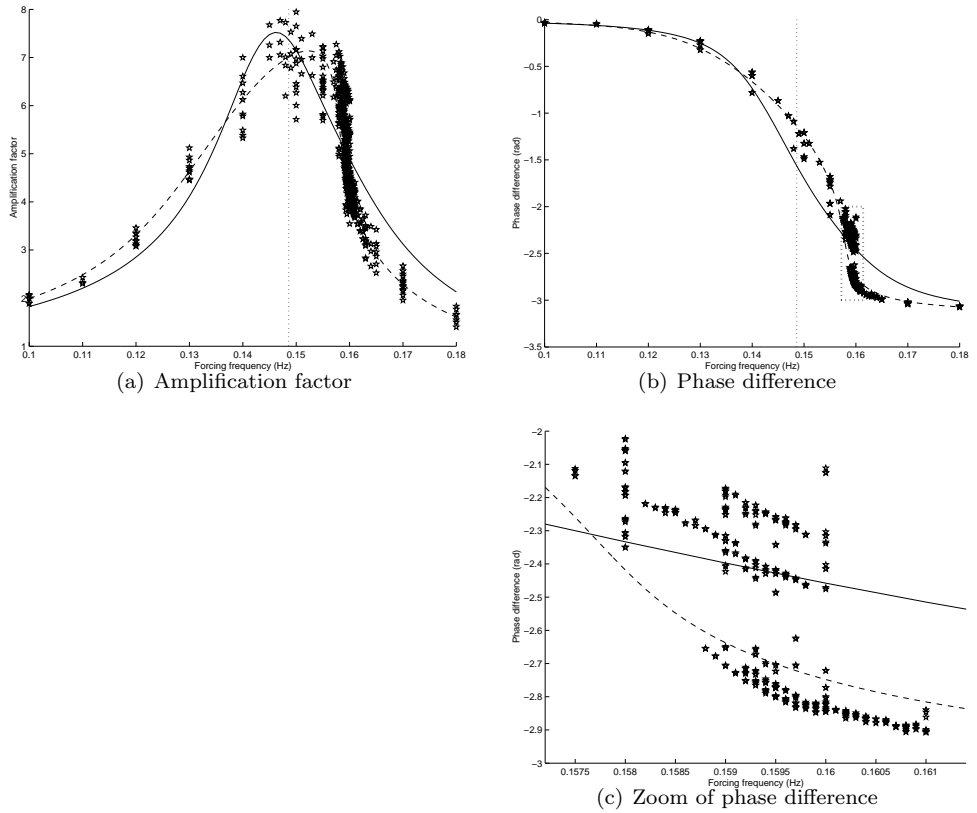
(c) Zoom of phase difference

Figure 6.7: Response curves: amplification factor and phase lag between the tide at sea and in the basin as a function of forcing frequency with forcing amplitude $\alpha_e \approx 1$ mm. Solid curves show the fit to Lorentz's theory (6.4) with parameters $\omega_0 = 0.149$ Hz (indicated by a dotted vertical line) and $\nu_0 = 19.4$ m^{-1}, whereas the dashed curves show the extended nonlinear theory (6.6) with parameters $\omega_0 = 0.140$ Hz, $\nu_0 = 15.1$ m^{-1} and $\Gamma = 1.63 \cdot 10^3$ m^{-2}. Figure 6.7(c) zooms in on the small frequency range (indicated by the box in figure 6.7(b)) for which multiple equilibria were found: the upper branch was followed when gradually increasing the forcing frequency, the lower branch corresponds with gradually decreasing frequencies. Because the results for both basin sensors are plotted together, the two branches are less clearly identified in figure 6.7(a), as the amplitude differences between the two sensor locations are comparable to the gap between the branches.
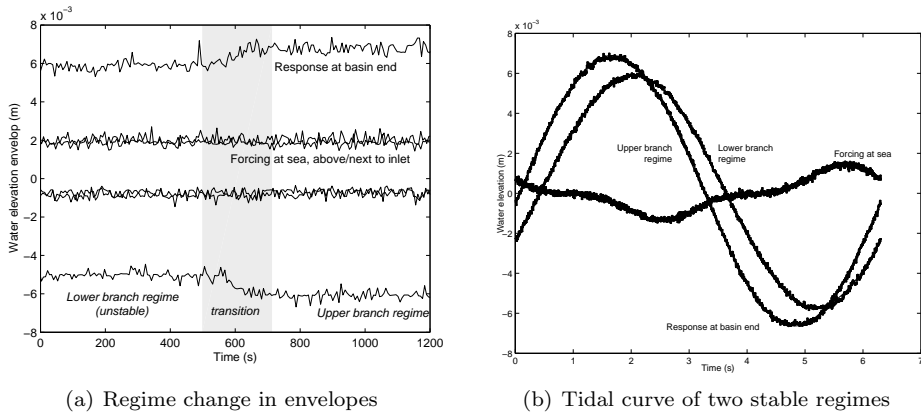
(a) Regime change in envelopes

(b) Tidal curve of two stable regimes

Figure 6.8: Illustrations of multiple equilibria: 6.8(a) Time series of the envelop of forcing at sea and response in the basin by plotting measurements of high and low tide. The forcing conditions remain at frequency 0.1592 Hz and amplitude 1 mm during the entire time series, but the response shifts to a higher amplitude regime. 6.8(b) Measured tidal curves of forcing at sea and two different stable response regimes under the very same forcing conditions. Forcing is at 0.1588 Hz frequency, 1 mm amplitude for both cases, but the response has a phase lag of 2.29 rad and amplitudes of 5.5–6.8 mm for the higher amplitude regime and a phase lag of 2.65 rad and amplitudes of 5.1–5.8 mm for the lower amplitude regime. Note that overtides are clearly present at sea but do not propagate into the basin.

by the fact that, having been derived from the small-amplitude limit near resonance, it captures the first order correction to the effective eigenfrequency only.

Tantamount to the presence of multiple equilibria is the occurrence of hysteresis: when performing a series of measurements gradually increasing the forcing frequency, the tidal response in the basin remains in the higher amplitude (less phase lag) regime until it 'suddenly' collapses to the lower amplitude branch. Subsequently decreasing the forcing frequency the lower branch is followed until a 'sudden' transition to the higher amplitude regime occurs, see figure 6.8(a). In this figure only high and low tide measurements are plotted in order to obtain the envelop of the signals oscillating at forcing frequency 0.1592 Hz (6.3 s period). At the start of the time series, the basin response seems to be in the lower amplitude regime in which it started as the forcing frequency had just been decreased from higher values. However, although there is no change in the forcing conditions during the plotted interval the basin response shifts to the higher amplitude regime and remains there (also for long after the plotted part of the time series). Apparently the lower amplitude regime near which the basin started had ceased to exist under these conditions so the system is forced to transfer to the stable higher amplitude regime. The lower amplitude regime not only has lower amplitude, the phase lag with the forcing at sea is larger as well as can be seen in figure 6.8(b) which shows two different tidal curves of the response in the basin under the same forcing at sea in a single plot. The response amplitudes can be different only because the phase lag, hence the input of energy, differs. The phase lag is different because the effective eigenfrequency of the basin is different at different tidal amplitudes.

6.4.4   Smooth pipe entrance versus straight pipes

In the previous section we showed the occurrence of multiple equilibria after reducing friction by decreasing the basin area and introducing smooth trumpet-shaped pipe ends. Because vertical sidewalls were used, non-uniform hypsometry cannot be the mechanism responsible for this effect. Although the reduction of the basin area dramatically decreases effective friction, hence increases amplification, it is not the key factor either (see also section 6.4.5). Figure 6.9 shows that the key difference is the shape of the pipe ends: with straight pipe ends no nonlinear effects are observed, the curves for the best quasi-linear Lorentz's fit and the best extended nonlinear fit actually coincide. With smooth trumpet-shaped pipe ends the results clearly deviate from Lorentz's theory and are better described by the nonlinear extension. Apparently, it is the shape of the pipe entrance that causes the effective eigenfrequency to depend on the amplitude. The most likely scenario is that the effective length of the pipe depends on the fluid velocity and turbulent gyres of the flow through the pipe. In that case the first order correction to the quasi-linear dispersion relation (6.3) should lead to the same equation (6.6) as for non-uniform hypsometry. No quantitative analysis to corroborate this description is available yet however.

6.4.5   Dependence of resonance characteristics on basin area

Because of the apparent influence of basin area on the effective friction, a series of measurements at different basin areas have been performed. For this series a pipe with smooth trumpet-shaped ends (like in the previous section) was used. At the basin side it was cut in order to reduce the height of the opening and smoothen the transition to the bottom of the basin. The total pipe length is 340 mm, 2 cm longer than in section 6.4.3, for technical reasons. Figure 6.10 shows the response curve parameters fitted to the respective measurements. The eigenfrequency decreases with the square root of basin area A_0 in correspondence with its definition $\omega_0 = \sqrt{gO/(A_0 L)}$.

Equation (6.2) suggests a linear relation between the friction parameter ν_0 and A_0. However, figure 6.10(b) clearly shows a quadratic deviation from linear dependence. Perhaps this is related to statistical interdependence between ν_0 and the tilting parameter Γ which, besides tilting, has a damping effect on the response curve as well by detuning forcing and eigenfrequency.

There is no quantitative theory for Γ yet for the Helmholtz mode with uniform hypsometry. From figure 6.10(c) we conclude that it increases quadratically with A_0. Note that the tilting effect of Γ on the response curve is measured by $\Gamma|\alpha|^2$ in (6.6), so the increase of the friction parameter ν_0 decreasing the response amplitude $|\alpha|$ needs to be considered as well when assessing the importance of the tilting parameter.

For none of the cases in this series of measurements, multiple equilibria were found. For comparison, the parameters ω_0, ν_0 and Γ found for the configuration in section 6.4.3, for which multiple equilibria were found, are plotted with stars in figure 6.10 as well. Although ω_0 and Γ were slightly higher in that case (as was expected for the eigenfrequency ω_0 because the pipe was a bit shorter), the friction coefficient was significantly lower in that case, possibly because the care taken in preventing leakage was traded for being able to swiftly change the configuration. Apparently this causes the absence of multiple equilibria in the present series of measurements.

(a) Straight pipe end

(b) Smooth trumpet-shaped pipe end

(c) Amplification factor, straight pipe end

(d) Amplification factor, smooth pipe end

(e) Phase difference, straight pipe end

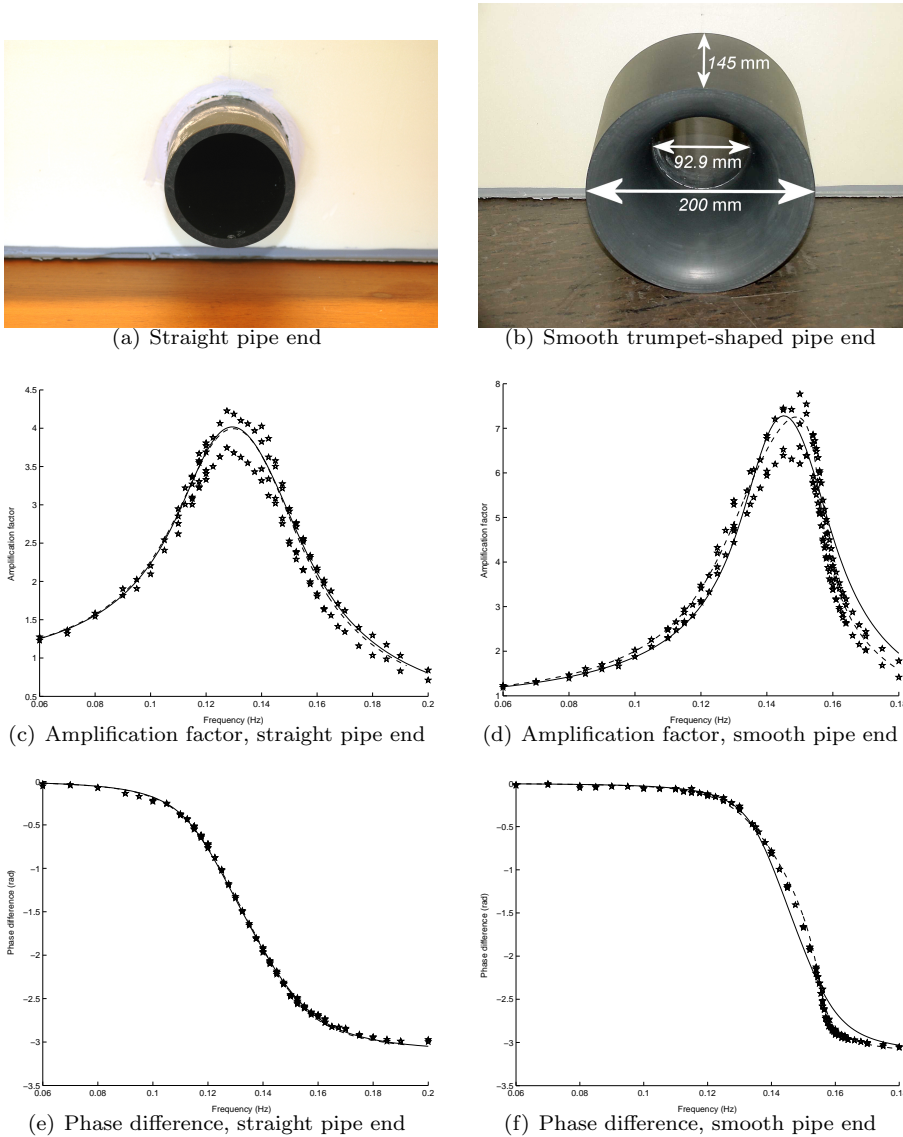(f) Phase difference, smooth pipe end

Figure 6.9: Response curves with and without smooth trumpet-shaped pipe ends. Forcing amplitude $\alpha_e \approx 1$ mm in both cases. The straight pipe (left) is 313 mm long with 92.9 mm inner diameter, the smooth pipe (right) has a total length of 340 mm including 145 mm trumpet-shaped openings at either side, in which the inner diameter increases from 92.9 mm at the interior to 200 mm at the ends. On the basin side, the lower part of the entrance has been cut to better merge with the basin's bottom. Solid curves show the fit to Lorentz's theory (6.4) with parameters $\omega_0 = 0.134$ Hz and $\nu_0 = 62.2$ m^{-1} in the straight pipe case, $\omega_0 = 0.147$ Hz and $\nu_0 = 18.1$ m^{-1} in the smooth entrance case. Dashed curves show the extended nonlinear theory (6.6) with parameters $\omega_0 = 0.133$ Hz, $\nu_0 = 61.1$ m^{-1} and $\Gamma = 0.60 \cdot 10^3$ m^{-2} in the straight pipe case, $\omega_0 = 0.141$ Hz, $\nu_0 = 16.0$ m^{-1} and $\Gamma = 1.08 \cdot 10^3$ m^{-2} in the smooth entrance case. Again amplitude differences within the basin can be seen between the sensors at the end and entrance of the basin respectively.
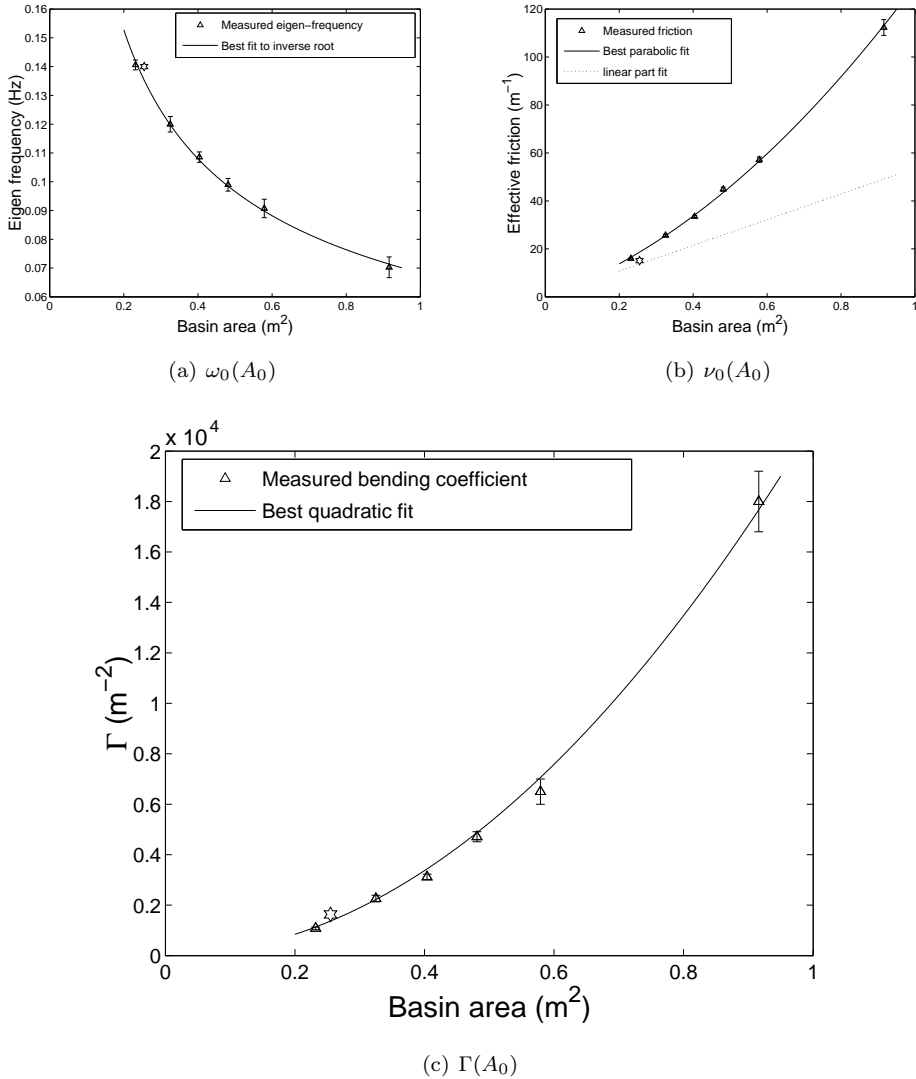
(a) $\omega_0(A_0)$

(b) $\nu_0(A_0)$

(c) $\Gamma(A_0)$

Figure 6.10: Response curve parameters as a function of basin area. Eigenfrequency ω_0 is inversely proportional with the square root of A_0 as expected from its definition just before section 6.3.1. Although a linear relation between the friction parameter ν_0 and basin area A_0 was expected on the basis of (6.2), it clearly comprises a quadratic deviation from linear dependence. No quantitative theory is available for the nonlinear tilting parameter Γ yet. It appears to depend on basin area A_0 quadratically. For comparison, six-pointed stars denoting the parameters found in section 6.4.3, with a slightly different pipe, have been added.

6.5   Discussion of alternative theories

The results presented in the previous section show that apart from non-uniform hypsometry there must be another process leading to a similar nonlinear effect. In this section a number of such processes are discussed, emphasizing the physical mechanisms rather than mathematical solution. First a number of effects related to the nonlinear character of advection and continuity are considered. The mechanism discussed in section 6.5.2 shows that the results are not exclusive for shallow water models but may occur in non-hydrostatic models as well. Finally, there is some discussion on different friction regimes as a less likely candidate for explaining the observed phenomena.

6.5.1   Advective and continuity effects

Apart from friction, there are two nonlinear terms in the two-dimensional depth-averaged **shallow water equations**

$$\frac{\partial \mathbf{U}}{\partial t} + [\mathbf{U} \cdot \nabla]\mathbf{U} \;\; = \;\; -g\nabla\zeta - \frac{\tau_{\mathbf{b}}}{\rho D}, \tag{6.7a}$$

$$\frac{\partial \zeta}{\partial t} + \nabla\cdot[D\mathbf{U}] \;\; = \;\; 0, \tag{6.7b}$$

where $\tau_{\mathbf{b}}$ is the bottom friction stress, ρ the density, $\zeta(\mathbf{x}, t), \mathbf{U}(\mathbf{x}, t)$ the water-level elevation and current at position $\mathbf{x}$, time t and $D = H(\mathbf{x}) + \zeta(\mathbf{x}, t)$ is the total water depth. The advective term $[\mathbf{U} \cdot \nabla]\mathbf{U}$ and the continuity term $\nabla\cdot[\zeta\mathbf{U}]$ not only induce the well-known nonlinear effect of distorting the tidal curve by exciting higher harmonics, but may also change response curves. In chapter 4 an extensive calculation for the same strongly resonant limit as in section 6.3.2 led to the nonlinear amplitude equations (4.30) of which the Helmholtz results are a special case.

The effects of **non-uniform hypsometry** discussed along the lines of Maas (1997), Maas & Doelman (2002) and Doelman *et al.* (2002) in section 6.3.2 can be interpreted as a continuity effect, because it is a consequence of the fact that the flux of water through the channel spreads out over a variable wet area of the basin. As a consequence the same current through the channel leads to a different rise in the basin's water level, hence the restoring force of the oscillator, depending on the phase of the tide. At high tide the resulting water-level change is less than at low tide.

The opposite effect emerges when considering the influence of water-level elevation changes on the cross-section of the channel itself (Miles, 1981). Indeed at high tide the same current velocities over larger channel cross-section leads to larger flux of water through the channel than at low tide when the channel cross-section is relatively small. Hence the nonlinear effect caused by the dependence of the **channel cross-section** on the water level reduces the high tide period and decreases water-level changes at low tide, so this also leads to an equation similar to (6.5).

Actually, (6.5) appears to be the **generic form** of the first-order nonlinear correction to the dispersion relation whenever the effective eigenfrequency depends on amplitude. Apart from explicit derivations for particular mechanisms the main motivation is along the lines of chapter 4: for oscillatory modes ($\omega \neq 0$) the condition for resonant feedback onto itself cannot be fulfilled for triad interactions. The condition for resonant quartic interactions ensures that $|\alpha|^2\alpha$ will generically be the first nonlinear term (see also Nayfeh & Mook, 1979, ch. 4). Although this suggests that it is

appropriate to use (6.5) to describe the results from our laboratory experiments as well, a proper analytical derivation has not been given yet. In particular, a theoretical value for Γ is not available for this situation.

The results in section 6.4.4 show that the smooth **trumpet-like shape** of the pipe entrance plays a key role in the occurrence of nonlinear changes to the response curve in the laboratory setting. Apparently, it too causes the effective eigenfrequency to depend on the amplitude. The most likely mechanism is that the effective pipe length changes because of the influence of the entrance shape on the flow in and out of the channel. With straight pipe ends, a jet of water flows out of the pipe into the adjacent sea at rest. As a result vortices are shed (see Wells & van Heijst, 2003), whereas the return flow into the pipe behaves more or less uniformly as potential flow. With smooth trumpet-shaped ends, which blend better with the surrounding water, vortices are diminished though not eliminated. The size and strength of these vortices depend on the velocity through the channel. At low amplitudes the outflow is like potential flow as well, at higher amplitudes a jet still forms. Possibly less water actually takes part in the oscillation in the latter case, hence reducing the added mass effect and increasing the effective eigenfrequency.

Indeed we observe that the occurrence of potential or jet-like outflow seems to coincide with the basin being in the lower or higher amplitude regime respectively. On the other hand, it is not yet proven whether this is consequence or cause. In this respect it would be interesting to see if the diffuse nature of the transition between the two regimes in Wells & van Heijst (2003) is reminiscent of hysteresis. They use the velocity through the channel as a control parameter so hysteresis in their experiments would indicate an intrinsic hysteresis mechanism in the change of flow regimes.

Because jet-formation is a consequence of the advection term, it makes sense to classify this effect under the present subsection as well. This effect of the shape of the pipe end may seem peculiar to the laboratory setting because in reality tidal basins are not connected to sea by pipes. However, funnel-shaped tidal inlets are very common. Probably the processes that occur within the trumpet-shaped pipe ends do apply to funnel-shaped tidal inlets as well.

6.5.2   Vertical accelerations

The continuity and advection effects described in the previous paragraph still play a role in shallow water systems. Another mechanism is feasible if the hydrostatic approximation is abandoned and vertical accelerations are taken into account. As the water level in the basin rises and falls, the distance over which the vertical pressure gradient is induced sustaining the corresponding accelerations, changes as well. Hence the corresponding pressure difference is larger at high tide than at low tide. In other words, inertia increases with water level; consequently the high tide period increases and the low tide period is reduced. A neat and to-the-point treatment of this effect is given by Lorenceau *et al.* (2002), considering oscillations in a liquid column in a partly submerged vertical tube. In fact, Bernoulli (1738) already set out the theory for gravitational oscillations in a U-shaped tube in which this effect plays a role if the two tubes have different cross-section. A rough but involved model shows that his equation can also be derived for the present configuration. The resulting estimate for Γ however is orders of magnitudes too low to explain the observed tilting of the resonance curves.

(a) Current in flood period   (b) Friction law   (c) Effective friction coefficient
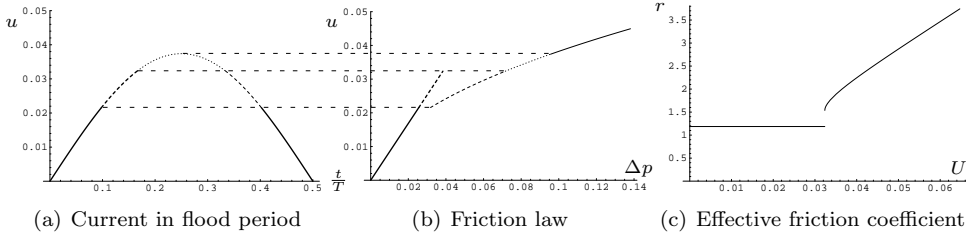
Figure 6.11: Sketch of frictional pressure difference during half a tidal period. 6.11(b) shows the friction law that was used, with a transition region between the laminar and turbulent regime. In 6.11(a) the regime of the flow at different intervals during the flood period is indicated. The effective friction coefficient determined from Lorentz's linearization procedure is shown in 6.11(c).

6.5.3 Friction regimes

It is a well-known fact that two regimes have to be distinguished with regard to pipe friction laws. In the laminar regime for low Reynolds numbers $Re = Ud/\nu$, with $U = \omega|\alpha| A_0/O$ the amplitude of the current, d the pipe diameter and $\nu \approx 10^{-6}$ $\mathrm{m^2\,s^{-1}}$ the viscosity of water, the friction law constitutes a linear increase of the frictional pressure difference with the velocity through the pipe. For high Reynolds numbers $Re \gtrsim 2500$, the flow becomes turbulent and we simplify the discussion by using a quadratic friction law in this regime, rather than one of more sophisticated empirical friction laws (such as Landau & Lifshitz, 1959, (43.5)). For the sake of the illustration, suppose the transition even leads to hysteresis, the transition from laminar to turbulent occurring at $Re = 3000$ and from turbulent back to laminar at $Re = 2000$. For the dimensions of the pipe described in section 6.4.3 for which multiple equilibria were found, this leads to the friction law shown in figure 6.11(b),

$$\Delta p = \begin{cases} r_0\, u, & \text{for } u < u_+ \text{ m/s (laminar)} \\ \gamma\, |u|u, & \text{for } u > u_- \text{ m/s (turbulent)} \end{cases} \tag{6.8}$$

with coefficients $r_0 = 1.19, \gamma = 68.4$ and a transition region ranging from $u_- = 0.022$ m/s to $u_+ = 0.032$ m/s.

Although the friction laws are derived for stationary flow, we use a *quasi-stationary approximation* and assume the frictional pressure difference to be given by (6.8) at each stage of the oscillatory tidal flow. If the amplitude of the current is below u_+ the flow remains in the laminar regime, but for higher amplitudes the flow becomes turbulent at maximum flood and maximum ebb, as is illustrated in figure 6.11. In view of the apparent success of Lorentz's linearization method (see chapter 3) we can consequently derive an effective linear friction coefficient as a function of the tidal amplitude according to the energy principle $\langle ru^2 \rangle = \langle \Delta p\, u \rangle$. Performing the integration over the complete tidal period, this leads to an analytical expression for the effective friction coefficient r. As long as the current amplitude U is below u_+, one simply has $r = r_0 = 1.19$. For U above this upper limit for laminar motion, the expression is much more elaborate. The resulting graph is shown in figure 6.11(c). Note that in the limit for high amplitude U, the effective friction coefficient r tends to the well-known result $\frac{8}{3\pi}\gamma U$ without taking into account the laminar regime. Next

we can solve the resulting linear system to the equivalent of (6.3):

$$|\alpha| = \frac{\omega_0{}^2 \alpha_e}{\sqrt{(\omega_0{}^2 - \omega^2)^2 + r^2 \omega^2}} \qquad (6.9)$$

in which the effective friction coefficient r depends on $U = A_0/O\,\omega|\alpha|$. Because $|\alpha|$ decreases monotonically as a function of r according to (6.9), multiple equilibria, with two different solutions for the response amplitude $|\alpha|$, are possible only if r decreases as a function of the current amplitude U. Under the quasi-stationary approximation this appears not to be the case.

The transition between friction regimes can be responsible for the observed phenomena only if the quasi-stationary approach used in this section is violated. In that case an *oscillatory pipe friction law* relating the amplitude of the velocity through the constriction (or pipe, in the present situation) to the amplitude of the pressure difference, is needed.

6.6   Conclusion

Several results of experiments on the response of a co-oscillating tidal resonator have been shown in this chapter. The first results in the standard setting with 'large' basin area $A_0 = 0.916$ m^2, uniform hypsometry (i.e. vertical sidewalls) and a straight pipe, corroborate the quasi-linear theory with Lorentz's linearization procedure for quadratic friction. This is an important result by itself, because although Lorentz (1922, 1926) proposed his linearization scheme at the beginning of the twentieth century already and computations using it on large-scale geophysical tidal systems have been corroborated, no experimental validation has been given so far (see also chapter 3).

Although the introduction of artificial topography in order to simulate the effect of hypsometry did show its influence on the tidal curve, reducing the low tide and increasing the high tide period, tilting of the response curve was found to be insignificant compared to the frictional width of the resonance peak. On the laboratory scale the importance of the hypsometry effect could not be sufficiently increased due to small scale effects. On the other hand, the influence of friction can be reduced by decreasing the basin area and introducing smooth trumpet-shaped pipe ends; the amplification factor of 1.5–2.5 increased to a factor of 8–12. More importantly, a nonlinear effect became significant: tilting of the response curve due to the dependence of the effective eigenfrequency on the amplitude of the tidal oscillation. In particular, under specific conditions multiple equilibria were found: at the same forcing amplitude and frequency two different tidal response regimes could occur in the basin, depending on initial conditions.

These multiple equilibria were found with uniform hypsometry, in which case no nonlinear effects are anticipated based on simple Helmholtz models. In section 6.5 however, a number of different nonlinear processes are discussed that give rise to similar effects. The derivation in chapter 4 shows that the amplitude equation for the Helmholtz case can be generalized to more general basins with a set of eigenmodes and nonlinear terms due to advection and continuity in the shallow water equations. The generic nature of the result suggests that a similar derivation can be performed in a three-dimensional setting, needed in order to describe the experimental basin with a pipe connecting the basin to the adjacent 'sea'. The experiments show that the shape

of the pipe ends plays a key role in the occurrence of the nonlinear effects. Intuitively this may be related to a dependence of the effective pipe length on the amplitude of the current. In order to explain the experiments, the added mass effect should decrease (for the effective eigenfrequency to increase) with increasing amplitude. However, a quantitative model to compare with the measurements is not available yet.

The apparent importance of the particular three-dimensional shape of the pipe ends used in the experiment may lead to the impression that the occurrence of multiple equilibria is more of an experimental peculiarity. However, two-dimensional funnel-shaped tidal inlets abound in geophysical reality, so the trumpet-shaped pipe ends seem to be more realistic than the straight ones. Moreover, the hypsometry effect is hampered mainly by small scale effects in the laboratory, which leaves the possibility of its relevance for instance in tidal flat systems with their fractal structure of channels (Cleveringa & Oost, 1999). Of course truly convincing proof of the relevance of the processes sketched in this thesis would lie in finding evidence of these processes in observational records of tidal motion. We think that the results of these experiments provide additional motivation to search for this kind of behaviour in tidal observations. It may be unlikely that sudden changes in the tidal regime and hysteresis, the response of the basin depending not only on the present forcing conditions but also on its history, have been overlooked in the principal tidal components, but they could play a role in secondary undulations. The latter are relatively unimportant for the water level, hence have been investigated less extensively until recently, but their influence on currents can be considerable and reports of irregular behaviour date back to the beginning of the previous century (Honda *et al.*, 1908; Nakano, 1932). Moreover the results from Maas & Doelman (2002), Doelman *et al.* (2002) and chapter 5 suggest to look for internally induced chaotic dynamics of the response amplitudes inside tidal basins without being linked directly to the dynamics of the forcing, i.e. for variations in harmonic 'constants' (such as reported by Doodson, 1924; Gutiérrez *et al.*, 1981).

Acknowledgments

Bibliography

ABRAMOWITZ, M. & STEGUN, I. A. 1965 *Handbook of mathematical functions*. New York: Dover.

AMIN, M. 1991 Superfine resolution of tidal harmonic constants. In *Tidal Hydrodynamics* (ed. B. B. Parker), pp. 711–724. New York: John Wiley & Sons.

APTÉ, A. S. & MARCOU, C. 1954 Seiche in ports. In *Fifth Conf. on Coastal Eng.*, pp. 85–94. Grenoble, France.

AUBREY, D. G. & SPEER, P. E. 1985 A study of non-linear tidal propagation in shallow inlet/estuarine systems, part I: Observations. *Estuarine, Coastal and Shelf Science* **21**, 185–205.

BERNOULLI, D. 1738 *Hydrodynamica, sive de viribus et motibus fluidorum commentarii*. Strasbourg: Joh. Reinholdi Dulseckeri, Argentorati.

BOWERS, E. C. 1977 Harbour resonance due to set-down beneath wave groups. *J. Fluid Mech.* **79** (1), 71–92.

BURLING, M. C., PATTIARATCHI, C. B. & IVEY, G. N. 2002 The tidal regime of Shark Bay, Western Australia. *Est. Coast. Shelf Sc.* **57**, 725–735.

CANDELA, J., MAZZOLA, S., SAMMARI, C., LIMEBURNER, R., LOZANO, C. J., PATTI, B. & BONNANO, A. 1999 The "Mad Sea" phenomenon in the Strait of Sicily. *J. Phys. Oc.* **29**, 2210–2231.

CARRIER, G. F., SHAW, R. P. & MIYATA, M. 1971*a* Channel effects in harbor resonance. *J. Eng. Mech. Div.* pp. 1703–1716, proceedings of the American Society of Civil Engineers.

CARRIER, G. F., SHAW, R. P. & MIYATA, M. 1971*b* The response of narrow-mouthed harbors in a straight coastline to periodic incident waves. *J. Appl. Mech.* pp. 335–344.

CARTWRIGHT, D. E. 1999 *Tides, a scientific history*. Cambridge: Cambridge University Press.

CHADWICK, D. B. & LARGIER, J. L. 1999*a* The influence of tidal range on the exchange between San Diego Bay and the ocean. *J. Geoph. Res.* **104** (C12), 29885–29899.

CHADWICK, D. B. & LARGIER, J. L. 1999*b* Tidal exchange at the bay-ocean boundary. *J. Geoph. Res.* **104** (C12), 29901–29924.

CLEVERINGA, J. & OOST, A. P. 1999 The fractal geometry of tidal-channel systems

in the Dutch Wadden Sea. *Geol & Mijnb* **78** (1), 21–30.

Cushman-Roisin, B. & Naimie, C. E. 2002 A 3D finite-element model of the Adriatic tides. *J. Marine Systems* **37**, 279–297.

De Girolamo, P. 1996 An experiment on harbour resonance induced by incident regular waves and irregular short waves. *Coastal Eng.* **27**, 47–66.

Defant, A. 1961 *Physical Oceanography*, , vol. 2. Oxford-London-New York-Paris: Pergamon.

Doelman, A., Koenderink, A. F. & Maas, L. R. M. 2002 Quasi-periodically forced nonlinear Helmholtz oscillators. *Physica* D **164**, 1–27.

Doodson, A. T. 1924 Perturbations on harmonic constants. *Proc. R. Soc. Lond.* A **106**, 513–526.

Dronkers, J. 1996 The influence of buoyancy on transverse circulation and on estuarine dynamics. In *Buoyancy effects on coastal and estuarine dynamics* (ed. D. G. Aubrey & C. T. Friedrichs), pp. 341–356. Washington D.C.: AGU.

Dronkers, J. J. 1962 The linearization of the quadratic resistance term in the equation of motion for a pure harmonic tide in a sea. In *Proc. Symposium Mathematical Hydrodyn. Method Phys. Oceanography*. Hamburg.

Dronkers, J. J. 1964 *Tidal computations in rivers and coastal waters*. North-Holland Publ. Cy.

Fabrikant, A. L. 1995 Harbour oscillations generated by shear flow. *J. Fluid Mech.* **282**, 203–217.

Falconer, R. A. & Guoping, Y. 1991 Effects of depth, bed slope and scaling on tidal currents and exchange in a laboratory model harbour. *Proc. Instn Civ. Engrs* **91**, 561–576.

Farmer, J. D. & Sidorowich, J. J. 1987 Predicting chaotic time series. *Phys. Rev. Lett.* **59** (8), 845–848.

Fischer, H. B., List, E. J., Koh, R. C. Y., Imberger, J. & Brooks, N. H. 1979 *Mixing in inland and coastal waters*. New York: Academic Press.

Flemming, B. W. & Bartholomä, A., ed. 1995 *Tidal Signatures in Modern and Ancient Sediments*, *Special publication* 24, International Association of Sedimentologists. Blackwell Science.

Friedrichs, C. T. & Aubrey, D. G. 1988 Non-linear tidal distortion in shallow well-mixed estuaries: a synthesis. *Estuarine, Coastal and Shelf Science* **27**, 521–545.

Frison, T. W., Abarbanel, H. D. I., Earle, M. D., Schultz, J. R. & Scherer, W. 1999 Chaos and predictability in ocean water levels. *J. Geoph. Res.* **104** (4), 7935–7951.

Fujiwara, T., Nakata, H. & Nakatsuji, K. 1994 Tidal-jet and vortex-pair driving of the residual circulation in a tidal estuary. *Cont. Shelf Res.* **14** (9), 1025–1038.

Gallagher, B. S. & Munk, W. H. 1971 Tides in shallow water: Spectroscopy. *Tellus* pp. 346–363.

Garrett, C. 1974 Normal modes of the Bay of Fundy and Gulf of Maine. *Can. J.*

Earth Sci. **11**, 549–556.

GARRETT, C. 1975 Tides in gulfs. *Deep-Sea Res.* **22**, 23–35.

GARRETT, C. J. R. & MUNK, W. H. 1971 The age of the tide and the "Q" of the oceans. *Deep-Sea Res.* **18**, 493–503.

GATTESCHI, L. & GIORDANO, C. 2000 Error bounds for McMahon's asymptotic approximations of the zeros of the Bessel functions. *Integral Transform. Spec. Funct.* **10** (1), 41–56.

GERBER, M. 1986 Modelling dissipation in harbour resonance. *Coastal Eng.* **10**, 211–252.

GEYER, W. R. & SIGNELL, R. 1991 Measurements and modeling of the spatial structure of nonlinear tidal flow around a headland. In *Tidal Hydrodynamics* (ed. B. B. Parker), pp. 403–418. New York: John Wiley & Sons.

GIESE, G. S. & CHAPMAN, D. C. 1990 Coastal seiches. *Oceanus* **36** (1), 38–46.

GODIN, G. 1991*a* The analysis of tides and currents. In *Tidal Hydrodynamics* (ed. B. B. Parker), pp. 675–709. New York: John Wiley & Sons.

GODIN, G. 1991*b* Frictional effects in river tides. In *Tidal Hydrodynamics* (ed. B. B. Parker), pp. 379–402. New York: John Wiley & Sons.

GODIN, G. & GUTIÉRREZ, G. 1986 Nonlinear effects in the tide of the Bay of Fundy. *Cont. Shelf Res* **5** (3), 379–402.

GOLMEN, L. G., MOLVAER, J. & MAGNUSSON, J. 1994 Sea level oscillations with super-tidal frequencies in a coastal embamyent of western Norway. *Cont. Shelf Res.* **14**, 1439–1454.

GOMIS, D., MONSERRAT, S. & TINTORÉ, J. 1993 Pressure-forced seiches of large amplitude in inlets of the Balearic Islands. *J. Geoph. Res.* **98** (8), 14437–14445.

GREEN, T. 1992 Liquid oscillations in a basin with varying surface area. *Phys. Fluids A* **4** (3), 630–632.

GUCKENHEIMER, J., BACK, A., MYERS, M., WICKLIN, F. & WORFOLK, P. 1992 dstool: Computer assisted exploration of dynamical systems. *Notices Am. Math. Soc.* **39**, 303–309.

GUCKENHEIMER, J. M. & HOLMES, P. J. 1983 *Nonlinear oscillations, dynamical systems, and bifurcations of vector fields*. New York: Springer.

GUTIÉRREZ, A., MOSETTI, F. & PURGA, N. 1981 On the indetermination of the tidal harmonic constants. *Nuovo Cimento* **4**, 563–575.

HAYASHI, T., KANO, T. & SHIRAI, M. 1966 Hydraulic research on the closely spaced pile breakwater. In *Proc. 10th ASCE Conf. Coastal Eng.*, pp. 873–884.

HIBIYA, T. & KAJIURA, K. 1982 Origin of the *Abiki* phenomenon (a kind of seiche) in Nagasaki Bay. *J. Oc. Soc. Japan* **38**, 172–182.

HONDA, K., TERADA, T., YOSHIDA, Y. & ISITANI, D. 1908 Secondary undulations of oceanic tides. *J. Coll. Sc. Imp. Univ. Tokyo* **24**, 1–113 and 95 plates.

HORIKAWA, K. & NISHIMURA, H. 1970 On the function of tsunami breakwaters.

Coastal Eng. Jap. **13**, 103–112.

Ito, Y. 1970 Head loss at tsunami-breakwater opening. In *Proc. 12th ASCE Conf. Coastal Eng.*, pp. 2123–2131.

Jay, D. A. 1991 Internal asymmetry and anharmonicity in estuarine flows. In *Tidal Hydrodynamics* (ed. B. B. Parker), pp. 521–543. New York: John Wiley & Sons.

Kabbaj, A. & Le Provost, C. 1980 Nonlinear tidal waves in channels: A perturbation method adapted to the importance of quadratic bottom friction. *Tellus* **32**, 143–163.

Kashiwai, M. 1984 Tidal residual circulation produced by a tidal vortex. Part 1. Life-history of a tidal vortex. *J. Oc. Soc. Jap.* **40**, 279–294.

Krauss, W. 1973 *Methods and results of theoretical oceanography*, , vol. I: Dynamics of the homogeneous and the quasihomogeneous ocean. Berlin-Stuttgart: Gebrüder Borntraeger.

Landau, L. D. & Lifshitz, E. M. 1959 *Fluid Dynamics*, *Course of Theoretical Physics*, vol. 6. Oxford-New York-Toronto-Sydney-Paris-Frankfurt: Pergamon.

Le Provost, C. 1973 Décomposition spectrale du terme quadratique de frottement dans les équations des marées littorales. *C.R. Acad. Sci. Paris* **276**, 571–574, 653–656.

Le Provost, C. 1991 Generation of overtides and compound tides (review). In *Tidal Hydrodynamics* (ed. B. B. Parker), pp. 269–295. New York: John Wiley & Sons.

LeBlond, P. H. & Mysak, L. A. 1978 *Waves in the Ocean*. Amsterdam-Oxford-New York: Elsevier.

Lee, J.-J. 1971 Wave-induced oscillations in harbours of arbitrary geometry. *J. Fluid Mech.* **45**, 375–394.

Lee, J.-J. & Raichlen, F. 1971 Resonance in harbors of arbitrary shape. In *Proc. 12th Conf. Coast. Eng.*, pp. 2163–2180. ASCE.

Lee, J.-J. & Raichlen, F. 1972 Oscillations in harbors with connected basins. *J. Waterways, Harbors and Coastal Eng. Div.* **98**, 311–332, proceedings of the American Society of Civil Engineers.

Lefèvre, F., Lyard, F. H., Le Provost, C. & Schrama, E. J. O. 2002 FES99: A global tide finite element solution assimilating tide gauge and altimetric information. *J. Atm. Oc. Tech.* **19** (9), 1345–1356.

Lepelletier, T. G. & Raichlen, F. 1987 Harbor oscillations induced by nonlinear transient long waves. *J. Waterway, Port, Coastal and Ocean Eng.* **113** (4), 381–400.

Lorenceau, E., Quéré, D., Ollitrault, J.-Y. & Clanet, C. 2002 Gravitational oscillations of a liquid column in a pipe. *Phys. Fluids* **14** (6), 1985–1992.

Lorentz, H. A. 1922 Het in rekening brengen van den weerstand bij schommelende vloeistofbewegingen. *De Ingenieur* p. 695, in Dutch.

Lorentz, H. A. 1926 *Verslag Staatscommissie Zuiderzee 1918-1926*. Den Haag: Alg. Landsdrukkerij, (in Dutch, report senate committee Zuiderzee).

Lorenz, E. N. 1993 *The essence of chaos*. London: University College London Press.

MAAS, L. R. M. 1997 On the nonlinear Helmholtz response of almost-enclosed tidal basins with sloping bottoms. *J. Fluid Mech.* **349**, 361–380.

MAAS, L. R. M. & DOELMAN, A. 2002 Chaotic tides. *J. Phys. Oc.* **32** (3), 870–890.

MARTINEZ, F. M. & NAVERAC, V. S. 1988 An experimental study of harbour resonance phenomena. In *Proc. 21st Int. Conf. Coast. Eng.* (ed. B. L. Edge), pp. 270–280. Torremolinos: ASCE.

MCNOWN, J. S. 1952 Waves and seiche in idealized ports. In *Gravity Wave Symposium*, *National Bureau of Standards Circular* 521, pp. 153–164.

MEI, C. C. 1989 *The applied dynamics of ocean surface waves*. Singapore: World Scientific.

MEI, C. C., LIU, P. L.-F. & IPPEN, A. T. 1974 Quadratic loss and scattering of long waves. *J. Waterways, Harbors and Coastal Eng. Div.* **100**, 217–239.

MILES, J. W. 1971 Resonant response of harbors: An equivalent-circuit analysis. *J. Fluid Mech.* **46**, 241–265.

MILES, J. W. 1974 Harbor seiching. *Ann. Rev. Fluid Mech.* **6**, 17–35.

MILES, J. W. 1981 Nonlinear Helmholtz oscillations in harbours and coupled basins. *J. Fluid Mech.* **104**, 407–418.

MUNK, W. H. & CARTWRIGHT, D. E. 1966 Tidal spectroscopy and prediction. *Phil. Trans. Roy. Soc. Lon.* **259** (1105), 533–581.

NAKANO, M. 1932 Preliminary note on the accumulation and dissipation of energy of the secondary undulations in a bay. *Proc. Phys.-Math. Soc. Japan* **14**, 44–56.

NAYFEH, A. H. & MOOK, D. T. 1979 *Nonlinear oscillations*. *Pure and applied mathematics* . New York: John Wiley & Sons.

NEWTON, S. I. 1687 *Philosophae Naturalis Principia Mathematica*. London: The Royal Society, 3 vols.

NYCANDER, J. & DÖÖS, K. 2001 Open boundary conditions for barotropic waves. Scientific report FOI-R–0078–SE. FOI - Swedish Defence Research Agency, Systems Technology, SE-172 90 Stockholm, ISSN 1650-1942.

OKIHIRO, M. & GUZA, R. T. 1995 Infragravity energy modulation by tides. *J. Geoph. Res.* **100** (8), 16143–16148.

OOST, A. P. 1995 Sedimentological implications of morphodynamic changes in the ebb-tidal delta, the inlet and the drainage basin of the Zoutkamperlaag tidal inlet (Dutch Wadden Sea), induced by a sudden decrease in the tidal prism. In *Tidal Signatures in Modern and Ancient Sediments* (ed. B. W. Flemming & A. Bartholomä), pp. 101–119. Blackwell Science.

PARKER, B. B. 1991*a* The relative importance of the various nonlinear mechanisms in a wide range of tidal interactions (review). In *Tidal Hydrodynamics* (ed. B. B. Parker), pp. 237–268. New York: John Wiley & Sons.

PARKER, B. B., ed. 1991*b* *Tidal Hydrodynamics*, New York. John Wiley & Sons.

PLATZMAN, G. W. 1991 Tidal evidence for ocean normal modes. In *Tidal Hydrodynamics* (ed. B. B. Parker), pp. 13–26. New York: John Wiley & Sons.

POLLI, S. 1960 La propagazione delle Maree nell'Adriatico. In *Atti del Convegno dell' Associazione Geofisica Italiana*. Roma, 1959.

PRANDLE, D. 1991 Tides in estuaries and embayments (review). In *Tidal Hydrodynamics* (ed. B. B. Parker), pp. 125–152. New York: John Wiley & Sons.

PRATT, L. J. 1997 Hydraulically drained flows in rotating basins. part II: Steady flow. *J. Phys. Oc.* **27**, 2522–2535.

PRATT, L. J. & LLEWELLYN SMITH, S. G. 1997 Hydraulically drained flows in rotating basins. part I: Method. *J. Phys. Oc.* **27**, 2509–2521.

RAICHLEN, F. 1966 Harbor resonance. In *Estuary and coastline hydrodynamics* (ed. A. T. Ippen), pp. 281–340. New York: McGraw-Hill.

RAICHLEN, F. & IPPEN, A. T. 1965 Wave induced oscillations in harbors. *J. Hydraulics Div.* pp. 1–26, proceedings of the American Society of Civil Engineers.

SIMON, B. 1991 The species concordance method of tide prediction. In *Tidal Hydrodynamics* (ed. B. B. Parker), pp. 725–735. New York: John Wiley & Sons.

SPEER, P. E. & AUBREY, D. G. 1985 A study of non-linear tidal propagation in shallow inlet/estuarine systems, part II: Theory. *Estuarine, Coastal and Shelf Science* **21**, 207–224.

SPEER, P. E., AUBREY, D. G. & FRIEDRICHS, C. T. 1991 Nonlinear hydrodynamics of shallow tidal inlet/bay systems. In *Tidal Hydrodynamics* (ed. B. B. Parker), pp. 321–339. New York: John Wiley & Sons.

STOMMEL, H. & FARMER, H. G. 1952 On the nature of estuarine circulation. *Ref. Nos.* 52–51, 52–63, 52–88. Woods Hole Oceanographic Institute.

TAKENS, F. 1981 Detecting strange attractors in turbulence. In *Dynamical systems and turbulence, Warwick 1980, Lecture Notes in Math. Vol. 898* (ed. D. Rand & L. S. Young), pp. 366–381. New York: Springer-Verlag.

TERRETT, F. L., OSORIO, J. D. C. & LEAN, G. H. 1968 Model studies of a perforated breakwater. In *Proc. 11th ASCE Conf. Coastal Eng.*, pp. 1104–1109.

THIJSSE, J. T. 1972 *Een halve eeuw Zuiderzeewerken*. Groningen: Tjeenk Willink, (in dutch).

ÜNLÜATA, U. & MEI, C. C. 1975 Effects of entrance loss on harbor oscillations. *J. Waterways, Harbors and Coastal Eng. Div.* **101**, 161–180.

VITTORI, G. 1992 On the chaotic structure of tide elevation in the Lagoon of Venice. In *Proceedings of the 23rd International Conference on Coastal Engineering*, pp. 1826–1839. Venice.

WELLS, M. G. & VAN HEIJST, G.-J. F. 2003 A model of tidal flushing of an estuary by dipole formation. *Dynamics of atmospheres and oceans* **37**, 223–244.

WIGGINS, S. 1988 *Global bifurcations and chaos*. New York: Springer.

ZIMMERMAN, J. T. F. 1982 On the Lorentz-linearization of a quadratically damped forced oscillator. *Physics Letters* **89A** (3), 123–124.

ZIMMERMAN, J. T. F. 1992 On the Lorentz-linearization of a nonlinearly damped tidal Helmholtz oscillator. *Proc. KNAW* **95** (1), 127–145.

Samenvatting

Deze samenvatting geeft een beknopte inhoud van dit proefschrift in het Nederlands. Het streven is geweest om het in principe toegankelijk te maken voor mensen met V.W.O.-natuurkunde als achtergrond. Nieuwe begrippen (cursief gedrukt) zijn zoveel mogelijk direct erna verklaard (bij een opsomming kan het nodig zijn om iets verder door te lezen). Het is echter onvermijdelijk zeer compact geschreven en de nieuwe begrippen volgen elkaar in een snel tempo op. Hulde aan de lezer die zich er met een dergelijke achtergrond toch doorheen weet te slaan. Onderstaand wordt eerst een korte inleiding gegeven in de "oude" (lineaire) theorie van getijden, om dan door te gaan met het bespreken van het nieuwe (niet-lineaire) werk. De kernvraag die in dit proefschrift is bestudeerd is in hoeverre niet-lineaire processen ertoe kunnen leiden dat de voorspelbaarheid en regelmaat van het getij worden verstoord. Hiertoe is enerzijds gebruik gemaakt van abstracte wiskundige modellen en anderzijds van laboratorium-experimenten waarbij op kleine schaal een zogenaamde Helmholtz resonator is nagebootst.

In veel kustgebieden is een belangrijke rol weggelegd voor *het getij*: de dagelijkse verandering van de waterstand (hoog- en laagwater) in oceanen, zeeën en aangrenzende (kust)wateren en de daarmee gepaard gaande eb- en vloedstromen. Het is een belangrijke factor voor de navigatie, maar ook kunnen de getijstromen grote hoeveelheden sediment (zand en klei) verplaatsen en zo de ligging van de bodem beïnvloeden en ze zijn van belang voor de verspreiding van vervuiling en voedingsstoffen in het water. Het woord "getij" vindt zijn oorsprong in het regelmatige voorspelbare karakter ervan. Over het algemeen zit er 12 uur en 25 minuten tussen twee opeenvolgende hoogwaters, met een laagwater ertussen. Al vroeg in de geschiedenis werd het verband gelegd met de maan, al heeft een adequate beschrijving van het mechanisme moeten wachten tot de zwaartekrachtswetten van Newton.

De zwaartekracht tussen de aarde en een hemellichaam, zoals de zon of de maan, doet deze om elkaar heen draaien. In het middelpunt van de aarde zijn de resulterende centrifugaal- (of middelpuntvliedende) kracht en de zwaartekracht met elkaar in evenwicht. Dichter bij het hemellichaam is de zwaartekracht groter, terwijl aan de tegenoverliggende kant van de aarde de centrifugaalkracht overheerst, zie ook figuur 1.2. Als de aarde geheel uit water zou bestaan, dan zou je het zogenaamde evenwichtsgetij verwachten: een "vloedberg" aan de kant van het hemellichaam door de daar overheersende zwaartekracht en een tweede "vloedberg" aan de andere kant door de daar overheersende centrifugaalkracht. Doordat de aarde in ongeveer 24 uur om zijn as draait, komt een vast punt op aarde dus twee keer per dag een hoogwater tegen en dus ook twee keer per dag een laagwater. Omdat daarnaast de maan zelf in 28 dagen om de aarde draait, duurt het iets langer (namelijk 24 uur en 50 minuten) voordat een vast punt op aarde zich weer op dezelfde plek t.o.v. de maan

bevindt, zodat de periode van het maansgetij 12 uur en 25 minuten bedraagt. De belangrijkste twee hemellichamen die het getij op aarde veroorzaken zijn de zon en de maan. Hoewel de zon veel groter en zwaarder is dan de maan, is de invloed van de laatste toch groter omdat de maan dichter bij de aarde staat. Met volle en nieuwe maan, wanneer de zon en de maan min of meer op een lijn staan, dan versterken zij elkaar en ontstaat een extra sterk *springtij*, met een hogere hoogwater- en lagere laagwaterstand. Bij eerste en laatste kwartier werken ze elkaar juist tegen en is het *doodtij*, met een minder hoog hoogwater en minder laag laagwater. Zo varieert het getij in kracht op een tijdschaal van 14 dagen. Andere veranderingen in de stand van de zon en de maan, zoals de declinatie t.o.v. de evenaar en de elliptische vorm van hun baan, zorgen voor weer andere tijdschalen die een rol spelen in het evenwichtsgetij.

Er zijn twee redenen waarom het getij op aarde afwijkt van het evenwichtsgetij. Ten eerste bestaat de aarde niet alleen uit water, maar wordt de getijgolf geblokkeerd door de continenten. Ten tweede draaien de vloedbergen van het evenwichtsgetij te snel om de aarde, zodat het water door zijn traagheid en door wrijving onvoldoende in staat is om te reageren. Daardoor treedt een vertraging (en verzwakking) op in de reactie van het water op de getijdekrachten van de zon en de maan. Het gangbare beeld is dat de directe forcering van het getij alleen in de zuidelijke oceaan, waar rondom Antarctica wel water is over een volledige breedtecirkel, een rol van betekenis speelt. Daarvandaan plant de getijgolf zich dan voort over de andere oceanen en kustzeeën, doordat die meebewegen met de schommelingen in de waterstand in de aangrenzende oceaan of zee (*co-oscillatie*). Dat verklaart dan ook waarom springtij en doodtij niet met volle/nieuwe respectievelijk eerste/laatste kwartier plaatsvinden, maar ongeveer twee dagen later. Uit het feit dat er op aarde ook plaatsen voorkomen waar deze "leeftijd van het getij" negatief is, blijkt echter dat dit beeld ook niet helemaal volledig is, maar daar zal hier verder geen aandacht meer aan besteed worden.

In het co-oscillatie-proces kan het getij flink versterkt worden. Het evenwichtsgetij zelf is namelijk vrij klein (27 cm getijverschil voor de zon en 54 cm voor de maan). Afhankelijk van de locale omstandigheden, zoals de diepte en de vorm van het getijdebekken, kunnen bepaalde *componenten* (tijdschalen waarop de variaties van het getij optreden) van het evenwichtsgetij resoneren met de *eigenmodi* van het bekken. Deze eigenmodi zijn de natuurlijke slingeringen van het water in het bekken. Net zoals bij het duwen van een kind op een schommel is er één bepaalde aandrijf-frequentie (in het geval van getijdebekkens zijn er méérdere eigenmodi) waarbij kleine duwtjes een grote uitwijking tot gevolg hebben. Als je sneller of langzamer aandrijft, dan is het resultaat minder groot. *Resonantie* in getijdebekkens treedt dus op als de frequentie van het getij overeenkomt met een eigenmode van het bekken. In een vereenvoudigd smal rechthoekig bekken van constante diepte dat aan één zijde in verbinding staat met een aangrenzende oceaan of zee, zoals weergegeven in figuur 1.6(a), betekent dit dat de lengte van het bekken overeen moet komen met een oneven aantal keren een kwart-golflengte, vandaar de naam *kwart-golflengte resonator*. Dit is vergelijkbaar met de resonantie van een orgelpijp. De Adriatische Zee, bij wijze van voorbeeld besproken in hoofdstuk 2, gedraagt zich als zo'n kwart-golflengte resonator. Terwijl het getij op de Middellandse Zee verwaarloosbaar is (zo'n 13 cm getijverschil aan de monding van de Adriatische Zee) neemt het toe tot een duidelijke 52 cm aan het eind bij Venetië. Een andersoortige eigenmode is te vinden in relatief kleine bekkens die bijna geheel zijn omsloten door land en slechts door een smalle doorgang verbonden zijn met de zee of oceaan. Deze *Helmholtz mode*, ook wel *pomp mode* genoemd, ken-

merkt zich door een nagenoeg vlak op en neer gaan van de waterstand binnen het bekken, terwijl het water door het smalle zeegat wordt geperst ten gevolge van het verschil in waterstand binnen het bekken en buiten op zee, zie ook figuur 1.7(b). Ook de Nederlandse Waddenzee kan worden opgevat als een aantal afzonderlijke getijde-bekkens van dit type.

De hiervoor besproken verschijnselen kunnen allemaal nog beschreven en verklaard worden met behulp van zogenaamde *lineaire getijdetheorie*. *Lineariteit* is een wiskundig begrip dat betekent dat de respons van een systeem evenredig is met de mate van forcering. Dus als de aandrijving toeneemt met een factor twee, dan wordt ook het gevolg twee keer zo groot. Lineaire systemen zijn voor wiskundigen relatief eenvoudig op te lossen. In dit proefschrift is echter vooral gekeken naar niet-lineaire processen die een rol spelen in het co-oscillatie-proces, in het bijzonder rond resonantie. De forcering is dan de getijdebeweging in de aangrenzende oceaan of zee en de respons is het co-oscillerende getij binnen het getijdebekken. In de ondiep-water-vergelijkingen (ondiep is relatief t.o.v. de golflengte, dus voor het getij kan zelfs de oceaan van 5 km diepte "ondiep" zijn) spelen drie niet-lineaire processen een rol: wrijving, advectieve versnellingen en het continuïteitseffect. Wrijving met de bodem en ook de turbulente *dissipatie* (verlies van energie) wordt vaak beschreven met een *kwadratische wrijvingswet*: als de snelheid met een factor twee (of 3) toeneemt, dan neemt de wrijving met een factor vier (of 9) toe. *Advectieve versnellingen* vinden plaats in stroomversnellingen en hebben te maken met het feit dat het water het liefst met een constante snelheid rechtuit wil bewegen; een grotere snelheid heeft dubbel effect omdat het betekent dat het water meer moet versnellen, maar ook dat één specifiek waterdeeltje sneller in en uit de stroomversnelling beweegt. Het *continuïteitseffect* heeft betrekking op het feit dat niet alleen de snelheid van het water maar ook de waterstand bepaalt hoeveel water er door het getij verplaatst wordt; bij hoogwater gaat er relatief meer volume aan water door een geul dan bij laagwater.

De gevolgen van de niet-lineaire processen laten zich ook in drie groepen onderverdelen: vervorming van de getijgolf, verandering van de stationaire amplitude en modulatie van het getij. Niet-lineaire processen kunnen extra getij-componenten opwekken met frequenties die een veelvoud zijn van de frequenties in het evenwichts-getij, hetgeen leidt tot een *vervorming* van de sinus-vormige getijgolf. Als het systeem slechts zwak niet-lineair is, dan kan dit veelal beschreven worden door herhaald toepassen van lineaire theorie zonder dat de dynamica van het getij essentieel wordt beïnvloed. Wel kan de asymmetrie van het getij (de gebruikelijkste vorm is een korte sterke vloed en een zwakkere langdurige eb) grote gevolgen hebben voor het transport van bijvoorbeeld sediment en dus voor de bodemligging. In dit proefschrift is deze niet-lineaire vervorming van de getijgolf grotendeels buiten beschouwing gelaten.

Onder *stationaire* forcering (d.w.z. een periodiek signaal van constante amplitude), valt in het algemeen ook een stationaire respons te verwachten. De resonantie-eigenschappen van het getijdebekken kunnen dan worden weergegeven met behulp van een *respons curve*, waarin men de amplitude-verhouding en het faseverschil van het stationaire getij in het bekken t.o.v. de forcering van buiten uitzet tegen de frequentie van het signaal (zie bijvoorbeeld figuur 3.4). In een lineair systeem heeft de amplitude van de forcering geen invloed op de respons curve; als de forcering toeneemt dan neemt de respons ook toe, maar de verhouding blijft gelijk. Kwadratische wrijving zorgt er echter voor dat wrijving relatief belangrijker wordt bij grotere amplituden. Daarom is de resonantie-piek scherper en hoger bij kleinere forcerings-amplituden; bij

toenemende forcering neemt ook de respons wel toe, maar relatief minder sterk dan de forcering. Om deze niet-lineariteit goed mee te nemen bedacht Nederlandse Nobel-prijswinnaar H.A. Lorentz al in het begin van de vorige eeuw een linearisatie-principe. Dat kwam erop neer dat de kwadratische wrijvingswet door een lineaire werd vervangen, maar de daarin voorkomende coëfficiënt werd stapsgewijs zodanig aangepast dat de dissipatie van energie per periode hetzelfde was als wanneer de kwadratische wrijvingswet zou zijn gebruikt. Hij gebruikte zijn methode om met succes te voorspellen wat het effect zou zijn van de Afsluitdijk op het getij in de Waddenzee. Hoewel de methode inmiddels onomstreden is dankzij zijn succesvolle toepassing, bleek een zorgvuldige validatie in een laboratorium-opstelling te ontbreken. In hoofdstuk 3 wordt dit gat opgevuld met experimenten die op het N.I.O.Z. zijn uitgevoerd. Ook dit effect lijkt echter nog erg op lineair gedrag, in de zin dat het nog steeds mogelijk is om een respons curve te definiëren die bij gegeven stationaire forcering voorspelt wat de stationaire respons zal zijn.

Niet-lineaire effecten kunnen de dynamica ook wezenlijk veranderen. Voortborddurend op eerder werk van Leo Maas, Arjen Doelman en Femius Koenderink, wordt in hoofdstuk 4 een wiskundig model afgeleid voor de modulatie van getij-amplitudes in een co-oscillerend getijdebekken. Hun werk beperkte zich tot de Helmholtz mode in bijna volledig afgesloten bekkens, waarvoor de wiskunde relatief eenvoudig is omdat de waterstand binnen het bekken overal gelijk is en dus met een enkele variabele kan worden beschreven. In dit proefschrift wordt het uitgebreid naar willekeurig gevormde bekkens zonder dat de waterstand overal in het bekken gelijk hoeft te zijn. Het model voor de Helmholtz mode blijkt daar dan een speciaal geval van te zijn. Voor de Helmholtz mode ontstaat de niet-lineariteit doordat de oppervlakte van het bekken verandert met de fase van het getij (een deel van het bekken valt droog met laag water), hetgeen in essentie ook een continuïteitseffect is. In het algemenere geval blijken meer niet-lineaire termen (advectie en continuïteit) binnen de ondiep-water-vergelijkingen tot dezelfde resultaten te leiden.

De belangrijkste fysische aannamen waarop de afleiding van het model is gebaseerd zijn dat sprake is van een kleine getij-amplitude en sterke resonantie. De getij-amplitude moet klein zijn t.o.v. de waterdiepte om de wiskundige analyse mogelijk te maken. Fysisch valt te verwachten dat de niet-lineaire effecten alleen maar groter zullen worden voor grotere amplituden, maar de wiskundige technieken om dat te onderzoeken ontbreken vooralsnog. Sterke resonantie houdt hier in dat we aannemen dat de frequentie(s) van de forcering dichtbij de eigenfrequenties van het bekken liggen en dat wrijving erg klein is. Vooral aan de laatste aanname zal in de praktijk vaak niet worden voldaan, aangezien wrijving en turbulentie in de relatief ondiepe kustgebieden in het algemeen wel belangrijk is. Op grond van deze aannamen kunnen, met behulp van zwak niet-lineaire theorie, vergelijkingen worden afgeleid die beschrijven hoe de amplitudes van de verschillende getij-componenten langzaam variëren in de tijd. Dit betekent dat het getij in de gebruikelijke 12 uur en 25 minuten tussen hoog- en laagwater op en neer gaat, maar dat de amplitude en fase van het getij langzaam verandert op een langere tijdschaal. In de praktijk bestaat een dergelijke modulatie al omdat de forcering varieert volgens de springtij-doodtij-cyclus, maar deze modellen suggereren daarnaast een intrinsieke niet-lineaire dynamica van de getij-amplituden, op dezelfde of op een andere tijdschaal.

In hoofdstuk 5 worden de consequenties van het afgeleide model voor de modulatie van de getij-amplitudes nader onderzocht. Omdat de resultaten van Leo Maas, Arjen Doelman en Femius Koenderink als speciaal geval worden teruggevonden, kan

daarbij voor een belangrijk deel worden teruggegrepen op hun werk. Allereerst wordt de stationaire respons op stationaire forcering (m.a.w. de respons curve) beïnvloed door de niet-lineaire effecten. De resonantie-piek blijkt te worden gebogen, zie figuur 5.1. Daardoor zijn *meervoudige evenwichten* mogelijk: onder dezelfde externe omstandigheden (vorm en diepte van het bekken, amplitude en fase van het getij op de aangrenzende oceaan of zee) kan het bekken zowel in een toestand met grote getijden terechtkomen als in een toestand met een zwakker getij. Het hangt van de voorgeschiedenis af welk getij in het bekken zal optreden en het kan niet meer direct voorspeld worden op grond van het getij zoals dat binnenkomt uit de aangrenzende oceaan of zee. Als de externe omstandigheden langzaam veranderen, bijvoorbeeld onder invloed van zeespiegelstijging of bodemdaling, dan kan een *bifurcatie* optreden. Het kan dan namelijk gebeuren dat de toestand van het getij niet langer een oplossing is. Het systeem zal zich dan "plotseling" aanpassen naar een nieuw getij, met wellicht een hogere of lagere amplitude. Ook al zouden de externe omstandigheden vervolgens weer teruggebracht worden naar de oude waarden, dan blijft het systeem in de nieuwe toestand hangen, een verschijnsel dat *hysterese* wordt genoemd.

Wanneer de externe omstandigheden voortdurend veranderen op een tijdschaal die overeenkomt met de tijd dat het bekken nodig heeft om zich aan de nieuwe omstandigheden aan te passen (de springtij-doodtij-cyclus zou zo'n voortdurende verandering van de externe getij-amplitude kunnen zijn), dan blijven de "plotselinge" overgangen van het getij binnen het bekken voortduren. Onder die omstandigheden is binnen het model aangetoond dat de dynamica *chaotisch* kan zijn. De wiskundige chaos-theorie beschrijft *deterministische systemen* (d.w.z. in principe volledig voorspelbaar) die door niet-lineaire processen toch een grillig gedrag zonder regelmaat laten zien. Het bekendste voorbeeld van een chaotisch systeem is het weer. Als we van alle moleculen op aarde exact zouden weten hoe ze op dit moment bewegen, dan zouden we in principe tot willekeurig ver in de toekomst het weer kunnen voorspellen. Echter, zoals de Amerikaanse meteoroloog/wiskundige E.N. Lorenz (niet te verwarren met de eerder genoemde H.A. Lorentz) het formuleerde: een vlinder in Brazilië zou door een slag van zijn vleugel een tornado in Texas kunnen veroorzaken. De volgende vleugelslag zou het effect ook weer teniet kunnen doen. Waar het om gaat is dat in chaotische systemen kleine verstoringen grote gevolgen kunnen hebben. Dat zorgt ervoor dat de voorspelbaarheid die in principe mogelijk is, in de praktijk niet gerealiseerd kan worden. Een chaotisch getij zou echter haast een contradictio in terminis zijn aangezien het woord getij zijn herkomst juist vindt in zijn regelmaat. Voorspellingen van het getij worden geacht al jaren vooruit gedaan te kunnen worden en afwijkingen daarvan worden toegeschreven aan meteorologische effecten. Deze studie stelt dit enigszins ter discussie.

Om de opmerkelijke conclusies van het theoretische werk op hun betrouwbaarheid te toetsen, zijn ook laboratorium-experimenten uitgevoerd. Daarbij werd in eerste instantie geprobeerd de niet-lineaire effecten van variabele bekken-oppervlakte (door het droogvallen van een deel van het bekken bij laagwater) na te bootsen voor de Helmholtz mode. Dat werd echter bemoeilijkt doordat wrijving het effect maskeert en het optimaliseren van de *hypsometrie* (bekken-oppervlakte als functie van de waterstand) stuk liep tegen effecten ten gevolge van de kleine schaal van de opstelling. Om de wrijving te beperken werd het bekken verder verkleind en werd de verbinding tussen het bekken en de "zee" glad afgerond. Vervolgens werden wel meervoudige evenwichten waargenomen! In tegenstelling tot wat de eenvoudige theorie voor de Helmholtz mode suggereert, gebeurde dit ook wanneer de bekken-oppervlakte niet

varieerde met de waterstand. De afgeronde verbinding tussen het bekken en de "zee" bleek het verschil te maken tussen het al dan niet optreden van dit niet-lineaire effect. Vooralsnog is echter geen afdoende verklaring voorhanden. Ook het onderzoek naar de voorspelbaarheid van het getij blijft voorlopig nog actueel.

Dankwoord

Zonder de mensen tekort te willen doen die hier niet aan bod komen, omdat ik me probeer te beperken of ze vergeet te noemen, zal ik hieronder een aantal bedanken voor hun bijdrage aan het tot stand komen van dit proefschrift. Allereerst zijn daar mijn promotor Arjen Doelman en co-promotor Leo Maas, die natuurlijk meer gedaan hebben dan het opstarten en aanvragen van de financiering van het project. Arjen was verantwoordelijk voor de pragmatische kijk op de begeleiding. Een gesprek met hem vulde me telkens met goede moed om weer geïnspireerd aan het werk te gaan. Helaas werd die dagelijkse begeleiding onherroepelijk minder intensief door de fysieke afstand die ontstond toen ik naar Texel verhuisde, anders had zijn pragmatisme mij ongetwijfeld tot een sneller schrijfproces weten aan te zetten. Leo's opbouwende kritiek is altijd goed geweest voor verbeteringen, op tal van punten. Daarnaast heeft hij voor mij het doen van literatuuronderzoek vergemakkelijkt, enerzijds doordat hij me met zekere regelmaat op de hoogte hield van relevante artikelen die hij tegenkwam, anderzijds door het enorme archief op zijn kamer. Voor het vinden van een artikel ging ik in eerste instantie niet naar de bibliotheek, maar keek eerst in de kamer naast me in Leo's dozen. Voor het experimentele werk binnen dit project, was ik officieel de dagelijkse begeleider van Willem Jan van de Berg. In de praktijk werkten we samen aan de opstelling en ik wil Willem Jan dan ook bedanken voor zijn belangrijke bijdrage daaraan. Daarnaast wil ik hem bedanken voor zijn bijdrage aan het op gang brengen van de bordspellenclub op Texel; zonder zijn aanwezigheid zouden de eerste keren niet succesvol zijn geweest. Naast mijn begeleiders heeft ook Huib de Swart een belangrijke bijdrage geleverd met zijn commentaar op de artikelen die de basis van dit proefschrift vormen. Daarnaast wist hij mij (en ik heb van diverse mensen gehoord dat ik niet de enige ben) met zijn bemoediging regelmatig weer te inspireren en te enthousiasmeren. Hij behoort tot een select gezelschap van wetenschappers die ik persoonlijk op een hoog voetstuk heb staan. Ik bewonder hem om zijn didactische kwaliteiten, waar ik tot mijn vreugde veelvuldig van heb kunnen genieten, en om zijn vaardigheid een complex probleem uit te kleden tot een eenvoudig model dat toch de essentiële ingrediënten duidelijk voor het voetlicht brengt.

Mijn collega's op het Nederlands Instituut voor Onderzoek der Zee (N.I.O.Z.) dank ik voor de uiteenlopende discussies en gesprekken, over het werk, de wetenschap, over politiek, het nieuws, zeilen en andere belangrijke onderwerpen in het leven. In het bijzonder wil ik Uwe Harlander noemen, waarmee ik met plezier mijn kamer heb gedeeld, al heeft hij zich veel te snel het Nederlands eigen gemaakt, want ik had veel meer Duits van hem moeten leren. Daar staat tegenover dat hij mij met tennis, bordspellen en zijn kinderen regelmatig de broodnodige ontspanning heeft bezorgd. Lucas Merckelbach stelde mij in staat gebruik te maken van een up-to-date Linux-systeem, aangezien het bijhouden van dit deel van het netwerk op het N.I.O.Z.

niet zoveel aandacht krijgt. Hij vormde zo mijn persoonlijke Linux-helpdesk, terwijl hij me tegelijkertijd extra motivatie gaf door zijn wiskundige problemen met mij te bespreken. Op het Korteweg-de Vries Instituut van de Universiteit van Amsterdam, waren het vooral de promovendi en postdocs waarmee de lunchgesprekken in de mensa wat luchtiger van aard waren en die zich gewillig lieten verleiden tot de wereld van de bordspellen. Vooral Harmen van der Ploeg wil ik bedanken voor de tijd dat we elkaar gezellig van het werk hielden, Misja Nuyens die weliswaar niet van bordspellen houdt maar altijd opgewekt aanwezig is, en Daniel Grünberg voor verkondigen van het ware verhaal achter het nieuws over de politieke uithoeken van de wereld. Ondanks het feit dat mijn eigen bijdrage zeer beperkt is gebleven doordat ik me in de drukste periode van de voorbereiding drukte voor een zeiltocht van ruim 6 weken, koester ik ook positieve herinneringen aan de andere organisatoren van de Studiegroep Wiskunde met Industrie van 2002, Mark Peletier, Bob Planqué, Geertje Hek, Misja Nuyens en Harmen van der Ploeg.

Mijn dank gaat verder nog uit naar de stichting voor Fundamenteel Onderzoek der Materie (F.O.M.), in het bijzonder naar Joost Weber, voor het faciliteren van en vertrouwen op de afronding van dit proefschrift, zelfs op het moment dat ik zelf vol twijfels zat. In dat kader zou ik ook mevrouw van Raalte willen noemen, die me met overleg en geduld geleidelijk weer naar het werk heeft begeleidt. In mijn mailprogramma staat de afkorting "studieclubje" nog steeds voor Gert-Jan Smit, Hennie Smit, Simon Kronemeijer, Michiel le Comte, Marijne le Comte, Femius Koenderink, Nicole Koenderink, Jeroen Zijlstra, Irene Gosselink, Ingrid Giebels en Lonneke de Swaaf. Ondanks het feit dat ik van mezelf niet goed ben in het onderhouden van contacten, prijs ik mij gelukkig dat ik me nog steeds in dit rijtje mag scharen. Vooral Nicole is de afgelopen tijd per mail steun en toeverlaat geweest. Naast deze "verre vrienden" heb ik ook uitermate goede buren getroffen in mijn huisbaas, de familie Wiering. Hun vriendelijke belangstelling, maar ook hun als vanzelfsprekende hulp op velerlei terrein, is mij nu alweer ruim drie jaar zeer dierbaar. Een andere steun is mijn familie. Mijn moeder wil ik bedanken voor haar niet aflatende liefde en zorg, mijn vader voor het beantwoorden van mijn nieuwsgierige vragen toen ik klein was en mijn broers Caspar en Joachim voor het feit dat we ieder onze eigen weg in het leven zoeken en toch zo onmiskenbaar bij elkaar blijven horen, mijn tante Hanneke voor haar interesse, mijn oom Gert en zijn gezin en de rest van de familie, in het bijzonder tenslotte Opa voor zijn betrokkenheid bij alles wat ik deed, die zich hopelijk tot over de dag van zijn heengaan is blijven uitstrekken.

Curriculum Vitae

Geboren in Amersfoort op 21 maart 1977, ging Guido Terra aldaar naar het Stedelijk Gymnasium Johan van Oldenbarnevelt, waar hij in 1994 eindexamen deed in de vakken Nederlands, Latijn, Engels, Wiskunde A, Wiskunde B, Natuurkunde, Scheikunde en Economie. Die zomer nam hij deel aan de nationale Scheikunde- en de internationale Natuurkunde-Olympiade, voordat hij natuur- en wiskunde ging studeren aan de Universiteit Utrecht. De tijdens de propedeuse gevolgde keuzevakken Meteorologie en Fysische Oceanografie (M.F.O.) bevielen zo goed dat in de loop van het derde jaar de aandacht werd verlegd van theoretische natuurkunde naar M.F.O. In het vierde studiejaar volgde hij de M.R.I.-Master Class "Spatio-Temporal Patterns", een programma van een jaar colleges rond het thema "patronen in ruimte en tijd". In het verlengde daarvan studeerde hij in juni 1999 *cum laude* af in de wiskunde met een scriptie getiteld "Existence and stability of stationary solutions in a singular reaction-diffusion system", over het optreden van gelocaliseerde patronen als oplossingen van een specifieke reactie-diffusie vergelijking. De studie M.F.O. werd in april 2000 *cum laude* afgerond met de afstudeerscriptie "Cyclic bar behaviour in an idealized nonlinear model for a short tidal embayment", over de verplaatsing van zandbanken onder de invloed van getijstromen. In zijn studieperiode gaf hij verder werkcolleges bij de hoofdvakken voor eerste- en tweedejaars natuur- en wiskundestudenten. Van 2000 tot 2005 deed hij promotieonderzoek dat uitmondde in dit proefschrift "Nonlinear tidal resonance". Deze aanstelling werd gefinancierd door de stichting voor Fundamenteel Onderzoek der Materie (F.O.M.) binnen het project "Secondary tides and quasi-periodically forced nonlinear oscillators" in de F.O.M.-projectruimte 1999. Het onderzoek vond deels plaats aan het Korteweg-de Vries instituut van de Universiteit van Amsterdam (UvA) en deels binnen de Afdeling Fysische Oceanografie van het Koninklijk Nederlands Instituut voor Onderzoek der Zee (N.I.O.Z.).

Guido Terra was born on March 21 1977, in Amersfoort. There he finished high school at the Johan van Oldenbarnevelt Gymnasium in 1994. He participated in the national Chemistry Olympiad and the international Physics Olympiad that summer and started studying Physics and Mathematics at Utrecht University. In his fourth year he followed the one-year Master Class "Spatio-Temporal Patterns" organized by the Mathematics Research Institute. He obtained his Master's degree in Applied Mathematics *cum laude* in June 1999 with his thesis entitled "Existence and stability of stationary solutions in a singular reaction-diffusion system" on localized pulse solutions to a specific reaction-diffusion equation. Subsequently he finished his Master's thesis for Meteorology and Physical Oceanography entitled "Cyclic bar behaviour in an idealized nonlinear model for a short tidal embayment" on the dynamics of channels and shoals due to the transport of sediment by tidal currents, to obtain his degree in April 2000, *cum laude*. During his study he assisted in teaching first and second year physics and math students. From 2000 until 2005 he was appointed by the Dutch Foundation for Fundamental Research on Matter (F.O.M.) to perform his PhD research within the project "Secondary tides and quasi-periodically forced nonlinear oscillators", partly at the Korteweg-de Vries Institute for mathematics of the University of Amsterdam (UvA) and partly at the Physics Department of the Royal Netherlands Institute for Sea Research (N.I.O.Z.). This research resulted in the PhD thesis "Nonlinear tidal resonance".

List of Publications

Publications related to this thesis

- TERRA, G. M., DOELMAN, A. & MAAS, L. R. M. 2004 Weakly nonlinear cubic interactions in coastal resonance. *J. Fluid Mech.* **520**, 93–134.

- TERRA, G. M., VAN DE BERG, W. J. & MAAS, L. R. M. 2005 Experimental verification of Lorentz' linearization procedure for quadratic friction. *Fluid Dyn. Res.* **36**, 175–188.

- TERRA, G. M., VAN DE BERG, W. J. & MAAS, L. R. M. 2005 Experimental evidence of multiple equilibria in a tidal resonator. *in preparation.*

- STORMS, J. E. A., WELTJE, G. J., TERRA, G. M. & CATTANEO, A. 2005 Stratigraphic forward modelling of isolated sandbodies in the Holocene transgressive systems tract of the Northern Adriatic shelf, Italy. *in preparation.*

Publications not related to this thesis

- CAHYONO E., HOCHSTENBACH, M. E., MOLENAAR, J., SCHILDERS, W. H. A. & TERRA, G. M. 2001 Velocity Estimation in Mixtures using Tomography. In *Proc. 39st E.S.G.I.* (ed. B. W. van de Fliert & G. Meinsma), pp. 1–19. Twente.

- VAN DEN BERG, J. B., DAVYDOVA, N., VAN DE FLIERT, B., PEETERS, F., PLANQUE, B., VAN DER PLOEG, H. & TERRA, G. M. 2002 Reconstruction of sea surface temperatures from the oxygen isotope composition of fossil planktic foraminifera. In *Proc. 42nd E.S.G.I.* (ed. G. M. Hek), pp. 91–120. Amsterdam.